OPTIMUM POLE COMBINATION TO MAXMIZE TORQUE DENSITY IN SWITCHED RELUCTANCE MOTORS FOR ELECTRIC VEHICLE APPLICATIONS

A THESIS SUBMITTED TO
THE GRADUATE SCHOOL OF NATURAL AND APPLIED SCIENCES
OF
MIDDLE EAST TECHNICAL UNIVERSITY

BY

RASUL TARVIRDILU ASL

IN PARTIAL FULFILLMENT OF THE REQUIREMENTS
FOR
THE DEGREE OF MASTER OF SCIENCE
IN
ELECTRICAL AND ELECTRONICS ENGINEERING

SEPTEMBER 2016

Approval of the thesis:

OPTIMUM POLE COMBINATION TO MAXMIZE TORQUE DENSITY IN SWITCHED RELUCTANCE MOTORS FOR ELECTRIC VEHICLE APPLICATIONS

submitted by **RASUL TARVIRDILU ASL** in partial fulfillment of the requirements for the degree of **Master of Science in Electrical and Electronics Department, Middle East Technical University** by,

Prof. Dr. Gülbin Dural Ünver _____
Dean, Graduate School of **Natural and Applied Sciences**

Prof. Dr. Tolga Çiloğlu _____
Head of Department, **Electrical and Electronics Engineering**

Prof. Dr. H. Bülent Ertan _____
Supervisor, **Electrical and Electronics Engineering Dept., METU**

Examining Committee Members:

Prof. Dr. Muammer Ermiş _____
Electrical and Electronics Engineering Dept., METU

Prof. Dr. H. Bülent Ertan _____
Electrical and Electronics Engineering Dept., METU

Asst. Prof. Dr. Ozan Keysan _____
Electrical and Electronics Engineering Dept., METU

Prof. Dr. Kemal Leblebicioğlu _____
Electrical and Electronics Engineering Dept., METU

Prof. Dr. İres İskender _____
Electrical and Electronics Engineering Dept., Gazi University

Date: 02.09.2016

I hereby declare that all the information in this document has been obtained and presented in accordance with academic rules and ethical conduct. I also declare that, as required by these rules and conduct, I have fully cited and referenced all material and results that are not original to this work.

Name, Last Name: Rasul Tarvirdilu Asl

Signature:

ABSTRACT

OPTIMUM POLE COMBINATION TO MAXMIZE TORQUE DENSITY IN SWITCHED RELUCTANCE MOTORS FOR ELECTRIC VEHICLE APPLICATIONS

Tarvirdilu Asl, Rasul

M.Sc., Department of Electrical and Electronics Engineering

Supervisor: Prof. Dr. H. Bülent Ertan

September 2016, 234 pages

Nowadays, using Switched Reluctance Motors (SRM) as a substitute for Interior Permanent Magnet Synchronous Motors (IPMSMs) in hybrid electric vehicle applications is of great interest. The main advantage of using SRM is elimination of permanent magnet materials in machine structure. In addition, simple and robust structure, high rotational speeds and operation at higher temperatures are other benefits of using switched reluctance motors.

In this study, a combined analytical and Finite Element (FE) based method is implemented which has both the rapidity of analytical computations and the accuracy of finite element method. Normalized permeance, force and MMF data are obtained using a finite element based software for a symmetrically slotted geometry. Data sets are produced for different normalized teeth widths, normalized air gap lengths, normalized rotor positions and MMF values. The produced data are used as a look up table in calculation of normalized permeance, force and flux density values in tooth-

air gap region of switched reluctance motors. It is worth mentioning that all nonlinearities and saturation effects are taken into account while using this method.

The proposed method is capable of calculating static and dynamic performance characteristics of switched reluctance motors with an acceptable range of accuracy. Furthermore, an analytical model based on actual variation of core flux and its harmonic components is developed to calculate core loss and efficiency of the SRM. In order to corroborate the precision of the proposed analytical model, two switched reluctance motors are simulated using 2D finite element method. Comparing analytical calculations with simulation results and measurements proves the accuracy of the model and its suitability to be used for optimization purposes.

A general design methodology is proposed which can be used in designing switched reluctance motors to be used in various applications. At the final step, Genetic Algorithm (GA) optimization method is implemented to determine the optimum pole combination, geometry and excitation pattern for a 50 kW switched reluctance motor to be used in a specific hybrid electric vehicle application. Designing a high torque density switched reluctance motor is the main aim of the optimization problem.

Finally, the optimized SRM is simulated using finite element method to validate optimization results. Improvements in torque density and efficiency of the machine is compared to existing prototypes in the literature for this specific application.

Keywords: Switched reluctance motors, Finite element method, Hybrid electric vehicles, Design optimization, Genetic algorithm, Analytical model, Core loss, Torque density.

ÖZ

ELEKTRİKLİ ARAÇ UYGULAMASI İÇİN MOMENT YOĞUNLUĞUNU ENÇOKLAMAK İÇİN ANAHTARLAMALI RELÜKTANS MOTORDA OPTİMUM KUTUP KOMBİNASYONU

Tarvirdilu Asl, Rasul
Yüksek Lisans, Elektrik ve Elektronik Mühendisliği Bölümü
Tez Yöneticisi: Prof. Dr. H. Bülent Ertan

Eylül 2016, 234 sayfa

Günümüzde, hibrit elektrikli araç uygulamalarında IPMSM'ler için bir alternatif olan Anahtarlamalı Relüktans Motorları (ARM) tip motorlara büyük bir ilgi söz konusudur. SRM kullanımının temel getirisi, makine yapısından kalıcı mıknatısların çıkarılmasıdır. Ayrıca, basit ve sağlam yapısı, yüksek dönme hızları ve yüksek sıcaklıklarda çalışabilme de SRM kullanımının diğer getirilerindendir.

Bu çalışmada, , sonlu eleman ve analitik yöntemlerin birleşiminden oluşan bir metod takip edilmiş olup, söz konusu metod sonlu eleman yönteminin hassasiyetine ve analitik yöntemlerin hızlılığına sahiptir. Normalize edilmiş permeance, güç ve MMF verileri, simetrik oluklu bir geometri için sonlu eleman yöntemi temelli bir yazılımdan elde edilmiştir. Normalize edilmiş diş genişlikleri, hava boşluğu uzunlukları, rotor konumları ve MMF değerleri için veri setleri oluşturulmuştur. Üretilen veri, SRM'nin diş ve hava boşluğu bölgesindeki normalize permeance , güç ve akı yoğunluğu değerlerinin hesaplanmasında tablo olarak kullanılmıştır. Bütün doğrusal olmayan etkilerin ve manyetik doyum etkilerinin hesaba katılmış olduğu not edilmedilir.

Önerilen yöntem, kabul edilebilir hassasiyet sınırları çerçevesinde, anahtarlamalı relüktans motorların dinamik ve statik başarım karakteristiklerini hesaplama yeteneğine sahiptir. Ayrıca, anahtarlamalı relüktans motorların çekirdek kayıpları ve verimlerinin hesaplanması için çekirdek akısı ve harmonikleri üzerinden bir analitik model de geliştirilmiştir. Önerilen analitik modelin hassasiyetinin doğrulanması amacıyla, iki adet anahtarlamalı relüktans motor için iki boyutlu sonlu eleman yöntemi metoduyla benzetimler yapılmıştır. Analitik hesapların ve benzetim sonuçlarının karşılaştırılmasıyla, önerilen modelin hassasiyeti ve optimizasyon çalışmalarında kullanımının uygunluğu kanıtlanmıştır.

Çok sayıda farklı uygulama için anahtarlamalı relüktans motorlar tasarımında kullanılabilecek genel bir tasarım metodolojisi teklif edilmektedir. Son aşamada, belirli bir hibrit elektrikli araç uygulamasında kullanılacak 50 kW gücünde bir anahtarlamalı relüktans motorları için, eniyi kutup kombinasyonu, geometrisi ve uyartım şeklinin belirlenmesi için Genetik Algoritma (GA) optimizasyon yöntemi kullanılmıştır. Yüksek tork yoğunluğuna sahip bir SRM tasarımı, optimizasyon sürecinin ana amacıdır.

Son olarak, optimize edilmiş SRM, sonlu eleman yöntemi ile incelenerek optimizasyon sonuçları doğrulanmıştır. Tork yoğunluğu ve verimde sağlanan ilerlemeler, söz konusu uygulama için literatürde var olan prototiplerle karşılaştırılmıtştır.

Anahtar kelimeler: Anahtarlamalı relüktans motorları, Sonlu elemanlar yöntemi, Hibrid elektrikli araçlar, Tasarım optimizasyonu, Genetik algoritma, Analitik model, Çekirdek kayıpları, Tork yoğunluğu.

To my family

ACKNOWLEDGEMENTS

I would like to express my sincere gratitude to my supervisor Prof. Dr. H. Bülent Ertan, for his continuous guidance, support, motivation and the confidence he has shown in me throughout my studies. His constant encouragements in my dissertation work has helped me to look forward to the future with enthusiasm and confidence.

I would like to thank Assistant Prof. Dr. Ozan Keysan for his precious suggestions during my studies.

I owe my deepest and warmest thanks to my family who give me strength and encouragement throughout my studies. I am so grateful to my father Mohammadbagher, my mother Fariba and my younger siblings Ali and Mahdieh for their everlasting supports both emotionally and financially, in completing this endeavor.

I would like to acknowledge the assistant of my invaluable friend, Reza Zeinali, who was always available for discussions on my dissertation ideas. I also appreciate the support of my friends Armin Taghipour, İlker Şahin, Meysam Foolady, Ramin Rouzbar, Siamak Pourkeivannour, Vahid Haseltalab, Sadra Azizi, Salar Koushan, Nina Razi and Payam Allahverdizadeh for always promoting me and believing in me throughout my studies.

TABLE OF CONTENTS

LIST OF TABLES

TABLES

LIST OF FIGURES

FIGURES

CHAPTER 1

INTRODUCTION

1.1 Motivation and purpose of the study

High power density and high efficiency of permanent magnet machines have made these motors a popular choice to be used in various applications including Hybrid Electric Vehicles (HEV). Cost and limited resources of permanent magnets, and especially rare earth materials like NdFeB causes a general trend towards using rare earth free machines. Switched Reluctance Motors (SRM) are considered as an option to replace rare earth permanent magnet motors. These motors have concentrated windings on stator teeth like DC motors and no windings or magnets on rotor [1]. Operational principles of switched reluctance motors can be found in [2] in details. Low cost, capability of operation in environments with high temperatures and robust structure of rotor are some advantages of switched reluctance motors [3]. On the other hand, lower power density, higher acoustic noise and vibration, lower efficiency and a unique inverter circuit are some disadvantages of SRM in comparison with permanent magnet machines [4].

Nowadays, a lot of research has been conducted on increasing torque density [5, 6], decreasing torque ripple [7-10] and design optimizations [11-14] of switched reluctance motors in order to make them a strong alternative for permanent magnet machines. Therefore, switched reluctance machines are selected to be studied in this research. Determination of optimum pole combination, geometry and excitation pattern for SRMs in order to maximize torque density of these machines to be employed in a specific HEV application is aimed in this study. However, the proposed optimization method can be implemented in designing switched reluctance motors to be used in variety of applications.

1.2 Requirements for EV applications

A comparative investigation while taking efficiency, weight and cost of four different types of electric motor drives is carried out in [15] to determine the most appropriate electric motor for EV applications. The results are reported in Table 1-1.

Table 1-1 Comparison of four different electric motor drives to be used in EV applications

index	DC motor drives	IM drives	PM BLDC motor drives	SRM drives
Efficiency	2	4	5	4.5
Weight	2	4	4.5	5
Cost	5	4	3	4
Total	9	12	12.5	13.5

Note that in this table, 5 marks represent the highest efficiency, lowest cost and lowest weight. Therefore, SRM drives are the most appropriate for this specific application in comparison with other three drive types. However, switched reluctance motors have lower torque density and higher torque ripple in comparison with other electric motors used for HEV applications. Maximization of torque density of SRMs is the main aim of this study.

Different switched reluctance motors have been designed during last two decades to be used in full and medium size vehicles. By defining torque density as maximum torque of the motor divided by the motor volume, a comparison can be made. Note that in calculation of motor volume stator outer diameter and the axial length of the machine are considered. Axial length consists of the core stack length and end winding lengths at both sides of the core.

In most of the designed switched reluctance motors in the literature, torque density of the machine is between 10-15 N.m./L [16-18]. A switched reluctance motor with outer diameter of 410 mm and axial length of 93 mm was tested in Australia to deliver the output torque of 300 N.m.. Therefore, torque per motor volume of this SRM reaches 25 N.m./L [19]. In [20], a SRM is designed with an outer diameter of 640 mm and an axial length of 190 mm. The proposed motor has the torque density of 30

N.m./L. A SRM with outer diameter of 396 mm and axial length of 96 mm is designed by Ford to deliver the maximum torque of 300 N.m. [21]. Hence, torque density of this SRM is expected to reach 45 N.m./L. However, maximum torque density of 38 N.m./L is obtained in experiments. It has to be noticed that the current density of this machine reaches 50 A/mm^2. In [22], a 50 kW SRM is proposed which is capable of developing a maximum torque of 340 N.m. at rotational speed of 1200 rpm. Torque density of this machine is reported to be 38.6 N.m./L. In this study, a switched reluctance motor with a maximum target torque or 400 N.m. at 1200 rpm is proposed by the author. It is aimed to reach the maximum torque density of 45 N.m./L. Outer diameter and axial length of the machine are set to 269 mm and 155 mm respectively.

It has to be mentioned that current density of the machine is an important factor which has to be taken into account in designing electrical machines. RMS current density of 33 A/mm^2 is reached in this study. This huge current density value can cause some problems related to operating temperature of the machine. So, a special attention has to be paid to design the cooling system and insulation of this machine.

In order to investigate the best combination of poles, optimum geometry and optimum switching pattern to reach the target of this thesis an accurate design method is needed. For this purpose, the static torque and flux linkage characteristics, torque-speed characteristic, and efficiency of the motor should be calculated with good accuracy. Other performance characteristics of the motor can be calculated from these fundamental performance parameters. Performance of a SR motor greatly depends on the drive and its control method. In the following sections each of the issues mentioned above will be briefly considered and the approach adopted by other researchers will be briefly discussed. In the succeeding chapters the methods used in this thesis for performance calculation will be discussed in detail. Also the accuracy of the adopted methods will be verified before going ahead with the search for the best SRM design for electric vehicle applications.

1.3 Structure of switched reluctance motors

A switched reluctance motor consists of a salient pole stator with concentrated windings on it. Moreover, there are no windings or magnets on a salient pole rotor which makes this machine capable of working at higher rotational speeds. Operation principle of these machines is based on the reluctance torque. Once a stator phase is excited, rotor starts rotating in order to align itself with the excited stator poles and reduces the flux path reluctance. A 3-D representation of an 18/12 SRM is depicted in Figure 1-1.

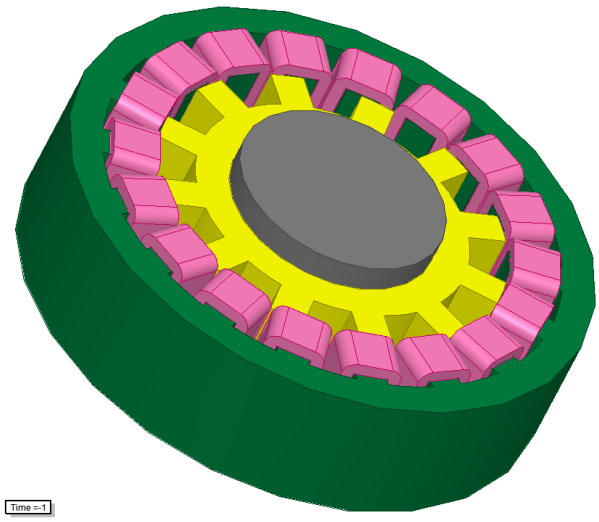

Figure 1-1 3-D representation of an 18/12 SRM

The most common pole combinations used in switched reluctance motors structures are summarized in Table 1-2. Moreover, number of phases in each pole combination is also determined.

Table 1-2 The most common pole combinations of switched reluctance motors and the corresponding number of phases

N_s / N_r	6/4	8/6	12/8	18/12	24/18
q (number of phases)	3	4	3	3	4

Note that number of phases in a switched reluctance motor with a specific N_s/N_r is unique and can be simply calculated using

$$q = \frac{N_s}{\mathrm{GCD}(N_s, N_r)} \tag{1-1}$$

where N_s and N_r stand for number of stator and rotor poles respectively. GCD (N_s,N_r) represents the Greatest Common Devisor of number of stator and rotor poles. It is obvious that in 6/4 and 8/6 switched reluctance motors, each phase consist of two opposite stator poles which are connected in series. However, in 12/8 each phase consists of 4 stator poles. Finally, in 18/12 and 24/18 motors each phase consists of 6 stator poles.

1.4 Static torque characteristic of a SR motor

Prediction of static torque-position-current and flux linkage-current-position characteristics of the SRM is an important task in determination of motor performance. Static torque-position-current characteristic represents the developed torque of the SRM at each rotor position between IN (completely aligned) and OUT (completely unaligned) conditions and for different excitation levels. On the other hand, flux linkage-current-position characteristic of a switched reluctance motor determines flux linkage of two opposite poles of a SRM which are connected in series for various excitation levels (winding currents) and at different rotor positions between IN and OUT conditions. Using these two static characteristics, steady state dynamic torque, current and flux variations and other performance characteristics of a SRM can be calculated.

Due to nonlinear nature of the magnetic circuit and saturation effects accurate determination of static characteristics is not an easy task. In [23, 24] Finite Element Method (FEM) is implemented to calculate static characteristics of a SRM. [25] discusses computer based methods to calculate the electromagnetic characteristics of these motors. Miller and McGilp introduce an analytical and fast method based on

piecewise analytical formulation. This method is implemented to calculate static characteristics of switched reluctance motors which can be used for rapid computer aided design and calculation purposes [26]. Static characteristics of a 4 phase switched reluctance motor is determined using experimental studies in [27]. However, a routine and general method is required to determine static characteristics of a SRM precisely. All above mentioned methods are used to calculate the characteristics for a specific switched reluctance machine.

In this study, Static characteristics of SRM are predicted using normalized permeance and force data calculated by Ertan [28]. Ertan uses a repetitive element method to determine permeance and force values on symmetrically slotted geometries. Further analytical calculations are carried out and a general method is proposed which calculates force and permeance data for any asymmetrically slotted geometries. Necip Besenek [29] expands the data using finite difference method to be used for structures with higher values of tooth pitch over air gap length ratio (λ/g). Ibrahim [30] investigates the accuracy of this data using Finite Element Method. In previous studies number of data were limited, and interpolation were used to estimate the data. However, in this study, data are expanded up to 100 times to cover more intermediate points which increases the accuracy of the predictions to a highest degree. Data production procedure is carried out using Maxwell 2D parametric solution option embedded inside the software. Furthermore, Artificial Neural Networks (ANN) are used to predict the static performance of the SRM which is more accurate in comparison with interpolation method. These normalized data sets are implemented in this study in order to calculate static torque-position-current and flux linkage-current-position characteristics of switched reluctance motors. Tangential force and MMF values can be simply determined for any asymmetrically slotted geometry with a specific normalized teeth width and air gap length, and at any rotor positions for different values of pole flux density. Hence, developed torque and the flux linkage values can be computed for different excitation levels and rotor positions. A detailed description on calculation method will be given in upcoming chapters.

1.5 Drive circuits for SR motors

The general structure of a prototype three phase switched reluctance motor drive is shown in Figure 1-2. In such a machine winding current directions do not have any contributions in machine performance, so a unipolar drive circuit can be used. This figure represents a unipolar drive scheme which is suitable to control a SRM.

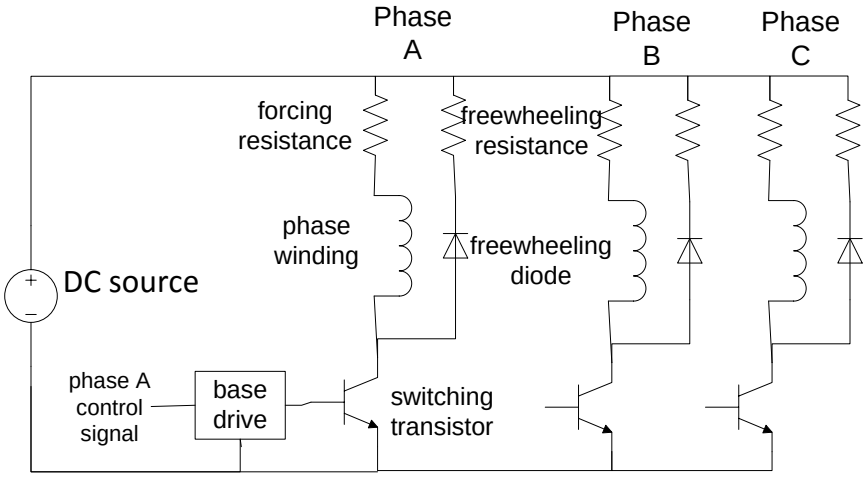

Figure 1-2 A prototype three phase switched reluctance motor drive

As it is obvious from the figure, the drive circuit consists of three separate legs, each one controlling the corresponding phase. Each phase winding is excited whenever the control signal is applied to switching transistor. This control signal is produced by taking a position feedback and analyzing it based on the exerted excitation pattern. Details of producing control signals to control switching sequences will not be discussed in this thesis. While a transistor is switched on the full DC voltage is applied to the corresponding phase winding and forcing resistance. This forcing resistance is added to reduce current rising and falling time constants at switching instants and have a better control over phase current.

The freewheeling path is also provided to let the current decay after the phase switch is turned off. Series combination of freewheeling and forcing resistances determines the current falling time constant. In switching off interval energy stored in phase winding inductance dissipated in the resistances.

It is worth mentioning that other topologies of drive circuits have been introduced in order to reduce losses in series resistances. Some circuits are designed in a manner that forcing resistance goes out of the circuit after the current reaches to its nominal value. This reduces unnecessary ohmic losses during one phase conduction and has a contribution in improving drive efficiency. Furthermore, in some applications falling current during switch off interval completes its path from the DC source and causes the phase inductance energy to be restored.

Two commonly used drive topologies are bilevel drive and chopper drive [31]. These configurations are shown in Figure 1-3 and Figure 1-4. As a brief explanation, in a bilevel drive high voltage source (V_H) is used during switching intervals to increase applied voltage and consequently reduce current rise and fall time constants. On the other hand, in normal conduction period only low voltage source (V_L) contributes in maintaining the current at rated value. So, additional losses in forcing and freewheeling resistances are omitted, and current is controlled by controlling over applied voltage.

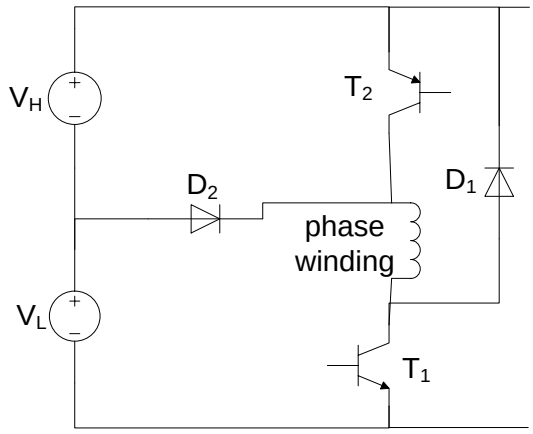

Figure 1-3 Bilevel drive topology

In a chopper circuit only a high voltage source is utilized. Current in phase windings are monitored via sensing voltage drop across resistance R_c. When the current passes slightly above rated value switch T_2 is turned off and current decays slightly in a loop containing phase winding, Rc, diode D_1 and switch T_1. On the other hand, while the current falls below rated value switch T_2 is closed. At the end of

excitation period both switches are turned off and current decays to zero rapidly in a loop containing the DC source.

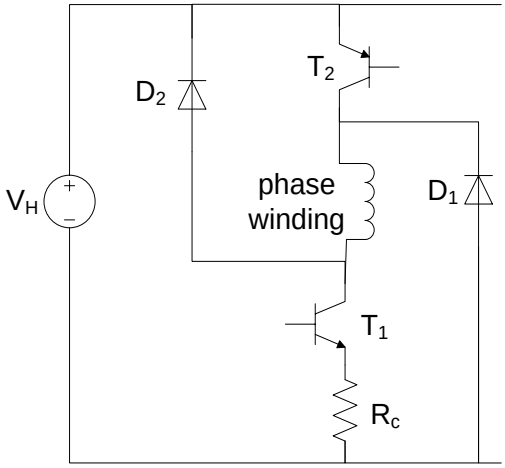

Figure 1-4 Chopper drive topology

In order to improve the acceleration or deceleration capability of the drive voltage boosting scheme is used. This circuit works by storing energy in a capacitor which can be discharged quickly to increase the exerted voltage during acceleration or deceleration intervals.

In this thesis an ideal drive circuit is considered. Switching losses and voltage drops on switches in drive circuit and chopper topologies will be neglected in analytical calculations. It means that in normal conduction period of a phase, the DC source is assumed to be directly connected to the phase winding. When it is desired to reduce the current using chopping action, the phase winding is short circuited and the current completes its path through a freewheeling diode which can be easily seen in Figure 1-2. Note that, as stated before, freewheeling and forcing resistances and voltage drops on diodes and switches are neglected in this study. Finally, at turning off point of a phase, DC voltage source is reversely connected to phase winding to accelerate the current falling and cause energy to move back to the DC supply.

1.6 Dynamic steady state performance calculations and predictions of torque-speed curves of SR motors

After determination of Static characteristics and drive circuit specifications of a SRM, its dynamic performance can be predicted. Exact prediction of flux linkage and static torque characteristics of a SRM is necessary in precise determination of instantaneous torque and current values. In several studies, calculated inductance values are used to solve differential equations to determine dynamic characteristics of SRMs [32-34]. Inductance values can be calculated using static flux linkage characteristic. Once the inductance values are determined, instantaneous currents can be calculated by solving the following differential equation using iterative methods.

$$V = Ri + L(\theta,\mathrm{i})\frac{di}{dt} + \frac{dL(\theta,i)}{d\theta}\omega_m i \tag{1-2}$$

Once the instantaneous current is determined in each iteration, instantaneous torque can be calculated easily by interpolation from static torque-position-current data at the specified rotor position. It has to be mentioned that mutual inductances between adjacent phase windings are neglected. Furthermore, the developed torque can also be computed in each iteration using the following equation.

$$T_e = \frac{1}{2} i^2 \frac{dL(\theta,i)}{d\theta} \tag{1-3}$$

However, in this study, dynamic current calculations are carried out based on flux linkage data obtained in static computations stage [35]. Elimination of inductance calculation omits the possible error sources due to highly nonlinear characteristic of the machine and is the main advantage of this method. It is noticeable that in the method used in this study, it is needed to solve differential equations, however, instead of inductance data, static flux linkage data are implemented in calculation of the instantaneous current value. Runge-Kutta method is implemented to solve differential equations in this study. Furthermore, instantaneous torque is calculated using normalized force data obtained using finite element method which increases the

calculation precisions to a highest degree. It has to be taken into account that static torque calculation can also be carried out using flux linkage data using co-energy method [36-38] which cannot be as precise as the proposed method because of nonlinear nature of the motor. In calculation of static torque characteristics using co-energy method, the electromagnetic torque equals the derivative of the magnetic co-energy with respect to angular position under the constant current condition.

$$T_e = \frac{\Delta W_{co-energy}}{\Delta \theta} \Big|_{i=constant} \tag{1-4}$$

So, by integrating static flux linkage data while changing the rotor position and under a constant current condition, electromagnetic torque can be simply computed.

It has to be mentioned that dynamic current and torque are calculated for a constant rotational speed. However, the above mentioned differential equations can be solved at different speeds to determine the torque speed characteristic of the switched reluctance motor. Note that torque speed characteristic of a SRM is also dependent on the excitation pattern. This characteristic can be used to determine the speed range in which the motor is capable of developing the desired power.

1.7 Copper and core loss calculation

Accurate calculation of copper and especially core losses in a SRM is a crucial step in determination of motor efficiency. Various methods have been proposed to compute losses and efficiency of switched reluctance motors in the literature. A new method based on variable loss coefficients by discretizing the machine into limited number of elements based on magnetic flux density distribution is proposed in [39]. [40] proposes a new method based on Reluctance Network Analysis (RNA) in which the core is modeled using nonlinear reluctances and magnetic inductances. This paper implements a method based on determination of real flux variation and its harmonic components in the SRM in order to calculate core losses of the machine (see chapter 3) [41-43]. Core losses of the machines with M36 steel type are then determined using

a method proposed by Pillay [44-46]. Determination of core loss coefficients are also discussed in [47]. Core loss coefficients of super core 10JNEX900 which is used as a core material for this specific HEV application, can be easily found in corresponding data sheets. Core loss data and magnetization curves of all the core materials used in this study are also given in the appendix.

1.8 The aim of the thesis

Once the proposed analytical model is capable of predicting SRM static and dynamic characteristics as accurate as possible, the model can be utilized for design purposes. Lack of a thorough optimization method which considers all stator and rotor pole combination selection, dimensions and excitation patterns together as independent variables of optimization was an incentive which encouraged the author to consider such a general optimization problem as the purpose of this study. Existing studies in the literature examine the effect of limited number of variables on performance of switched reluctance motors. Funda [7, 8] discusses effects of SRM air gap geometry to minimize torque ripple of the machine. Effects of switching pattern and stator teeth/rotor teeth ratio are not taken into account in calculations. The optimization is carried out based on static data, and dynamic behavior of the SRM is not considered. High speed capabilities of 6/4 and 8/6 switched reluctance motors for Electric Vehicle (EV) applications are discussed and compared in [48]. This paper fails in thorough consideration of effects of different pole combination types in SRM performance. Static and steady state characteristics of SRM are discussed for four different selected pole combinations in [49]. Four different SRM motors are studied. However, the effect of geometry variations and switching patterns are not considered in this study. Determination of optimum design for a 6/4 SRM to be used as an electric vehicle drive is studied in [50]. This paper considers the geometric dimensions of SRM as the independent variables of optimization. An analytical method based on reluctance network is developed which takes magnetic nonlinearities into account. Finite Element Method is utilized in order to validate the proposed analytical model. However, this

paper fails in investigation of the effects of changing pole combination of the SRM in optimization results. Moreover, solving the proposed analytical method is time consuming which is not appropriate for optimization purposes. Akira Chiba [4] claims that 18/12 pole combination has the highest torque density in comparison with others, but the idea is based on experimental results and a general optimization has not been carried out. This motor is introduced as an alternative for Interior Permanent Magnet Synchronous Motors (IPMSM) that can be used in Hybrid Electrical Vehicle (HEV) applications.

Reduction of air gap effect (decreasing air gap length) on efficiency and torque density of a SRM to be used in servo drive applications is discussed in [51]. Design of a high torque density and high efficiency 400 W SRM for servo drive applications is aimed in this study. It is claimed that the SRM can compete with 400 W permanent magnet synchronous servo motor. In other words, it is mentioned that SRM can compete with PM synchronous machines in small rated power range applications. A flux tube based nonlinear magnetic analysis is proposed. Finally, a genetic algorithm based optimization under the constraints of equal outer dimensions and equal power ratings is carried out. A SRM with 0.1 mm air gap with an efficiency higher than 85% is built and tested. This paper claims that SRM can compete with PM synchronous motors in lower power ranges. However, performance of these motors are not compared with PM motors with large power ratings.

A combination of Particle Swarm Optimization (PSO) and Design of Experiments (DoE) methods is used to solve a multi-objective optimization problem in order to find the optimum SRM geometry in [12]. Sensitivity analysis is done to detect the important design variables of the optimization. It is aimed to increase torque per motor active mass, SRM efficiency, and reduce the torque ripple of the machine. Finally, a sample 1.5 kW, 6/10 SRM is optimally designed and the results are compared to traditional optimal design methods, using finite element methods. It is claimed that the proposed analytical method has the same accuracy as the finite element method. The author states that using this approach, the time needed to perform the optimizations is significantly reduced. However, effects of pole combinations,

commutation angles and conduction period on objective functions are not taken into account.

Numerous other papers discuss the effects of SRM parameters on machine performance via optimization [11, 13, 14, 51-56]. However, the impact of limited variables are considered in machine performance optimization in these papers. Author of this thesis noticed that a thorough optimization method which can be as a general design guide for switched reluctance motors that can be used in variety of applications is needed.

In this study, a comprehensive optimization is carried out which considers the effects of variations in all stator teeth/rotor teeth ratio, machine geometry, turning on and off angles and conduction period in SRM performance.

An initial design of SRM is performed for each switched reluctance motor in this study based on independent variables of optimization. Various design methodologies have been proposed in the literature [57-60] for SR motors. In this paper a design methodology based on [61] and [62] is developed which includes the design of machine geometry, and winding configuration which will be discussed in detail in this thesis. Once the main dimensions of the SRM are determined, using Genetic Algorithm (GA) optimization method, an initial design is done to determine other geometric dimensions and drive circuit characteristics. Stator pole height and number of turns per pole are determined by consideration of constraints on maximum allowable slot fill factor and maximum current density. Furthermore, an analytical method is proposed to determine the end winding length of the machine. Note that a constraint is imposed on maximum axial length of the SRM including stack length and end winding length. Hence, minimization of end winding length is an important step towards increasing torque density of the SRM. Maximum and minimum chopping currents are also determined based on the maximum allowable current density and maximum magnetic flux density values. A detailed discussion on above mentioned initial design process is given in chapter 5.

At the end, a mathematical optimization problem is carried out in which maximization of the SRM developed torque, as the objective function of the

optimization, under specific constraints on machine geometry, and magnetic and electric loadings is aimed. Genetic Algorithm (GA) is implemented as the optimization tool to determine the optimum geometry and excitation patterns for each pole combination. A detailed discussion on optimization results for each pole combination is given in chapter 6. Finally, an optimized 50 kW switched reluctance motor to be used in hybrid electric vehicle applications is proposed which has a higher torque density in comparison with prototypes in the literature. The optimized motor is simulated using finite element method to validate analytical optimization results. Improvements in torque-speed characteristics of the optimized motor will also be discussed. It will be shown that the optimized motor can develop the desired output power of 50 kW at a wider speed range (in the desired speed range of 1200-6000 rpm) in comparison with the existing prototype in the literature. Improvements in motor output torque, effective mass of the machine and other performance characteristics of the optimized SRM will be discussed in detail in chapter 6. It is worth mentioning that the method proposed in this study can be considered as a design guide for researchers in designing switched reluctance machines to be used in variety of applications.

CHAPTER 2

ANALYTICAL CALCULATIONS OF THE SRM PERFORMANCE

The initial aim of this study is the accurate prediction of switched reluctance motor static and dynamic characteristics for any given machine geometry. In this case, an optimization method can be developed based on a precise analytical model. For this purpose, a method which calculates motor characteristics using a procedure, which utilizes FEM-based normalized data to carry out analytical calculations, is developed. In this chapter, analytical method implemented in calculation of tangential and normal forces, tooth flux density and normalized permeance data will be described. Finally, static torque and flux linkage characteristics computations and dynamic performance calculations of SRM using normalized data will be explained. This accurate analytical model can then be used for optimization purposes. Torque density optimization of a 50 kW SRM to be used in HEV applications is the main aim of this study, which will be discussed in detail in chapters 5 and 6. Optimum geometry, pole combinations and excitation pattern will be sought for a switched reluctance motor to be used in this specific application. It has to be mentioned that the proposed optimization method is general and can be used in designing different kinds of switched reluctance motors to be used in variety of applications.

2.1 Prediction of tooth flux density, normalized permeance and force data

In previous studies, sets of normalized data are used as a look up table to predict static torque and flux linkage curves and dynamic performance characteristics of a SRM. Necip [29] uses finite difference method to compute normalized data. Moreover, finite element method is utilized by Ibrahim [30] to reproduce the above mentioned data. In the previous studies, if data are needed for intermediate parameters,

interpolation methods were used. However, the author of this thesis preferred to use a neural network for predicting force and permeance for intermediate parameter values. For this reason, normalized data is produced using finite element method using a parametric solution option embedded inside Maxwell software, however, number of produced data is 100 times larger than what is produced by Necip and Ibrahim. Advantage of increasing number of normalized data sets is increasing the accuracy of analytical interpolations and predictions using artificial neural networks. So, the accuracy of static and dynamic performance computations is increased.

In this section, tangential and normal forces, tooth flux density and normalized permeance data are produced for various normalized geometries using Finite Element Method (FEM). This data (see Appendix C) then will be utilized in prediction of static and dynamic characteristics of switched reluctance motors. The geometry based on which the normalized data are produced is discussed in the first section. Then some selected calculated results are compared to the results in previous works in section 2.1.4.

2.1.1 Geometry specifications

In order to produce a set of data which can be used in design of Switched Reluctance Machines (SRMs) the geometry which is shown in Figure 2-1 is used. In this study, from now on, this geometry will be referred as Ertan's geometry. Corresponding dimensions are shown on the figure in millimeters. Model depth in Z direction is taken as 1 meter.

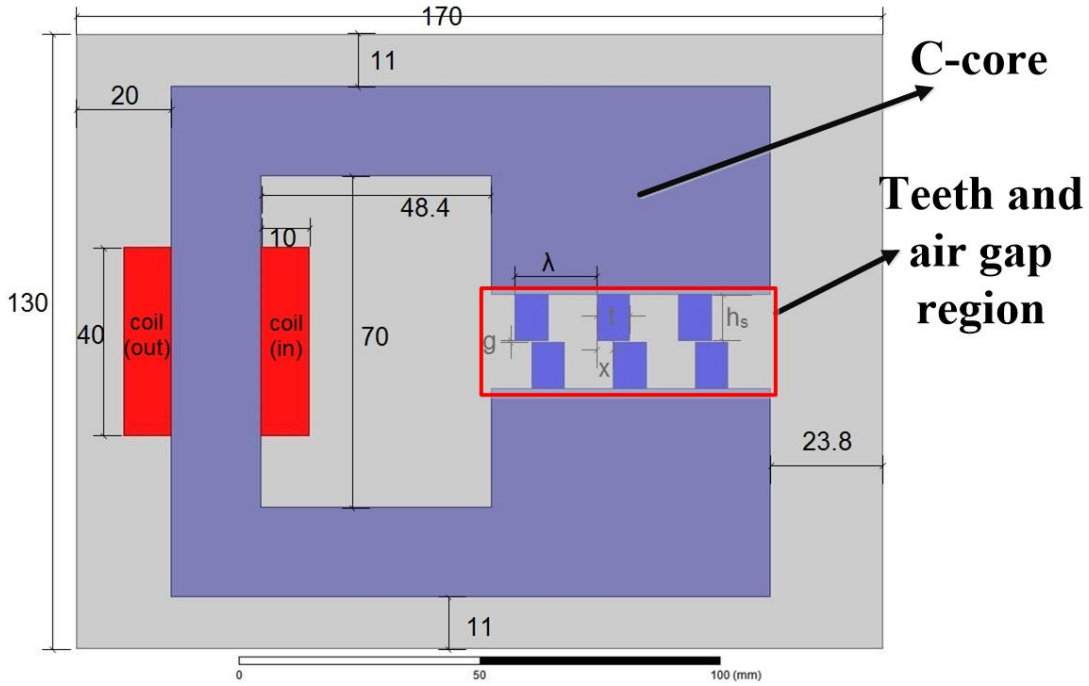

Figure 2-1 Basic geometry for production of normalized data sets (g=0.245, λ/g=70, and all dimensions in mm)

In this geometry C-core is taken as infinitely permeable to eliminate effects of any MMF drops on it. Also an air region is considered outside of the model to take into account flux leaking the air due to possible teeth saturation. This region can be simply distinguished in Figure 2-1 as a grey area around the C-core. B-H curve of the material used in teeth is same as the material used in the literature [8, 29, 30, 63-65]. B-H curves (magnetization curves) and core loss curves of all the materials used in this study are given in the appendix A.

Tooth pitch is 17.2 mm for this geometry. Flux density, permeance and tangential and normal forces on upper and middle tooth are calculated for different sets of variables. Normalized geometric variables used to produce data sets are summarized in Table 2-1. It is obvious that 41580 different geometries will be produced using these four input parameters. These 41580 geometries will be used to train neural networks which will be discussed in upcoming sections. The reason why the total number of

geometries is 41580 can be simply understood by multiplying total number of variations of four variables (λ/g, t/ λ, MMF and x_n).

$$11\times3\times60\times21=41580 \quad (2\text{-}1)$$

Table 2-1 Variable parameters of the basic geometry

variable	explanation	Variation range	Number of points
λ/g	Tooth pitch to air gap length ratio	40 to 250 with steps of 15	11
t/ λ	Tooth width to tooth pitch ratio	0.3 to 0.5 with steps of 0.1	3
MMF	Excitation MMF by the winding	50 to 3000 A with steps of 50 A	60
$x_n=2x/\lambda$	Normalized position	0 to 1 with the steps of 0.05	21

It is worth mentioning that the reason of selecting maximum value of 3000 Ampere turns for MMF is that for MMF values higher than 3000 Ampere turns the teeth operate at a very high flux density and consequently in a heavy saturation region. So, maximum MMF value of 3000 Ampere turns covers all possible operating points of the core, even under heavily saturated conditions, for all possible variations of λ/g, t/ λ and x_n. Covering all possible operating points of the core by normalized data sets is essential in order to predict the tooth flux, winding flux linkage and dynamic performance characteristics of the SRM even under heavily saturated conditions. The calculation of tooth flux density, tangential and normal forces and normalized permeance form the field solution is explained below.

2.1.2 Calculated parameters

For different combinations of λ/g, t/ λ, MMF and x_n, average tooth flux density, normalized permeance and tangential and normal forces are calculated for the given geometry. A detailed description on calculation procedure is given below. This data will then be utilized in training neural networks in order to predict static and dynamic

characteristics of a switched reluctance motor. It is worth mentioning that the main advantage of the proposed calculation method is using sets of normalized and dimensionless data which are independent from geometric parameters and can be used for performance calculations and design purposes of switched reluctance motors to be used in variety of applications. Because the normalized data are produced using FEM, the proposed computation method has the high accuracy.

2.1.2.1 Average tooth flux density

Average flux density is calculated in upper and middle tooth. Total flux passing the tooth pitch is divided by the tooth width. The total flux passing a tooth pitch is calculated by integration of the flux density on a line shown in Figure 2-2.

$$B_{av} = \frac{1}{t}\int_{0}^{\lambda} B_t.dl \qquad (2\text{-}2)$$

It has to be emphasized that the flux is calculated in one tooth pitch. However, flux density (B_{av}) is computed by dividing this flux by corresponding tooth width (t).

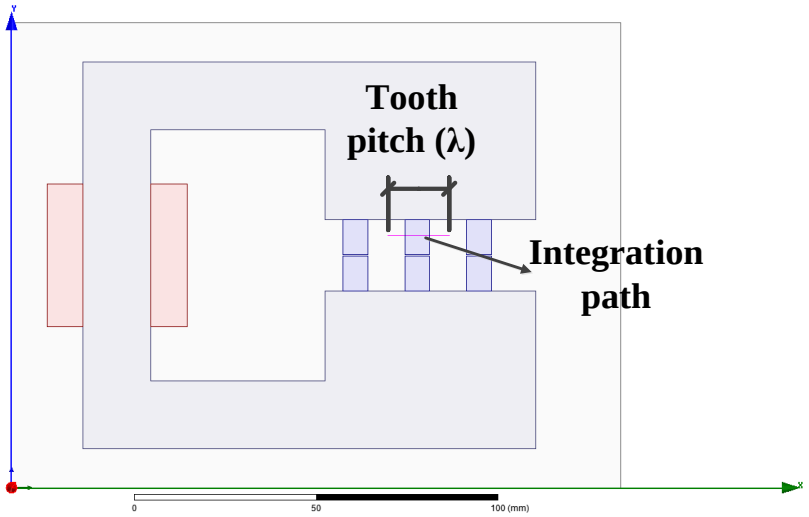

Figure 2-2 Flux density integration line

2.1.2.2 Normalized permeance

Once the flux passes through the tooth pitch region of upper and middle tooth and completes its path through the corresponding air gap region and bottom teeth, it faces a permeance which is depicted by P_x in this study. So, this tooth pitch permeance can be calculated using equation (2-3). Note that φ stands for the flux passes from one tooth pitch of the upper and middle tooth as stated in previous section.

$$P_x = \frac{\varphi}{N \times I} \tag{2-3}$$

N×I is the total MMF excited by the winding. Furthermore, φ represents total flux passing the tooth pitch as shown in Figure 2-2. This flux is calculated easily as follows.

$$\varphi = \int_0^l B_t . dl \tag{2-4}$$

However, in this study, it is aimed to produce normalized and dimensionless data which can be utilized for performance calculations and design purposes of switched reluctance motors. Hence, this flux path permeance is normalized by dividing it into a base permeance. So, normalized permeance (P_n) is calculated using

$$P_n = \frac{P_x}{P_{base}} \tag{2-5}$$

Base permeance (P_{base}) is defined as the permeance of an air gap region (with length of g) with an axial length of 1 m and width of λ=17.2 mm (tooth pitch) and can be computed using equation (2-6). Note that in this equation λ/g is normalized tooth pitch length of the geometry.

$$P_{base} = \frac{\mu_0 \lambda L_c}{g} \tag{2-6}$$

L_c stands for core length which is 1 meter in our calculations. By substituting equation (2-6) into equation (2-5), a closed expression for normalized permeance can be written.

$$P_n = \frac{\varphi}{\mu_0 (\mathrm{N}\times \mathrm{I})(\frac{\lambda}{g})} \tag{2-7}$$

μ_0 is the permeability of air which equals $4\pi\times10^{-7}$. Since, it is desired to carry out normalized calculations, equation (2-7) has been written in terms of normalized tooth pitch(λ/g) and MMF (N×I) which are the input variables in producing normalized data sets.

2.1.2.3 Tangential force

In order to calculate tangential force exerted on the middle upper tooth, a contour is considered on which force is calculated. This closed contour can be seen in Figure 2-3. It is depicted by a yellow rectangular area which the force is calculated on its perimeter. It is worth mentioning that the contour is selected in a way that it passes through the middle of the slots and air gap region. Therefore, contour length equals to tooth pitch of the geometry. Its width can also be calculated by adding tooth height (40g) and half of the air gap length (0.5g). So, contour width is 40.5g. FEM simulations reveal that once the closed contour encloses the tooth, results of force calculations are the same. In other words, length and width of rectangular contour does not affect force calculation results if the contour encloses the middle upper tooth completely.

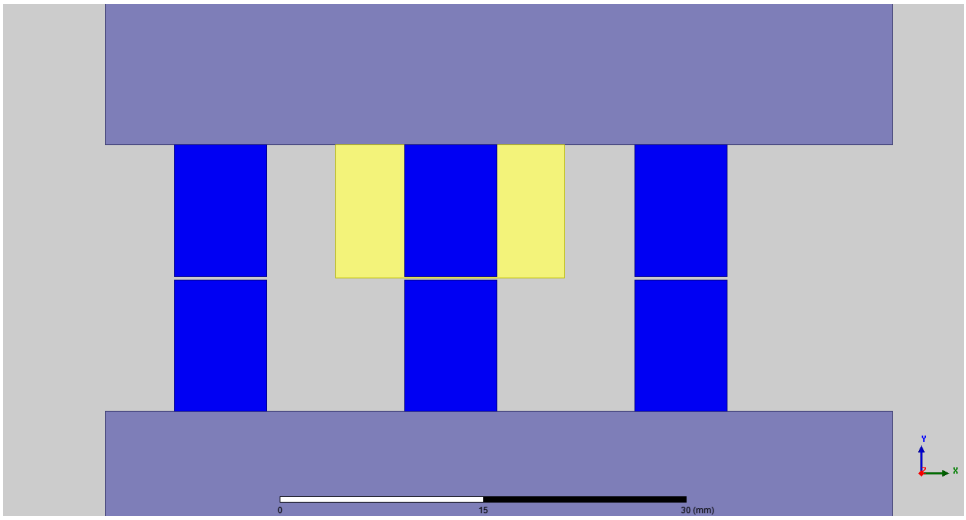

Figure 2-3 Closed contour for calculation of tangential force

Tangential force is calculated using Maxwell software. This software uses energy method in force calculation. In energy method, exerted force can be calculated by taking the partial derivative of stored energy with respect to displacement. It is obvious that because the proposed geometry is linear and determination of tangential force is aimed, displacement will be in x direction.

$$F_t = -\frac{\partial W_e}{\partial x} \tag{2-8}$$

To investigate calculation accuracy, force is calculated by the author also using Maxwell stress tensor method [66]. Tangential force can be easily calculated using the following Maxwell tensor formula.

$$F_t = \frac{1}{2\mu_0}\int\int B_n B_t dA \tag{2-9}$$

Integration path is defined as a line which encloses the tooth and passes from middle of the air gap and slots which is depicted in Figure 2-4.

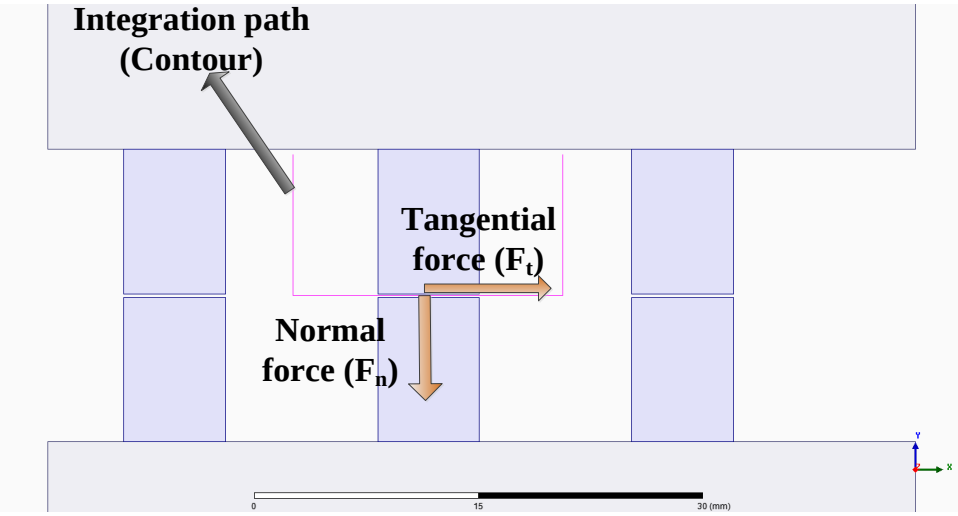

Figure 2-4 Integration path for calculation of tangential and normal forces

2.1.2.4 Normal force

Normal force is calculated in a similar way. Force is calculated on a contour shown in Figure 2-3 using Maxwell software. The force is again calculated by the author using Maxwell stress tensor method.

$$F_n = \frac{1}{2\mu_0}\int\int (B_n^2 - B_t^2)dA \qquad (2\text{-}10)$$

Integration path is defined similar to tangential force calculation method (Figure 2-4).

2.1.3 Comparison of force calculation results:

Tangential and normal forces are calculated using both Maxwell software (energy method) and Maxwell stress tensor method. Table 2-2 summarizes force calculation data for a sample geometry with $\lambda/g=70$, $t/\lambda=0.4$ and $x_n=0.2$. Calculations are done for different MMF values while the geometric variables (λ/g and t/λ) and normalized position (x_n) are unchanged.

Table 2-2 Force calculation data for a sample geometry

MMF (A.turns)	F_t (Maxwell) (N)	F_t (Maxwell tensor method) (N)	Error (%)	F_n (Maxwell) (N)	F_n (Maxwell tensor method) (N)	Error (%)
175	65.53	65.55	0.03	1642.3	1643.5	0.07
220	103.41	103.38	0.03	2581.3	2583.4	0.08
470	328.22	327.58	0.19	6439.5	6449.5	0.15
707	504.61	503.01	0.31	7644.1	7662.5	0.24

By comparing results obtained by Maxwell using energy method and Maxwell stress tensor method, validity of calculated tangential and normal forces is proven.

2.1.4 Comparison of the results with results in literature

In this section author's results are compared to those obtained by Necip Besenek [29], Funda Sahin [8], and Ibrahim Mahariq [30] in order to investigate the accuracy of calculations. Table 2-3 summarizes these results for a sample geometry with $\lambda/g=70$, $t/\lambda=0.4$ and $x_n=0.4$. Note that the results are compared for four different MMF values (excitation levels) in each geometry. Furthermore, it is worth mentioning that comparisons are made under a constant MMF value. In other words, MMF is the same in each row of the following tables. Note that in calculation of the percentage of error, the difference between author's results and the results obtained by Funda (or Necip) is divided by the results obtained by Funda (or Necip).

The second comparison is also done by changing geometric variables, MMF and normalized position. Table 2-4 includes calculation results and their comparison with the literature for a sample geometry with $\lambda/g=150$, $t/\lambda=0.5$ and $x_n=0.8$. Again it has to be mentioned that comparisons are done under a constant MMF values. It means that MMF values remain unchanged in each row of the table.

Table 2-3 Comparison of calculation results with results in the literature for a sample geometry with $\lambda/g=70$, $t/\lambda=0.4$ and $x_n=0.4$

MMF (A.turns)	B_t (T)					P_n (Wb/A.turns)					F_t (N)					F_n (N)		
	Funda	Rasul	Necip	Ibrahim	Error (%)	Funda	Rasul	Necip	Ibrahim	Error (%)	Funda	Rasul	Necip	Ibrahim	Error (%)	Rasul	Ibrahim	Error (%)
175	0.649	0.617	-	0.621	4.9	-	0.276	-	0.277	0.36	68.6	68.95	-	69.7	0.5	1141	1172	2.6
220	0.819	0.776	-	0.779	5.2	-	0.276	-	0.276	0	108.3	108.9	-	110.2	0.55	1793	1843	2.7
470	1.378	1.343	-	1.328	2.5	-	0.223	-	0.221	0.9	443	448.6	-	447.1	1.2	4965	4983	0.38
707	1.578	1.55	-	1.507	1.77	-	0.172	-	0.168	2.3	764.7	781.6	-	749.6	2.2	5891	5776	1.9

Table 2-4 Comparison of calculation results with results in the literature for a sample geometry with $\lambda/g=150$, $t/\lambda=0.5$ and $x_n=0.8$

MMF (A.turns)	B_t (T)					P_n (Wb/A.turns)					F_t (N)					F_n (N)		
	Funda	Rasul	Necip	Ibrahim	Error	Funda	Rasul	Necip	Ibrahim	Error	Funda	Rasul	Necip	Ibrahim	Error	Rasul	Ibrahim	Error (%)
90	0.316	0..316	0.316	0.298	0	-	0.16	0.16	0.151	0	39.6	39	40	39	1.5	692	684	1.16
150	0.503	0.506	0.503	0.478	0.6	-	0.15	0.15	0.145	0	108.1	107	110	108	1	1731	1720	0.63
250	0.663	0.681	0.663	0.641	2.7	-	0.12	0.12	0.117	0	254.5	258	250	267	1.3	2658	2640	0.68
380	0.804	0.831	0.804	0.778	3.3	-	0.1	0.1	0.093	0	443.8	459	440	485	3.4	3167	3100	2.16

As it can be understood from the table, discrepancies between author's results and results calculated in the literature are negligible and these normalized and dimensionless data can be used to calculate SRM static and dynamic characteristics which will be discussed in the following sections.

2.2 Neural networks training

Once the sets of dimensionless and normalized data are produced using the calculation methods explained in previous sections, static and dynamic performance characteristics of SRM can be predicted using this data. In other words, this

dimensionless data are used as a look up table in determination of MMF, normalized permeance and tangential force for symmetrically slotted geometries which will be discussed in details in section 2.3. However, an interpolation is needed to obtain the desired output values (MMF, P_n and F_t) from data sets for each input vector (λ/g, t_n, x_n and B). For this purpose, Artificial Neural Networks (ANNs) are used to predict the output parameters for each input vector. A thorough discussion on neural networks and various kinds of training algorithms can be found in [67, 68].

It has to be mentioned that neural networks are used to predict the MMF value, normalized permeance and tangential force for symmetrically slotted geometries. It is obvious that a SRM can be modeled as an asymmetrically slotted geometry. Hence, the proposed method has to be extended to be capable of calculating normalized permeance, tangential force and MMF for asymmetric geometries. The procedure of creating two equivalent symmetrically slotted geometries for a switched reluctance motor will be discussed in details in section 2.4.

Four input parameters which are used as input variables in training neural networks are normalized air gap length (λ/g), normalized tooth width (t_n), normalized position (x_n) and average tooth flux density (B_t). Once these parameters are determined for a particular symmetrically slotted geometry, three output parameters need to be determined (MMF, normalized permeance and tangential force). These output parameters can then be used in calculating static torque-position-current and flux linkage-current-position curves of a SRM. Therefore, the aim of training neural networks is prediction of three output parameters once four input variables are known. This can be done by training a single neural networks with four inputs and three outputs, or three different neural networks with four inputs and one input.

In this study, three neural networks are trained for each three normalized outputs; MMF, normalized permeance and tangential force. The accuracy of a single neural network with 4 inputs and 3 outputs is tested by the author. The results reveal that using 3 separate networks leads to more accurate estimation of the normalized parameters.

Table 2-5 summarizes the characteristics of three feedforward neural networks used to estimate the intermediate points of normalized data sets in analytical calculations. Note that the number of data sets used for training these three networks is 41580. This is the number of normalized and dimensionless data sets produced using the procedure explained in previous sections.

Table 2-5 Characteristics of three feedforward neural networks

	Input vector	Output variable	Number of hidden neurons	Training function
Network1	(λ/g t_n x_n B)	MMF	300	trainlm
Network2	(λ/g t_n x_n B)	P_n	100	trainlm
Network3	(λ/g t_n x_n B)	F_t	100	trainbr

2.3 Calculation of static force and permeance-position characteristics for symmetrically slotted geometries

In general, a switched reluctance motor can be considered as an asymmetrically slotted geometry, however, in this section, in order to start with a simpler case, calculation of parameters for a symmetrically slotted geometry are explained. This model will then be elaborated to consider asymmetrically slotted case in section 2.4.

After production of normalized force, flux density and permeance data, calculation of static force, normalized permeance and excited MMF of symmetrically slotted geometries can be studied. At first stage, the tooth pitch has to be calculated for any symmetrically slotted geometry (Note that tooth pitches are the same for upper teeth and lower teeth in symmetrically slotted geometries). The tooth pitch is defined as the distance between the middle points of two consecutive teeth. The tooth pitch is then modified based on the normalized position of teeth using equation (2-11). This approximation is utilized if the distance to the next pair of the moving teeth is lower than 25g in the actual geometry [69].

$$\lambda = \max(\lambda, t_s + \mathrm{X}_1 + 25\mathrm{g}) \tag{2-11}$$

Therefore, in the calculations, λ/g and t/λ values will be different if the distance to the next pair of teeth is lower than 25g. So, the effects of neighboring teeth will be considered as an important issue. Following figure of a symmetrically slotted geometry illustrates the given geometric parameters in equation above clearly.

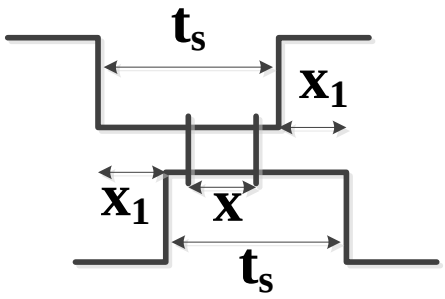

Figure 2-5 Representation of geometric parameters

In next step, using the calculated tooth pitch value, values of λ/g, x_n and t_s/λ are calculated for the geometry.

$$x_n = \frac{2x}{\lambda} \tag{2-12}$$

Now, normalized permeance, MMF, and force data can be simply calculated for the symmetrically slotted geometry for any given flux or flux density value. So, the main aim of this section is determining normalized permeance, force and excited MMF values for a symmetrically slotted geometry while having the required geometric parameters (λ/g, t/λ, x_n) in hand. It is mentioned in producing normalized and dimensionless data sets that if normalized air gap length (λ/g), normalized tooth width (t/λ), normalized position (x_n) and tooth flux density (B_t) of a symmetrically slotted geometry are known, normalized permeance, force and excited MMF values will be simply obtained using the three above mentioned neural networks. Hence, for any given flux or flux density values, the desired parameters can be determined.

It has to be noticed that all mentioned parameters (λ/g, t/λ, x_n and B_t) are normalized, so, these parameters will be the same in both Ertan's model and symmetrically slotted geometry. However, flux value in a symmetrical slotted

geometry has to be transformed into the equivalent values in Ertan's model (see Figure 2-1). Ertan's model is thoroughly explained in section 2.1.1. Tooth pitch flux in a symmetrically slotted geometry can be easily calculated from tooth flux density.

$$\varphi = B_t t_s L \tag{2-13}$$

Then transformation of the flux value to the equivalent flux in Ertan's geometry is an easy task.

$$\varphi_{data} = \frac{0.0172\varphi}{L \times \lambda} \tag{2-14}$$

0.0172 is the tooth pitch of Ertan's model which is used to obtain normalized data. Moreover, axial length of Ertan's model in Z direction is 1 meter. Now, tooth flux density in Ertan's model can be determined.

$$B_{t_{data}} = \frac{\varphi_{data}}{t_{data}} = \frac{0.0172 B_t t_s L}{L \times \lambda (0.0172 \frac{t_s}{\lambda})} = B_t \tag{2-15}$$

Therefore, it is proven that B_t is the same in both Ertan's model and the symmetrically slotted geometry. Once all four input variables of the neural networks are calculated (λ/g, t/λ, x_n and B_t), MMF, normalized permeance and Force values are determined from the normalized data using neural networks. Normalized permeance of two models are the same. On the other hand, MMF and force values obtained using neural networks, have to be transformed into equivalent values in symmetrically slotted geometry.

$$MMF = \frac{\lambda \times MMF_{data}}{0.0172} \tag{2-16}$$

$$F = \frac{\lambda \times F_{data}}{0.0172} \tag{2-17}$$

Thus normalized permeance, MMF and tangential force values are easily calculated for any given symmetrically slotted geometry using the procedure described above. However, this method has to be generalized to be used in computation of these parameters for asymmetrically slotted geometries which will be discussed in upcoming sections.

2.4 Force and permeance calculations for asymmetrically slotted geometries

The method proposed by Ertan [28, 63] is utilized in this study to calculate the normalized data for any asymmetrically slotted geometries. In this method, an asymmetric geometry is divided into two symmetric geometries in a manner which is shown in the following figure.

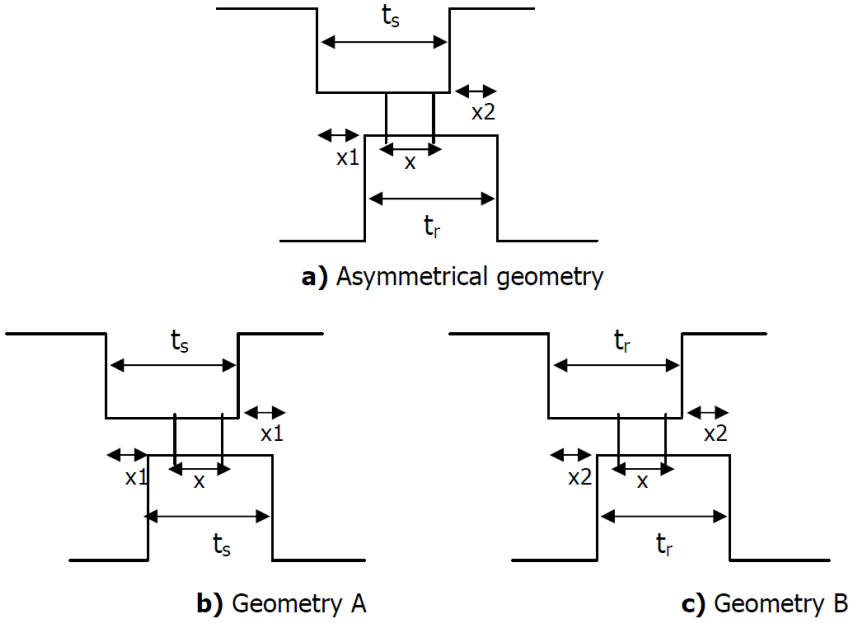

Figure 2-6 Division of an asymmetrically slotted geometry into two symmetric geometries with normalized tooth pitches of λ_A/g and λ_B/g

The same calculation method for symmetric geometries can then be used to calculate normalized data for both geometries A and B separately. Note that in calculation of these normalized parameters for geometries A and B, equivalent tooth

pitch has to be determined for both stator and rotor separately using equations (2-18) and (2-19). It is obvious that geometry A is an equivalent symmetrically slotted geometry for the stator of a SRM. On the other hand, geometry B is an equivalent geometry for the rotor part of the same SRM.

$$\lambda_A = \max(\lambda_s, t_s + \mathrm{X}_1 + 25\mathrm{g}) \tag{2-18}$$

$$\lambda_B = \max(\lambda_r, t_r + \mathrm{X}_2 + 25\mathrm{g}) \tag{2-19}$$

Given a SR motor, stator and rotor tooth pitches (λ_s and λ_r) can be simply determined using

$$\lambda_s = \frac{\pi(D_{or} + 2g)}{N_s} \tag{2-20}$$

$$\lambda_r = \frac{\pi D_{or}}{N_r} \tag{2-21}$$

Where D_{or}, g, N_s and N_r stand for rotor outer diameter, air gap length, number of stator poles and number of rotor poles of the switched reluctance motor respectively.

Note than in the fully aligned position λ_s and λ_r values are dominant. However, while the rotor moves towards fully unaligned position, X_1 and X_2 terms are enlarged and consequently t_s+X_1+25g, and t_r+X_2+25g terms will be considered as the equivalent tooth pitch values for geometries A and B.

Once normalized permeance, MMF and tangential force are calculated for the two symmetric geometries A and B, normalized values of the asymmetric geometry can be easily computed.

$$P_n = \frac{2P_{n_A}P_{n_B}}{P_{n_B} + P_{n_B}} \tag{2-22}$$

$$MMF = \frac{MMF_A + MMF_B}{2} \tag{2-23}$$

$$F = \frac{F_A + F_B}{2} \tag{2-24}$$

At this stage, normalized permeance, force and excited MMF values can be easily computed for any asymmetrically slotted geometries. Upcoming sections deal with generalization of the proposed method to calculate the static torque and flux linkage characteristics of SRM.

2.5 Static force and flux linkage calculations for the SRM

In order to calculate static characteristics of the SRM, the switched reluctance motor is divided into two sections. One section consists of stator and rotor teeth and the air gap region. Other section includes the remaining part of stator and rotor tooth and back core sections. Both sections can be easily distinguished in Figure 2-8. A set of computations which will be described in detail in the succeeding sections, are carried out on tooth and air gap regions using normalized data and the proposed method. In these computations, if the air gap region is asymmetrically slotted, this geometry is divided into two equivalent symmetrically slotted geometries using the method proposed in the previous section. Then, the normalized permeance, tangential force and MMF values for the air gap region of the SRM are determined using the method which will be described in upcoming sections. Another MMF drop calculation is done for stator and rotor back tooth and back core sections. These sections are shown in a typical 8/6 SRM in the following figure. Figure 2-7 represents the flowchart of calculating static torque and flux linkage characteristics of an SR motor. The corresponding section number for each block is depicted inside the blocks. The calculation procedure is discussed in detail in following sections.

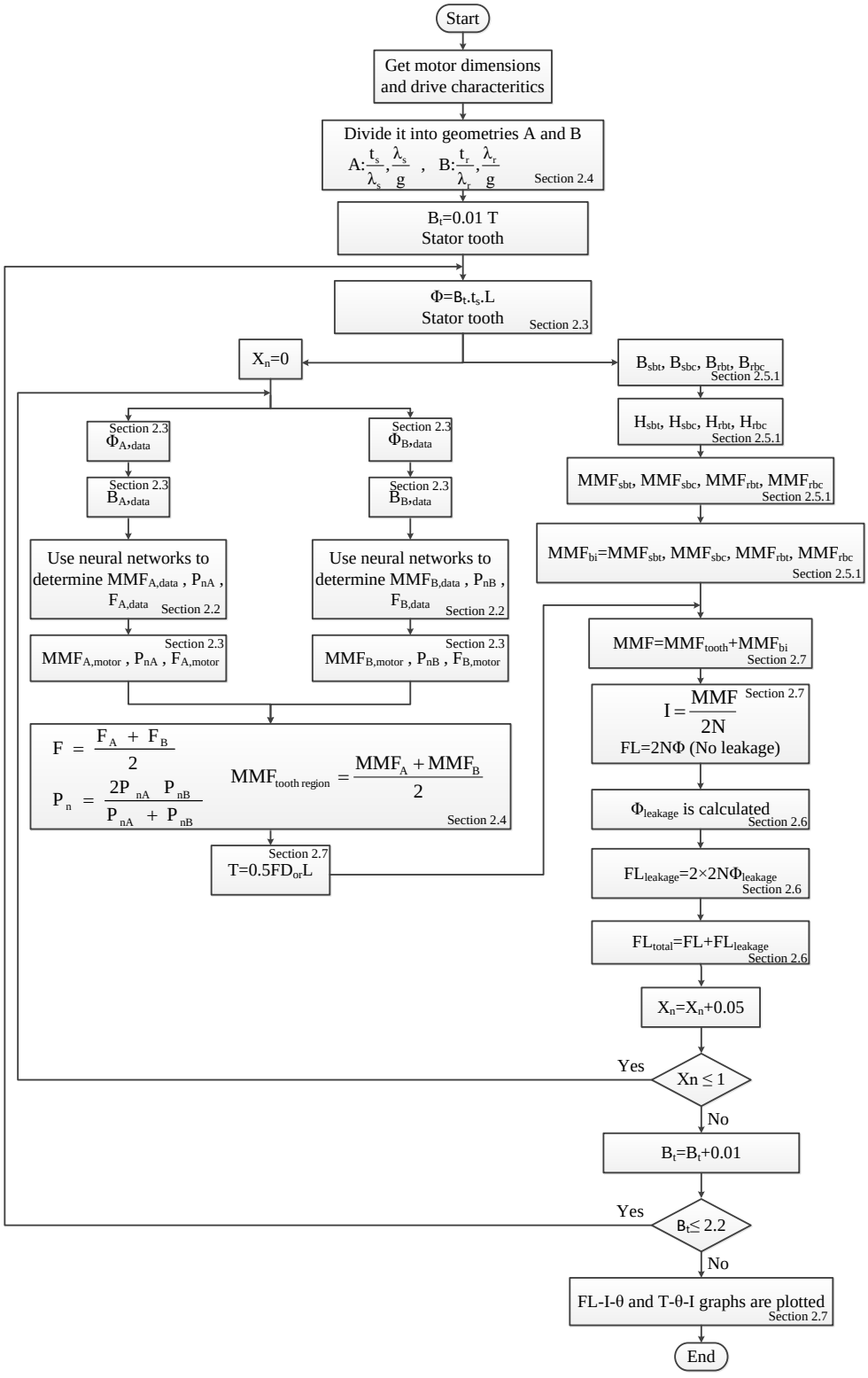

Figure 2-7 Flowchart of SR motor static characteristics (torque and flux linkage) calculation

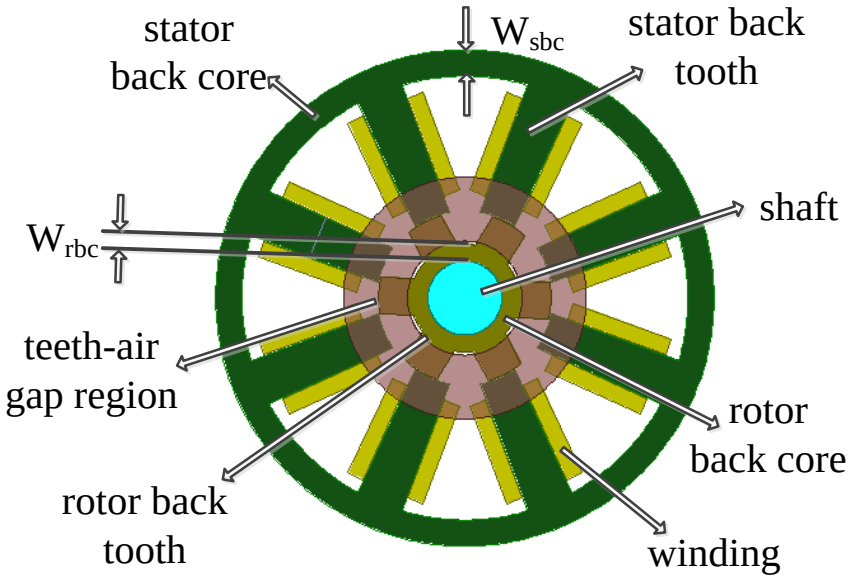

Figure 2-8 Air gap and back core regions of a typical 8/6 SRM

2.5.1 Calculation of MMF drop on back tooth and back core regions in one phase on mode

In a SR motor two opposite poles are excited. The applied MMF by a pole is spent pushing the flux through half of the back iron path, through the teeth and one air gap. The MMF drop across the teeth region is available from the data. For the rest of the flux path, MMF drop versus flux characteristics must be obtained in order to determine the operating point.

Because the normalized data are produced using a model in which tooth height is 40g, rest of the tooth height in the actual machine is defined as back tooth region and it forms part of the back iron MMF drop. The schematic diagram of back tooth region is represented in Figure 2-9.

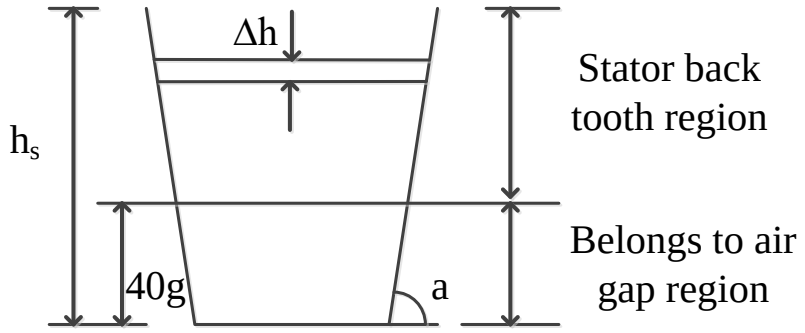

Figure 2-9 Schematic diagram of back tooth region

In this figure, parameter 'a' stands for tooth tapering angle. In order to calculate the MMF drop on stator back tooth region, the back core region is divided into 10 equally divided sections to take the tooth tapering effect into account. Therefore, length of each section can be simply calculated.

$$\Delta h = \frac{h_s - 40g}{10} \tag{2-25}$$

In this equation, h_s stands for stator tooth height. On the other hand, tooth width is also calculated in each section. Tooth width in the first section can be easily calculated using

$$t_1 = t_s + 2 \times (40g + \frac{\Delta h}{2}) \tan(a) \tag{2-26}$$

Width of next 9 sections can then be computed using

$$t_i = t_1 + 2(i-1)\Delta h \tan(a) \qquad i=2,3,4,...,10 \tag{2-27}$$

Flux density in each equally divided section can be simply calculated.

$$B_i = \frac{\varphi}{L t_i} \tag{2-28}$$

In this equation, φ and L represent tooth flux and stack length in the SRM. After calculation of flux density (B), flux intensity (H) values for each section is

determined using B-H curve of the SRM core. Then, MMF drop on stator back tooth section is simply computed.

$$MMF_{sbt} = \sum_{i=1}^{10} H_i \Delta h_i = \Delta h \sum_{i=1}^{10} H_i \tag{2-29}$$

MMF drop on rotor back tooth section can be determined in a same manner. However, rotor teeth are assumed to be without tapering. Therefore, MMF drop on rotor back tooth region can be computed using

$$MMF_{rbt} = H_{rbt}(\mathrm{h}_r - 40\,\mathrm{g}) \tag{2-30}$$

where h_r stands for rotor tooth height. H_{rbt} is flux intensity of rotor back tooth section which is determined based on flux density in rotor back tooth region (B_{rbt}) and using core B-H curve.

$$\mathrm{B}_{rbt} = \frac{\varphi}{Lt_r} \tag{2-31}$$

t_r represents rotor tooth width. After determination of MMF drops on stator and rotor back tooth regions, MMF drops on back core areas have to be investigated. Flux density in stator back core region can be easily calculated from the stator pole flux value (φ) using

$$B_{sbc} = \frac{\varphi}{2LW_{sbc}} \tag{2-32}$$

where W_{sbc} is stator back core thickness. Stator back core flux intensity is calculated using B-H curve of the core. Then, MMF drop on stator back core can be simply computed.

$$MMF_{sbc} = H_{sbc} l_{sbc} = H_{sbc}\left(\frac{2q}{N_s} \times \frac{\pi(\mathrm{D}_{os} - \mathrm{W}_{sbc})}{2}\right) \tag{2-33}$$

In this equation, q, Ns, l_{sbc} and D_{os} stand for number of SRM phases, number of stator poles, flux path length in stator back core region and stator outer diameter respectively. Rotor back core MMF drop can be computed in a same manner.

$$MMF_{rbc} = H_{rbc} l_{rbc} = H_{rbc} \left(\frac{2q}{N_s} \times \frac{\pi (D_{or} - 2h_r - W_{rbc})}{2} \right) \quad (2\text{-}34)$$

In this equation, l_{rbc}, h_r, W_{rbc} and D_{or} represent flux path length is rotor back core, rotor tooth height, rotor back core thickness and rotor outer diameter respectively.

Finally, total MMF drop on back tooth and back core regions of the machine can be determined by summing all the MMF drops for the flux path in the back iron .

$$MMF_{bi} = 2(MMF_{sbt} + MMF_{rbt}) + MMF_{sbc} + MMF_{rbc} \quad (2\text{-}35)$$

In analytical calculations, the MMF drops on back iron regions are calculated for stator tooth flux densities varying between 0.01T to 2.2 T with the steps of 0.01T which covers all possible conditions for the SRM to operate below maximum allowable flux density (2T). It is worth mentioning that although the step size of 0.01 T seems to be unnecessarily small, when the SRM operates in its saturation region it is important to consider variations of flux density with such a small step size. In the saturation region, a small change in flux density value, leads to huge change in flux intensity and consequently the MMF drop on the core. So, accurate determination of core flux density is very important.

In determination of back core MMF drops of the SRM under two phase on excitation mode, superposition principle is utilized in this study. Distribution of flux lines in a typical 8/6 SR motor in two phase on excitation mode is depicted in Figure 2-10. Excitation polarity (N or S) and flux lines directions are also depicted on the figure. Note that two excited phases have the same currents.

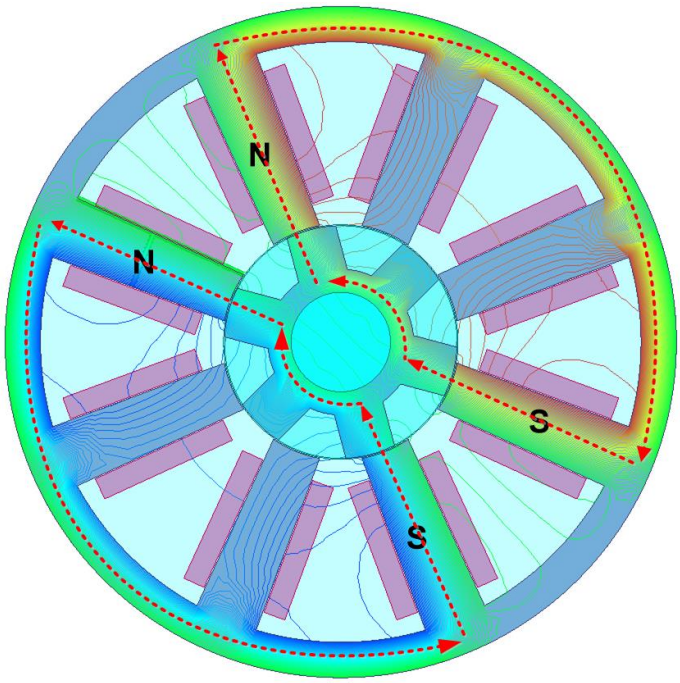

Figure 2-10 Flux lines of a typical 8/6 SRM in two phase on excitation mode

It can be seen that there are no flux lines in the back core region between two excited poles. So, superposition principle can be utilized in handling two phase on excitation case.

Note that the core flux waveforms in various parts of the machine are determined for each phase taking into account the turn on angle and excitation periods for the particular case studied. So, for a typical 8/6 SRM, if the excitation periods are lower than 90 electrical degrees, only one phase of the machine will operate at any instant. However, if the excitation period is larger than 90 electrical degrees, there will be overlaps between conduction periods of consecutive phases and two phases of the SRM will be in conduction at the same time. Effect of this overlap is entered into analytical model and calculations based on superposition principle in determination of back core flux waveforms which will be discussed in chapter 3.

Note that MMF drop data are obtained up to 2.2T which is higher than the maximum allowable flux density in order to guarantee the desired accuracy of neural networks which will be trained to be used in determination of dynamic performance characteristics of the SRM which will be discussed in upcoming sections. Calculated

back iron MMF drop data are tabulated to be used in predicting static torque and flux linkage characteristics of the SRM after determination of tooth and air gap regions normalized permeance, MMF drop and tangential force which will be discussed in upcoming sections. It is worth mentioning that in this study, normalized permeance and tangential force are calculated for different flux density values and normalized positions. Furthermore, MMF drops are computed for both teeth and air gap regions and back iron region for all variations of tooth flux density and normalized position. Finally, this tabulated data will be utilized in determination of static and dynamic performance characteristics of the switched reluctance motor.

2.5.1.1 Discussion on the effect of end fringing flux, end winding leakage flux and slot leakage flux on back iron MMF drop

It has to be mentioned that the back iron MMF calculation method in this study does not take into account the MMF drops due to end fringing flux, end winding leakage and slot leakage flux (flux leaking to adjacent stator poles). This is because it is found that considering pole leakage and end leakage has very small influence on back iron MMF calculation.

Core end fringing flux occurs at both ends of SRM core. A small portion of the flux completes its path through the air section which is not exactly between two sections of core (stator and rotor). End leakage flux fringing the core is depicted in Figure 2-11. Fringing flux depends on the air gap length between two core sections (stator and rotor). By increasing the air gap length, the ratio of fringing flux to main flux will also be increased. Note that by increasing air gap length, total flux will be reduced. A detailed discussion on end fringing flux and its analytical calculation method are given in chapter 4.

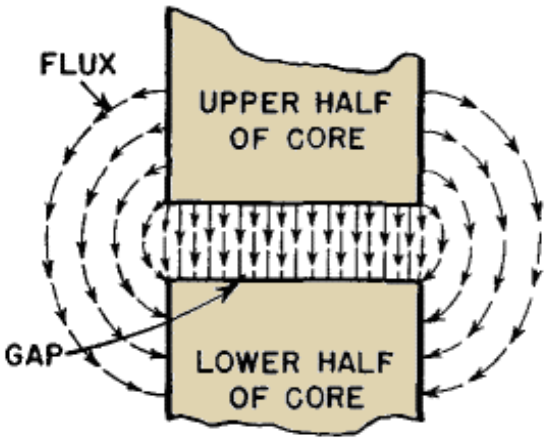

Figure 2-11 Illustration of the flux fringing at both ends of the core

The current flowing through the end winding produces the magnetic flux which is usually referred to as end winding leakage. This leakage flux is shown in Figure 2-12. Based on comparison of FE simulations with measurements which will be presented in chapter 4, the end winding leakage will be neglected in this study.

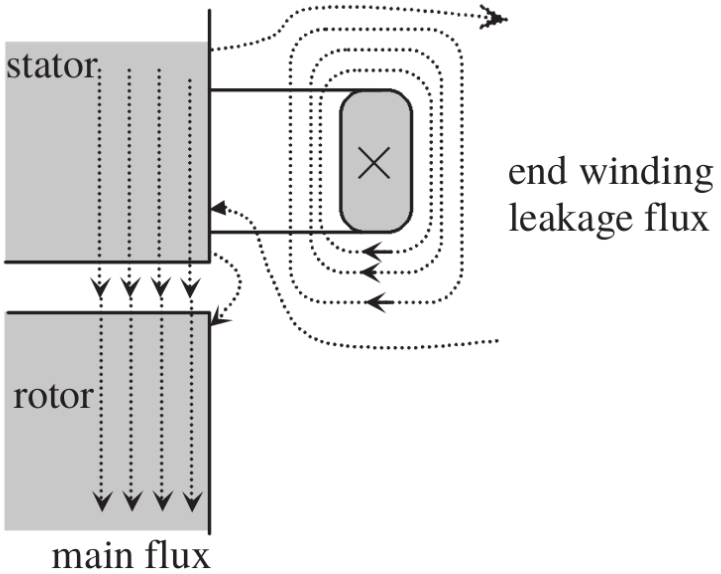

Figure 2-12 Main flux and end winding leakage flux representation

Another leakage flux which can be taken into account in back iron MMF drop calculations, is the flux leaking between an excited pole and the pole adjacent to it (see

section 2.6). This flux will be referred to as slot leakage flux in this study. Following figure represents slot leakage flux and the main flux in a typical 8/6 SRM.

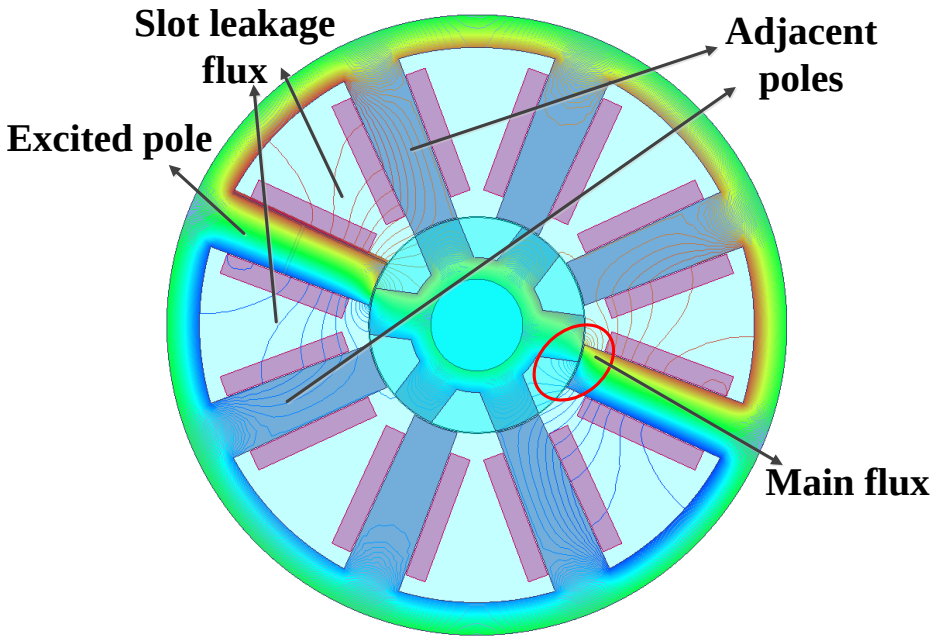

Figure 2-13 Main flux and slot leakage flux representation (one-phase on)

It is worth mentioning this component of flux does not have any contributions in torque production of the SRM, and acts as a leakage component. Same as the end fringing flux, effect of slot leakage flux can also be taken into account in back iron MMF drop calculation of the machine. However, it has to be noticed that in spite of the end fringing flux, slot leakage flux affects only the MMF drop calculation of stator back teeth regions and half of the total stator back core section (if stator back core is divided into 8 sections between 8 poles, slot leakage effect has to be taken into account in four of these sections (see Figure 2-14)). It can be easily distinguished that this leakage component of the flux completes its path through two adjacent poles of an excited pole.

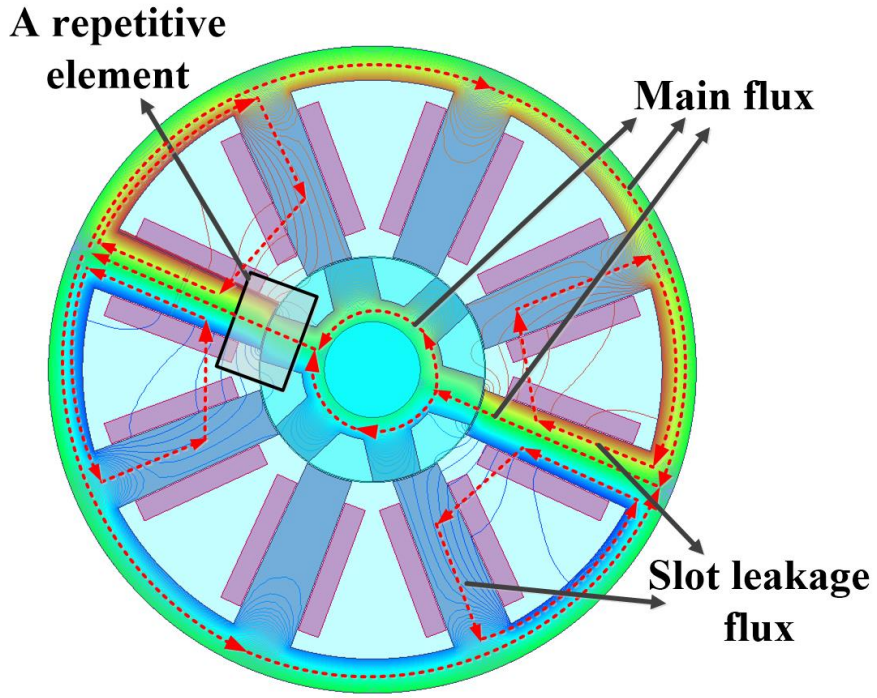

Figure 2-14 Representation of main and slot leakage flux lines and repetitive element on a typical 8/6 SRM (one phase on)

2.5.2 Calculation of air gap and teeth region permeance and force produced by a SR motor using normalized permeance and force data

Using the method described in previous sections, the permeance (hence flux linkage) and force versus position curves of asymmetrically slotted geometries can be obtained. Therefore, the static torque and flux linkage position curve of a given motor geometry can be found. Once the static characteristics of a SRM are determined torque-speed curves of the machine can be determined.

Once one phase winding of a switched reluctance motor is excited, stator and rotor teeth and corresponding air gap region can be considered equivalent to the repetitive element based model proposed by Ertan. It can be assumed that stator and rotor have different tooth pitches, so, the SRM may be viewed as formed of repetitive elements. A repetitive element on a typical 8/6 SRM is depicted in Figure 2-14. Note

that only the tooth height of 40g in both stator and rotor are considered inside the teeth and air gap region. If the tooth height is more than 40g, it will be considered in MMF calculations of the back iron region. Description of the permeance and force variation calculation of a given geometry with position and excitation is the main aim of this section.

Using the method described in sections 2.3 and 2.4, teeth and air gap regions of a SRM is modeled as an asymmetrically slotted geometry. Normalized permeance, MMF and tangential force values are determined for the SRM from the quantities obtained for both geometries A and B.

$$MMF = 2 \times \frac{MMF_A^{'} + MMF_B^{'}}{2} \tag{2-36}$$

$$P_n = \frac{2P_{nA}^{'}P_{nB}^{'}}{P_{nA}^{'} + P_{nB}^{'}} \tag{2-37}$$

$$F = \frac{N_s}{2q} \times 2 \times \frac{F_A^{'} + F_B^{'}}{2} \tag{2-38}$$

For a given SR motor, as in the calculation of back-iron MMF drop, in calculation of the tooth region characteristics, stator tooth flux density is varied from 0.01 to 2.2T by the steps of 0.01T, and the normalized permeance, and tangential force and MMF across this region are calculated against normalized rotor position and stored.

A switched reluctance motor may be excited in one phase on mode or two phase on mode. Furthermore, as a phase turns off its current may not decay to zero instantly and therefore although the motor is operating in one phase on excitation mode, two phases may carry current. Superposition principle is utilized in handling both one phase on and two phase on excitation modes. In other words, flux calculations are performed by consideration of turn on angle and excitation period of one phase. Then, flux waveforms of other phases are determined by shifting the obtained waveforms by an electrical angle which equals to the electrical distance between consecutive phases.

The total force is determined by adding the force contribution of contributing phases (or poles).

Note that in the above calculation, end leakage or slot leakage flux is not taken into consideration. With the assumption of back-iron MMF drop remaining unchanged due to these flux components, it is obvious that the force produced by the teeth will not be influenced by these flux components. Both main flux and slot leakage flux components are calculated for different excitation levels and rotor positions for a prototype 8/6 SRM which can be used for comparison purposes. The results are presented and discussed in section 4.2.1 and Table 4-8.

Phase winding flux linkage of a SR motor is affected by slot leakage. As discussed in section 2.9 this characteristics is used in the calculation of phase current. In the following section how the slot (pole) leakage is taken into account will be described.

2.6 Calculation of slot leakage flux (flux leaking to the adjacent pole)

The above calculation of flux linkage is based on a model which does not include the effect of flux leaking to two adjacent poles of an excited pole which is referred as slot leakage in this study. Another flux component which has not been taken into account in above calculations is the flux which fringes at both ends of the core. This is known as end fringing flux in this study. Consideration of end fringing flux in analytical computations will be explained in chapter 4 in details. However, a detailed discussion on calculation of slot leakage flux is given here.

Comparison of Finite Element simulations results and measurements with analytically computed flux linkage data shows a slight discrepancy. Analytically calculated flux linkage data are less than FEM simulations and measurements results. It is proved that this discrepancy in flux linkage data is due to the leakage flux which completes its path through two adjacent poles of an excited pole. A detailed discussion on simulation results and leakage flux calculation procedure is given in verification chapter. A slight discrepancy in flux linkage data, results in discrepancies in torque

prediction of the machine, especially at higher rotational speeds. For this purpose, calculation of this leakage flux has to be entered into analytical model. In this study, this flux is referred as slot leakage or winding leakage.

In this section, a pure analytical method is developed to calculate the flux leaking to two adjacent poles of an excited phase. It is assumed that this flux completes its path through the slot (air region) between two adjacent poles. In other words, it does not enter the rotor poles. Validity of this assumption will be proved later in verification chapter of this study. Some parameters used in deriving the analytical expression are shown in Figure 2-15. Note that in the calculation tooth taper is not taken into account as it has a secondary importance.

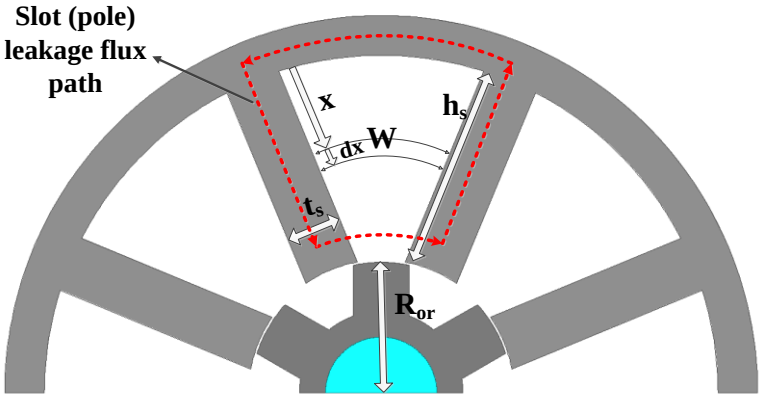

Figure 2-15 graphical representation of calculation parameters on a SRM

This figure depicts a half symmetric representation of an 8/6 switched reluctance motor. Using Ampere's law, following equation can be written in a red closed loop (which shows the slot leakage flux path) in Figure 2-15.

$$\frac{x}{h_s} NI = \frac{x}{h_s} F_{excited\ pole} + F_{bc} + F_{slot} + \frac{x}{h_s} F_{adjacent\ pole} \qquad (2\text{-}39)$$

In this equation, $F_{excited\ pole}$, $F_{adjacent\ pole}$ and F_{bc} stand for MMF drops on the excite pole, adjacent pole and the corresponding back core section respectively. NI is the total MMF applied by the winding. F_{slot} represents the MMF drop on the slot section. The MMF drop in adjacent pole is only due to the slot leakage flux which is negligibly small, so, it can be neglected in analytical calculations. However, MMF

drops on back core and excited pole are due to the main flux. So, MMF drop on the slot can be determined using

$$F_{slot} = \frac{x}{h_s}(NI - F_{excited-pole}) - F_{bc} \tag{2-40}$$

It is obvious that the leakage flux passing through the slot region to the adjacent pole can be simply calculated using

$$\varphi_{leakage} = \int BdA = \int \mu_0 HdA = \int_0^{h_s} \mu_0 HLdx \tag{2-41}$$

It is obvious that $B = \mu_0 H$ and the small element of area (dA) can be expressed as a function of dx and motor axial length (L).

$$dA = Ldx \tag{2-42}$$

At distance x, the flux path length (W) can be calculated using (see Figure 2-15)

$$\mathrm{W} = \frac{\pi(\mathrm{D}_{or} + 2\,\mathrm{g} + 2(\mathrm{h}_s - \mathrm{x}))}{N_s} - t_s \tag{2-43}$$

Where D_{or}, g, h_s, t_s and N_s stand for rotor outer diameter, air gap length, tooth (slot) height, tooth width and number of stator poles respectively. Hence, following equation can be written to express flux intensity (H) in terms of x and geometric parameters (F_{slot} is substituted from equation (2-40)).

$$F_{slot} = HW \rightarrow H = \frac{1}{W}\left(\frac{x}{h_s}(NI - F_{excited-pole}) - F_{bc}\right) \tag{2-44}$$

By substituting equation (2-44) in (2-41) leakage flux can be easily calculated.

$$\varphi_{leakage} = \mu_0 L \int_0^{h_s} \frac{1}{W}\left(\frac{x}{h_s}(NI - F_{excited-pole}) - F_{bc}\right)dx \tag{2-45}$$

This equation can be separated into two parts as follows.

$$\varphi_{leakage} = \frac{\mu_0 L}{h_s}\int_0^{h_s} \frac{NI - F_{excited-pole}}{W} x dx - \mu_0 L \int_0^{h_s} \frac{F_{bc}}{W} dx \tag{2-46}$$

Because total excited MMF and MMF drops on excited pole and back core are constant parameters, the equation can be further simplified.

$$\varphi_{leakage} = \frac{\mu_0 L}{h_s}(NI - F_{excited-pole})\int_0^{h_s} \frac{x}{W} dx - \mu_0 L F_{bc} \int_0^{h_s} \frac{1}{W} dx \tag{2-47}$$

Calculation of two integral values is of interest at this stage. Note that parameter W inside the integral is a function of x itself. So, the first integral can be computed as follows.

$$\int_0^{h_s} \frac{x}{W} dx = \int_0^{h_s} \frac{x}{\frac{\pi(\mathrm{D}_{or} + 2\mathrm{g} + 2(\mathrm{h}_s - \mathrm{x}))}{N_s} - t_s} dx \tag{2-48}$$

It can also be further simplified as follows.

$$\int_0^{h_s} \frac{x}{\frac{\pi(\mathrm{D}_{or} + 2\mathrm{g} + 2(\mathrm{h}_s - \mathrm{x}))}{N_s} - t_s} dx = \frac{N_s}{2\pi}\int_0^{h_s} \frac{x dx}{(\mathrm{R}_{or} + \mathrm{g} + \mathrm{h}_s) - \mathrm{x} - \frac{t_s N_s}{2\pi}} \tag{2-49}$$

The term $\mathrm{R}_{or} + \mathrm{g} + \mathrm{h}_s - \frac{t_s N_s}{2\pi}$ is taken as K for further simplifications. Note that R_{or} is rotor outer radius.

$$\int_0^{h_s} \frac{x}{W} dx = \frac{N_s}{2\pi}\int_0^{h_s} \frac{x dx}{K - \mathrm{x}} \tag{2-50}$$

Now this integral value can be simply determined.

$$\frac{N_s}{2\pi}\int_0^{h_s} \frac{x dx}{K - \mathrm{x}} = -\frac{N_s}{2\pi}[\mathrm{h}_s + \mathrm{K}(\ln(\mathrm{K} - \mathrm{h}_s) - \ln(\mathrm{K}))] \tag{2-51}$$

Calculation of the second integral in equation (2-47) is straightforward. It can be computed as follows (see equation (2-50)).

$$\int_0^{h_s} \frac{1}{W} dx = \frac{N_s}{2\pi} \int_0^{h_s} \frac{dx}{K - \mathrm{x}} = -\frac{N_s}{2\pi} (\ln(\mathrm{K} - \mathrm{h}_s) - \ln(\mathrm{K})) \tag{2-52}$$

Once two integral values are determined flux leaking to one adjacent pole can then be simply calculated by substituting equation (2-51) and (2-52) into equation (2-47). It has to be noticed that the term ($\ln(K-h_s)-\ln(K)$) is substituted by Q in order to simplify the final equation.

$$\varphi_{leakage} = -\frac{\mu_0 N_s L}{2\pi} [\frac{NI - F_{excited-pole}}{\mathrm{h}_s} (\mathrm{h}_s + \mathrm{K}\, Q) - \mathrm{F}_{bc}\, Q] \tag{2-53}$$

It has to be noticed that in order to calculate the total leakage flux of one excited pole, the computed value has to be multiplied by two, because the leakage flux completes its path through two adjacent poles of one excited pole. As it is obvious from equation above, in a specific SRM slot leakage flux changes by variations in excited MMF value. It will also be proven in verification chapter that leakage flux completes its path through the air region (slot) between two adjacent poles.

Finally, leakage flux linkage can be easily determined which has to be added to the flux linkage calculated using the main flux of the machine to determine the final leakage included flux linkage-current-position characteristic of the SRM. Leakage flux linkage component of the SRM can be computed using

$$FL_{leakage} = 2 \times 2 \times N \varphi_{leakage} \tag{2-54}$$

Where N is number of turns per pole of the SRM. $\varphi_{leakage}$ is the flux leaking to one adjacent pole of an excited pole. Calculated leakage flux linkage value is the flux linkage of two opposite poles of a switched reluctance motor which are connected in series. This leakage flux is added to the main flux linkage characteristic of the SRM to be considered in dynamic current and torque calculations of the machine. The procedure is thoroughly explained in section 4.2.1.

It is mentioned that superposition principle is used in order to calculate slot leakage flux while the SRM operates in 2 phase on excitation mode. In order to prove the validity of using this method, a prototype 8/6 SRM is simulated using finite element method. It is assumed that two phases of the SRM are in conduction at the same time. Simulations are carried out for three different excitation levels. The winding has 322 turns per pole. It is taken into account that the slot leakage flux is independent from rotor position which will be proven in section 4.2.1. The flux passing through different paths is calculated which can be seen in Table 2-6. The flux paths are shown in Figure 2-16.

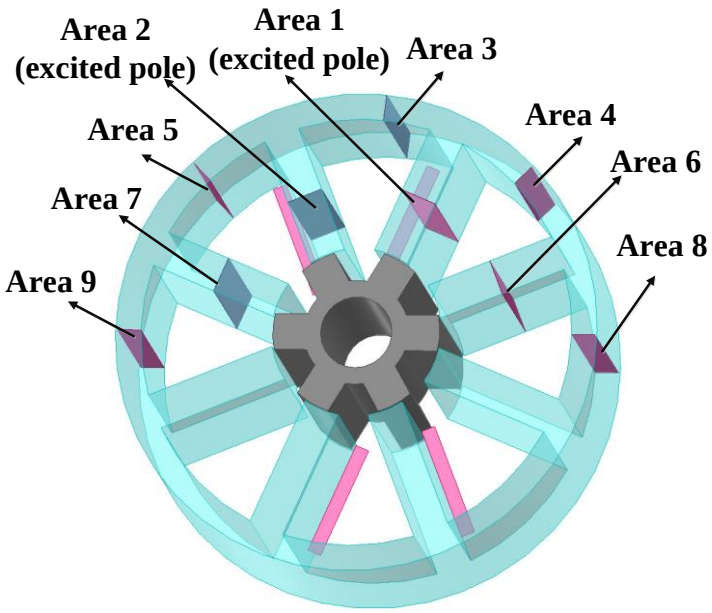

Figure 2-16 Representation of areas for flux calculation on a prototype 8/6 SRM

Table 2-6 Calculated flux values under two phase on excitation mode

Flux (m.Wb.)	Area1	Area2	Area3	Area4	Area5	Area6	Area7	Area8	Area9
I=1A	0.3	0.3	0.005	0.27	0.28	0.02	0.02	0.25	0.25
I=2A	0.39	0.39	0.013	0.33	0.34	0.04	0.04	0.29	0.29
I=3A	0.43	0.43	0.02	0.36	0.37	0.045	0.044	0.3	0.3

As it can be understood from the table, flux in the back core area between two excited poles is approximately zero. Moreover, a symmetric distribution of flux can be

observed. Therefore, superposition principle can be utilized in handling two phase on excitation case. Flux lines on a typical 8/6 SRM while two phases of the motor are in conduction simultaneously (two phase on excitation mode) are depicted in Figure 2-10.

2.7 Determination of static characteristics of the SRM

In this section, prediction of static torque and flux linkage characteristics of a given switched reluctance motor is described. Accurate determination of these characteristics is crucial in order to compute motor dynamic performance characteristics.

Summation of individual MMF drops on both teeth and air gap area and back iron region which was calculated earlier gives the total MMF drop of the SRM. The schematic diagram of teeth and air gap area and back iron region MMF drops and total MMF drop on switched reluctance motor for a specific pole flux value is represented in Figure 2-17. (note that from the figure at this particular operating point the total MMF (excitation) required can be found)

$$MMF_{total} = MMF + MMF_{bi} \tag{2-55}$$

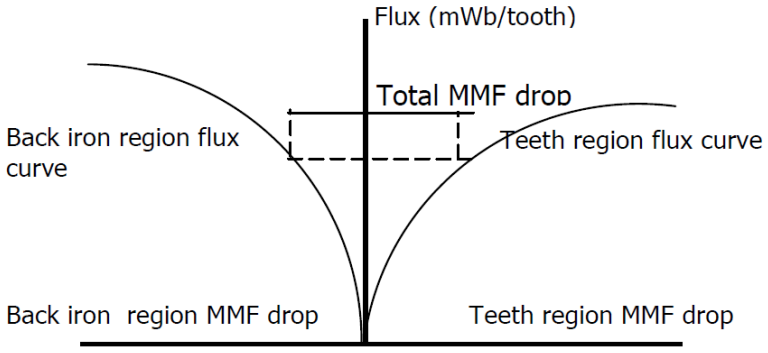

Figure 2-17 Teeth region, back iron and total MMF drops of a SRM

The initial aim of this section is accurate prediction of static torque-position-current and flux linkage-current-position characteristics of the SRM which are necessary in determination of motor dynamic performance characteristics. For this

purpose, torque, flux linkage and current values have to be determined from computed MMF and force data.

Once the total MMF drop on the SRM is determined, the required current can easily be calculated based on number of turns per pole (N) of the winding.

$$I = \frac{MMF_{total}}{2N} \tag{2-56}$$

From this current, the torque produced can be found at each position with the specified values of t/ λ and λ /g. The calculated tangential force can be easily transformed into developed torque by this motor at this particular position and excitation by using coefficients of the particular SRM geometry.

$$T = 0.5FD_{or}L \tag{2-57}$$

Because the stator pole flux is known, flux linkage of the phase winding (FL) can be simply determined using

$$FL = 2N\varphi \tag{2-58}$$

At this stage, for 220 flux density values (B=0.01, 0.02, …, 2.2) and 21 normalized rotor positions (x_n=0, 0.05, 0.1, ..., 1) from fully aligned to fully unaligned conditions, 220×21=4620 sets of data are produced. For data points the developed static torque, phase flux linkage and required phase current are calculated using the method described in this section. Finally, static- torque-position-current and flux linkage-current-position characteristics of the SRM are plotted. Typical static torque and flux linkage characteristics of a switched reluctance motor are depicted in Figure 2-18 and Figure 2-19. These characteristics will be plotted for a typical 8/6 SRM and the accuracy of the analytical calculations will be investigated in the following chapters. Precise prediction of these static characteristics is an important step towards dynamic performance calculations of the SRM. Static data produced in this section will be implemented to train two neural networks to be used in dynamic calculations of the SRM which will be discussed in the following section.

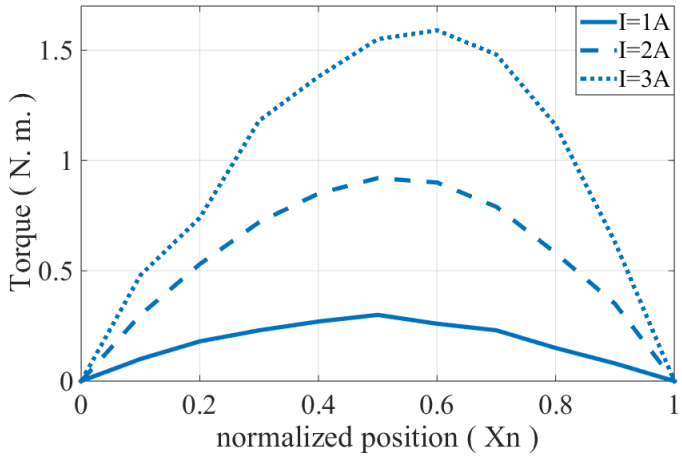

Figure 2-18 Typical torque-position-current characteristic of a SRM

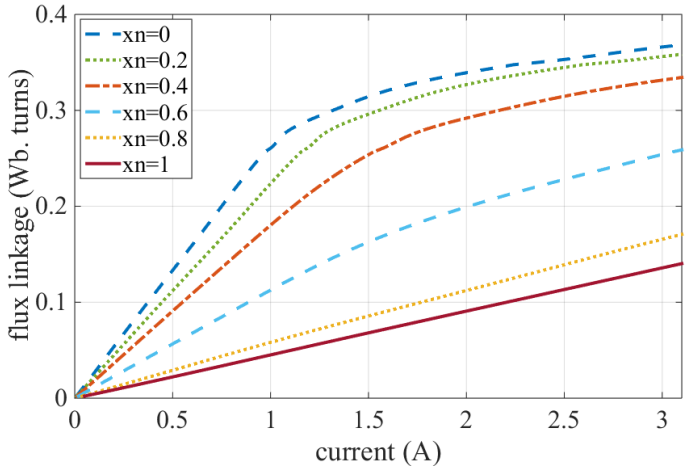

Figure 2-19 Typical flux linkage-current-position characteristic of a SRM

2.8 Training neural networks for dynamic calculations

After determination of static characteristics of the SRM, steady state dynamic performance characteristics (instantaneous current, torque and flux waveforms and torque-speed curves) have to be obtained. In dynamic calculations, it will be needed to estimate instantaneous current and torque values for any given geometry at a specified normalized rotor position and for a specific phase winding flux linkage value. For this purpose, static torque and flux linkage characteristics obtained in section 2.7 are used. As it is mentioned in previous sections 4620 data sets (static data for 220

variations in flux density and 21 variations in normalized position) are produced after calculation of static characteristics of the machine. However, interpolation and extrapolation methods have to be used to predict the intermediate points of static data.

Both interpolations methods and neural networks can be utilized for this purpose. In previous studies, interpolation methods were implemented to determine motor torque and current from normalized position and flux linkage data. The drawback of this method is lower accuracy especially when number of data sets is small. Therefore, in order to increase the precision of the calculations, neural networks are utilized to estimate SRM torque and current in dynamic calculations in this study. However, training these networks is time consuming which is a disadvantage.

Neural networks are used in each iteration of the utilized iterative methods (in this study, Runge Kutta) to predict instantaneous current and torque. Note that, normalized position and flux linkage are input variables of the networks. On the other hand, output parameters are current and torque.

Static data obtained in previous sections, are used to train two neural networks. For this purpose, two neural networks with two inputs and one output are trained to be used in dynamic calculations. It has to be mentioned that one neural network with two inputs and two outputs can also be utilized. However, accuracy of predictions is higher while using two separate neural networks with two inputs and one output for each one. Number of data sets used to train these networks is 4620 which is very high in comparison with previous works. Highest number of training data sets guarantees the accuracy of neural networks. These data sets are produced in static calculations of the SRM. The characteristics of these feedforward networks are summarized in the following table. The table includes input and out vectors of the neural networks, number of hidden neurons for each networks and the training functions which have been utilized.

Table 2-7 Characteristics of neural networks

	Input vector	Output variable	Number of hidden neurons	Training function
Network1	(x_n FL)	I	30	trainlm
Network2	(x_n FL)	T	30	trainlm

2.9 Dynamic performance calculations of SRM

Once static torque-position-current and flux linkage-current-position characteristics of the SRM are obtained, dynamic performance characteristics need to be calculated. What is meant by dynamic characteristics of the motor is the calculation of phase current, flux linkage and torque variation with time and torque-speed curves of the SRM. These characteristics are calculated at steady state conditions here, in other words, assuming that the motor is operating at a particular speed at a given time instant.

It has to be noticed that because a constant speed is considered in calculations, rotor position can be considered as a representative of time. Hence, by determining instantaneous current and torque in each rotor position, variation of torque and current versus time can then be simply calculated by transforming rotor positions into the corresponding time. Note that rotor positions in which calculations are carried out are determined based on turn on angle and conduction period. Same as the literature, step size in which rotor position is varied is set to 1/4000 radian in this study.

It is worth mentioning that a drive is assumed to be current controlled. In other words, a chopper circuit is utilized which controls the upper and lower limits of the phase currents. Furthermore, the SRM is assumed to be operating under one phase on or two phase on excitation modes. For the static calculations in this section, only one phase on mode is considered. Two phase on mode will be discussed in section 2.10. The drive is assumed to operate with specified turn on and conduction angle. Calculations take into account the rise and decay of phase currents and the overlap of contributions from different poles due to the drive operation. Consideration of overlaps between consecutive phase currents in analytical calculations are discussed in details in section 2.10.

Steady state dynamic calculation flowchart of an SR motor is depicted in Figure 2-20. Corresponding section for each block is also revealed inside the blocks.

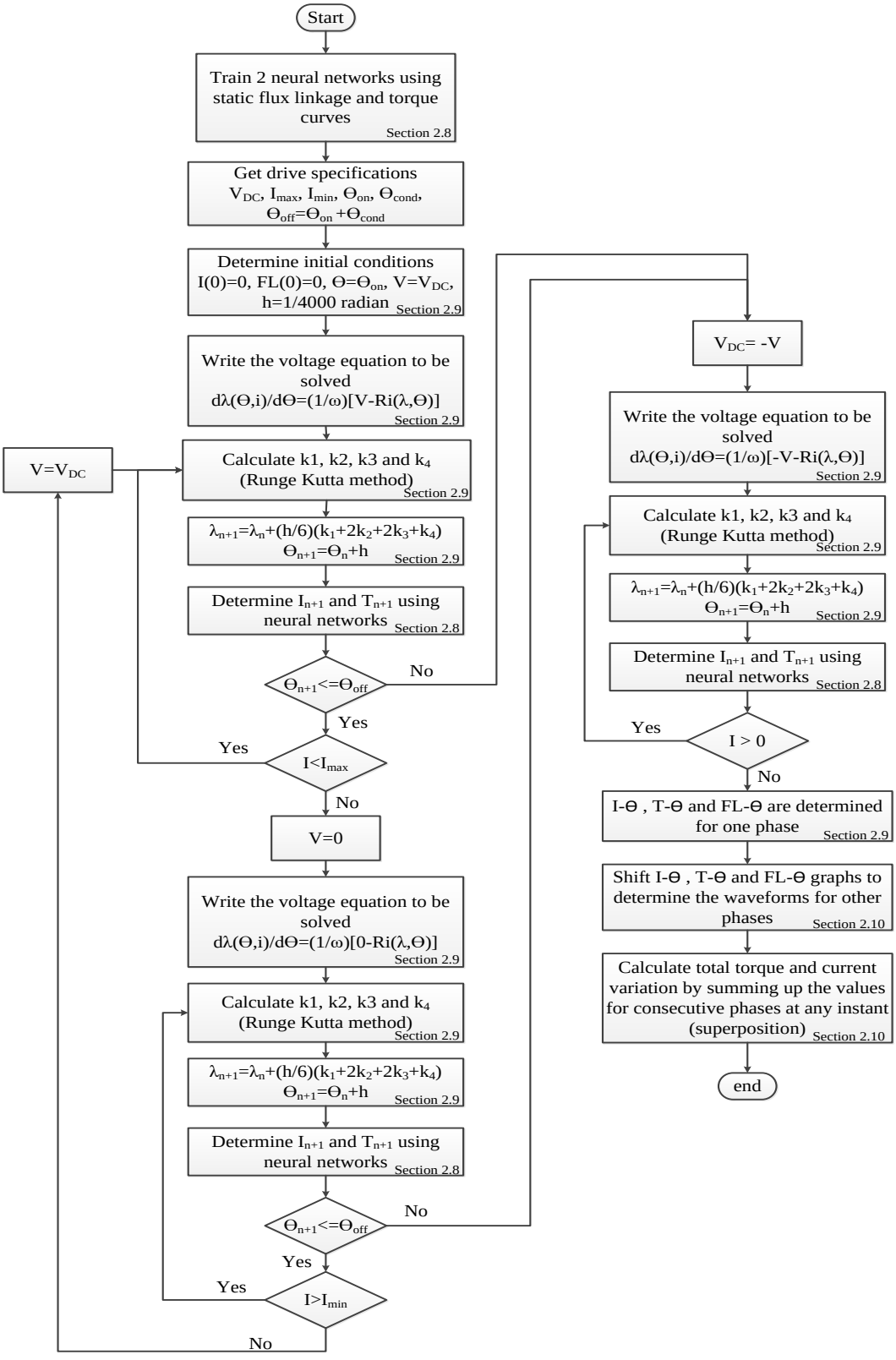

Figure 2-20 Steady state dynamic calculation flowchart of an SR motor

Instantaneous current and torque of an SR motor can be obtained by considering steady state equivalent circuit of the machine. The electrical equivalent circuit of a switched reluctance motor for one phase is shown in the following figure.

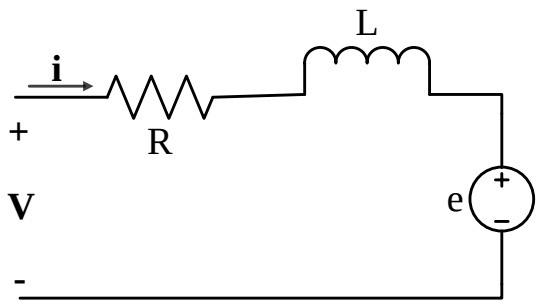

Figure 2-21 One phase electrical equivalent circuit of a switched reluctance motor

Initial current and flux linkage are assumed to be zero before the phase switch is turned on. The initial value of rotor position (θ_0) is also set to the rotor position angle in electrical radians in which the phase switch is desired to be turned on.

Based on the equivalent circuit following equation can be written.

$$V = Ri(\lambda,\theta) + \frac{d\lambda(\theta,\mathrm{i})}{dt} \tag{2-59}$$

In this equation V and i are DC side voltage and instantaneous phase current respectively. R, L and e stand for phase resistance, phase inductance and induced back EMF respectively. This equation can be simply rewritten as follows.

$$V = Ri + \frac{d\lambda(\theta,\mathrm{i})}{d\theta}\frac{d\theta}{dt} = Ri + \omega\frac{d\lambda(\theta,\mathrm{i})}{d\theta} \tag{2-60}$$

ω is rotor speed in electrical radians/sec which is assumed to be constant in analytical calculations. In other word, mechanical transients of the machine are not taken into account in calculations. Therefore, this first order differential equation can

be rewritten in a way which is suitable to be solved using the desired numerical method.

$$\frac{d\lambda(\theta,\mathrm{i})}{d\theta} = \frac{1}{\omega}(V - Ri(\lambda,\theta)) \tag{2-61}$$

In this study, 4th order Runge Kutta method is utilized in order to solve this differential equation. For this purpose, a general form is considered for this first order ordinary differential equation to be solved using Runge Kutta method.

$$\frac{d\lambda}{d\theta} = f(\lambda,\theta) \qquad \lambda(0)=0 \tag{2-62}$$

Starting from an initial point and using Runge Kutta method, quantities of variables for the next iteration can be easily computed using

$$\lambda_{n+1} = \lambda_n + (\frac{h}{6})(\mathrm{k}_1 + 2\,\mathrm{k}_2 + 2\,\mathrm{k}_3 + \mathrm{k}_4) \tag{2-63}$$

$$\theta_{n+1} = \theta_n + h \tag{2-64}$$

In these equations h is the step size of the numerical method. Value of h is taken as 1/4000 radians to increase the accuracy of the solution as much as possible. Four coefficients in the above equation are calculated in each iteration using

$$k_1 = f(\theta_n, \lambda_n) \tag{2-65}$$

$$k_2 = f(\theta_n + \frac{h}{2}, \lambda_n + \frac{\mathrm{hk}_1}{2}) \tag{2-66}$$

$$k_3 = f(\theta_n + \frac{h}{2}, \lambda_n + \frac{\mathrm{hk}_2}{2}) \tag{2-67}$$

$$k_4 = f(\theta_n + h, \lambda_n + \mathrm{hk}_3) \tag{2-68}$$

It has to be noticed that in equations (2-65) to (2-68) the value of k found in each equation is used in the subsequent one. Moreover, as mentioned earlier, the step size (h) is set to 1/4000 radians. The iterative calculations are carried out and instantaneous values of flux linkage, current and torque are determined. These quantities are used as initial conditions for the subsequent iteration.

As a brief summary of the calculation method, in each iteration the corresponding rotor position in electrical radians (θ) is transformed into normalized rotor position (x_n). Furthermore, the flux linkage value calculated in previous step is considered as an initial condition for this iteration. Using the input vector of (x_n FL), instantaneous current and torque values are determined using two neural networks discussed in the previous section. These networks have been trained earlier using static torque and current data of the machine which were computed in previous stages. Then, Runge Kutta coefficients are calculated and flux linkage value is determined to be used as the initial condition for the next iteration. Rotor position angle is increased by the step size (h) and the same procedure is repeated until complete instantaneous current and torque waveforms are attained.

Note that depending on the operating condition of the drive circuit, the differential equation will vary. The only difference in these differential equations is the value of DC side voltage (V). While the current is rising DC side voltage is taken as V in the equation. Once the current passes I_{max} level imposed by the chopper, and it has to be reduced to I_{min} level, phase circuit is disconnected from the source, and the DC side voltage is set to zero in the equation. Finally, when the phase switch is turned off, DC side voltage is considered to be –V in the equation in order to hasten the current falling process and consequently avoid the negative torque production. A sample phase current waveform over time is represented in Figure 2-22. Current rising and falling sections and chopping actions can be easily distinguished in the figure.

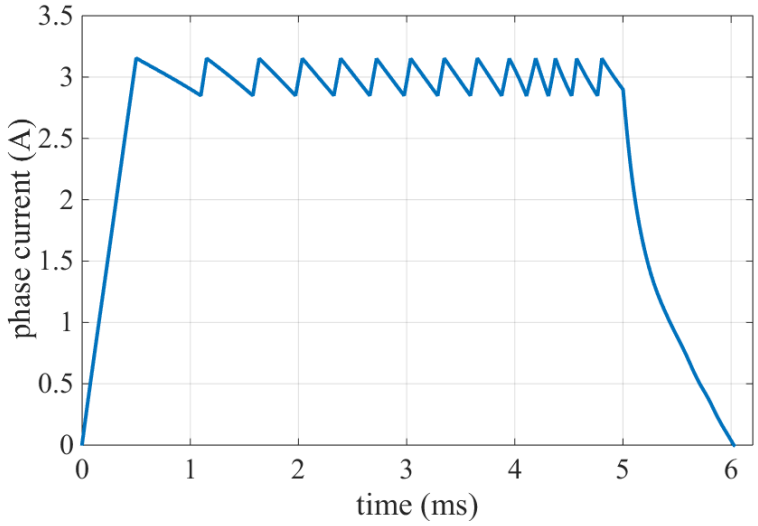

Figure 2-22 Sample phase current waveform of a SRM

The repetition process is continued until the excitation period is finished and the turn off angle is reached. At this stage, the DC side voltage is set to –V and the iterations are continued until the phase current reaches zero.

It is worth mentioning that slot leakage flux values are entered into the flux linkage curves as mentioned earlier. Hence, by prediction of flux linkage values in each iteration using Runge Kutta method, leakage flux effect and the corresponding MMF drop is also considered in analytical calculations. Therefore, computed torque and flux values include the effect of slot leakage flux.

It is possible that the current does not reach to its maximum chopping value. This is a condition which happens at higher rotational speeds. In this case, the differential equation is solved by taking DC side voltage as +V. Once turn off angle is reached, voltage is changed to –V in the equation. There will be no chops and hence, no current decays between chopping actions.

If a phase of the SR motor is turned on before the previously conducting phase current reaches zero, then two phases of the SRM will be in conduction at the same time. The problem will be handled based on superposition principle which will be discussed in the following section.

2.10 Overlaps in consecutive phases currents and total torque calculation

If a phase of the SR motor is turned on before the previous phase is in conduction yet, there will be overlaps between consecutive phases currents. Based on the flux distribution in an SR motor in two phase on excitation mode (see Figure 2-10), calculations for each phase current can be performed independently. For this purpose, current and torque developed due to one phase can be calculated while neglecting overlaps between phases. Then, due to repetitive nature of the SRM, consecutive phase current and torque waveforms can be easily created by shifting the corresponding waveforms of the calculated phase for a specified amount depending on the number of stator and rotor poles. Using the superposition principle total developed torque and input current waveform of the SRM can be easily determined by summing consecutive phase torque and current waveforms. It has to be mentioned that the effect of simultaneously conducting phases on MMF drops on teeth and air gap regions and back tooth regions are all taken into account in the proposed analytical model.

It is obvious that once phase conduction period and firing angle are known, current and torque waveforms of one phase can be easily determined and plotted versus electrical angle. Choosing switching pattern (conduction period and firing angle) of the SRM determines the operating condition of the machine. Different excitation patterns including one phase on excitation, two phase on excitation and combination of these two methods can be easily created by controlling conduction period and firing angle. In this study, an optimization algorithm is used to determine the optimum point for the excitation pattern in which the objective function of the optimization is minimized.

Once the instantaneous torque waveform of one phase is determined, the developed torque of the SRM can be easily computed which will be discussed in details in verification of analytical results chapter. Typical instantaneous torque waveform of a switched reluctance motor is shown in Figure 2-23. Note that all overlaps in subsequent phase excitations are taken into account in developed torque and phase current calculations of the SRM. A sample instantaneous phase currents over time

graph for a typical 8/6 SRM can be seen in Figure 2-24. Furthermore, Instantaneous current and flux linkage waveforms are implemented in order to calculate copper and core losses and consequently the efficiency of the SRM which is discussed in the following chapter.

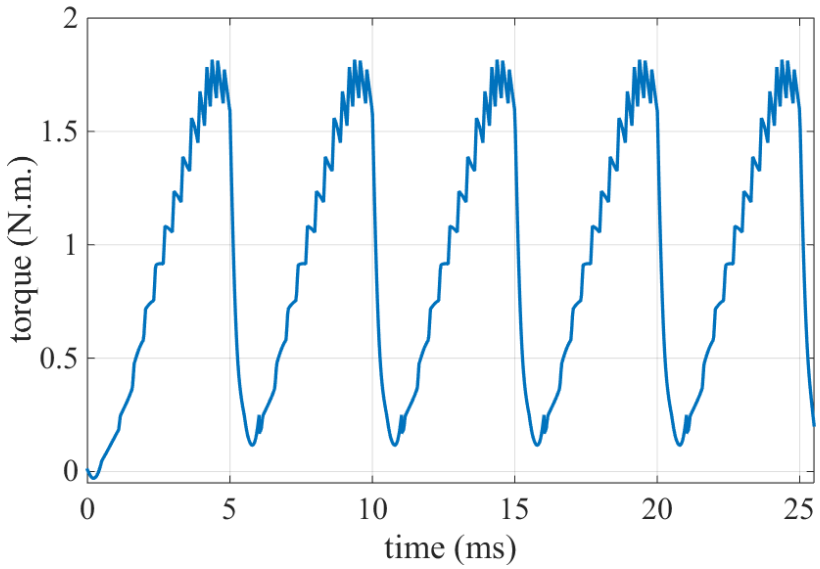

Figure 2-23 Typical instantaneous torque waveform of a switched reluctance motor

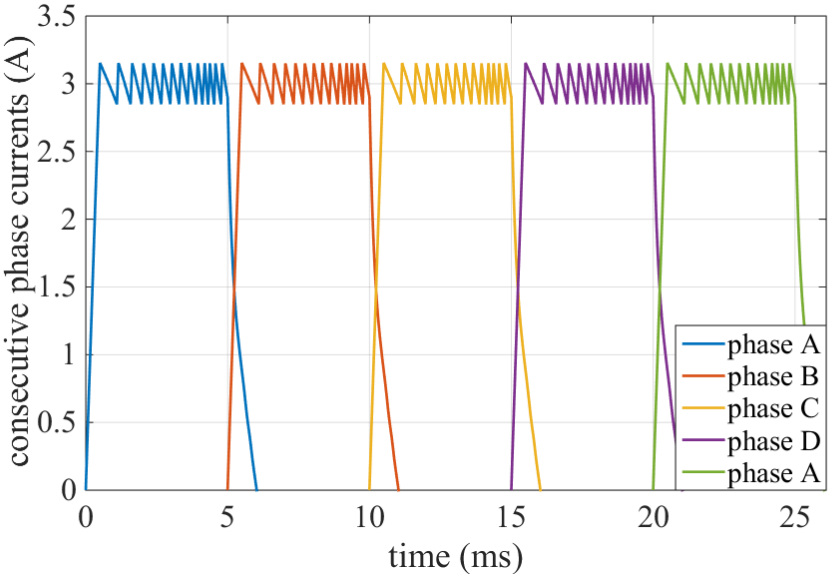

Figure 2-24 Typical instantaneous current waveforms of a 4 phase switched reluctance motor

2.11 Calculation of slot and tooth areas and SRM weight

Calculation of stator and rotor teeth and slots areas, copper length and weight and active mass of the SRM is an important step towards determination of slot fill factor, torque density, volume and material consumption of the machine. In this section, an analytical method which takes the effect of tooth tapering into account in calculation of slots and teeth areas is developed. Precise determination of copper length, area and weight is a vital step towards calculation of phase resistance and winding area of the SRM. Moreover, a comparison of motor weight and torque densities between the existing prototypes in the literature and the optimized SRM can be done by determination of motor active mass.

In this section the method which is used in order to compute slot and tooth areas and weight of the machine is discussed. An indirect slot area calculation method is implemented is this study which calculates area of slots based on calculated stator tooth area to prevent the complexities of direct slot area computations [69]. In order to have an exact computation of motor weight, effect of tooth tapering has to be taken into account in tooth area calculations. For this purpose, mean tooth width of the SRM is calculated.

$$t_{s_{mean}} = \frac{t_{s_{bore}} + t_{s_{backcore}}}{2} \tag{2-69}$$

$t_{s_{bore}}$ and $t_{s_{backcore}}$ represent stator tooth width at bore and near back core sections respectively. Stator tooth width at bore which is the minimum stator tooth width is easily calculated using normalized tooth width value.

$$t_{s_{bore}} = \lambda t_{sn} = \frac{\pi(\mathrm{D}_{or} + 2\,\mathrm{g})}{N_s} t_{sn} \tag{2-70}$$

On the other hand, in order to calculate maximum stator tooth width near back core section, tapering effect is taken into account. Hence, maximum stator tooth width is easily calculated using

$$t_{s_{backcore}} = t_{s_{bore}} + 2h_s \tan(\mathrm{a}) \tag{2-71}$$

Where h_s and a stand for stator tooth height and tapering angle respectively. Once mean tooth width is calculated, tooth area can then be easily computed.

$$\mathrm{A}_{s_{tooth}} = t_{s_{mean}} h_s \tag{2-72}$$

At this stage, computation of stator slot area is an easy task. For this purpose, one tooth area is subtracted form summation of one stator tooth and one stator slot areas.

$$A_{s_{slot}} = \frac{\pi}{4N_s}[(\mathrm{D}_{or} + 2\mathrm{g} + 2h_s)^2 - (\mathrm{D}_{or} + 2\mathrm{g})^2] - \mathrm{A}_{s_{tooth}} \tag{2-73}$$

This calculated slot area will be used in determination of wire diameter and stator winding configuration of the machine. Once stator slot area is calculated, active mass of the machine has to be determined which is used in definition of objective function of the optimization problem. For this purpose, weight of copper used in stator winding and stator and rotor teeth and back core sections are computed separately. At first stage, volume of each section has to be determined. Volume of stator teeth can be calculated based on teeth area.

$$V_{s_{teeth}} = N_s \mathrm{A}_{s_{tooth}} L \tag{2-74}$$

Because tapering effect is neglected in rotor teeth, calculation of rotor teeth area ($\mathrm{A}_{r_{tooth}}$) and volume ($V_{r_{teeth}}$) is straightforward.

$$V_{r_{teeth}} = N_r \mathrm{A}_{r_{tooth}} L = N_r t_r h_r L \tag{2-75}$$

In this equation, h_r, N_r and L stand for rotor tooth height, number of rotor poles and motor axial length respectively. Stator and rotor back core section volumes can then be simply computed using

$$V_{s_{bc}} = \frac{\pi L}{4}[(\mathrm{D}_{os})^2 - (\mathrm{D}_{os} - 2W_{bcs})^2] \quad (2\text{-}76)$$

$$V_{r_{bc}} = \frac{\pi L}{4}[(\mathrm{D}_{or} - 2h_r)^2 - (\mathrm{D}_{or} - 2h_r - 2W_{bcr})^2] \quad (2\text{-}77)$$

Where D_{or}, D_{os}, W_{bcs} and Wbcr represent rotor outer diameter, stator outer diameter, stator yoke width, and rotor yoke width respectively. While having stator and rotor material mass density (ρ_{Fe} =7650 kg/m3) in hand, active iron mass of the machine can be computed.

$$M_{Fe} = \rho_{Fe}(V_{s_{teeth}} + V_{s_{bc}} + V_{r_{teeth}} + V_{r_{bc}}) \quad (2\text{-}78)$$

After determination of iron weight, copper weight of stator windings has to be calculated. For this purpose, wire length of the SRM is computed.

$$l_w = 2 \times (\mathrm{L} + \mathrm{t}_{s_{mean}} + 2 \times (\frac{W_{slot}}{2})) \times 2\,\mathrm{N}_{pole} \quad (2\text{-}79)$$

In this equation N_{pole} represents number of turns per pole of the stator winding. W_{slot} represents the stator slot width. It has to mentioned that in this study, effect of end winding length is also taken into account in calculation of copper length and phase resistance. It can be said that end winding length at each end of the SRM can be roughly estimated to be equal to the half of stator slot width. A detailed discussion on end winding length effect will be given in chapter 5. It has to be mentioned that l_w is the copper length in one pole pair of the SRM. So, total copper length of the machine can be calculated using

$$L_w = \frac{N_s}{2} l_w \quad (2\text{-}80)$$

Now, computation of total copper volume of the machine is an easy task.

$$\mathrm{V}_{Cu} = \frac{\pi}{4} D_w^2 L_w \tag{2-81}$$

D_w stands for wire diameter of the SRM. Hence, copper weight of the machine can be simply calculated using

$$M_{Cu} = \rho_{Cu}\, \mathrm{V}_{Cu} \tag{2-82}$$

Where ρ_{Cu} is copper mass density and is taken as 8960 kg/m3 in analytical calculations. Finally, total active mass of the machine which consists of both iron weight as a representative of magnetic material and copper weight as a representative of electric material is computed.

$$M_{active} = M_{Fe} + M_{Cu} \tag{2-83}$$

Calculated active mass of the SRM will be implemented in defining objective function of the optimization problem.

2.12 Conclusions

In this chapter, analytical performance calculation of the SRM is discussed. The main aim of this chapter is developing a pure analytical model based on normalized and dimensionless data in order to calculate static torque and flux linkage characteristics of the SRM. Moreover, steady state dynamic current, flux and torque waveforms and torque speed curves of the machine are also computed. Analytical equations for calculation of slots and teeth areas and motor weight are also given.

Derivation of normalized force and permeance data based on Finite Element Method (FEM) and using Ertan's geometry is discussed at the first section of this chapter. This data is used to train three artificial neural networks which are used in analytical calculation procedure of the machine.

Static torque-position-current and flux linkage-current-position graphs of the SRM are determined. The precision of this data will be investigated in verifications of

analytical results chapter. Static data obtained at this section are implemented to train two neural networks which will be used in dynamic performance calculations of the machine.

Finally, the repetitive 4th order Runge Kutta method is introduced as a method for solving the differential equation. By carrying out the iterative analytical calculations, instantaneous current, flux density and torque waveforms of the SRM are determined. These waveforms will then be used to determine motor losses and efficiency in the following chapter. Accuracy of the proposed analytical method will be investigated in verifications of analytical method chapter using Finite Element Method (FEM) and measurements results.

It has to be noticed that in carrying out analytical calculations for dynamic performance computations, effects of both turn on angle and conduction period are taken into account. In other words, operation of SRM in one phase on and two phase on excitations are considered and overlaps between consecutive phases currents are discussed. A current controlled chopper is used to control the output torque of the SRM by setting minimum and maximum chopping current values.

At the end, calculation of slot area, and active mass of the SRM is discussed. Slot area will be used in determination of electric loading and winding configuration of the machine in subsequent chapters. Active mass of SRM which includes both iron weight and copper weight will be used in defining objective function of the optimization problem.

The analytical approach proposed in this study can be used in determination of static and dynamic performance characteristics of switched reluctance motors to be used in variety of application. It is worth mentioning that the normalized data are obtained using a specific core material. Hence, analytical calculations results are obtained by assuming that the core material is the same in SRMs. Effects of changing the core material in analytical calculations will be discussed in details in chapters 5 and 6.

CHAPTER 3

CALCULATION OF LOSSES AND EFFICIENCY

Precise calculation of losses and efficiency in a switched reluctance machine is a crucial point in determination of motor performance characteristics. The main losses of a switched reluctance machine are winding copper losses and core losses. The copper losses are easily calculated by computing the RMS value of the phase currents using a method which will be described in detail in upcoming sections. In order to calculate core losses of the machine, determination of flux waveforms in different parts of the machine is of interest. Fourier transform will be used to determine the main harmonics of the flux and subsequently the core losses of the motor. Next section deals with the explanation of the procedure used in calculation of losses and efficiency.

3.1 Calculation of copper losses

Complexities in copper loss calculations are due to non-sinusoidal nature of phase current waveforms. The current waveform in a switched reluctance motor changes under various operating conditions. In order to calculate copper losses of the machine accurately, the RMS value of the current has to be determined.

Because of the periodic nature of phase currents, the copper losses can be easily calculated in one period. In the first section the copper losses of the main conducting phase are calculated. A sample current waveform of a conducting phase is shown in Figure 3-1.

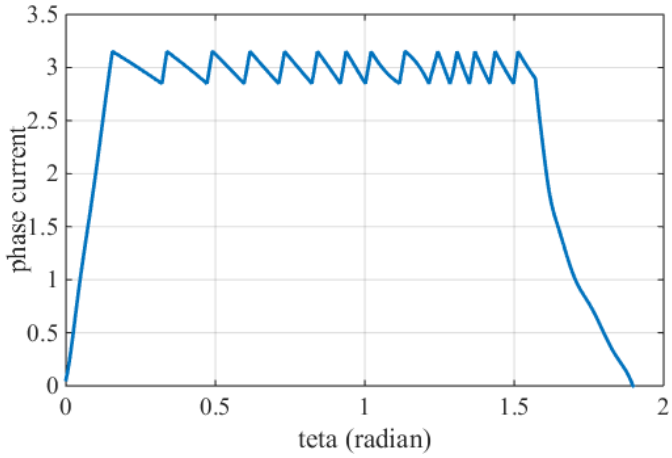

Figure 3-1 Sample phase current of a SRM

The RMS value of this current waveform is easily calculated using

$$I_{rms} = \sqrt{\frac{1}{T}\int_0^T i^2 dt} \tag{3-1}$$

Note that value of T in this equation is the repetition period of one phase current. This repetition period can be seen in Figure 3-2 which reveals the current of one phase in a typical 4 phase 8/6 switched reluctance motor.

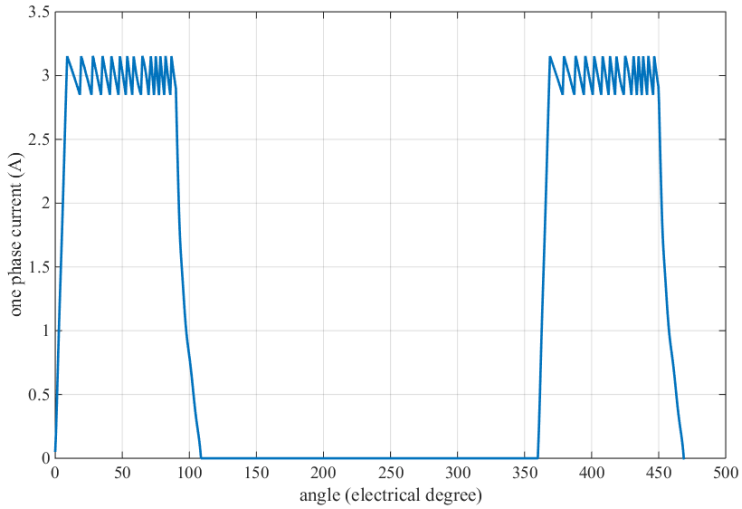

Figure 3-2 One phase current in one repetition period

It has to mentioned that the switched reluctance motor can operate under one phase on or two phase on excitation modes. The analytical copper loss calculation method will be the same for all operating conditions of a SRM. Figure 3-2 represents a state in which current of one phase does not decay to zero at the time that the next phase is turned on. Note that in a 4 phase SRM electrical distance between two consecutive phases is 90 electrical degrees.

The copper losses of one phase of the machine can then be simply calculated using

$$P_{cu1} = R \times I_{rms}^2 \tag{3-2}$$

In the above equation, R is the resistance of a phase winding. It is obvious that in an 8/6 SRM, phase winding resistance is resistance of a series winding in two opposite stator teeth which are 180 mechanical degrees far apart.

Once copper losses related to one phase of the machine is calculated, total copper losses of the machine can then be easily determined using following equation in which q in total number of phases in a switched reluctance motor.

$$P_{cu} = qP_{cu1} \tag{3-3}$$

3.2 Core loss computation

Precise calculation of stator tooth flux is a vital factor in determination of core losses in the machine. Knowing flux and flux density variations in stator teeth will lead to determination of flux density variations in all parts of the machine. Consequently, core losses corresponding to different parts of the motor can be computed by considering the main harmonic components of periodic flux waveforms in each part. The procedure will be discussed in details in later sections.

3.2.1 Determination of flux and flux density variations over time

Calculation of flux linkage-current-position characteristics of a SR motor was described in section 2.7. A sample flux linkage-current-position characteristic of a typical 8/6 SRM is shown in Figure 3-3.

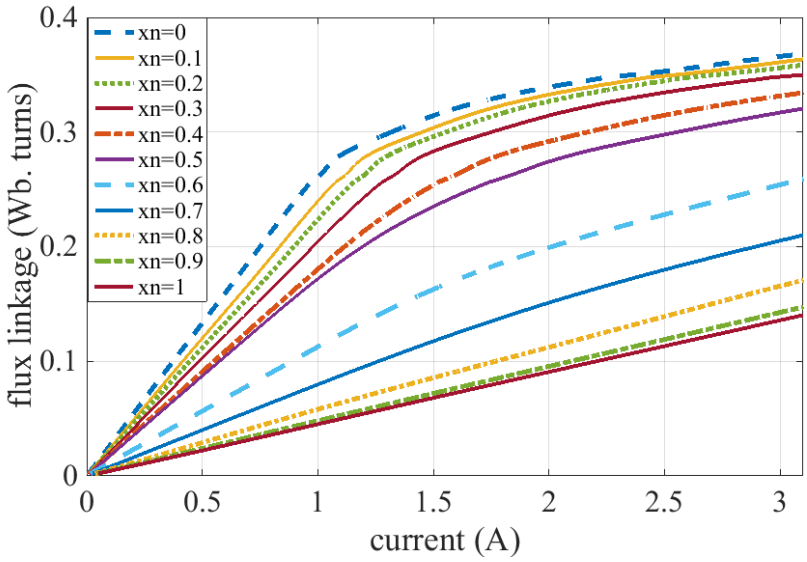

Figure 3-3 Flux linkage-current-position characteristic

The flux linkage of the winding which is carrying current is computed in each iteration of dynamic calculation process of the machine. While having variation of flux linkage over time the tooth flux waveform can be easily found using

$$\varphi_{pole} = \frac{\lambda}{N_{pole}} \tag{3-4}$$

The typical flux variation in one stator tooth is represented in the following figure.

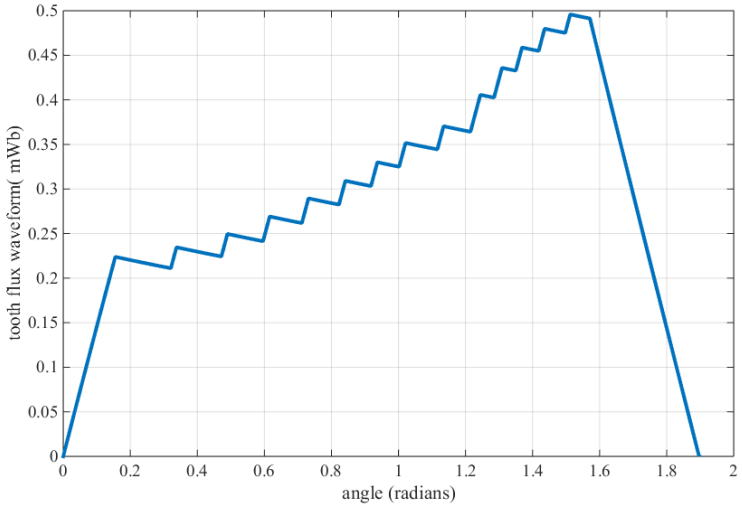

Figure 3-4 Flux variation in one stator tooth

This figure reveals the flux variation in a stator tooth at a time period in which the corresponding phase winding is conducting. Due to the periodic nature of the drive system, the flux waveform in stator teeth is periodic as well. The typical flux variation in a stator tooth in a prototype 8/6 switched reluctance motor can be seen in Figure 3-5.

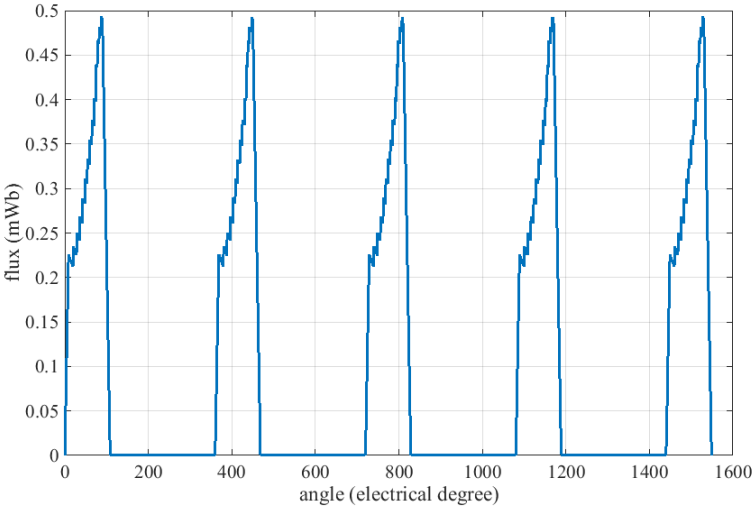

Figure 3-5 Flux variation in one stator tooth

It is worth mentioning that for any excitation mode of the SRM, the analytical computations of flux waveforms in stator teeth are the same. The proposed method is valid for both one phase on and two phase on excitation modes.

By having the flux variation in stator teeth, determination of the flux variation over time in a rotor tooth is an easy task. The repetition period of stator tooth flux waveform equals to 360 electrical degrees. It has to be noticed that in a switched reluctance machine, the repetition period of the rotor tooth flux density is found using [43, 70]

$$T_{rotor-flux-density} = \frac{N_r}{N_s} T_{stator-flux-density} = \frac{6}{8} T_{stator-flux-density} \tag{3-5}$$

If it is desired to calculate rotor tooth flux frequency, following equation can be used.

$$f_{rotor-flux} = \frac{1}{N_r} f_{stator-flux} \tag{3-6}$$

Thus the rotor tooth flux density variation waveform has a repetition period of 270 electrical degrees. Figure 3-6 represents variation of flux in one rotor tooth in the same 8/6 SRM.

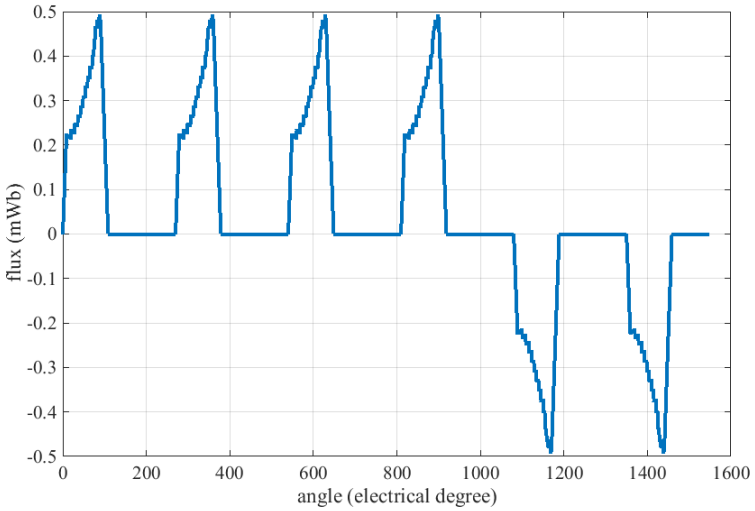

Figure 3-6 Flux variation in one rotor tooth

Because the excitation of a SRM drive is unidirectional, the stator tooth flux variation waveform has always positive or negative values of flux depending on flux variation of which tooth is being considered. In other words, in a switched reluctance motor, half of the stator teeth always have a positive flux, however, in the other half, flux polarity is always negative. On the other hand, rotor flux waveform changes its sign after passing four consecutive stator teeth.

Determination of back core flux variations in both stator and rotor is straightforward after calculation of stator and rotor teeth flux waveforms. Figure 3-7 represents the distribution of stator back core fluxes in different sections of stator back core.

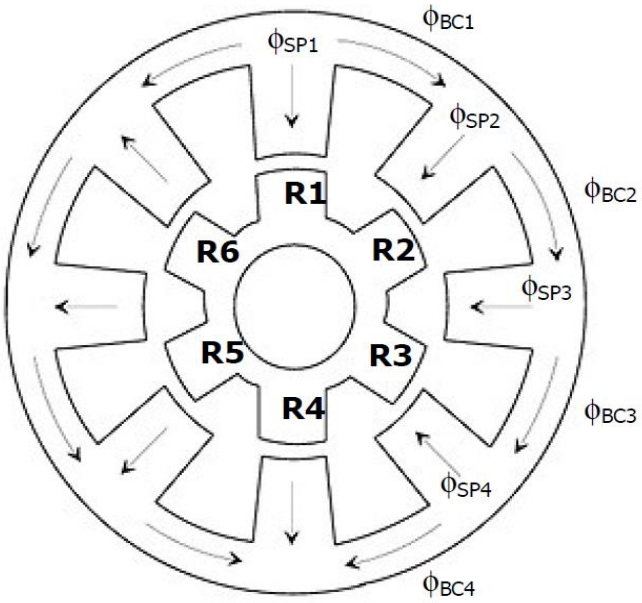

Figure 3-7 Distribution of stator pole and back core fluxes

Thus the flux waveforms in each separate section of stator back core can be calculated easily using above figure. Following equations are used to calculate the stator back core flux distribution in each section. The validity of each equation can be simply corroborated using Figure 3-7.

$$\varphi_{bc1}(\theta)=\frac{(-1)\times\varphi_{sp1}(\theta)+1\times\varphi_{sp2}(\theta)+1\times\varphi_{sp3}(\theta)+1\times\varphi_{sp4}(\theta)}{2} \tag{3-7}$$

$$\varphi_{bc2}(\theta)=\frac{(-1)\times\varphi_{sp1}(\theta)+(-1)\times\varphi_{sp2}(\theta)+1\times\varphi_{sp3}(\theta)+1\times\varphi_{sp4}(\theta)}{2} \tag{3-8}$$

$$\varphi_{bc3}(\theta)=\frac{(-1)\times\varphi_{sp1}(\theta)+(-1)\times\varphi_{sp2}(\theta)+(-1)\times\varphi_{sp3}(\theta)+1\times\varphi_{sp4}(\theta)}{2} \tag{3-9}$$

$$\varphi_{bc4}(\theta)=\frac{(-1)\times\varphi_{sp1}(\theta)+(-1)\times\varphi_{sp2}(\theta)+(-1)\times\varphi_{sp3}(\theta)+(-1)\times\varphi_{sp4}(\theta)}{2} \tag{3-10}$$

The typical stator back core flux variation in one of the four separate sections is revealed in following figure.

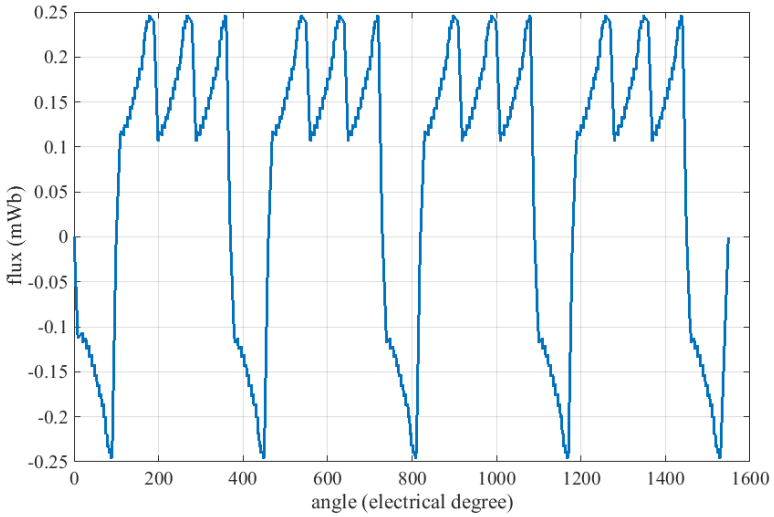

Figure 3-8 Flux variation in one stator back core section

The same procedure can be utilized to determine rotor back core flux variation over time. Again the back core in divided into separate sections and the flux values corresponding to each section are computed.

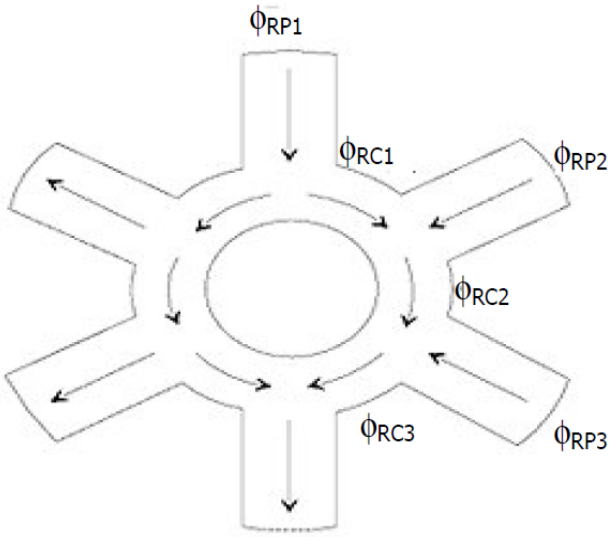

Figure 3-9 Distribution of rotor pole and back core fluxes

Following equations are obtained simply based on above figure to calculate rotor back core flux variation.

$$\varphi_{rc1}(\theta) = \frac{1\times\varphi_{rp1}(\theta) + (-1)\times\varphi_{rp2}(\theta) + (-1)\times\varphi_{rp3}(\theta)}{2} \tag{3-11}$$

$$\varphi_{rc2}(\theta) = \frac{1\times\varphi_{rp1}(\theta) + 1\times\varphi_{rp2}(\theta) + (-1)\times\varphi_{rp3}(\theta)}{2} \tag{3-12}$$

$$\varphi_{rc3}(\theta) = \frac{1\times\varphi_{rp1}(\theta) + 1\times\varphi_{rp2}(\theta) + 1\times\varphi_{rp3}(\theta)}{2} \tag{3-13}$$

The calculated rotor back core flux variation is shown in the following figure. Note that this figure reveals the variation of flux in just one of the three sections shown in Figure 3-10.

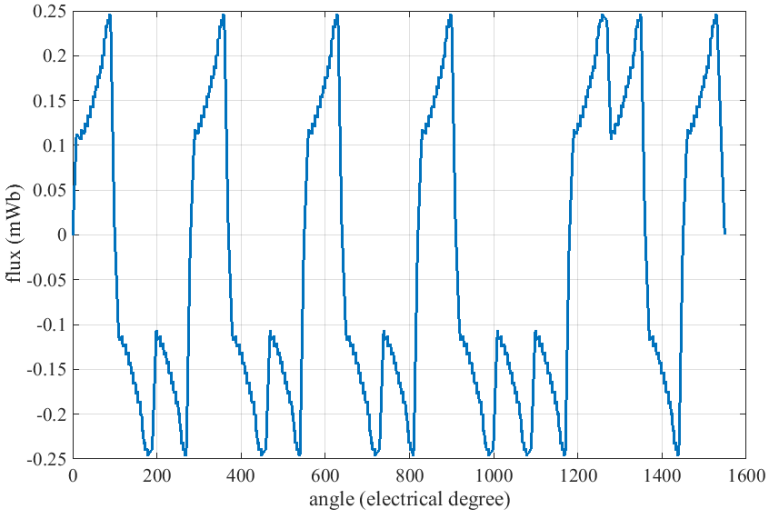

Figure 3-10 Flux variation in one rotor back core section

Once the flux variation is determined in all parts of the motor, flux density values can be easily found. In computation of flux density values in each section, flux values are divided into the corresponding area from which the flux passes. Typical flux density variation waveforms in a prototype 8/6 switched reluctance motor are shown for different parts of the machine in following figures. It is worth mentioning that a uniform flux distribution is assumed in all stator and rotor teeth and back core sections.

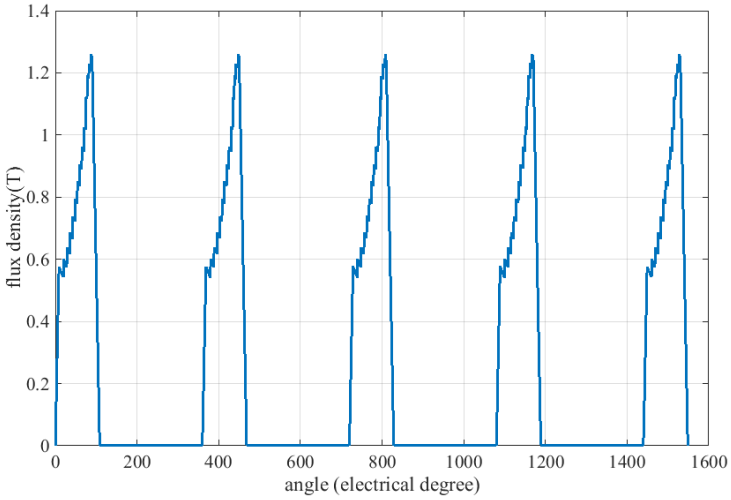

Figure 3-11 Flux density variation in one stator tooth

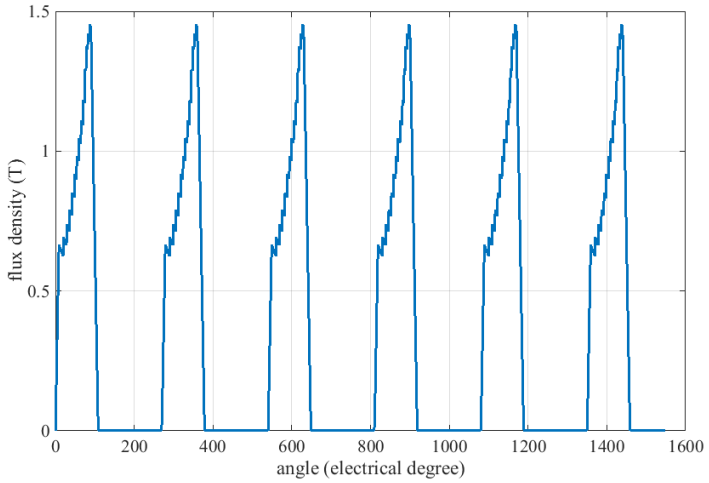

Figure 3-12 Flux density variation in one rotor tooth

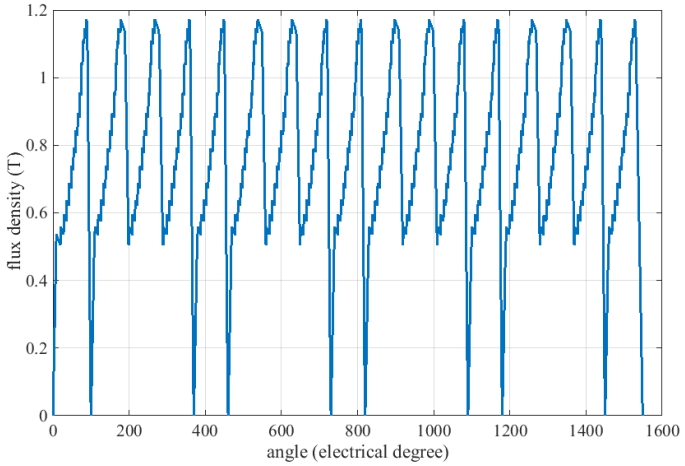

Figure 3-13 Flux density variation in one stator back core section

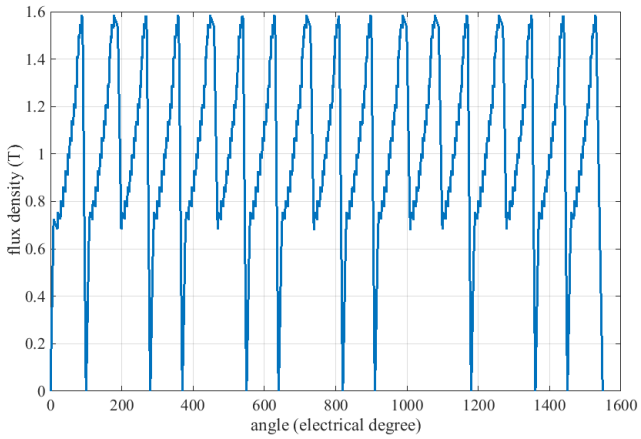

Figure 3-14 Flux density variation in one rotor back core section

3.2.2 Calculation of harmonic components of flux density waveforms

Calculation of core losses in different parts of the machine, due to the non-sinusoidal nature of flux density waveforms, has some degrees of complexity. Several SRM core loss calculation methods are introduced and discussed in the literature. A detailed description of the proposed methods in the literature can be found in section 1.7.

In this section, Fast Fourier Transform (FFT) method is used to determine the most dominant harmonic components which will be considered in core loss calculations. A comprehensive discussion on Fast Fourier Transform can be found in [71, 72].

For any periodic function f(t), with a repetition period of T, the Fourier expansion is defined as

$$f(t) = \frac{a_0}{2} + \sum_{n=1}^{\infty} [a_n \cos(n\omega t) + b_n \sin(n\omega t)] \tag{3-14}$$

Where

$$\omega = \frac{2\pi}{T} \tag{3-15}$$

And, the terms a_0, a_n and b_n can be simply calculated using

$$a_0 = \frac{2}{T} \int_T f(t)\, dt \tag{3-16}$$

$$a_n = \frac{2}{T} \int_T f(t) \cos(n\omega t)\, dt \tag{3-17}$$

$$b_n = \frac{2}{T} \int_T f(t) \sin(n\omega t)\, dt \tag{3-18}$$

The harmonic distribution of stator and rotor fluxes is calculated using Fast Fourier Transform (FFT) in MATLAB software. Harmonic spectrum of fluxes in stator tooth, stator back core, rotor tooth, and rotor back core are depicted in four following figures respectively.

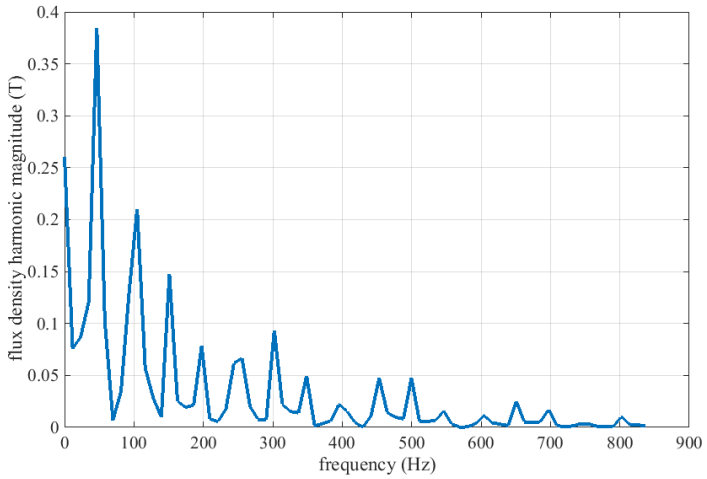

Figure 3-15 Flux density harmonic spectrum in one stator tooth

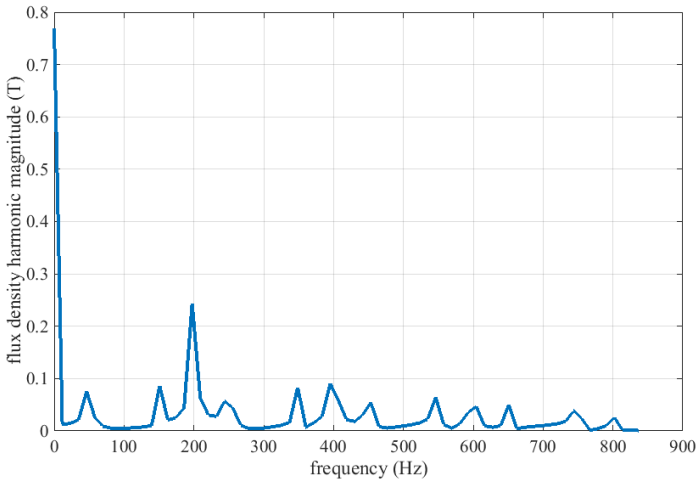

Figure 3-16 Flux density harmonic spectrum in one stator back core section

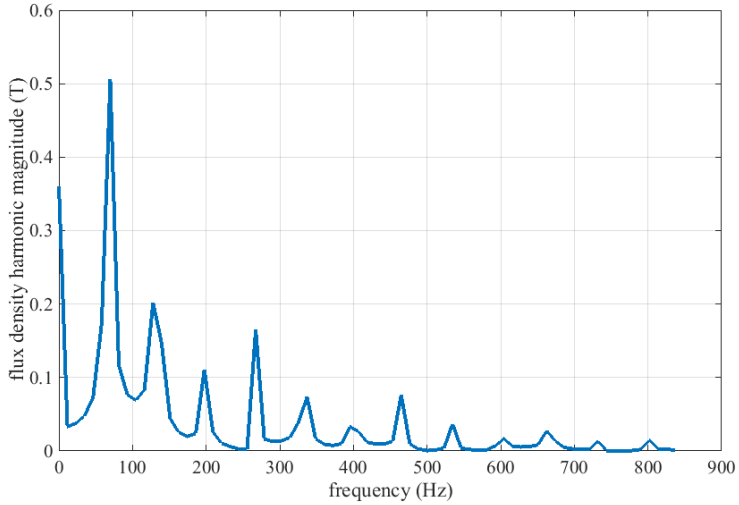

Figure 3-17 Flux density harmonic spectrum in one rotor tooth

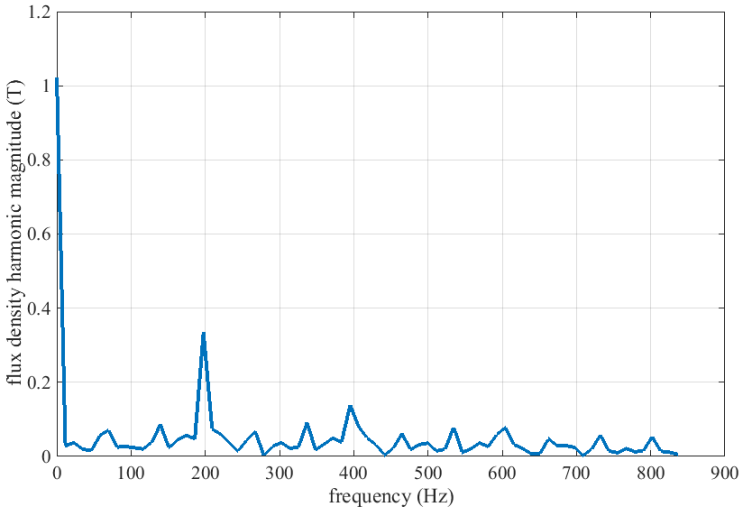

Figure 3-18 Flux density harmonic spectrum in one rotor back core section

The prominent harmonic components of each flux density waveform can be easily determined. As it is obvious from the figures the fundamental frequency of stator fluxes is 50Hz. On the other hand, rotor teeth and back core flux densities in a typical 8/6 switched reluctance motor have a fundamental frequency of 66.67 Hz which is found simply using

$$f_r = \frac{N_s}{N_r} f_s = \frac{8}{6} \times 50 = 66.67 Hz \quad (3\text{-}19)$$

The harmonic components of flux waveforms are used to calculate the core losses in different parts of the machine. Because as it is obvious from harmonic spectrums of flux waveforms, flux density magnitude becomes negligible in higher order harmonic components, effects of the harmonic components in core loss calculations are considered up to 10th harmonic.

3.2.3 Core loss coefficients

Once basic harmonics of flux waveforms in different parts of the machine are known, core losses can then be simply calculated. In this part, core loss coefficients of two different core materials will be presented. The first one is M36 steel which is used in calculation of core losses in an 8/6 SRM used for washing machine applications. The second material is high silicon steel, which is so called Super Core 10JNEX900 with lamination thickness of 0.1 mm which is used in the structure of a switched reluctance motor designed to be used in electric vehicle applications. This material has very low iron losses. On the other hand, its saturated flux density is low.

3.2.3.1 Core loss coefficients of M36 steel

Core losses of M36 steel are computed in three separate sections; eddy current, hysteresis, and excessive losses [44-46]. In next sections the detailed procedure of loss calculation will be described in three separate parts. It is worth mentioning that a conventional Steinmetz equation can be utilized in order to calculate core losses of the machine. However, core loss calculations for M36 steel are carried out based on a novel work done by Pillay which takes the effects of excessive losses into account as well. Calculation of core losses for 10JNEX900 which will be discussed in upcoming sections is based on the conventional Steinmetz equations. All analytically obtained results will be verified in chapter 4.

3.2.3.1.1 Eddy current losses

In order to calculate eddy current losses in different parts of the machine, the well-known Steinmetz equation is used.

$$P_e = k_e f^2 \hat{B}^2 \tag{3-20}$$

In this equation f and B represent frequency and peak flux density values respectively. k_e stands for eddy current loss coefficient. Frequency and peak flux density values calculated in the previous section are used to compute eddy current losses of the machine. The most important stage is the prediction of k_e value. This value is predicted based on a novel study done by Pillay [44-46]. The approximation of k_e for a wide range of frequencies can be seen in the following figure.

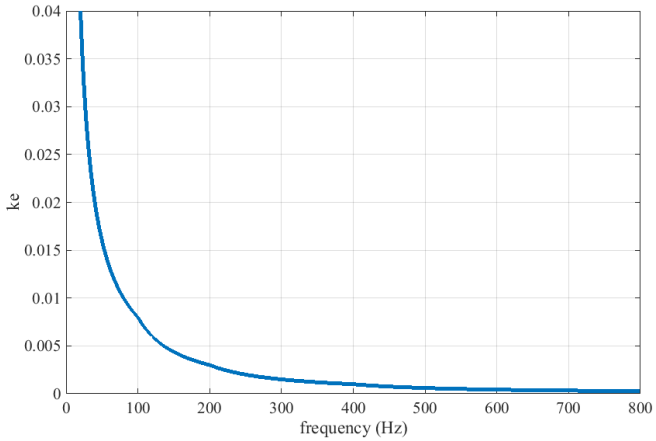

Figure 3-19 k_e approximation versus frequency

Thus, the eddy current losses corresponding to each harmonic component is calculated for stator and rotor teeth and back core sections. Using superposition principle, the total eddy current losses are computed for different parts of the machine by summing up the eddy current losses for various harmonic components. Note that the unit of eddy current losses calculated using this procedure is W/kg.

This is worth mentioning that eddy current losses per unit mass are computed in stator and rotor teeth and back core sections separately. Multiplying these per unit

of mass values by mass of each segment gives the total eddy current losses in each section. Then total eddy current losses of the machine are simply calculated using

$$P_e = P_{e_{st}} + P_{e_{rt}} + P_{e_{sbc}} + P_{e_{rbc}} \tag{3-21}$$

where $P_{e_{st}}$, $P_{e_{rt}}$, $P_{e_{sbc}}$ and $P_{e_{rbc}}$ stand for eddy current losses in stator teeth, rotor teeth, stator back core, and rotor back core sections respectively.

3.2.3.1.2 Hysteresis losses

Like eddy current losses, hysteresis losses of the machine are dependent on both excitation frequency and the peak flux density in the core. A newly introduced method expresses these losses per unit of frequency. The following figure represents hysteresis losses variation versus peak flux density in the core.

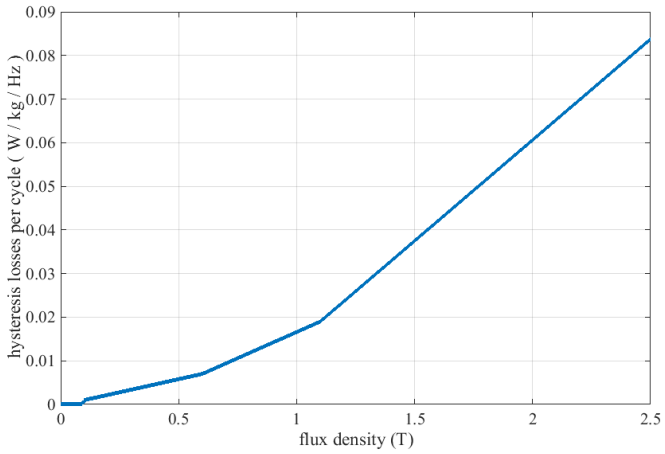

Figure 3-20 Hysteresis losses per cycle versus flux density approximation

It has to be noticed that the hysteresis losses obtained using Figure 3-20 have the unit of W/kg/Hz. If the hysteresis losses per cycle value which is determined using the figure is shown by P_h', then hysteresis losses per unit of motor mass (W/kg) can be simply calculated using

$$P_h = f \times P_h' \tag{3-22}$$

The same procedure used in calculation of total eddy current losses is used again to compute total hysteresis losses. Thus, these losses are calculated easily using

$$\mathrm{P}_h = P_{h_{st}} + P_{h_{rt}} + P_{h_{sbc}} + P_{h_{rbc}} \tag{3-23}$$

where $P_{h_{st}}$, $P_{h_{rt}}$, $P_{h_{sbc}}$, and $P_{h_{rbc}}$ stand for hysteresis losses in stator teeth, rotor teeth, stator back core, and rotor back core sections respectively.

3.2.3.1.3 Excessive losses

By taking only eddy current and hysteresis losses into account, experimental results show a higher value than predicted values. This difference is known as excessive losses of the core material. These losses can be approximated using

$$P_{ex} = k_{ex} f^{1.5} \hat{B}^{1.5} \tag{3-24}$$

In this equation, k_{ex} represents excessive losses coefficient. This coefficient is approximated using Figure 3-21 based on a novel work done by Pillay [44-46].

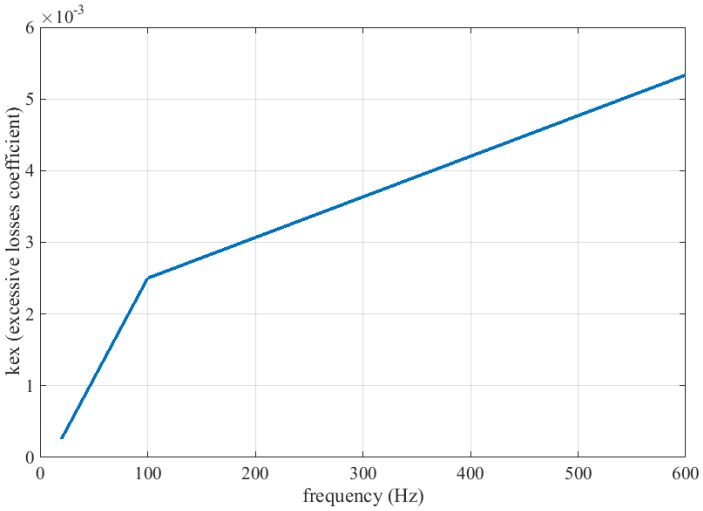

Figure 3-21 k_{ex} approximation versus frequency

Note that the excessive losses calculated using this method are per unit mass (W/kg) of the machine. Like what is done in calculation of total eddy current and hysteresis losses of the SRM motor, total excessive losses are calculated simply using

$$\mathrm{P}_{ex} = P_{ex_{st}} + P_{ex_{rt}} + P_{ex_{sbc}} + P_{ex_{rbc}} \tag{3-25}$$

In this equation $P_{ex_{st}}$, $P_{ex_{rt}}$, $P_{ex_{sbc}}$ and $P_{ex_{rbc}}$ represent excessive losses in stator teeth, rotor teeth, stator back core, and rotor back core respectively.

Total core losses of the machine are computed by summing up eddy current, hysteresis and excessive losses.

$$P_c = P_e + P_h + P_h \tag{3-26}$$

3.2.3.2 Core loss coefficients of 10JNEX900

Core loss curves of Super Core 10JNEX900 for two different frequencies (400 and 1000 Hz) are shown in the following figure. Note that core loss unit in these graphs is W/kg.

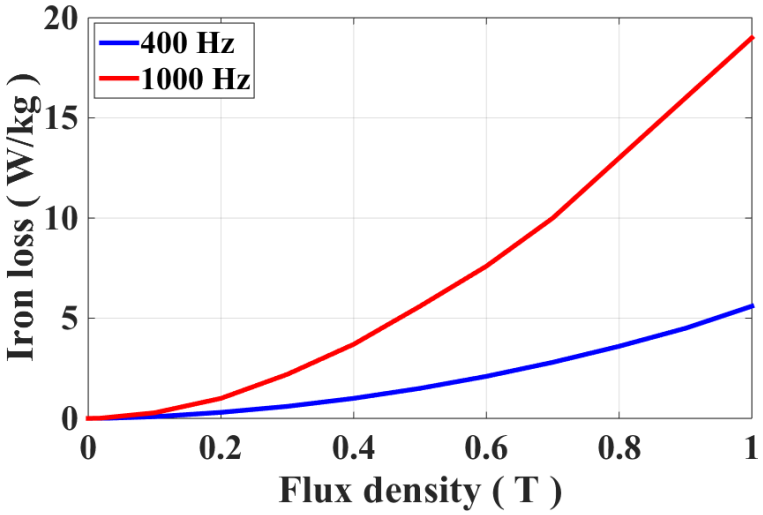

Figure 3-22 Core loss curves of 10JNEX900

It is obvious that core loss coefficients can be simply calculated using the above graph. For this purpose, core loss values at B=0.4 T are taken into account for both given frequencies. Then, eddy current (k_e) and hysteresis (k_h) coefficients are computed by substituting the iron loss values in well-known Steinmetz equation.

$$P_c = k_e f^2 \hat{B}^2 + k_h f \hat{B}^n \tag{3-27}$$

Note that parameter n in Steinmetz equation is taken as 2. Therefore, eddy current and hysteresis coefficients for 10JNEX900 material are simply calculated.

$$k_e = 1.25 \times 10^{-5} \tag{3-28}$$

$$k_h = 0.01063 \tag{3-29}$$

At this stage, the same method used for calculation of iron losses in M36 steel is implemented to calculate core losses of 10JNEX900. For this purpose, iron loss is computed in unit of W/kg using Steinmetz equation for 10 first flux harmonic components for different machine parts. Then by multiplying core loss values by mass of each section iron loss is determined in each part. Finally, summing up 4 separate core loss values in stator and rotor teeth and back core sections gives total iron loss of the SRM.

$$\mathrm{P}_c = P_{c_{st}} + P_{c_{rt}} + P_{c_{sbc}} + P_{c_{rbc}} \tag{3-30}$$

In this equation $P_{c_{st}}$, $P_{c_{rt}}$, $P_{c_{sbc}}$ and $P_{c_{rbc}}$ stand for core losses in stator teeth, rotor teeth, stator back core and rotor back core sections respectively.

3.3 Total loss and efficiency calculation

Calculation of total losses is an easy task while knowing copper losses and core losses of the machine. Then, total losses of the SRM can be simply calculated by summing up copper losses and core losses.

$$P_{loss} = P_{cu} + P_c \tag{3-31}$$

In order to calculate efficiency of the machine, computing both input and output powers is necessary. Output power is simply calculated using

$$P_{out} = T_{avg} \times \omega_{mech} \tag{3-32}$$

Where ω_{mech} is rotor mechanical speed in rad/sec. T_{avg} is mean output torque calculated in the dynamic calculation section. Due to periodic nature of machine behavior, the average torque is obtained by computing average value of output torque in one period.

Then, determination of motor efficiency is a straightforward task using

$$\eta = \frac{P_{out}}{P_{in}} = \frac{P_{out}}{P_{out} + P_{loss}} \tag{3-33}$$

Note that calculation of P_{in} directly from input voltage and current is considerably complicated. Because of the chopping action, the input DC voltage is connected and disconnected repeatedly from drive circuit. So, input power has to be calculated in periods in which the DC voltage supply is connected to excitation circuit.

3.4 Conclusions

Precise determination of copper and core losses of the SRM is a vital step towards accurate prediction of motor efficiency. In this chapter, an analytical method is described in order to calculate resistive losses of a SR motor. Results of analytical copper loss calculations will be verified using measurements and FEM simulations results in next chapter.

Moreover, an analytical method based on actual flux variations and its harmonic components is proposed to determine core losses of the machine. For this purpose, flux and flux density waveforms are determined in stator and rotor teeth and back core sections. It is worth mentioning that the proposed analytical method is valid

for all operating modes of switched reluctance motors (one phase on or two phase on excitation modes).

Harmonic components of flux waveforms are calculated using Fast Fourier Transform (FFT). Core loss coefficients are given for both M36 steel and 10JNEX900 material which will be used as core materials in switched reluctance motors studied in this thesis. It has to be stated that the proposed calculation method is general and can be used in calculation of core losses for SRMs with different core materials. However, the corresponding core loss coefficients have to be entered into analytical computations.

Finally, an analytical method of core loss calculation based on Steinmetz equations, the calculated flux harmonics and given core loss coefficients is discussed. At the end, while having both copper and core losses of the machine in hand, total losses, output power and SRM efficiency can be computed. All analytically obtained results will be verified using measurements and finite element simulations in the following chapter.

CHAPTER 4

VERIFICATION OF ANALYTICAL MODEL

In previous chapters, it is shown that determination of static torque-position-current and flux linkage-current-position curves of a SRM is a crucial step in calculation of motor performance. Static torque characteristic is necessary in determination of motor steady state dynamic output torque. On the other hand, flux linkage characteristic is used to calculate phase current. Flux linkage graph is also needed in calculation of pole flux and core losses of the machine. Thus, accurate determination of static characteristics of the machine is an important task. In previous chapters it is claimed that these two curves (torque and flux linkage) can be predicted using a sets of normalized and dimensionless data. The main purpose of this chapter is to verify the accuracy of the performance calculation results that can be obtained using this data for predictions. Once the accuracy of the method is verified, it can be used for optimization purposes.

4.1 Test motors

In order to validate the accuracy of proposed analytical model, analytical performance calculations are carried out on two switched reluctance motors. The first motor is an 8/6 SRM existing in Electrical Machines laboratory of Electrical and Electronics Engineering department of Middle East Technical University (METU) which is designed to be used in washing machine applications known as SRM1. The specifications of the test motor are summarized in Table 4-1.

Table 4-1 Geometric specifications of SRM1

Rotor outer diameter	38.6 mm
Stator outer diameter	110.4 mm
Core length	40.4 mm
Stator back core width	5.2 mm
Shaft diameter	16.5 mm
Air gap length	0.325 mm
Rotor back core width	3.9 mm
Stator tooth Tapering angle	2.215 degree
Stator tooth width	8.35 mm
Rotor tooth width	8.4 mm
Stator pole depth	30.4 mm
Rotor pole depth	7.2 mm
Number of turns per pole	322 turns
Wire diameter	0.7 mm

Table 4-2 includes drive circuit specifications of the 8/6 SRM which is used for washing machine applications (SRM1).

Table 4-2 Drive circuit and chopper specifications of SRM1

Rated power	350W
Rated speed	12500 rpm
torque	0.25 N.m.
DC voltage	300 V
Rated current	3A
Number of phases	4

The second test motor is an 18/12, 50kW switched reluctance motor used in HEV applications known as SRM2. It has to be noticed that this motor is cooled using a water jacket which is attached around the stator core. Motor geometric specifications are summarized in Table 4-3.

Table 4-3 Geometric specifications of SRM2

Rotor outer diameter	179mm
Stator outer diameter	269mm
Core length	135mm
Axial length	155mm
Stator back core width	17.25mm
Shaft diameter	105.5mm
Air gap length	0.5mm
Rotor back core width	17.25mm
Stator tooth Tapering angle	2.215 degree
Stator tooth width	16.49mm
Rotor tooth width	17.2mm
Stator pole depth	27.25mm
Rotor pole depth	19.5mm
Number of turns per pole	17turns
Wire diameter	0.6mm
Number of strands	22

Table 4-4 reports drive circuit and chopper specifications of SRM2.

Table 4-4 Drive circuit and chopper specifications of SRM2

Rated power	50kW
Rated speed	1200-6000 rpm
torque	400 N.m. (maximum torque at 1200rpm)
DC voltage	500 V
peak current (per pole)	320A
Number of phases	3

At the first part of this section, verification of predicting static characteristics of the SRM using analytical method is done by comparing analytical results with measurements and finite element method solutions. Steady state current and torque waveforms of prototype motors are calculated using analytical method and compared to FEM results to prove the accuracy of analytical model. Finally, verification of the loss and efficiency calculations is done at the end of this section.

4.2 Verification of analytical method using SRM1

In this section, analytical calculations are carried out on a prototype 8/6 SRM existing in METU Electrical and Electronics Engineering department laboratory which is used in washing machine applications (SRM1). Then, accuracy of analytical model will be investigated by comparing the results with Finite Element Method (FEM) simulation results and measurements.

First part includes the static calculations of the motor. Static torque-position-current and flux linkage-current-position graphs are derived for the machine using normalized permeance and force data. In the second section, dynamic output torque and currents are calculated. Finally, the accuracy of loss and efficiency calculations is investigated.

4.2.1 Static torque and permeance-position calculations of SRM1

Accurate prediction of static characteristics of the SRM is a crucial point in calculation of motor performance. Flux linkage-current-position and static torque-position-current curves of the prototype motor are calculated using the proposed analytical model. The calculation procedure is explained in details in chapter 2.

4.2.1.1 Static torque-position-current of SRM1

Figure 4-1 reveals static torque-position-current graph derived using analytical calculations. In order to investigate the accuracy of analytical model, Finite Element Method (FEM) simulation and measurement results are also provided. Note that 3-D finite element simulations with magneto static solution type are carried out in order to obtain static data. Static torque data are obtained for three different excitation levels and various rotor positions between fully aligned (IN) and fully unaligned (OUT) conditions. It has to be noticed that the static torque is calculated once one phase of the SRM is excited.

If torque is produced by the contribution of two phases either because of current overlap between consecutive phases or when two phase on excitation mode is used, the resultant torque is calculated by summing up the force produced by the excited phases while calculating dynamic performance of the machine (see section 4.2.2).

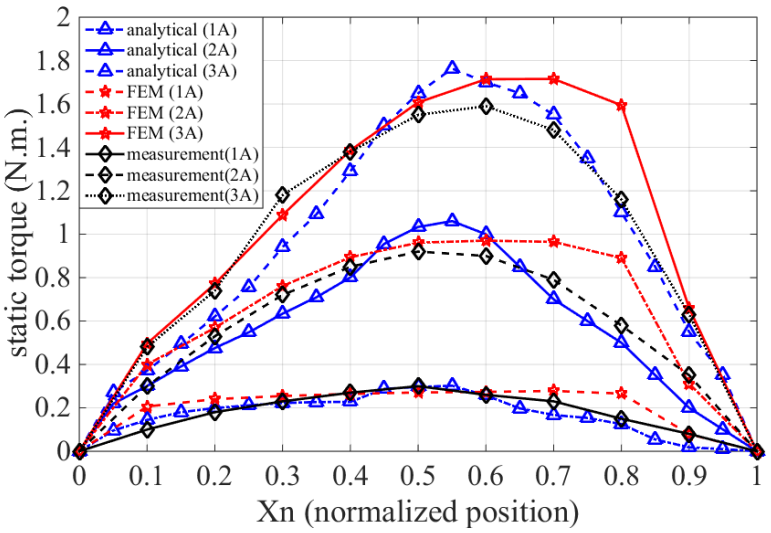

Figure 4-1 Static torque-position-current graph of SRM1

Analytical computations are based on sets of normalized data obtained using 2-D finite element simulations. The force produced by this test motor are solved using both 2D and 3D magnetic field solutions. The discrepancy between 2-D and 3-D Finite Element (FE) simulations are found to be negligibly small. From this finding, it can be concluded that end leakage effect can be neglected in calculation of dynamic torque in this study. It has to be mentioned that in the literature, dynamic torque is calculated using co-energy method, and consequently, an end fringing correction method is developed in order to compensate for the discrepancies between measurements and analytical results. However, in this study, normalized tangential force data is used in prediction of static and dynamic torque of the machine. Consequently, need for end fringing correction method is effectively eliminated.

To ease the comparison, static torque data obtained using analytical model, measurements and 3-D FEM simulations are summarized in Table 4-5 for different current values, and 4 different rotor positions between aligned and unaligned

conditions. It is obvious that torque values for fully aligned (x_n =0) and fully unaligned (x_n=1) rotor positions are zero.

Table 4-5 Static torque data of SRM1

		X_n=0.2	X_n=0.4	X_n=0.6	X_n=0.8
1A	Analytical	0.2	0.23	0.26	0.13
	Measurement	0.18	0.27	0.26	0.15
	FEM 3D	0.24	0.26	0.27	0.26
2A	Analytical	0.48	0.8	1	0.5
	Measurement	0.53	0.85	0.9	0.58
	FEM 3D	0.56	0.89	0.97	0.89
3A	Analytical	0.62	1.29	1.7	1.1
	Measurement	0.74	1.38	1.59	1.16
	FEM 3D	0.77	1.39	1.71	1.59

As it is obvious from both Figure 4-1 and Table 4-5, measurements and analytical calculations are in a relatively good agreement. However, a discrepancy is observed while comparing analytical results and measurements with finite element simulations at normalized position of 0.8. This difference could be due to saturation effects in tooth tips at rotor positions near to OUT position.

In modeling the SRM using finite element method, Maxwell software is utilized. The SRM motor is simulated using 3D magneto static solution type. Figure 4-2 reveals a cross sectional view of the prototype 8/6 SRM motor geometry in the finite element environment. The maximum error percentage is set to 1% in the simulations. In other words, when the difference between two consecutive iterations results is less than 1%, simulation stops. Maxwell itself adjusts mesh automatically for the system, and refines number of meshes and meshing structure in each iteration. Initial number of meshes is chosen to be 2427 by the software.

Separate simulations are done by changing the constant MMF applied to one phase of the machine and the rotor position to derive static torque-position-current characteristic of SRM which can be seen in Figure 4-1.

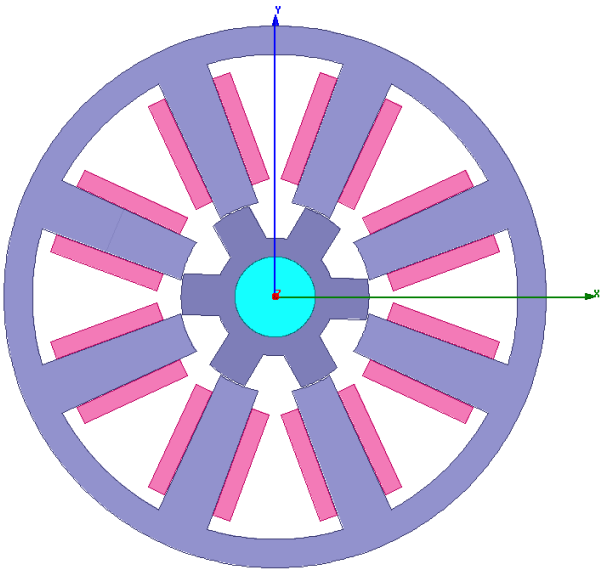

Figure 4-2 SRM1 geometry

4.2.1.2 Static flux linkage-current-position characteristics of SRM1

Flux linkage-current-position curve is also essential in determination of pole flux and hence the performance of the machine. Figure 4-3 reveals the graph calculated using the analytical model given in chapter 2.

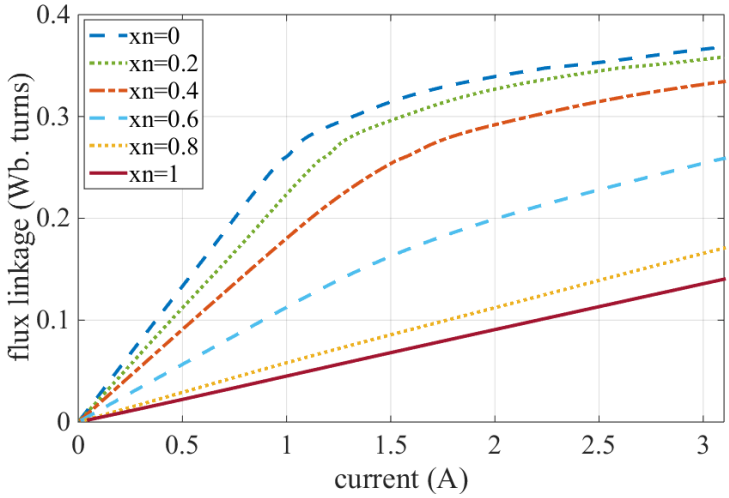

Figure 4-3 Flux linkage-current-position characteristic of SRM1

The same curves are also derived using ANSYS RMxprt software to investigate whether this analytical approach shows a good agreement with the analytical calculations presented here. Figure 4-4 depicts motor structure used to analyze the performance of the machine in RMxprt. Note that winding structure is not shown in the figure. Furthermore, it is not possible to model stator tooth tapering effect using this software, so the results may vary slightly with analytical calculations. However, the discrepancies between simulation results and analytical calculations are small enough to be neglected.

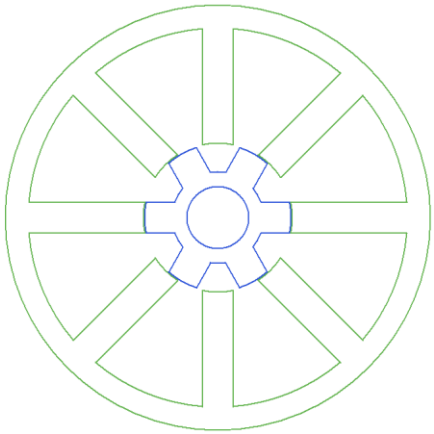

Figure 4-4 SRM1 structure in RMxprt software

By analyzing SRM motor using RMxprt, flux linkage-current-position graph is calculated which is represented in Figure 4-5.

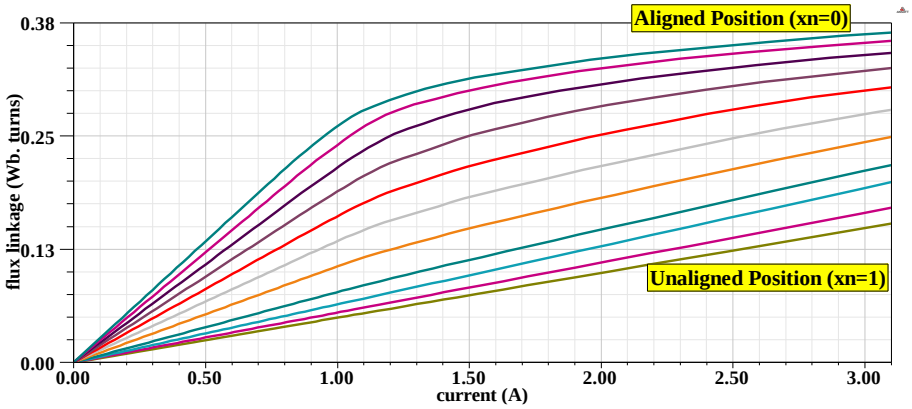

Figure 4-5 Flux linkage-current-position graph of SRM1

Obtained flux linkage-position-current characteristics are tabulated in Table 4-6. Measured flux linkage data are also provided for comparison purposes.

Table 4-6 Comparison of SRM1 flux linkage data (analytical, RMxprt and measurements)

Flux linkage (Wb. turns)		X_n =0	X_n =0.2	X_n =0.4	X_n =0.6	X_n =0.8	X_n =1
1A	Analytical	0.26	0.22	0.19	0.11	0.06	0.05
	RMxprt	0.26	0.21	0.17	0.11	0.07	0.05
	Measurement	0.29	0.26	0.2	0.15	0.1	0.08
2A	Analytical	0.34	0.33	0.29	0.18	0.11	0.09
	RMxprt	0.34	0.31	0.26	0.18	0.13	0.1
	Measurement	0.42	0.39	0.35	0.28	0.2	0.16
3A	Analytical	0.37	0.36	0.33	0.25	0.17	0.14
	RMxprt	0.35	0.34	0.3	0.25	0.19	0.15
	Measurement	0.46	0.44	0.41	0.35	0.28	0.25

As it can be concluded form Table 4-6, analytical findings and RMxprt results are in a relatively good agreement. However, a discrepancy is observed between analytically calculated flux linkage data and measurements. This difference can be due to a phenomenon which has not been taken into account in developing the analytical model. In an earlier study, flux fringing from the end of the core was thought to be the reason for this discrepancy. The other possibility is the flux leaking to adjacent poles from the excited pole. This issue is studied in the following sections. In order to investigate the reasons behind this error, first, finite element simulations are carried out which is discussed in the following sections.

4.2.1.3 Finite element verification of SRM1 flux linkage-current-position characteristics

In this section, flux linkage-current-position curves of SRM1 are obtained using FE simulations. Both 2-D and 3-D finite element environments are used to carry out the simulations. It is worth mentioning that in order to calculate the flux linkage,

corresponding flux is calculated in the middle height of the excited tooth. The calculated flux includes the flux crossing to adjacent poles to the excited pole. Moreover, pole flux can be determined by multiplying a far back core section (see Figure 4-6) flux by two. In this case, adjacent pole flux (slot leakage flux) in not taken into account. Flux linkage is calculated in this section using both of the mentioned methods. A comprehensive analytical discussion on slot leakage flux is also given in section 2.6. Note that in 2-D finite element simulations, flux is only calculated in the middle height of the excited pole which includes the slot leakage flux.

The rectangular area which is used for calculation of pole flux in stator back core region can be simply distinguished in Figure 4-6. It has to be mentioned that the rectangular area is selected in the middle of the corresponding back core section. Notice that, core ends fringing flux effect is taken into account in flux linkage calculation using this method from a 3-D FEM solution. Of course when a 2D solution is considered the flux fringing at the core end is not considered.

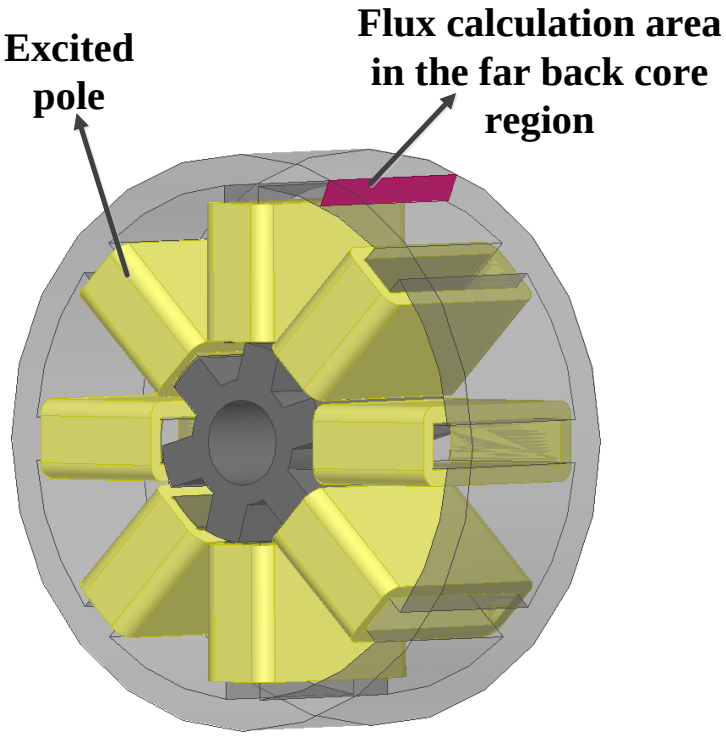

Figure 4-6 Rectangular area in stator back core in order to calculate pole flux (slot leakage is not included)

However, when pole flux is calculated using a rectangular area inside stator tooth (Area 1 in Figure 4-7), slot (between poles) leakage flux is also included in calculations. It has to be noticed that flux fringing from core ends is again taken into account in the calculations in 3-D case.

The results are shown up to 3A which is the rated current of the machine. The table includes flux linkage data calculated using 2-D and 3-D finite element methods. In order to ease the comparison, analytical results and measurements are also provided.

Table 4-7 Comparison of SRM1 flux linkage data

Flux linkage (Wb. turns)		X_n =0	X_n =0.2	X_n =0.4	X_n =0.6	X_n =0.8	X_n =1
1A	Analytical	0.26	0.22	0.19	0.11	0.06	0.05
	FEM 3D (adjacent pole flux not included)	0.24	0.21	0.17	0.12	0.07	0.05
	FEM 3D (adjacent pole flux included)	0.28	0.25	0.2	0.15	0.1	0.078
	FEM 2D (adjacent pole flux included)	0.28	0.24	0.19	0.14	0.08	0.06
	Measurement	0.29	0.26	0.2	0.15	0.1	0.08
2A	Analytical	0.34	0.33	0.29	0.18	0.11	0.09
	FEM 3D (adjacent pole flux not included)	0.35	0.33	0.29	0.23	0.15	0.1
	FEM 3D (adjacent pole flux included)	0.4	0.38	0.36	0.29	0.21	0.15
	FEM 2D (adjacent pole flux included)	0.37	0.35	0.32	0.24	0.17	0.13
	Measurement	0.42	0.39	0.35	0.28	0.2	0.16
3A	Analytical	0.37	0.36	0.33	0.25	0.17	0.14
	FEM 3D (adjacent pole flux not included)	0.39	0.36	0.32	0.25	0.19	0.15
	FEM 3D (adjacent pole flux included)	0.44	0.42	0.39	0.33	0.27	0.23
	FEM 2D (adjacent pole flux included)	0.4	0.39	0.37	0.31	0.24	0.2
	Measurement	0.46	0.44	0.41	0.35	0.28	0.25

It can be observed from the table that analytical calculations are in a good agreement with 3-D finite element simulations without including adjacent pole flux. On the other hand, measurements and 3-D finite element simulation results with

including adjacent pole flux are in a good agreement as well. However, a discrepancy is observed between 2-D and 3-D FE simulations while the adjacent pole flux is included under excitation currents of 2A and 3A. This can be due to core end fringing and end winding leakage effects which are not taken into account in 2-D finite element simulations. By comparing 3-D finite element simulations with and without including adjacent pole flux, it can be concluded that the difference between measurements and analytical results is due to slot leakage flux (adjacent pole flux). That's why measured flux linkage values (or flux linkage values obtained in a rectangular area in the excited pole) are higher in comparison with flux linkage data obtained using analytical method (or in rectangular area in a far stator back core region (Area 3, far from the excited pole as seen in Figure 4-7)). Hence, the analytical model has to be modified in a way that takes the effect of slot leakage flux into account. A comprehensive discussion on analytical calculations of the slot leakage is given in section 2.6.

4.2.1.4 Calculation of slot leakage (pole leakage) flux

In order to determine the accurate value of flux linkage of an excited winding, 3-D finite element simulations are carried out. Flux linkage of the excited pole is calculated by computing the flux passing through 5 different areas which can be distinguished in the following 3-D representation of the SRM (Figure 4-7). Flux linkage of the excited winding can be calculated either by multiplying the flux computed from area 3 and 2 by two or directly from area 1. Notice that the flux which is calculated from area 1 and 2 includes slot leakage flux. On the other hand, flux calculated form area 3 does not include the flux which completes its path through the adjacent pole.

Notice that area 4 (as well as areas 1 and 5) is in the middle of the corresponding pole. As mentioned earlier, the flux between the poles leaks from the side of the pole, however, as the distance between poles get larger towards the stator yoke, the significance of the flux leaking becomes smaller (see Figure 2-13). The study in section 4.2.1.5 indicates that for all practical purposes calculation of flux leakage in mid-pole position is sufficient for this test motor.

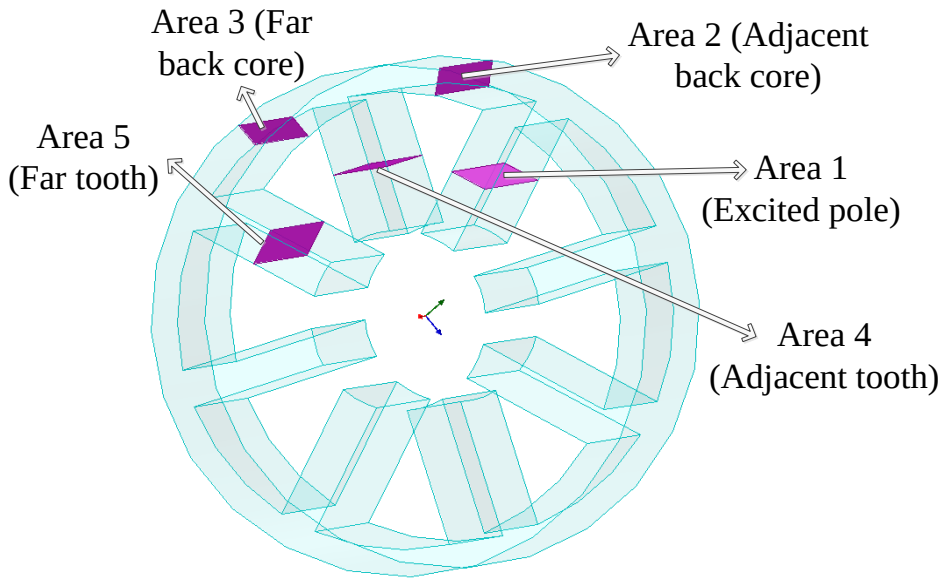

Figure 4-7 Rectangular areas in stator in order to calculate main and leakage flux linkage components

Table 4-8 Flux linkage values in 5 different rectangular areas in stator

Phase winding Flux linkage (Wb. turns)		X_n =0	X_n =0.2	X_n =0.4	X_n =0.6	X_n =0.8	X_n =1
1A	Area 1 (excited tooth)	0.29	0.26	0.21	0.15	0.1	0.08
	Area 2 (adjacent back core flux×2)	0.29	0.25	0.2	0.15	0.1	0.08
	Area 3 (far back core flux×2)	0.25	0.22	0.17	0.12	0.07	0.5
	Area 4 (adjacent tooth flux×2) Slot leakage	0.03	0.031	0.03	0.023	0.02	0.016
	Analytically calculatesd slot leakage	0.03	0.05	0.04	0.03	0.03	0.02
	Area 5 (far tooth flux×2)	0	0	0	0	0	0
2A	Area 1 (excited tooth)	0.4	0.38	0.36	0.29	0.21	0.15
	Area 2 (adjacent back core flux×2)	0.4	0.37	0.36	0.28	0.2	0.15
	Area 3 (far back core flux×2)	0.36	0.33	0.31	0.23	0.16	0.12
	Area 4 (adjacent tooth flux flux×2) Slot leakage	0.04	0.045	0.055	0.05	0.04	0.033
	Analytically calculatesd slot leakage	0.06	0.05	0.06	0.07	0.07	0.06
	Area 5 (far tooth flux×2)	0	0	0	0	0	0
3A	Area 1 (excited tooth)	0.44	0.42	0.39	0.33	0.27	0.23
	Area 2 (adjacent back core flux×2)	0.44	0.41	0.38	0.33	0.27	0.23
	Area 3 (far back core flux×2)	0.39	0.36	0.32	0.27	0.19	0.16
	Area 4 (adjacent tooth flux×2) Slot leakage	0.05	0.051	0.063	0.063	0.06	0.05
	Analytically calculatesd slot leakage	0.07	0.07	0.07	0.08	0.08	0.08
	Area 5 (far tooth flux×2)	0	0	0	0	0	0

The results indicate that some of the excited pole flux flows via adjacent unexcited poles. Other poles virtually have no flux component in them. It can be observed that the flux linkage calculated from Area 1 and 2 are almost identical as they both include the slot leakage flux. On the other hand, the flux linkage calculated from Area 3 is smaller as it excludes slot leakage. It can be further observed that when the flux flowing in adjacent tooth (which is slot leakage) is added, the result matches with flux linkage computed for Area 1. This finding confirms that inclusion of slot leakage is essential for accurate analytical calculation of excited winding flux linkage. It is proved in section 4.2.1.5 that this leakage flux component completes its path through two near teeth and air gap regions.

4.2.1.5 Distribution of slot leakage along the pole height

Another 3-D finite element simulation is carried out to prove that leakage flux linkage component completes its path through air region between excited pole and the near poles. In this simulation, leakage flux linkage component is calculated on 6 different surfaces located at different parts inside a near pole. These six different flux paths inside a pole near to an excited phase can be simply distinguished in Figure 4-8. It has to be mentioned that the pole height of SRM1 is 30.4 mm. The radial distance between each area and the tooth end near stator yoke is also shown in the figure.

Leakage flux linkage components are calculated for these six rectangular areas. Table 4-9 reports 3-D finite element simulation results.

As it is obvious from this table, leakage flux linkage increases when calculated from an area close to the stator yoke as expected, since all of slot leakage is taken into account.

So, an analytical method which is described in detail in chapter 2 is developed to take the effect of this leakage flux component into account. In order to prove that analytical calculations match the result obtained from FEM, analytically obtained data will be compared to FEM results in section 4.2.1.7.

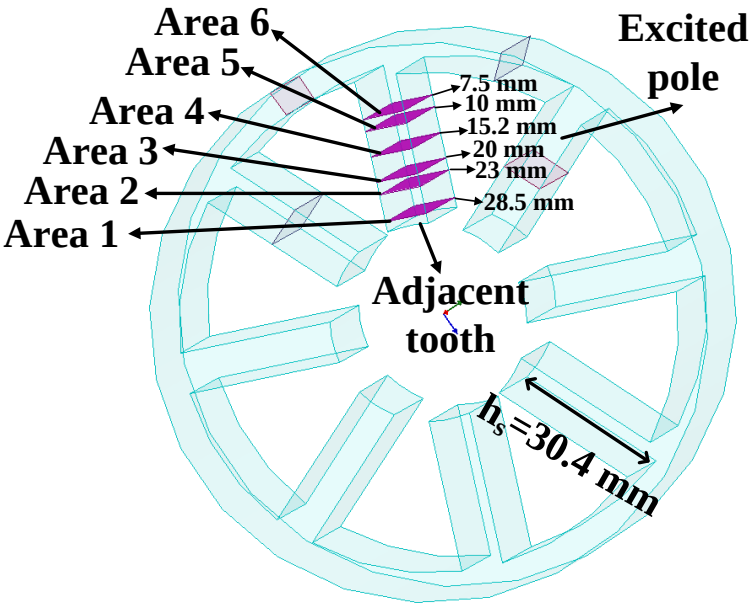

Figure 4-8 Six rectangular flux paths inside a pole near to an excited phase

Table 4-9 Leakage flux linkage components passing through six rectangular areas inside a pole near to an excited phase

Flux linkage (Wb. turns)		X_n =0	X_n =0.2	X_n =0.4	X_n =0.6	X_n =0.8	X_n =1
1A	Area 1	0.015	0.018	0.017	0.011	0.007	0.006
	Area 2	0.023	0.026	0.024	0.017	0.013	0.011
	Area 3	0.025	0.028	0.027	0.019	0.015	0.013
	Area 4	0.028	0.031	0.03	0.023	0.018	0.016
	Area 5	0.03	0.033	0.032	0.025	0.02	0.018
	Area 6	0.033	0.035	0.033	0.025	0.02	0.019
2A	Area 1	0.022	0.027	0.032	0.022	0.016	0.013
	Area 2	0.03	0.037	0.0.44	0.035	0.027	0.023
	Area 3	0.033	0.04	0.048	0.039	0.03	0.026
	Area 4	0.036	0.045	0.055	0.046	0.037	0.033
	Area 5	0.038	0.047	0.057	0.049	0.04	0.036
	Area 6	0.04	0.049	0.059	0.051	0.041	0.037
3A	Area 1	0.028	0.032	0.039	0.031	0.025	0.019
	Area 2	0.039	0.044	0.052	0.049	0.04	0.034
	Area 3	0.041	0.046	0.056	0.054	0.046	0.039
	Area 4	0.045	0.051	0.063	0.063	0.055	0.049
	Area 5	0.047	0.05	0.066	0.067	0.06	0.054
	Area 6	0.049	0.056	0.068	0.07	0.063	0.055

4.2.1.6 Effect of end winding leakage flux

It has to be noticed that normalized permeance, MMF and force data are obtained and tabulated using 2-D finite element simulations in this study. So, end winding leakage inductance component is not considered in calculations. However, it is proven that most of the leakage flux linkage component passes through two adjacent teeth of an excited pole, and as mentioned earlier its effect is effectively considered in analytical calculations. Furthermore, 3-D FEM simulations reveal that end winding leakage consists a negligible percent of total leakage flux linkage component and can be neglected in analytical model.

4.2.1.7 analytical model flux linkage calculations with slot leakage effect

It has to be noticed that because leakage flux linkage component has very little effect on the air gap flux distribution, it is possible to assume that torque calculation from method based on normalized torque data (see section 2.5.2) which is used in this study would lead to correct results. In fact, the static torque curve prediction for the two test motors confirms this assumption.

However, static flux linkage characteristic of the machine needs to be modified to take into account the effect of slot leakage flux. Table 4-10 presents analytically calculated flux linkage values including pole leakage flux, measurements and 3-D finite element simulation results (slot leakage included). Percentage of error between measurements and modified analytical results are also provided in the table.

It can be observed that analytical calculations of flux linkage curves match the measurements and FEM 3-D flux linkage calculations with a very good accuracy. So, the model is accurate enough to be used to predict motor steady state dynamic performance characteristics. The corresponding results are presented in section 4.2.2.

Table 4-10 Comparison of flux linkage data for SRM1 after consideration of slot leakage effect

Flux linkage (Wb. turns)		X_n =0	X_n =0.2	X_n =0.4	X_n =0.6	X_n =0.8	X_n =1
1A	Analytical	0.29	0.27	0.23	0.14	0.09	0.07
	Measurement	0.29	0.26	0.2	0.15	0.1	0.08
	Error (%)	0	3.8	15	6.6	10	12.5
	FEM 3D (slot leakage included)	0.28	0.25	0.2	0.15	0.1	0.078
2A	Analytical	0.4	0.38	0.35	0.25	0.18	0.15
	Measurement	0.42	0.39	0.35	0.28	0.2	0.16
	Error (%)	4.7	2.5	0	10.7	10	6.2
	FEM 3D (slot leakage included)	0.4	0.38	0.36	0.29	0.21	0.15
3A	Analytical	0.44	0.43	0.4	0.33	0.25	0.22
	Measurement	0.46	0.44	0.41	0.35	0.28	0.25
	Error (%)	4.3	2.2	2.4	5.7	10.7	12
	FEM 3D (slot leakage included)	0.44	0.42	0.39	0.33	0.27	0.23

4.2.2 Prediction of characteristics of SRM1 with speed and time

In order to investigate the accuracy of SRM1 at varying speeds, drive circuit characteristics, chopper circuit operating conditions and excitation pattern have to be known. In this section, current, torque and flux variation of SRM 1 are predicted using the analytical approach and FEM and are compared. In both analytical and FEM simulations, the drive circuit is considered to be ideal. In other words, switching losses, and voltage drops on semiconductor devices in chopper circuit are neglected. Drive circuit operating characteristics and excitation pattern are summarized in Table 4-11. DC side voltage is 300 V [64].

Table 4-11 SRM1 drive circuit operating characteristics and excitation pattern

Chopper I_{max}	3.15 A
Chopper I_{min}	2.85 A
Excitation period	0.5 p.u.
Phase turn on angle	- 45
speed	500 rpm

The excitation angle of 0.5 p.u. means that the excited phase will be on for 90 electrical degrees, which corresponds to one phase on mode. The reference point for the firing angle is taken as the crossover point of successive torque curves as shown in Figure 4-9.

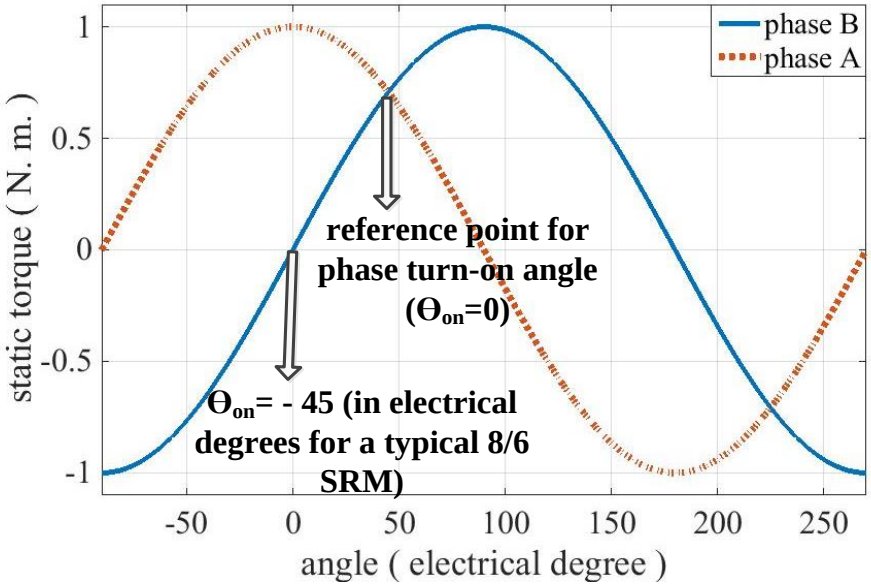

Figure 4-9 Schematic diagram of consecutive phase torques and the reference point for the turn on angle

Note that conduction period of 90 electrical degrees in an 8/6 SRM is the one phase on excitation mode. In which none of the phases are in conduction simultaneously except in current rising and falling sections.

Phase turn on angle reveals the angle in which one phase starts conducting the current by turning the corresponding phase switch on.

One phase current of SRM1 is calculated at 1000 rpm while the turn on angle and conduction periods are set to -66 electrical degrees and 0.5 p.u. respectively. Analytically calculated current waveform is depicted in Figure 4-10. Measured current waveform is also provided for comparison purposes.

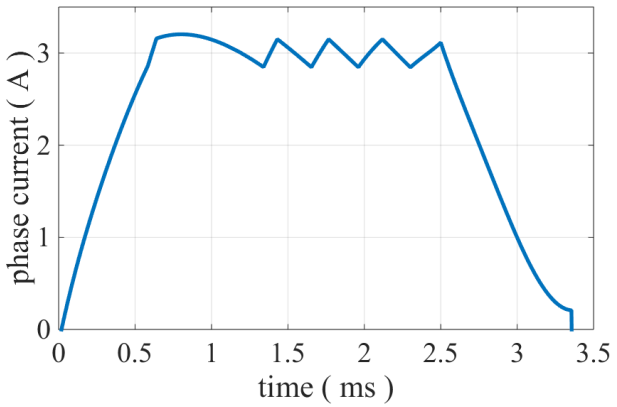

(A)

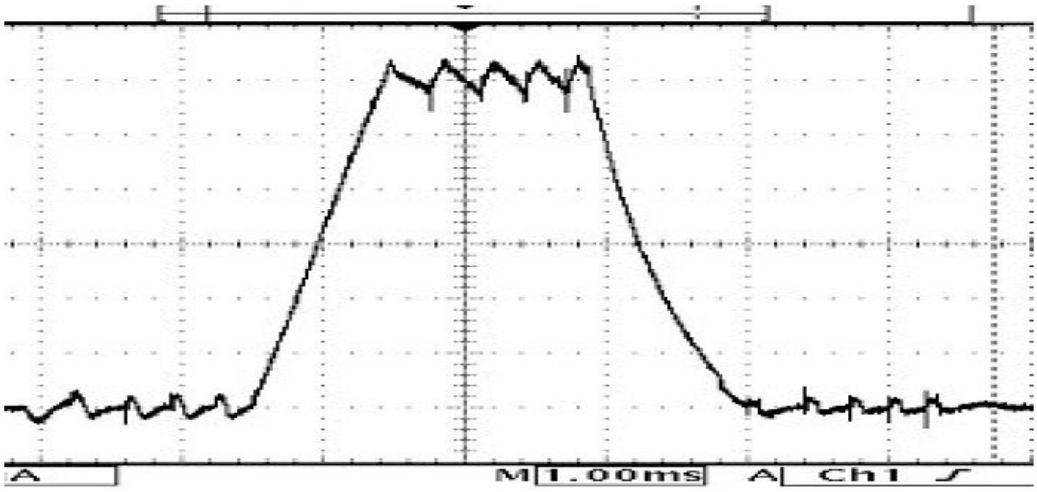

(B)

Figure 4-10 SRM1 one phase current waveform at θ_{on} = -66, conduction angle=0.5 p.u. and speed=1000 rpm obtained using A) analytical method B) measurements

As it can be understood form the figure, there are five chops in both analytically calculated current and the measured one, and the current waveforms are very similar.

One phase current waveform of the SRM is again calculated, but under different operating conditions. Rotational speed is 500 rpm. Phase turn on angle and conduction angle are set to -45 electrical degrees and 0.5 p.u. respectively. Analytically obtained current waveform is shown in Figure 4-11. 2-D FE simulation result is also provided in this figure.

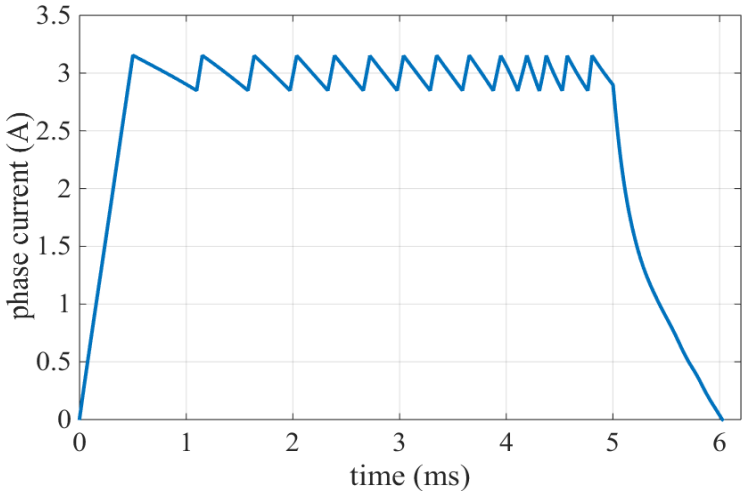

(A)

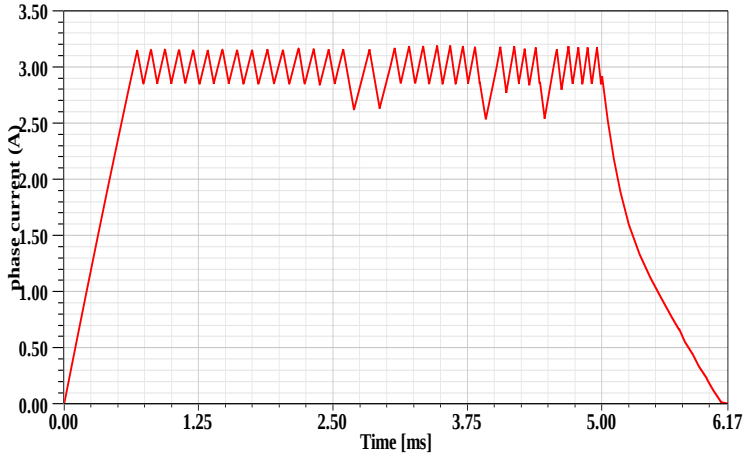

(B)

Figure 4-11 SRM1 one phase current waveform at θ_{on} =-45, conduction angle=0.5 p.u. and speed=500 rpm obtained using A) analytical method B) FEM

By comparing two figures it can be simply understood that the only discrepancy between them, is the chopping frequency in conduction period. In FEM simulations, chopping frequency is more than analytical calculations. This difference can be interpreted as the difference in current rising and falling time constants. The resistance of the circuit is same in both calculations methods, but the inductance of the phase winding can be different. It is worth mentioning that the same finite element simulations are also done in a 3-D finite element environment. Again, the phase current

has a higher chopping frequency in the conduction period same as the results obtained using 2-D FEM. The discrepancy in chopping frequency virtually has no effect on the average value of the phase current, and does not affect the dynamic calculations of the machine.

Consecutive phase currents can be plotted easily. Figure 4-12 reveals the phase currents of the sample 8/6 SRM while operating in a one phase on excitation mode obtained using analytical calculations and FEM simulations respectively.

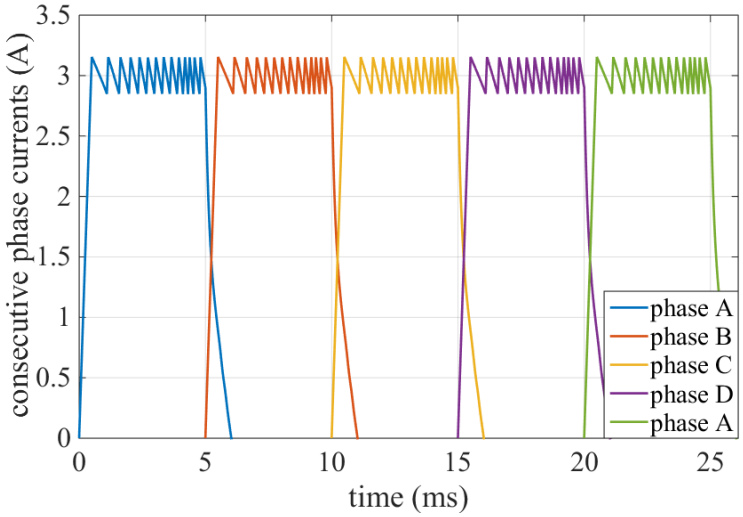

(A)

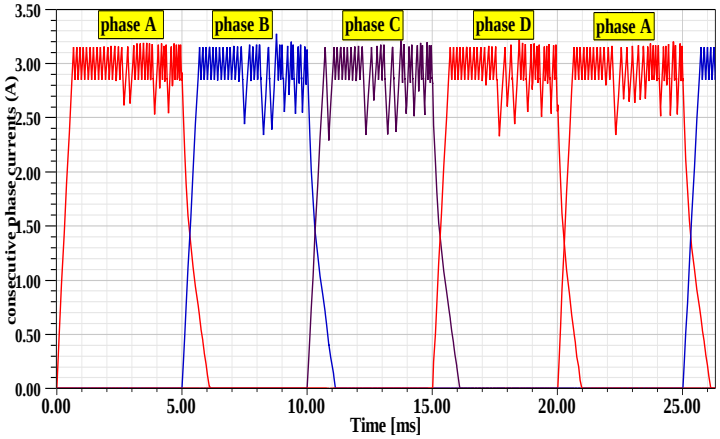

(B)

Figure 4-12 SRM1 consecutive phase currents waveforms at θ_{on} =-45, conduction angle=0.5 p.u. and speed=500 rpm obtained using A) analytical method and B) FEM

Variation of one phase flux linkage of the machine versus the phase current locus of the sample 8/6 SRM while operating in one phase on excitation mode is shown in Figure 4-13. This graph is obtained using analytical calculations. The regions corresponding to chopping actions and current rising and falling sections can be easily distinguished in the figure.

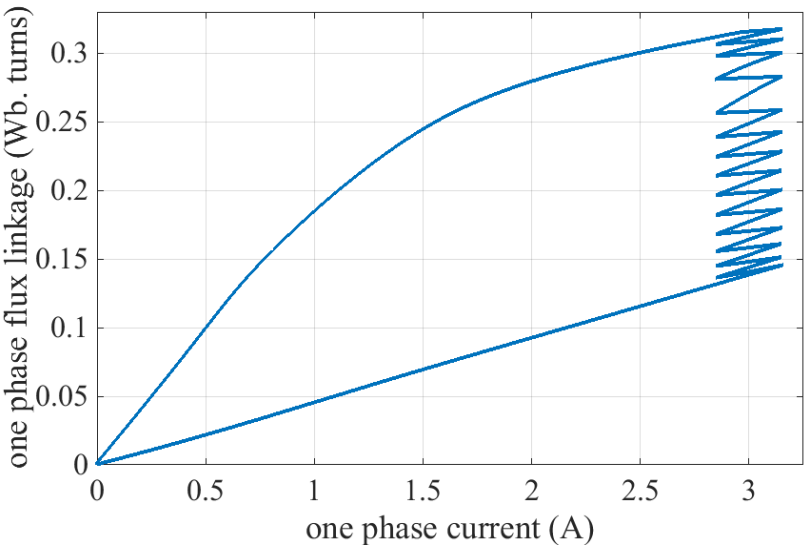

Figure 4-13 SRM1 Variation of phase flux linkage versus the phase current at θ_{on} =-45, conduction angle=0.5 p.u. and speed=500 rpm

In order to investigate the accuracy of analytical model, variation of flux linkage in one phase is plotted using both analytical and FEM simulations. Figure 4-14 represents the variation of phase flux linkage obtained using analytical method and finite element simulations. Utilized finite element based software is capable of calculating phase flux linkage of the SRM. The negligible discrepancies between two figures will verify the accuracy of flux and flux density calculations in analytical model.

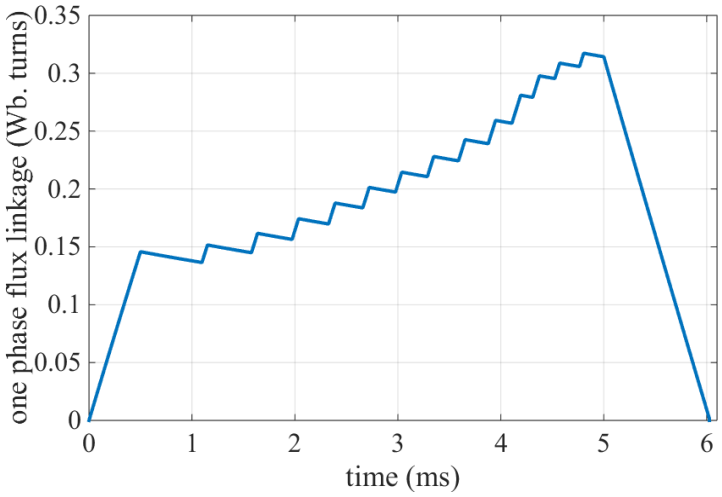

(A)

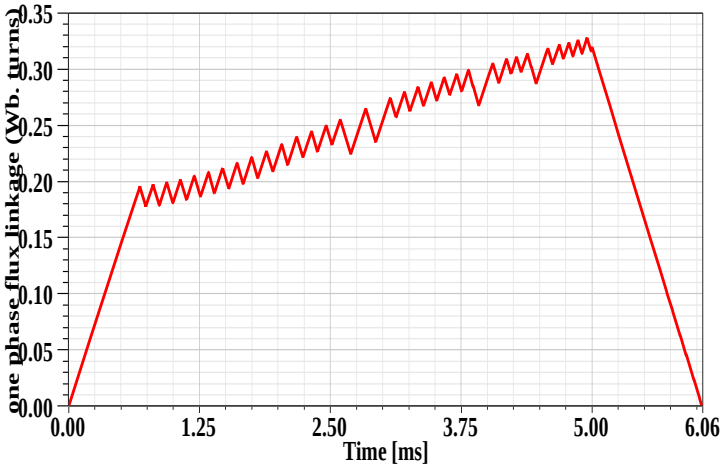

(B)

Figure 4-14 Variation of phase flux linkage of SRM1 obtained at θ_{on} =-45, conduction angle=0.5 p.u. and speed=500 rpm using A) analytical calculations and B) FEM

As it is obvious from both above figures, flux linkage calculations in both analytical and FEM simulations are in a relatively good agreement. Both graphs reach the maximum flux linkage of 0.32 Wb. turns at 5 ms. The same discrepancies regarding the chopping frequency can be easily distinguished by comparing two graphs. The reason was interpreted in previous section.

Once, the flux linkage calculation is precise enough, determination of flux and consequently flux density computations in different parts of the machine is simple. Fig 4. 17 displays analytically calculated tooth flux density for the operating conditions above.

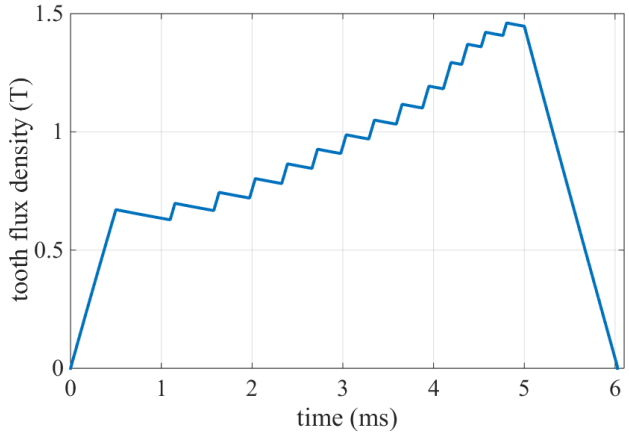

Figure 4-15 SRM1 variation of tooth flux density at θ_{on} =-45, conduction angle=0.5 p.u. and speed=500 rpm (analytical method)

Torque developed due to one phase excitation while the SR motor is running with the current shown in Figure 4-11 is represented in Figure 4-16. It has to be mentioned that the torque is calculated using normalized tangential force data in analytical calculations.

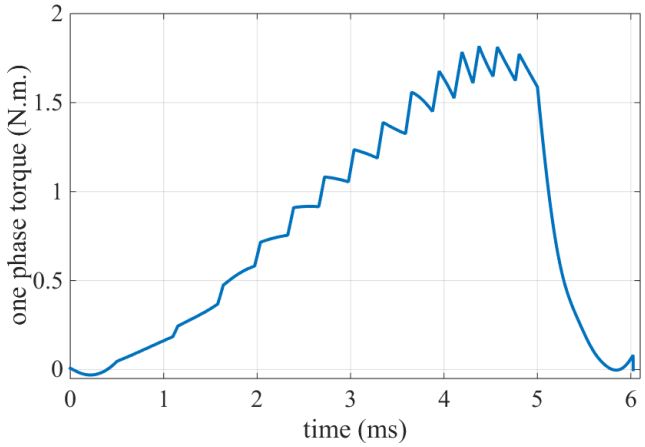

Figure 4-16 Torque developed due to one phase excitation of SRM1 at θ_{on} =-45, conduction angle=0.5 p.u. and speed=500 rpm (analytical method)

Due to natural symmetry in geometry of a SRM, torque which is developed due to excitation in other phases is the same. Thus, obtaining the total torque developed by the machine is an easy task. Based on superposition law, total torque developed by the machine is sum of the torque values each phase develops individually at any time. The overlap between excitation periods in which two or even three phases are in conduction at the same time is simply taken into account using this superposition principle. In one phase on excitation mode of the sample 8/6 SRM (SRM1), torques corresponding to consecutive phases are represented in Figure 4-17. It has to be noticed that in one phase on excitation mode, none of the phases are in conduction at the same time except for current rising and falling sections. Hence, in this mode the phase switch is turned on at the moment in which the previous phase is turned off.

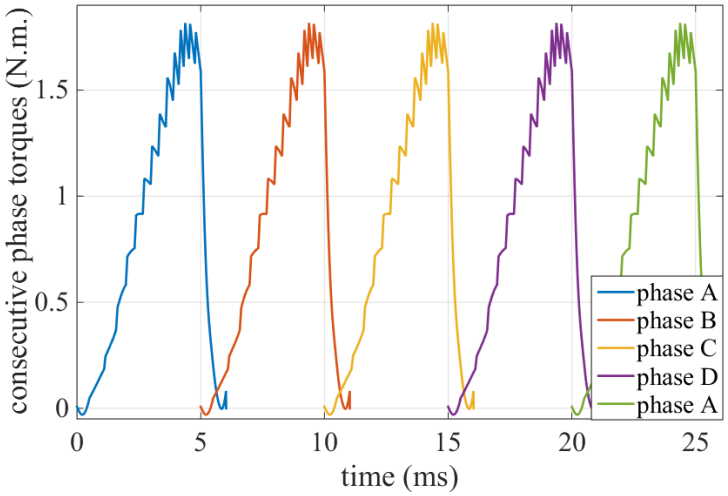

Figure 4-17 Consecutive phase torques of SRM1 at θ_{on} =-45, conduction angle=0.5 p.u. and speed=500 rpm

Calculation of the current drawn from the DC bus is important. The current waveform is calculated using analytical calculations and is shown in Figure 4-18. Note that this waveform is obtained by summing up current waveforms in all consecutive phases at any specified time. The significant point is that in current falling sections in which current flows thorough the DC source in a reverse direction, the polarity of the

current has to be negative. These regions in the waveform can be distinguished easily in which the current has negative values. The advantage of such a drive system is transferring power back to the DC source which improves motor efficiency.

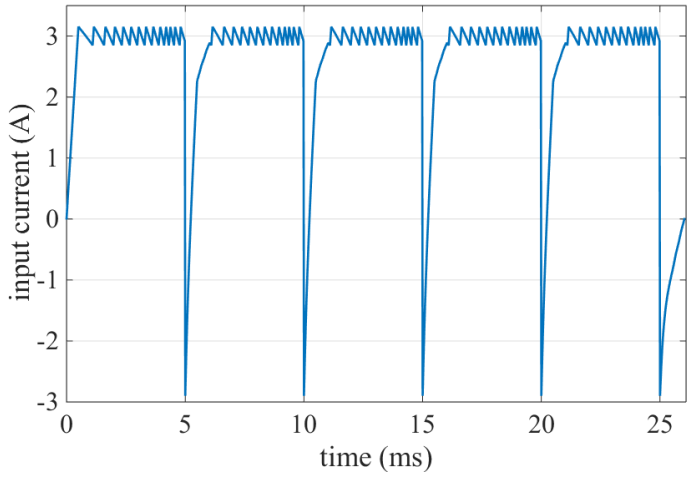

Figure 4-18 Total branch current of SRM1 at θ_{on} =-45, conduction angle=0.5 p.u. and speed=500 rpm

In a same manner, total developed torque can be obtained by summing up torque waveforms corresponding to each phase at any specified time. Total output torque of the prototype SRM operating at one phase on excitation mode which is obtained using both analytical calculations and FEM is shown in Figure 4-19.

By comparing analytical results with FEM the validity of analytical calculations can be easily proved. It has to be mentioned that in a personal computer with 3.4 GHz Core i7 CPU and 8 GB RAM it takes an approximate 10 minutes to complete a 25 ms performance calculation in a finite element environment with steps of 0.1 ms. Again the only difference between two figures is high number of chopping actions in FEM simulation results which was discussed earlier in comparing current waveforms. By comparing analytical results and FEM simulation results for flux, current and torque waveforms, it can be simply inferred that the proposed analytical model has sufficient degrees of accuracy to be used for optimization purposes.

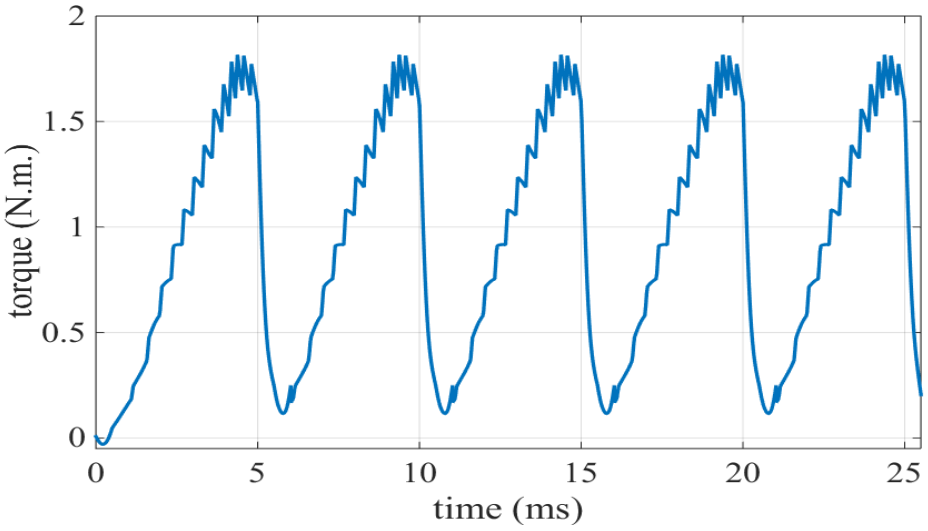

(A)

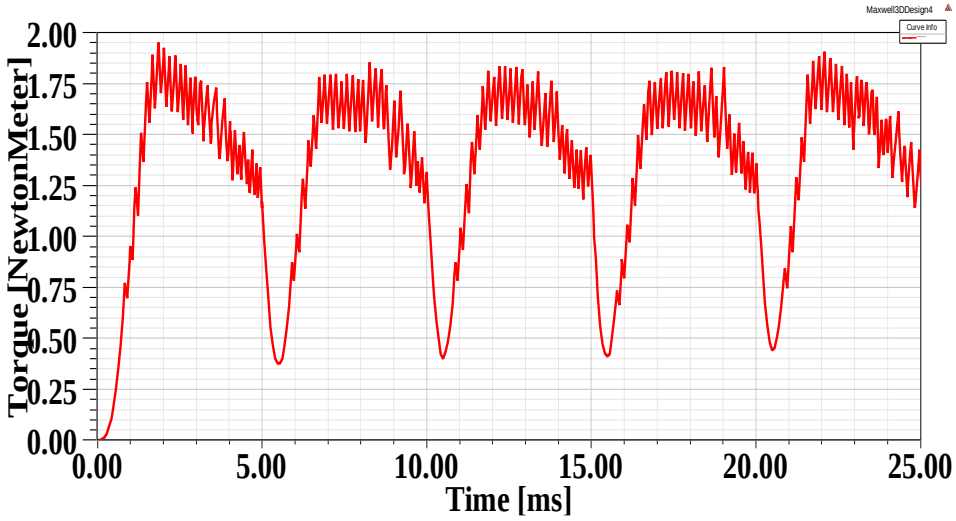

(B)

Figure 4-19 SRM1 developed torque obtained at θ_{on} =-45, conduction angle=0.5 p.u. and speed=500 rpm using A) analytical method and B) FEM

4.2.3 Torque-speed characteristic of SRM1

In this section, torque-speed characteristic of SRM1 is determined using analytical calculations and compared with measurements. Input DC voltage is 300 V and chopper average current is 3A. Computed and measured torque-speed characteristic of SRM1 (turn on angle= - 45 electrical degree) under one phase on excitation mode are presented in Figure 4-20. the same characteristic is also computed using 3-D finite element method which is given in the same figure

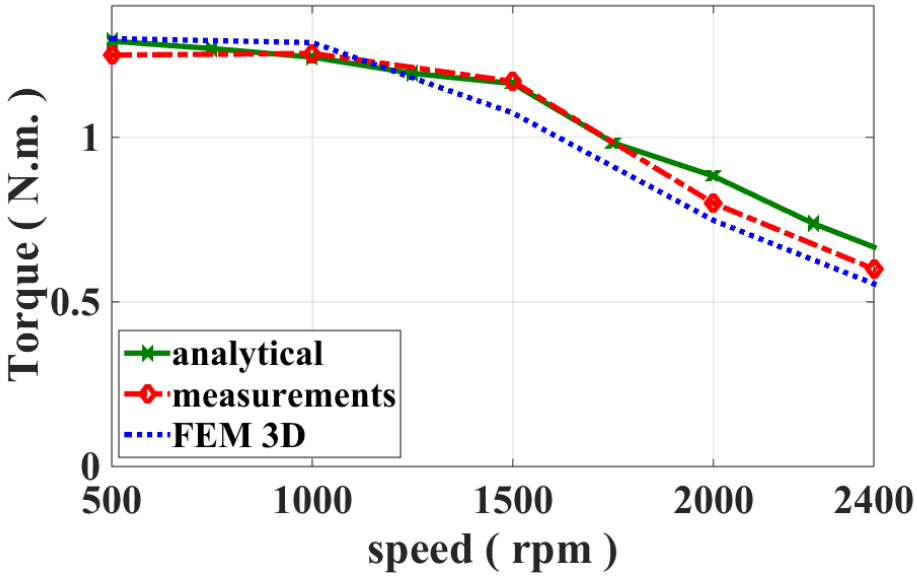

Figure 4-20 Torque-speed characteristic of SRM1 (turn on angle= - 45 electrical degree) under one phase on excitation mode

As it is obvious form the figure, the accuracy of the analytical calculation method is very good.

Torque speed characteristic of the SRM is again calculated for chopper average current of 3A and phase turn on angle of - 24 electrical degree. Excitation period is the same as the previous characteristic (90 electrical degrees). Measurement results are also provided to verify the accuracy of analytical model.

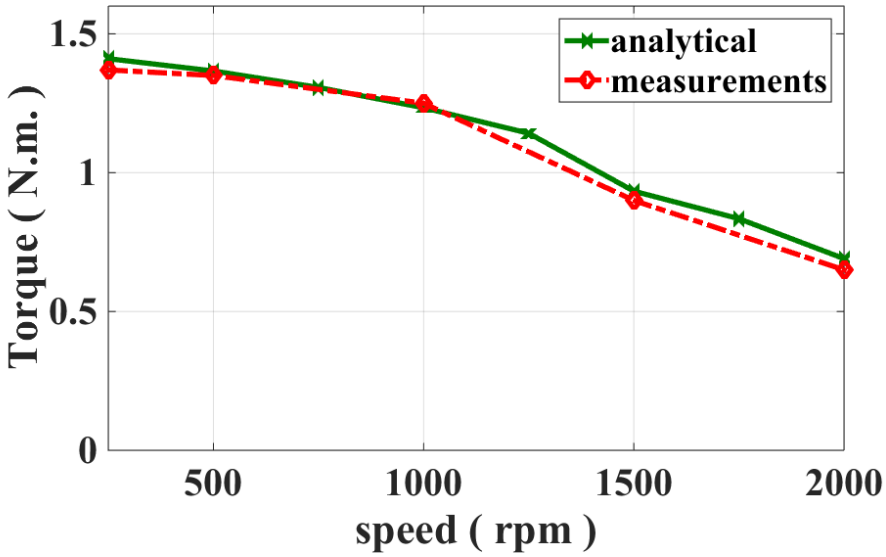

Figure 4-21 Torque-speed characteristic of SRM1 (turn on angle= -24 electrical degree) under one phase on excitation mode

As it is obvious form Figure 4-21 measurements and analytical results are in a very good agreement, which proves the accuracy of proposed model.

4.2.4 Verification of loss and efficiency calculations

The proposed analytical model has to be capable of predicting not only motor performance (phase currents and developed torque), but also core and copper losses of the machine and finally motor efficiency with the highest possible accuracy. Analytical calculations are carried out on the sample 8/6 SRM to compute losses, input and output powers, torque ripple and efficiency of the machine. This motor is simulated using finite element method as well. DC side voltage is 300 V. Results of analytical calculations, FEM simulations and measurements are provided in Table 4-12.

Table 4-12 SRM1 Performance calculation results (θ_{on} = - 45, conduction angle=0.5 p.u.)

	Speed (rpm)	Average torque (N.m.)	RMS current (A)	Output power(W)	Copper loss (W)	Core loss (W)	Total loss (W)	Input power (W)	Torque ripple(%)	Efficiency (%)
Analytical	500	1.19	1.45	62.4	43.69	29	72.69	135.1	93.4	46.1
FEM simulations	500	1.23	1.49	64.37	46.5	31	77.5	141.8	88	45.4
Measuremens	500	1.25	-	65.45	-	-	-	-	-	-

Comparing the results summarized in Table 4-12, reveals that analytical calculations, measurements and FEM simulations are in a very good agreement. It has to be mentioned that drive circuit switches in finite element simulations and analytical calculations are assumed to be ideal.

Performance of the SRM is calculated in another operating point. Motor speed is 1000 rpm. Phase turn on angle and conduction period are set to -66 electrical degree and 0.5 p.u. respectively. The results are reported in Table 4-13.

Table 4-13 SRM1 Performance calculation results (θ_{on} = - 66, conduction angle=0.5 p.u.)

	Speed (rpm)	Average torque (N.m.)	RMS current (A)	Output power(W)	Copper loss (W)	Core loss (W)	Total loss (W)	Input power (W)	Efficiency (%)
Analytical	1000	0.93	1.45	97.4	43.7	34.5	78.2	175.6	55.47
Measuremens	1000	0.84	1.36	88	38.5	-	-	-	-

Comparing analytically calculated results with measurements reveals that there is a good agreement between results. Error between average torque values is approximately 10% which is acceptable.

By comparing analytical model calculation results with FEM simulations and results obtained from RMxprt software the accuracy of analytical model is verified in this section. Thus, the model can be used for design and optimization purposes.

4.3 Verification of analytical method using SRM2

The same verification method is carried out for another 50kW, 18/12 switched reluctance motor which is used for hybrid electric vehicle applications (SRM2). 1/6 symmetry of the machine is depicted in Figure 4-22.

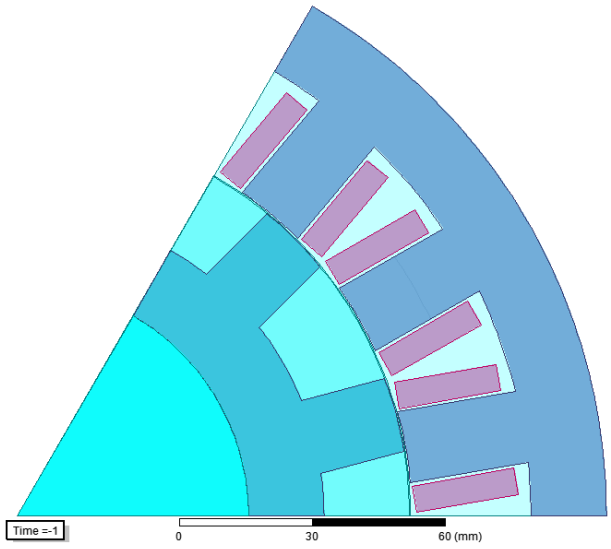

Figure 4-22 SRM2 motor geometry (1/6 symmetry)

Static and dynamic characteristics of the machine are calculated using proposed analytical model and 2D finite element simulations. Obtained results will be compared to measurement results provided by Akira Chiba [4, 22] in order to verify the accuracy of the method. A 3-D representation of SRM2 with above mentioned dimensions is depicted in Figure 4-23.

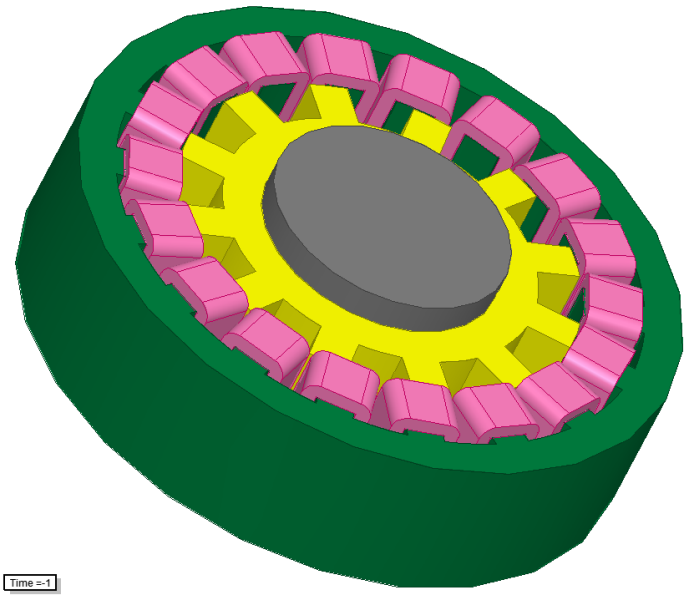

Figure 4-23 3-D representation of SRM2

Core material is 10JNEX900 with 0.1mm lamination thickness. B-H curve of the utilized material is given in Figure 4-24.

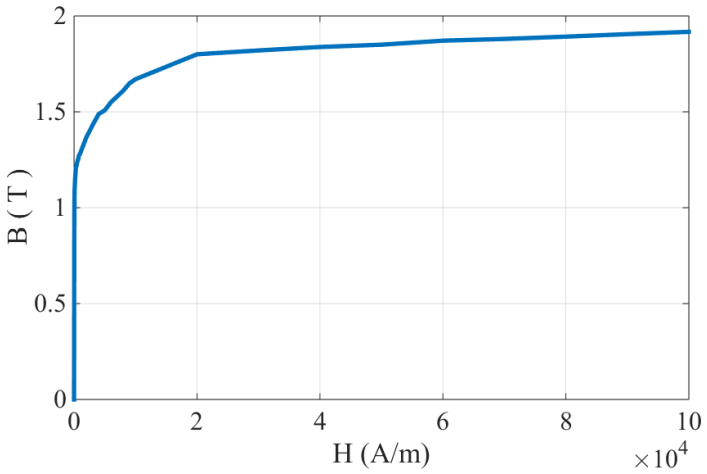

Figure 4-24 B-H curve of 10JNEX900

Core loss characteristic of 10JNEX900 material is given in APPENDIX A. Chopper circuit is considered to operate between 300 and 320A. These values are operating currents per pole of the machine. Chopper circuit characteristics and

excitation pattern of the machine is depicted in Table 4-14. It has to be added that DC side voltage is 500 V.

When the references [22] and [4] are investigated, it is found that the following characteristics of the SR2 motor are available. In this chapter, these characteristics will be predicted to find out the degree of accuracy that may be expected from the analytical calculation method.

Table 4-14 SRM2 excitation pattern

I_{max}	320 A
I_{min}	300 A
Excitation period	0.83 p.u. (150 electrical degree)
Phase turn on angle	- 4 (electrical degree)
speed	1200 rpm

It has to mentioned that a three phase 18/12 SRM will operate in one phase on excitation mode, if the conduction period of each phase is 120 electrical degrees. Setting excitation period to 150 electrical degrees leads to overlaps between consecutive phase conduction periods. In other words, two phases of the SRM will be in conduction at the same time.

4.3.1 Static calculations of SRM2

At the first stage, static characteristics of the SRM are predicted using analytical calculations. Accurate determination of static flux linkage and torque characteristics of a switched reluctance motor is a vital step towards accurate calculation of its steady state dynamic performance characteristics.

4.3.1.1 Static torque-position-current characteristic

Static torque curve of SRM2 is calculated using both analytical calculations and FEM simulations which is shown in Figure 4-25.

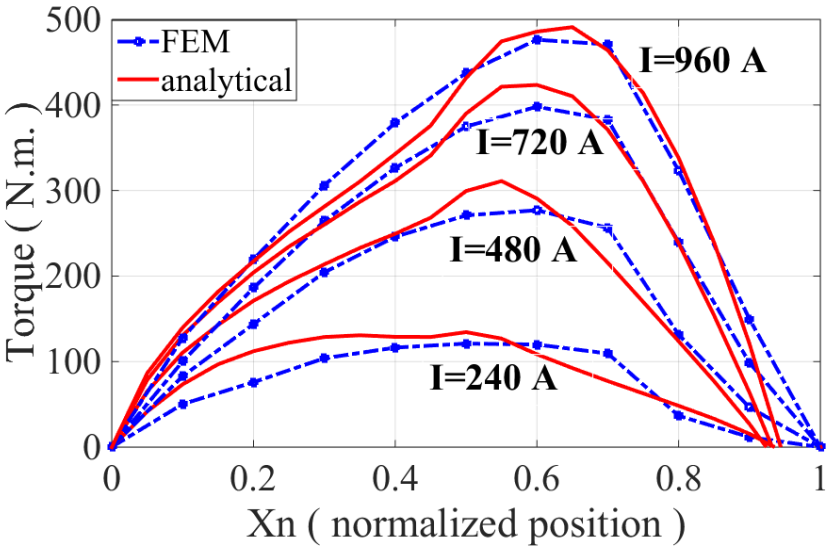

Figure 4-25 Torque–position-current graph of SRM2

By comparing analytical calculations and finite element simulation results it can be concluded that analytical results and FEM simulation results are in a good agreement.

4.3.1.2 Static flux linkage-current-position characteristic

In verification of results for SRM1, it is proved that taking slot leakage effect in analytical calculation of SRM flux linkage curves is essential. Leakage flux linkage is calculated for SRM2 at normalized rotor position of x_n=0.5 (as a point between IN and OUT positions). Figure 4-26 represents variation of leakage flux linkage versus phase current for this specific rotor position. It has to be mentioned that the calculated leakage flux linkage is leakage flux of 4 adjacent poles multiplied by number of turns per pole of the SRM, because in calculation of flux linkage in switched reluctance motors two opposite poles which are connected in series are considered.

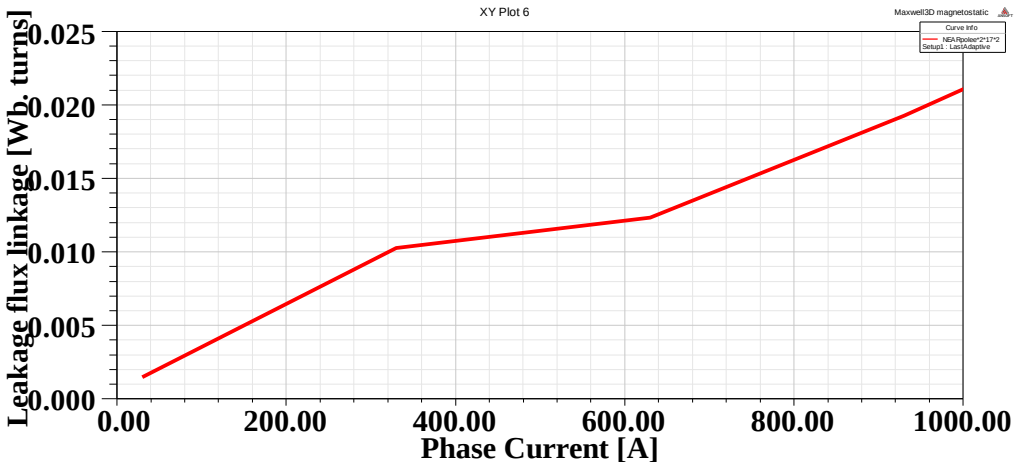

Figure 4-26 Leakage flux linkage of SRM2 for normalized rotor position of x_n=0.5

In this section, in order to have an insight towards the magnitude of leakage flux, total flux linkage (slot leakage included) of two opposite poles of SRM2 which are connected in series and leakage flux linkage component are plotted in the same graph for normalized rotor position of x_n=0.5. The results are shown in Figure 4-27.

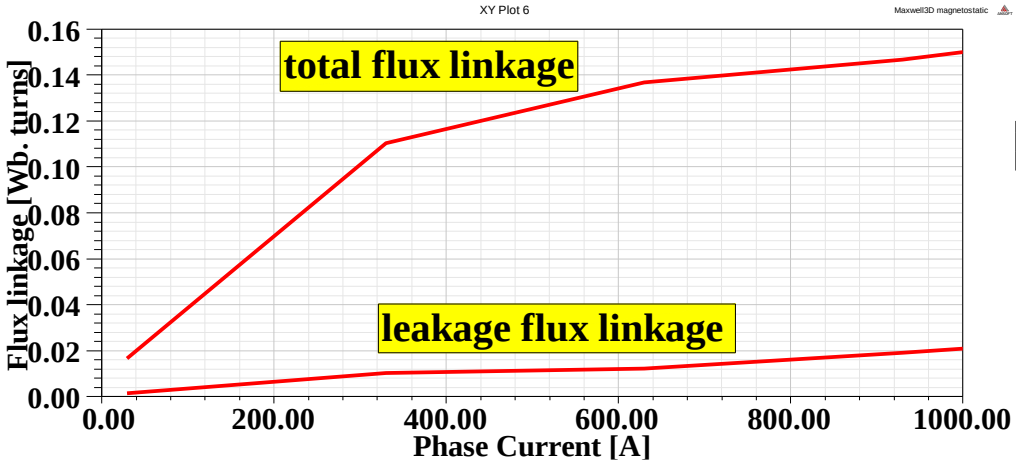

Figure 4-27 Total flux linkage and leakage flux component of SRM2 for normalized rotor position of x_n=0.5

As it is obvious from Figure 4-27, leakage flux is approximately 10% of the total flux linkage of SRM2. This leakage component does not have any effects in static torque-position-current characteristic of the machine. However, in determination of

torque speed characteristic of the SRM especially at higher rotational speeds where the current cannot reach to maximum specified chopping current, exact prediction of leakage flux component is necessary. In other words, it is important in determination of rise time and fall time of the circuit in dynamic calculations at higher rotational speeds. Therefore, accurate calculation of this leakage flux component is needed.

Leakage flux linkage of SRM2 is calculated using 3-D FEM for different excitation levels and various normalized rotor positions between IN (x_n=0) and OUT (x_n=1) positions. Results are summarized in Table 4-15.

Table 4-15 Calculation of leakage flux linkage for SRM2 for various excitation levels and rotor positions

	X_n =0	X_n =0.2	X_n =0.4	X_n =0.6	X_n =0.8	X_n =1
300A	0.0136	0.0125	0.0108	0.0086	0.0067	0.0072
450A	0.0175	0.014	0.0127	0.0106	0.0104	0.0109
600A	0.0195	0.0191	0.0147	0.0126	0.014	0.134
750A	0.0222	0.0212	0.0191	0.0136	0.0169	0.0185
900A	0.0241	0.024	0.0225	0.0146	0.0194	0.0214
1050A	0.0248	0.0255	0.0241	0.0187	0.0222	0.0239

Flux linkage-current-position characteristic of SRM2 is also calculated using analytical model with consideration of slot leakage effect. Finite Element simulations results and measurements at two normalized positions of x_n=0 (IN) and x_n=0.8 are also provided to investigate the accuracy of proposed analytical model. The results are revealed in Figure 4-28. Note that analytical and FEM results are for normalized positions of 0, 0.2, 0.4, 0.6, 0.8 and 1.

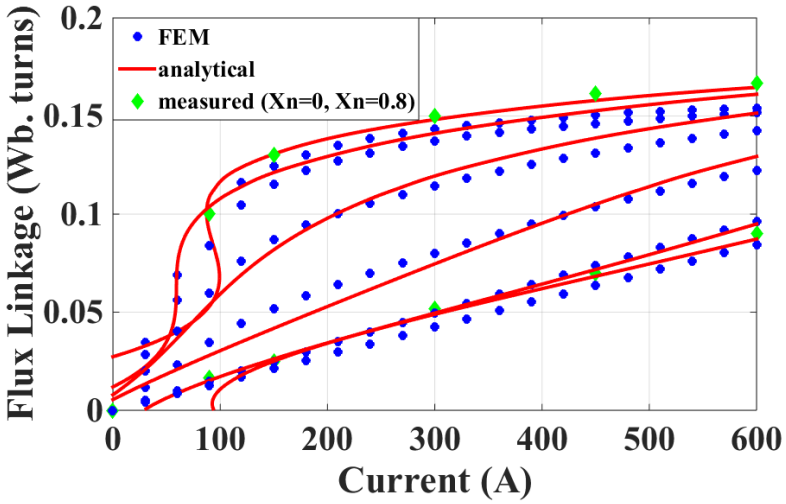

Figure 4-28 Flux linkage–current–position graph of SRM2

As it is obvious from the figure, there is a significant agreement between FEM results and analytical calculations especially in positions closer to OUT position (x_n=1). On the other hand, the observed slight discrepancy at IN position (x_n=1) is because of a high amount of flux and heavy saturation. However, comparison of analytical dynamic calculations and FEM simulation results will show that this slight discrepancy does not affect the final performance results and is acceptable. It can be figured out that measurements and analytical results are in a good agreement as well.

In next step, dynamic performance characteristics of the SRM2 will be calculated and model accuracy will be verified by comparing the results with Finite Element simulations and measurements.

4.3.2 Dynamic calculations of SRM2

Note that operating speed range of this machine is between 1200 to 6000 rpm to be used in HEV applications and the motor has to be capable of developing output power of 50 kW at this specified speed range. However, in this section, motor performance is calculated at constant speed of 1200 rpm and the results will be compared to FEM and measurements.

The switched reluctance motor is simulated using 2-D finite element method with a transient solution type. Total number of meshes is selected to be 1266 by software automatic meshing. Furthermore, accuracy of the solution is set to be 0.0001.

Torque waveform of the switched reluctance motor obtained using Finite Element simulations can be seen in Figure 4-29.

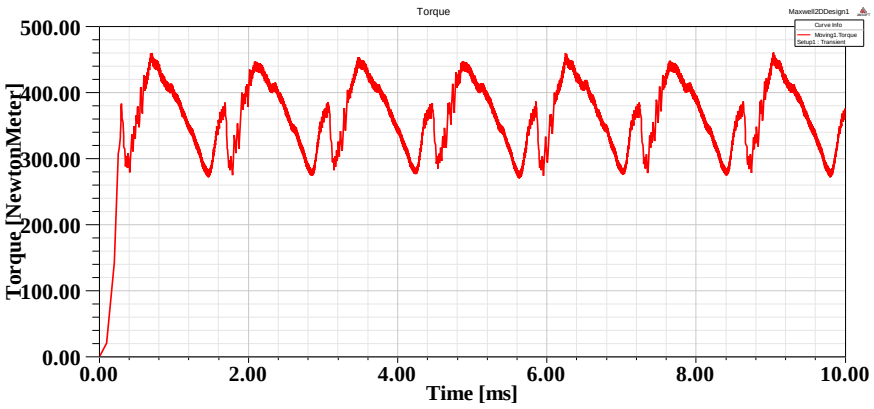

Figure 4-29 Developed torque of SRM2 with 10JNEX900 steel material

Analytical calculation results for the SRM are provided in Table 4-16. Furthermore, in order to ease the comparison and investigate the accuracy of the model, FEM simulations and measurement results are also included in the table. It has to be mentioned that in analytical calculation of this SRM and the computations which are done for optimization purposes in chapter 6, although the material is M36 steel (This material is used to obtain normalized permeance and force data), 10JNEX900 core loss data are entered. Therefore, core loss value which is calculated is for a SRM with 10JNEX900 core. Core loss curves of 10JNEX900 are given in Appendix A. It has to be mentioned that in calculation of core losses using a finite element based software, flux harmonics are also taken into account. In other words, the software calculates core losses by consideration of different flux harmonics. In the proposed analytical model in this study, core loss is also calculated by taking different flux harmonics into account. Flux harmonics are determined using Fourier transform. A detailed description of core loss calculations based on flux waveform and its harmonics is given in chapter 3.

Table 4-16 Analytical calculation results of SRM2

	Speed (rpm)	Average torque (N.m.)	Output power (kW)	RMS Current (A)	Copper loss (kW)	Core loss (W)	Total loss (kW)	Input power (kW)	Efficiency (%)
Analytical calculations	1200	406.6	51.1	190	12.23	348	12.5	63.67	80.25
FEM simulations	1200	364	45.74	191.3	12.42	418.3	12.84	58.58	78.1
Measurement results	1200	366	45.99	206	----	----	----	----	----

As it is obvious form the table, measured values are in a relatively good agreement with analytical and FEM simulation results. The only difference is in developed torque value which is higher in analytical calculations. This can be interpreted by noticing that the B-H curve of the basic geometry which is used to produce normalized force and permeance data sets is different than the SRM material. Knee point and consequently saturation flux density of 10JNEX900 which is used in SRM structure is lower than the M36 steel which is used to obtain normalized permeance and flux linkage data sets. B-H curves of both M36 steel and 10JNEX900 materials are depicted in Figure 4-30.

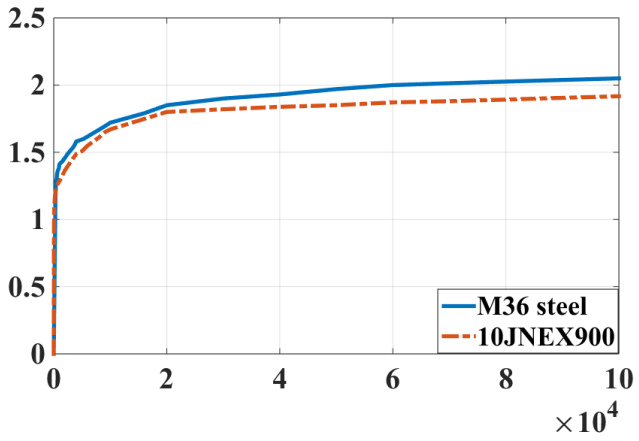

Figure 4-30 B-H curves of M36 steel and 10JNEX900

In order to prove this claim and correlate that the difference in developed torque is due to difference in magnetic material, the SRM is simulated using FEM while the core material is selected the same as basic geometry material (M36 steel). Developed torque waveform of the simulated machine is shown in Figure 4-31.

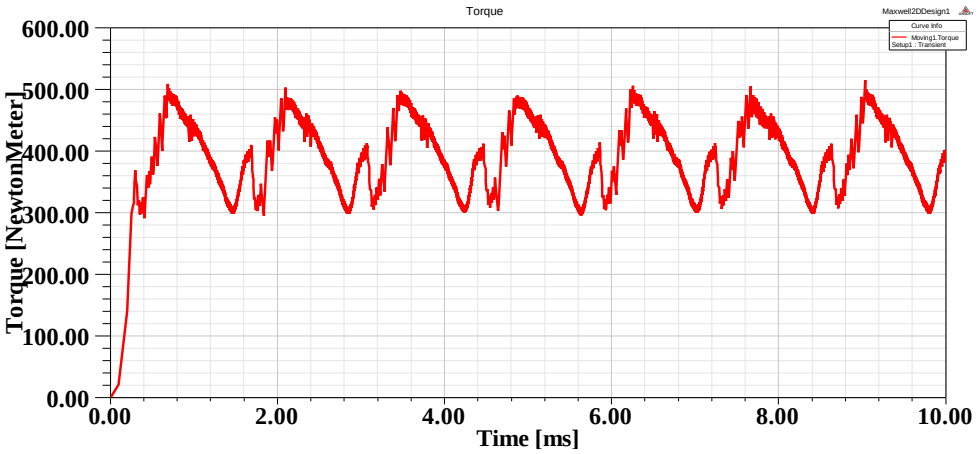

Figure 4-31 Developed torque of SRM2 with M36 material

Table 4-17 summarizes performance calculations of the SRM. Note that analytical simulations data are also provided to investigate the accuracy of the proposed model.

Table 4-17 SRM2 performance calculation results

	Speed (rpm)	Average torque (N.m.)	Output power (kW)	RMS Current (A)	Copper loss (kW)	Core loss (W)	Total loss (kW)	Input power (kW)	Efficiency (%)
Analytical calculations	1200	406.6	51.1	190	12.23	348	12.5	63.67	80.25
FEM simulations	1200	394.6	49.6	190.7	12.34	435	12.77	62.37	79.5

As it can be concluded from the table, analytical and FEM simulations results are in a very good agreement and the accuracy of the proposed analytical model is proven.

An important point which has to be taken into account is high flux density and high current densities of the machine. Maximum RMS current density of the SRM is 33 A/mm^2 which is very high. Furthermore, the core operates in its highly saturated area. Reduction of losses and increasing motor efficiency while motor is capable of developing 50kw power at the speed range of 1200-6000 rpm will be discussed in the optimization section. Optimum geometry, pole combination and excitation pattern will be selected in a way that maximum torque is achieved. Detailed description of optimization procedure will be given in chapters 5 and 6.

4.3.3 Comparison of losses and efficiency at 3000 rpm

In order to investigate the accuracy of loss and efficiency calculations, copper loss, core loss and efficiency of SRM2 are calculated analytically at rotational speed of 3000 rpm. Turn on angle and conduction period are set to -4 and 150 electrical degrees respectively as stated in Table 4-14. Analytically calculated results are compared to measurements provided in [4]. It has to be mentioned that motor output power is controlled by controlling maximum and minimum chopping currents under a constant turn on angle and conduction period.

Copper losses of the machine are plotted against output power in Figure 4-32. Note that because the temperature of windings during the tests are not given, analytical calculations are provided at both 20 C and 100 C. Measurement results are also provided for comparison.

As it can be seen from the figure, there is a good agreement between analytical results and measurements, especially when the temperature is increased in analytical computations. Further increment of temperature will lead to error reduction between analytical results and measurements. Cooling type and the method of doing experiments is important factors which affect the winding temperature.

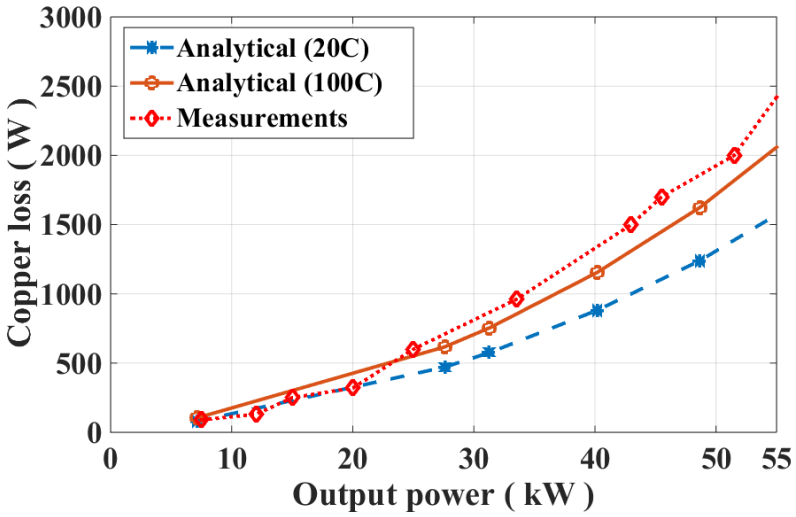

Figure 4-32 SRM2 copper losses at 3000 rpm

Another important point is that analytical calculations are carried out using normalized data obtained for a normal steel. However, SRM2 has a different core material (10JNEX900). Difference in B-H curves and saturation points of these two materials is depicted in Figure 4-30. SRM2 material has a lower saturation flux density. Hence, in order to get equal output powers from both motors, phase currents in SRM2 with 10JNEX900 material has to be higher. That's why analytically calculated copper loss curves are below the measured copper loss curve.

Figure 4-33 depicts variation of measured and analytically calculated core losses of SRM2 versus motor output power.

It can be observed that analytical results and measurements are in a relatively good agreement. A discrepancy can be seen in the output power range of 20 kW and 30 kW. It has to be noticed that due to complexities in accurate analytical modeling of core losses, this discrepancy can be acceptable. In this study an analytical core loss calculation method based on actual flux variations and its harmonics is utilized.

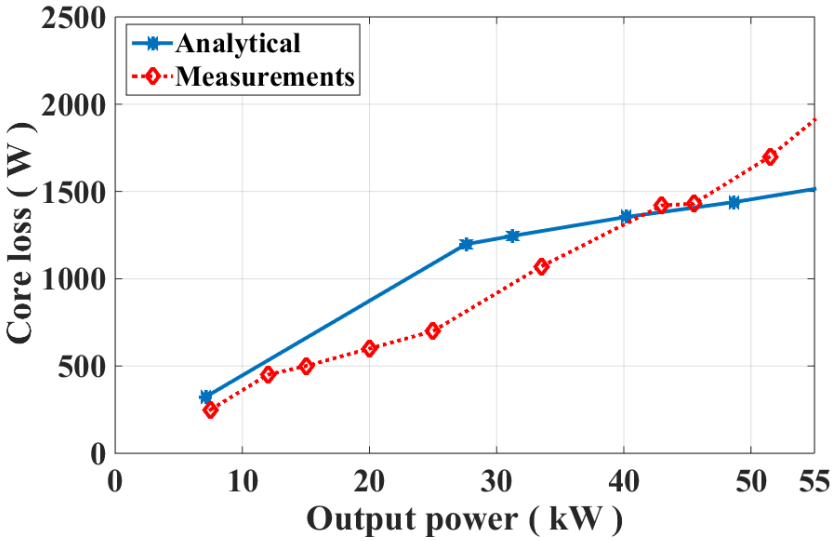

Figure 4-33 SRM2 core losses at 3000 rpm

Once copper losses, core losses and output power of a machine are known, motor efficiency can be determined. Figure 4-34 represents analytically calculated efficiency at two winding temperatures of 20C and 100 C. Measured efficiency is also provided in the figure.

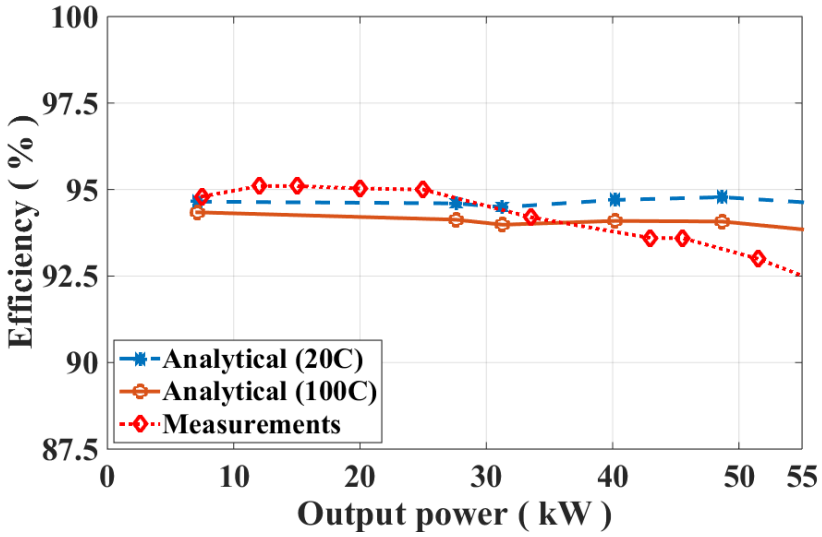

Figure 4-34 SRM2 efficiency at 3000 rpm

It can be seen from the figure that analytical results are in a very good agreement with measurements. Moreover, it can be figured out that a temperature rise of 80 C, reduces motor efficiency less than 1 %. It has to be noticed that the motor reaches to maximum efficiency (at this specific speed) of 95% between output powers of 10 kW and 25 kW.

4.3.4 End winding leakage inductance effect

Same as SRM1, because normalized force and permeance data are derived in a 2-D environment using magneto static solution type, end winding leakage inductance is not taken into account in normalized data sets. However, as mentioned earlier, 3-D FEM simulation results and comparison of analytical calculations with measurements reveal that end winding leakage component of the flux is completely negligible. Thus, this effect is not taken into account in the proposed analytical model.

4.3.5 Torque-speed characteristic of SRM2

In this section, torque-speed and power-speed characteristics of the 18/12 switched reluctance motor are determined using analytical calculations. Furthermore, the motor is simulated using FEM to investigate the accuracy of proposed analytical model. Note that in order to be able to compare analytical results with finite element simulations, these simulations are carried out using normal steel as the core material. Figure 4-35 and Figure 4-36 depict torque-speed and output-power-speed characteristics of SRM2 respectively. It has to be added that the torque-speed characteristics are obtained while the SRM is operating under the drive circuit conditions (turn on angle, excitation period and maximum and minimum chopping currents) specified in Table 4-14.

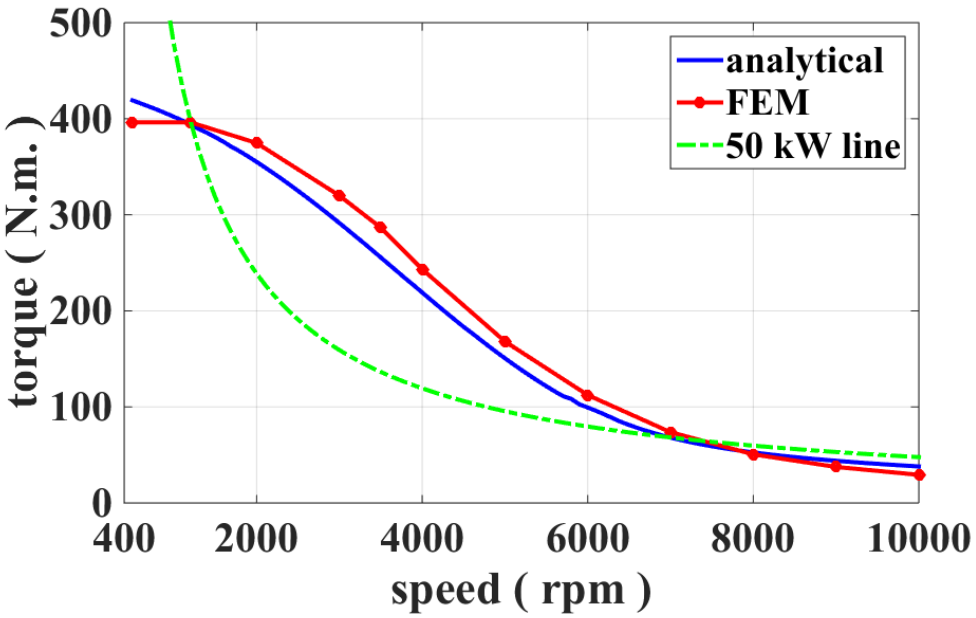

Figure 4-35 SRM2 torque speed characteristics

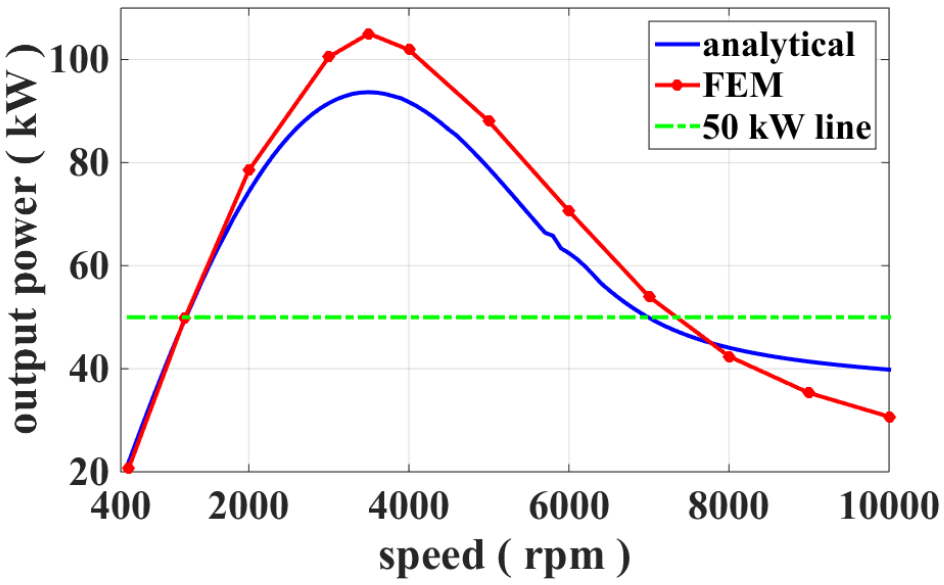

Figure 4-36 SRM2 output power speed characteristics

As it is obvious form the figures, analytical calculations and finite element simulation results are in a good agreement and torque-speed characteristic of the machine is well-predicted. Therefore, the accuracy of the model in predicting torque speed

characteristic of switched reluctance motors is proved. Once the accuracy of analytical model is corroborated, the model is suitable to be used for optimization purposes.

CHAPTER 5

OPTIMIZATION PROBLEM

5.1 Introduction

As discussed earlier, in a recent paper [4, 22], an SR motor was developed for Toyota Prius to replace its Interior PM Synchronous Motor (IPMSM). In this study, the authors concentrated on an 18/12, 50 kW SR motor and illustrated that a motor with similar performance could be developed using an advanced sheet steel core material. It has to be added that the motor is cooled using a water jacket which is attached around its stator core. In this thesis, with the tools we have, it is aimed to illustrate that even better performance can be obtained. For this purpose, the task is considered as an optimization problem searching for an SR motor with the same outer diameter and core length as the existing IPMSM motor, for different N_s/N_r combinations (6/4, 8/6, 12/8, 18/12 and 24/18) and geometry (t/λ, λ/g, etc.) and drive conditions (turn on angle, conduction angle) in which developed torque reaches its maximum value.

Of course it is possible to optimize the SR motor in many ways. In electric car applications the efficiency map of the motor is very important as this determines how efficiently the energy available is used. In this thesis, the analysis is not exhaustive, however, torque per unit mass (TMM) which is an important issue that affects the cost will be calculated for optimized machines and compared to that of existing SR motors in the literature. TMM may be calculated as follows.

$$TMM = \frac{T_{avg}}{M_{copper} + M_{iron}} \tag{5-1}$$

In this research, Genetic Algorithm (GA) package available in MATLAB optimization toolbox is used. This algorithm will be briefly discussed in section 5.3.

Although the optimization is done under a constrained volume of an SR motor, in section 5.5 it will be mentioned that the proposed optimization method can be implemented in designing a switched reluctance motor to be used in various applications, and for a wide range of output powers. Hence, the proposed optimization procedure is universally valid.

5.2 The optimization problem

In this optimization problem, average output torque of the machine at 1200 rpm is defined as the objective function. Stator poles/rotor poles (N_s/N_r), rotor tooth pitch per air gap length ratio (λ/g), normalized stator and rotor teeth widths (t_s/λ and t_r/λ), rotor outer diameter (D_{or}), back core width to half stator tooth width ratio (K), conduction period and phase turn on angle are taken as eight independent variables of the optimization. Note that, determination of optimum values of machine geometry and excitation pattern in order to maximize the torque for each pole combination is aimed in this study.

Basic dimensions of a typical SR motor designed to be used in Hybrid Electric Vehicle (HEV) applications [4, 6, 22, 73-76] are considered for all motors studied in this study. Following table summarizes basic dimensions and characteristics of SRM motors which are considered to be constant among all motors simulated during optimization procedure.

Table 5-1 Constant parameters of optimization problem

Parameter	Speed	DC voltage	Stator outer diameter (D_{os})	Motor axial length (L)
value	1200 rpm	500 V	269 mm	155mm

5.2.1 Objective function of the optimization

Mean output torque of the SR motor (T_{avg}) is defined as the objective function of the optimization problem. In other words, maximizing output torque of the SRM at 1200 rpm, under a constrained volume (constrained axial length and stator outer diameter) is aimed in this study. Average torque of an SR motor can be calculated by integrating steady state torque variation versus time of the machine and dividing it to the length of that specific time period (T_1).

$$T_{avg} = \frac{1}{T_1}\int_0^{T_1} T(\mathrm{t})\,\mathrm{dt} \tag{5-2}$$

Because optimizations are carried out at a constant speed of 1200 rpm, the optimization problem can be considered as maximizing output power of the machine at 1200 rpm.

5.2.2 Constant parameters of the optimization

In this section, the parameters which will be kept constant during optimization procedure are briefly discussed. Because the axial length and stator outer diameter of the machine are chosen in a way which is suitable for motors used in HEV applications, the constant parameters are also selected to meet this criteria of application.

1. DC side voltage

DC side voltage of the drive circuit is kept constant at 500V. This is the value which is used in hybrid electrical vehicle switched reluctance motors drive circuit [4, 6, 22, 73, 74].

2. Rotational speed

Rotational speed of the machine is another important parameter which depends significantly on the application criteria. The rotor speed of all simulated switched reluctance machines is set to be 1200 rpm which is the minimum speed in which a SRM has to be capable of developing its maximum output torque [4, 6, 22, 73, 74].

5.2.3 Independent variables of the optimization problem

This section summarizes the variables which change independently during optimization procedure. Because the proposed method tries to introduce a general method to find an optimum geometry to maximize torque density in switched reluctance motors, the independent variables determine general geometry characteristics of the machine. The independent variables of the optimization are listed below.

1. N_s/N_r

There are some common standard values for number of stator and rotor poles which designer can choose from based on the specific application. Because the converter configurations and drive circuits are designed for standard number of stator and rotor poles, deviation from standard values is not advised and is done only in some exceptional applications. Choosing N_s/N_r ratio determines number of phases of the machine and basically depends on the application criteria. Following equation is used to determine number of phases based on number of stator and rotor poles.

$$q = \frac{N_s}{\mathrm{GCD}(N_s, N_r)} \tag{5-3}$$

In above equation q represents number of phases of the machine. The denominator of the fraction is Greatest Common Divisor of number of stator and rotor poles. Standard numbers for stator and rotor poles and number of phases in each combination are summarized in Table 5-2.

Table 5-2 Number of SRM phases for different pole combinations

N_s / N_r	6/4	8/6	12/8	18/12	24/18
q (number of phases)	3	4	3	3	4

2. λ/g

The ratio of λ/g determines the air gap of the machine based on rotor pole pitch value. Rotor pole pitch value can be easily calculated using

$$\lambda = \frac{\pi D_{or}}{N_r} \tag{5-4}$$

Where D_{or} stands for the rotor outer diameter. Because developing a general design methodology for switched reluctance machines is aimed in this study, all calculations have to be independent from geometric dimensions like bore diameter and motor length. Thus, a general normalized λ/g value is used as an independent variable of the optimization problem. Having rotor outer diameter of the SRM in hand, rotor pole pitch and subsequently motor air gap length can be simply computed using normalized λ/g value.

Several previous studies reveal that ratio of λ/g, varies between 40 and 250 for any kind of switched reluctance machines which is used in variety of applications. Thus, in this study this variable will be changed from 40 to 250 during optimization procedure.

3. t_s/λ

This independent variable represents the normalized stator tooth width of the SRM. In this ratio t_s stands for stator tooth width. Same as λ/g value, t_s/λ is another normalized quantity which can be used in designing any kind of switched reluctance machine. By having rotor bore diameter, value of λ, and consequently stator tooth width of the SRM can be easily determined.

Studies on different topologies of switched reluctance machines show that varying t_s/λ ratio between 0.3 and 0.5 covers all possible design criteria for switched reluctance motors to be used in variety of applications.

4. t_r/λ

This ratio indicates normalized rotor tooth width, which is defined as rotor tooth width (t_r) divided by rotor pole pitch. Same as normalized stator tooth width (t_s/λ), the ratio of t_r/λ is changed between 0.3 and 0.5 during optimization procedure.

It is obvious that rotor tooth width (t_r) can be simply computed by knowing rotor outer diameter of the SRM.

Note that when three above mentioned ratios are specified for a SRM, its basic geometric dimensions are determined. So, while knowing bore diameter of the machine based on the specific application criteria, air gap length and stator and rotor teeth widths of the machine can be easily calculated. Stator and rotor teeth heights and back core widths are other geometric dimensions that have to be specified in designing any kind of SRM. Discussion on calculation of these quantities is the subject of section 5.4.

5. Rotor outer diameter (D_{or})

Because of the constraint imposed on maximum allowable stator outer diameter, the optimum rotor outer diameter of the SRM in which torque per active mass of the machine is maximized, can be determined using the implemented optimization method. Because maximum stator outer diameter is set to 269mm for this specific automotive application, the range of variation in rotor outer diameter is determined to be between 100mm and 200mm to cover all the range of possible and feasible diameter values. If rotor outer diameter is too large, because of the constraint on stator outer diameter, winding area inside the slots and consequently electrical loading of the machine will be low. On the other hand, by choosing a small rotor outer diameter, not only the developed torque is reduced, but also the fill factor will be very low and slots will not be used efficiently. Therefore, an optimum point has to be determined using the proposed optimization procedure.

6. Back core width to half stator tooth width ratio (K)

One of the important steps in designing any kinds of electrical machines is determination of back core width. If back core thickness is selected to have a large value, motor weight is increased and consequently torque density of the machine will be decreased. On the other hand, if a small yoke is designed for an electrical machine, the core may operate in its saturation region. In this case MMF drop on motor yokes will be considerable and required current and electric loading of the machine will be unnecessarily increased.

In this study, back core width to half stator tooth width ratio is selected as an independent variable of the optimization problem.

$$K = \frac{W_{bcs}}{t_s / 2} = \frac{W_{bcr}}{t_s / 2} \tag{5-5}$$

The optimization problem will determine an optimum back core width for the machine. It is noticeable that because the stator tooth flux passes from both stator and rotor back core areas, the optimum yoke thickness is selected proportional to stator tooth width. In other words, a normalized back core width is selected to be an independent variable of optimization. This selection makes the optimization problem universal.

7. Conduction period

After determination of basic geometric dimensions, an important variable which is related to the electrical behavior of the machine has to be taken into account. The conduction period, is the range in which a phase winding is in conduction until the phase switch is turned off, and is represented in electrical degrees. To cover all possible switching conditions which may happen in a SRM, this value will be changed between 90 and 180 electrical degrees during optimization procedure. If the excitation period is chosen less than 90 electrical degrees, the input current will not be continuous. In other words, there will be a delay after one phase is turned off until the next one is turned on. This delay will result in a significant reduction in average output torque and will intervene in the continuous rotation of rotor. On the other hand, choosing excitation period higher that 180 electrical degrees will result in negative torque production in the machine, which will cause vibration and again intervenes in continuous rotation of the rotor. It is obvious that the excitation period value determines number of phases of the SRM which are in conduction simultaneously. Hence, overlaps in consecutive phases conductions are taken into account while changing the excitation period in analytical calculations.

8. Phase turn on angle

Another crucial variable in determination of excitation pattern of the machine is turning on angle of the phase winding. When both excitation period and turn on

angle are known, the excitation pattern is determined. The schematic diagram of consecutive phase torques in a typical 8/6 SRM and the reference point of the turn on angle ($\theta_{on} = 0$) is represented in Figure 4-9.

Note that choosing phase turn on angle less than -45 (in an 8/6 SRM) electrical degrees will result in negative torque production in the SRM. However, at higher rotational speeds, the firing angle may be set to a negative value in order to compensate for the current rise time and maximize the developed torque. On the other hand, choosing this value higher than 45 electrical degrees again will lead to production of negative torque, because the excitation periods are set to be higher than 90 electrical degrees. Furthermore, based on Figure 4-9 by setting firing angle larger than 90 electrical degrees, maximum achievable torque of the machine cannot be attained. Thus, changing phase turn on angle from -45 to 45 electrical degrees (for 8/6 SRM), and excitation period from 90 to 180 electrical degrees covers all feasible excitation patterns which may happen in driving any switched reluctance motor. As it is mentioned before, at higher rotational speeds firing angle can have a negative value.

It has to be noticed that once the conduction period and firing angle (excitation pattern) of the SRM are known, one phase current and torque waveforms are simply determined using dynamic calculations. Then, these waveforms are shifted for a specified amount on the degree axis depending on stator and rotor pole numbers, and total input current and developed torque can be determined which was discussed in details in chapters 2 and 4. By changing conduction period and firing angle of the SRM, different excitation patterns including one or two phase on excitations can be obtained. In this study an optimization is carried out in order to determine the optimum point of the switching pattern in which torque is maximized.

5.2.4 Constraints of the optimization

1. Stator outer diameter (D_{os})

Based on the range of the desired output torque and specific application criteria which is considered for the optimized machine, a constraint has to be imposed on outer

diameter of stator. Because optimization of a prototype machine to be used in HEV applications is aimed in this study, maximum allowable stator outer diameter is set to 269mm [4, 6, 22, 73, 74].

$$D_{os} \leq 269mm \tag{5-6}$$

However, depending on the specific application for which designing a SRM is desired, constraint on stator outer diameter will vary.

2. Tooth flux density

Based on the finite element simulation results of existing 18/12 SRM used for HEV applications, maximum tooth flux density reaches 2T. So, in analytical optimization procedure, maximum tooth flux density constraint is set to 2T.

$$B_{t_{\max}} \leq 2T \tag{5-7}$$

Once the maximum allowable flux density is determined, the equivalent flux value can be simply calculated based on tooth geometry.

3. Current density

Maximum allowable electrical loading of the machine is restricted by determining maximum allowable value for current density in stator windings. Current density in a wire can be easily computed by dividing current passing thorough the copper to the corresponding wire area.

$$J = \frac{I}{A} \tag{5-8}$$

Maximum allowable current density depends on cooling method which is used in a specific electrical machine. In the existing 18/12 SRM maximum RMS current density reaches 33 A/mm^2. Therefore, in designing wire diameter of the machine, this value is limited to 33 A/mm^2 in analytical calculations.

$$J_{rms} = \frac{I_{rms}}{A} \leq 33A / mm^2 \tag{5-9}$$

It has to be noticed that such a high current density requires a liquid cooling system.

4. Turning on angle and conduction period

As discussed in previous sections, choosing turning on angle of the phase winding less than -45 electrical degrees will cause to a negative torque which is not desired (in a 4 phase SRM). Thus turning on angle of the phase winding is set to be higher than - 45 electrical degrees to avoid negative torque production.

$$\theta_{on_{elec.}} \geq -45^{\circ} \tag{5-10}$$

It is obvious that in a 3 phase SR motor, turn on angle has to be more than -30 electrical degrees. It has to be taken into account that at higher rotational speeds, firing angle can be set to a negative value in order to compensate for the time constant of winding circuit and provide sufficient amount of time for phase current to reach to the desired value. Note that electrical angle of 0 happens at intersection points of consecutive phases torque curves. Another constraint which will be imposed on determination of excitation pattern of SRM is that the summation of phase turning on angle and excitation period in electrical degrees (which shows phase turn off angle) has to be less than 135 electrical degrees to avoid negative torque development (again for a 4 phase SRM).

$$\theta_{on_{elec.}} + ep_{elec.} \leq 135^{\circ} \tag{5-11}$$

In other words, phase switch has to be turned off before the rotor reaches its fully aligned position (x_n=0). Thus, excitation pattern has to be set in a way that two above constraints are met. It has to be noticed that in a 3 phase SR motor turn off angle has to be below 150 electrical degrees.

5. Slot fill factor

Slot fill factor is a quantity which has to be taken into consideration in designing winding, and determination of number of phase turns and wire diameter of the machine. This value is defined as the winding area divided by total slot area.

$$k_f = \frac{A_{winding}}{A_{slot}} \tag{5-12}$$

Upper limit for slot fill factor is set to 0.55 in analytical calculations. Note that in the 18/12 SR motor in the literature (SRM 2), slot fill factor is 0.57. This value is highly dependent on wire diameter and slot insulation type.

Because the stranded winding is utilized in the SR motors in this study, an additional stranded factor of 1.3 is also taken into account while calculating the required slot area and slot fill factor of the SR motors. The constraint for slot fill factor is given below.

$$k_f \leq \frac{0.55}{1.3} = 0.42 \tag{5-13}$$

6. Shaft diameter

From a mechanical point of view, motor shaft has to have sufficient strength to transmit torque and not to be overstressed. Shaft diameter of the designed 18/12 SR motor in the literature (SRM 2) is 105.5 mm. Hence, the minimum possible shaft diameter for all SR machines designed in analytical calculations is set to 105.5 mm.

$$\text{Shaft diameter } (D_s) \geq 105.5\,\text{mm} \tag{5-14}$$

A detailed explanation of shaft diameter calculation and design procedure will be given in section 5.4.4.

7. Operating temperature

Core and copper losses of the machine are transformed into heat, which causes the temperature rise. Maximum allowable operating temperature of electrical machines is highly dependent on insulation class and type of cooling. Thermal analysis has to be carried out after completion of design stage, however in this study thermal analysis will not be considered and can be taken into account as a future work.

5.3 Optimization method and tool

At this stage, the problem can be considered as a mathematical optimization problem. The aim is to find optimum motor geometry and excitation pattern for each pole combination of switched reluctance machines in which torque has its maximum value. Therefore, having an eight input and one output parameter (average torque) in hand which has to be maximized, the most appropriate optimization method can be selected.

5.3.1 The Genetic Algorithm (GA)

Because the problem has many local maximum and minimum values, optimization methods which are based on derivative methods are not suitable to solve this problem. For this purpose, evolutionary optimization algorithms have to be utilized.

In this study, Genetic Algorithm (GA) is utilized to optimize the objective function. The GA is a subclass of evolutionary optimization algorithm which mimics the biological evolution process. The main advantage of the GA is using derivative-free approach, which makes it a powerful tool for non-linear optimization problems.

The GA is an iterative optimization method which generates a set of design candidates based on individuals' fitness values. The set of individuals in each generation is called population. The GA utilizes the best individuals of each generation to generate the individuals of next generation. Different crossover, mutation and recombination methods are used to generate the individuals of next generation. Elites count is the number of individuals that directly pass from one generation to another. Higher number of crossover and mutation is suggested when it is intended to search in a wider area and minimize the chance of trapping in a local minimum.

The MATLAB software has a powerful GA optimization toolbox. In this study the MATLAB GA toolbox is utilized to perform the optimization. In this toolbox, the number of generations, populations, elite count and values of mutation and crossover

factors are assigned by user. Furthermore, the convergence criteria are determined by stopping criteria of GA toolbox. When one of the stopping criteria is satisfied, the optimum solution is achieved and optimization is ceased. Various stopping criteria are available in MATLAB GA toolbox. In this study the following stopping criteria are used to determine the convergence criteria of the optimization problem.

- Generations : the algorithm stops when the number of generations reaches the maximum specified value.
- Function Tolerance : the algorithm runs until the average relative change in the fitness function value over Stall generations is less than function tolerance.

For more information about the MATLAB GA toolbox theory and options refer to the MATLAB Help documentations.

In this study number of populations are set to 200 in each generation. Objective function is calculated for all 200 SR motors in each generation, and GA creates the next generation with a population of 200 based on the results of the previous generation. The process is repeated until the optimum point for the objective function is found and genetic algorithm stops. It is worth mentioning that in specifying stopping criteria for genetic algorithm, function tolerance and number of stall generations are set to 0.1 and 10 respectively.

5.3.2 Optimization flowchart

Once the optimization problem is completely defined by giving the objective function, constraints, independent variables and constant parameters, a mathematical optimization problem can be solved using the optimization tool (GA) which was described in the previous section. Flowchart of the optimization algorithm is shown in Figure 5-1.

As a brief description of this flow chart, genetic algorithm determines initial points for seven input variables of the optimization in each generation. It has to be mentioned that separate optimizations are carried out for each N_s/N_r ratio, and optimum geometry and excitation pattern are determined for each pole combination

separately. Finally, the results for different pole combinations are compared and the best combination can be selected.

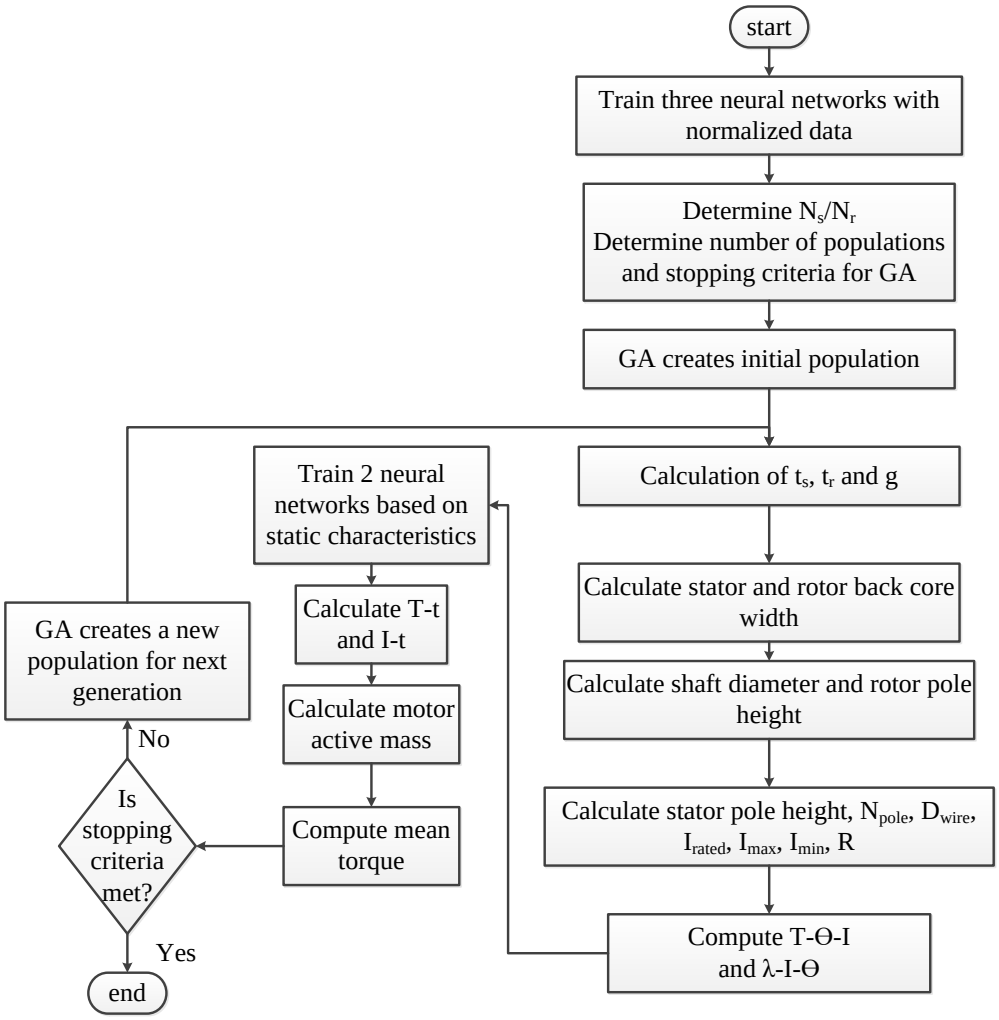

Figure 5-1 Optimization algorithm flowchart

It has to be mentioned that once all eight independent variables of the optimization are known, an initial design process is needed (the blocks related to initial design process can be distinguished in Figure 5-1) to determine motor dimensions, winding configuration and drive specifications. The design process is described in detail in section 5.4.

5.4 Initial design of the SRM

Having a preliminary design and determination of motor dimensions and winding configuration are necessary in order to calculate static and dynamic performance of the SRM. As it is mentioned earlier, the dimensions of a prototype SRM designed for HEV applications [4, 6, 22, 73, 74] are used to carry out analytical calculations. Thus, maximum motor length (including end winding length) and maximum stator outer diameter are set to 155 mm and 269mm respectively which are suitable values to be used in this specific HEV applications. Once motor stack length and outer diameter of rotor are specified, designing stator and rotor teeth and back core sections is an easy task. The design procedure which is used in analytical model is discussed in detail in this part.

5.4.1 Stator and rotor teeth width and air gap length

Because λ_r/g, t_s/λ_r, t_r/λ_r and D_{or} are all independent variables of the optimization, stator and rotor teeth widths and air gap length can be simply calculated. In the first stage, rotor pole pitch (λ_r) can be calculated using

$$\lambda_r = \frac{\pi D_{or}}{N_r} \tag{5-15}$$

Where N_r represents number of rotor teeth which is an independent variable as well. Once rotor pole pitch is obtained, calculation of stator and rotor teeth widths and air gap length is straightforward.

$$t_s = \lambda_r \times (t_s / \lambda_r) \tag{5-16}$$

$$t_r = \lambda_r \times (t_r / \lambda_r) \tag{5-17}$$

$$g = \frac{\lambda_r}{(\lambda_r / g)} \tag{5-18}$$

5.4.2 Calculation of motor stack length with consideration of end winding length effect

End winding length effect is an important factor which has to be taken into account in determination of maximum allowable motor stack length. Figure 5-2 represents a 3D model of an 18/12 switched reluctance motor in which end winding sections can be easily distinguished.

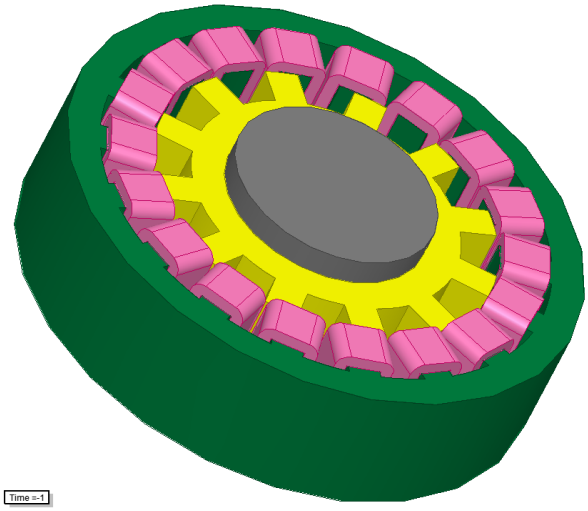

Figure 5-2 3D model of a prototype 18/12 switched reluctance motor

In this study, end winding length at one side of the SRM is roughly estimated as half of the stator slot width of the machine. Hence, motor stack length can be simply estimated using

$$L = L_{total} - 2 \times (\frac{W_{slot}}{2}) - 0.002 \tag{5-19}$$

Where L_{total}, and W_{slot} stand for motor maximum total length including end winding length and stator slot width respectively. Maximum allowable length of the

machine including end windings is taken as 155mm for this specific HEV application. Note that, an empty distance of 1mm is considered at both ends of the machine as a safety margin. By increasing number of stator and rotor poles of the machine, number of winding turns per pole and consequently end winding length is reduced. As a result, developed torque will be increased.

5.4.3 Stator and rotor yoke thickness

Stator back core thickness has to be chosen in a way that saturation is avoided. The flux density in stator yoke is approximately half of its value in stator poles, because the flux is divided by 2 while passing from stator pole thorough back core. However, in some excitation patterns, flux density may be higher. So, it is proposed to choose stator yoke thickness wider than half of stator poles width [77]. Thus stator yoke is calculated using

$$W_{bcs} = K \times \frac{t_s}{2} \qquad \text{K>1} \tag{5-20}$$

Rotor back core thickness has to be chosen in a manner that conditions for mechanical stiffness and maximum allowable flux density to avoid saturation are met. For the same reasons which provided in determination of stator back core thickness, rotor yoke thickness has to be higher to an extent than half of one stator pole width.

$$W_{bcr} = K \times \frac{t_s}{2} \qquad \text{K>1} \tag{5-21}$$

Note that K is the independent variable of the optimization problem, So, K value is determined in a way that torque of the machine gains its maximum value under specific geometric and electrical constraints.

5.4.4 Rotor pole height (h_r)

If the rotor pole height is short, and the outer diameter of stator has to be set to a constant value, there will be more space for winding in stator slots. Furthermore, in a SRM with short rotor poles the inductance ratio between aligned and unaligned positions is small. On the other hand, increasing rotor height leads to a higher value of bore diameter and consequently a higher developed torque, because torque is proportional with bore diameter for the same MMF value. So, there has to be an optimum value for rotor pole height [61]. In [78] it is proposed that optimum value of rotor pole height can be expressed in terms of air gap length.

$$h_r = k_{hr} g (15 < k_{hr} < 35) \tag{5-22}$$

It has to be noticed that in obtaining normalized permeance, MMF and force data, pole heights in both sides of the symmetrically slotted geometry (Ertan's model) are set to 40g. Therefore, in analytical calculations, pole heights of all simulated switched reluctance motors are taken as 40g. Once both rotor pole height and rotor yoke are known determination of shaft diameter is an easy task.

$$D_s = D_{or} - 2(h_r + W_{bcr}) \tag{5-23}$$

However, when λ_r/g ratio decreases and air gap length is increased for the same bore diameter value, the constraint imposed on shaft diameter may not be satisfied. In analytical calculations a penalty factor is defined for situations in which shaft diameter becomes less than 20% of the rotor outer diameter. An exponential penalty factor is selected for this purpose.

$$\text{penalty factor} = 100(e^{1-\frac{0.2D_{or}}{D_s}} - 1) \tag{5-24}$$

D_{or} and D_s stand for rotor outer diameter and shaft diameter respectively. Note that the defined penalty factor varies between 0 and -100 for different values of calculated shaft diameter. By subtracting the calculated penalty factor from the objective function of the optimization, the corresponding point will be considered to

have a lower torque, and the motor will be automatically out of the selection range as an optimized machine.

At this stage, rotor and shaft dimensional parameters have been designed completely and stator teeth, back core and winding design is of interest.

5.4.5 Stator pole height (h_s) and winding design

Stator pole height has to be large enough to provide required space for the winding which is embedded inside the slot. If the stator pole is too short, there will not be sufficient space for the winding and consequently electrical loading of the machine has to be set to a lower value. On the other hand, core material will not be used at its knee point while having shorter stator poles and consequently small slots. By choosing desired stator pole height and knowing number of turns per pole, wire diameter of the machine can be designed. In this section the procedure used in analytical calculations to design stator pole height and winding of the machine will be described.

At first stage, number of turns per pole of the machine is determined. [61] introduces a new method which gives a rough estimation of number of turns per pole in a switched reluctance machine. Under single pulse operation mode under DC supply voltage of V_{dc}, the maximum flux linkage value is given by the law of induction.

$$FL_{\max} = \frac{V_{dc}\Delta\theta}{\omega_{rated}} \tag{5-25}$$

In this equation, DC side voltage is represented by V_{dc}. ω_{rated} stands for the motor rated speed in mechanical radians per second. $\Delta\theta$ depicts the angle between consecutive phases of SRM in mechanical radians which is calculated simply using

$$\Delta\theta = \frac{2\pi}{qN_r} \tag{5-26}$$

Where q and N_r represent number of phases and number of rotor poles of the SRM. On the other hand, maximum flux linkage of a phase winding can be expressed in another way.

$$FL_{\max} = 2(\frac{N_s}{2q} N_{pole})\varphi_{\max} = \frac{N_s}{q} N_{pole} B_{st_{\max}} Lt_s \quad (5\text{-}27)$$

$B_{st_{\max}}$, L and t_s stand for maximum allowable peak flux density is stator tooth, stack length and stator tooth width respectively. The term $N_s/2q$ is number of pole pairs of the machine which are in conduction simultaneously once a phase is excited. This value for different pole combinations can be seen in the following table.

Table 5-3 $N_s/2q$ value for different pole combinations

Pole combination	6/4	8/6	12/8	18/12	24/18
$N_s/2q$	1	1	2	3	3

So, by combining equations (5-25) and (5-27), number of turns per pole can be estimated based on DC voltage value, motor rated speed, maximum allowable tooth flux density and some geometric dimensions.

$$N_{pole} = \frac{V_{dc}\Delta\theta}{2\frac{N_s}{2q} B_{st_{\max}} Lt_s \omega_{rated}} \quad (5\text{-}28)$$

In design methodology used in this study, stator pole height is changed between 40g and 250g. At each step, and for the specific pole height, stator outer diameter and slot area of the machine can be easily calculated. On the other hand, the required slot area is calculated as well by computing total MMF drop in the aligned position and maximum allowable flux density condition which is considered as the worst case scenario [62]. The maximum allowable current can then be simply calculated.

$$I_{\max} = \frac{MMF_{\max}}{2N_{pole}} \tag{5-29}$$

Maximum permissible RMS current density is set to 33 A/mm^2. So, the wire area inside a slot is calculated. This required slot area is compared with the calculated slot area based on specific value for pole height which varies between 40g and 250g starting from 40g. At any step in which required slot area is lower than the calculated area, the algorithm stops. If the condition is not satisfied even at stator pole height of 250g, the same algorithm is repeated but this time maximum allowable current is reduced by 1%. The procedure is repeated until the required slot area is lower than or equal to the slot area of the SRM calculated using geometric dimensions. Flowchart of the algorithm can be seen below. Note that a stranded factor of 1.3 is taken into account in calculation of required slot area.

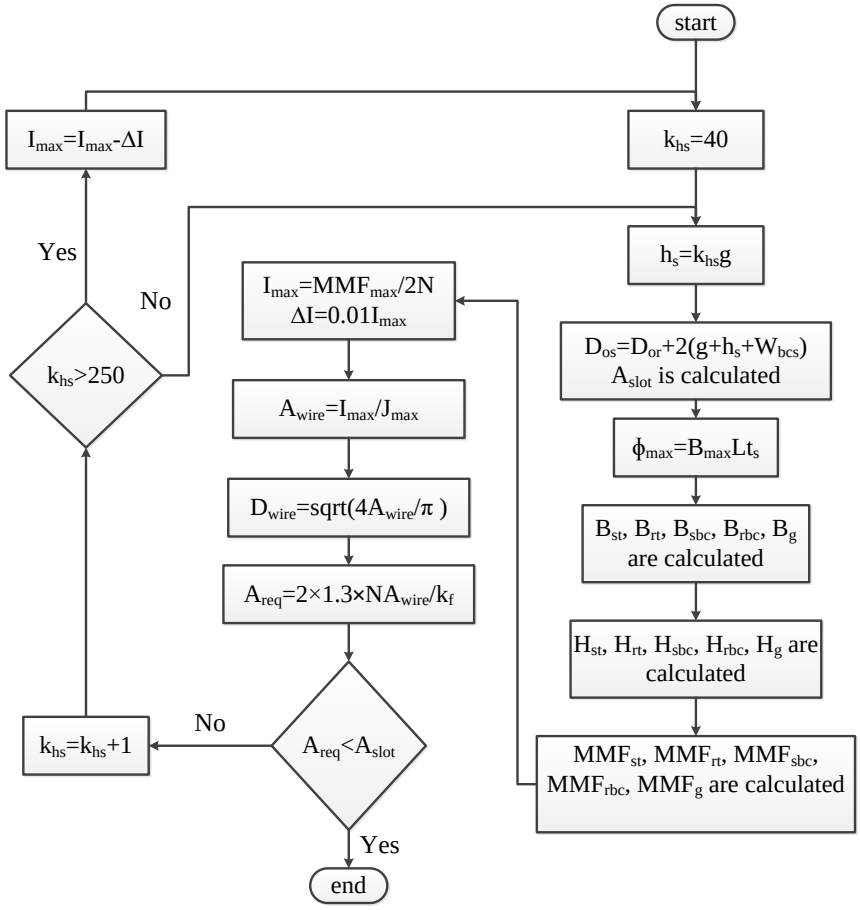

Figure 5-3 Stator pole height and winding design algorithm flow chart

5.4.6 Determination of maximum and minimum chopping currents

After determination of maximum allowable current, maximum and minimum chopping currents can be determined. Note that if the winding current is more than the maximum value, some problems related to winding temperature and insulation will be faced. Maximum and minimum chopping currents are set to 100% and 92% of the total maximum allowable current of the SR motor respectively.

$$I_{\max_{chopper}} = I_{\max} \tag{5-30}$$

$$I_{\min_{chopper}} = 0.92 I_{\max} \tag{5-31}$$

5.4.7 Calculation of winding resistance with consideration of end winding length effect

After determination of number of turns per pole and wire dimeter, winding resistance has to be calculated. Accurate calculation of phase resistance is an important step in determination of both copper losses and dynamic characteristics of the SRM. First step in computation of winding resistance is calculation of copper length. Winding length of a pole pair can be calculated easily using

$$l_w = 2 \times (\mathrm{L} + \mathrm{t}_{s_{mean}} + 2 \times (\frac{W_{slot}}{2})) \times 2\,\mathrm{N}_{pole} \tag{5-32}$$

Where $\mathrm{t}_{s_{mean}}$ represents mean stator tooth width. Note that due to tooth tapering effect tooth width is in its minimum value on motor bore, and gains its maximum near stator back core section. Moreover, end winding length at both ends of the SRM is also added to the total copper length. It is mentioned that end winding length of the SRM can be roughly estimated to be equal to half of the stator slot width

($W_{slot}/2$). Therefore, resistance of two poles of one phase which are in series can be computed.

$$R = \rho \frac{l_w}{A_{wire}} \tag{5-33}$$

In this equation, ρ and A_{wire} stand for wire resistivity and wire area respectively. A 3-D model of a typical 8/6 SRM is shown in Figure 5-4 in which end windings can be easily distinguished.

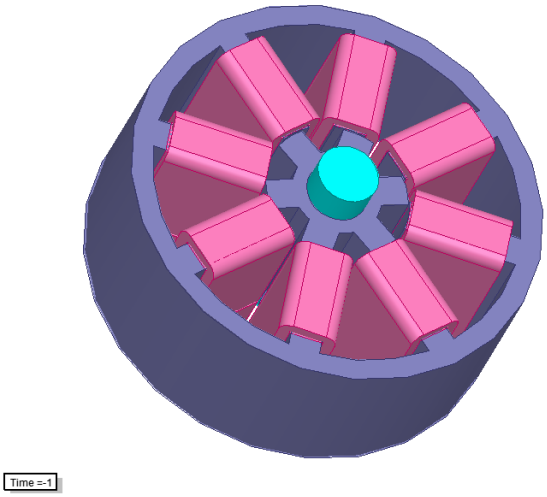

Figure 5-4 3-D model of a typical 8/6 SRM

5.4.8 Determination of stator outer diameter and defining the corresponding penalty factor

Once stator pole height is determined, stator outer diameter can be calculated.

$$D_{os} = D_{or} + 2(g + h_s + W_{bcs}) \tag{5-34}$$

In this equation, D_{or}, g, h_s and W_{bcs} stand for rotor outer diameter, air gap length, stator pole height and stator yoke thickness respectively. If the calculated stator

outer diameter is larger than the maximum allowable value ($D_{os_{\max}}$ =269 mm), a penalty factor is used.

$$\text{penalty factor} = 2500\,(1\text{-}e^{1-\frac{D_{os}}{D_{os_{\max}}}}) \tag{5-35}$$

Note that the penalty factor varies between zero and 2500 based on the value of D_{os}. By subtracting the calculated penalty factor from objective function of the optimization (mean output torque), the calculated geometry will automatically have a lower average torque. Hence, the motor will be out of the selection range as an optimized machine.

The discussed analytical design method is capable of designing any SRM for different N_s/N_r combinations by receiving seven input variables which are independent variables of optimization and were discussed in details in previous sections. Once the design process of the machine is complete, analytical calculations which was discussed in chapter 2 are carried out in order to determine static and dynamic performance characteristics of the SRM.

Note that, initial design and subsequently static and dynamic performance computation are carried out for each switched reluctance motor based on eight input independent variables using the proposed analytical method. A detailed discussion on optimization results and verification of the proposed method will be given in chapter 6.

5.5 General and dimensionless nature of the proposed optimization method

A general torque maximization method is introduced in this study which can be a helpful tool for designers in designing any kind of switched reluctance machines to be used in a wide range of applications.

Stator outer diameter and motor axial length are both crucial variables which determine motor basic dimensions and consequently range of the torque which will be developed by the machine. The bigger, the stator outer diameter and axial length of the

motor are, the higher, the developed torque will be. Based on switched reluctance motors applications in a wide range of output power from fractional horsepower motors used in hard disk drives to large ones used in Hybrid Electric Vehicles (HEV), selection of stator outer diameter and axial length is an important task in any design procedure.

It is worth mentioning that approximate length and stator outer diameter of prototype machines which are used in Hybrid Electrical Vehicles (HEV) are around 155mm and 269mm respectively [4, 6, 22, 73, 74]. Hence, in all optimization calculations, maximum stator outer diameter and maximum axial length of the SRM including end windings are taken as 269mm and 155mm respectively to carry out static and dynamic calculations of the machine.

In order to design switched reluctance motors to be used in different applications, it is only required to set maximum values for stator outer diameter and motor axial length and specify the desired DC voltage. The proposed optimization method will determine geometry characteristics and excitation pattern of the most optimum motor which has the highest developed torque. This proves that the proposed optimization method is universally valid and can be used in design of a wide range of switched reluctance machines to be used in variety of applications.

CHAPTER 6

OPTIMIZATION RESULTS

6.1 Introduction

In this chapter, results of the optimization problem which was described in details in chapter 5 will be discussed. As it is mentioned in previous chapter, maximizing the torque and consequently output power of the machine under specified constraints of geometry and electric and magnetic loadings is aimed in this study. In order to investigate the optimum geometry, pole combination and excitation patterns for maximization of mean torque Genetic Algorithm (GA) optimization method is used. Discussion on optimization results for different pole combinations and Finite Element simulations of the optimized motor will be presented in this chapter. Finally, capability of the optimized motor in developing the desired power (50 kW) at speed range of 1200-6000 rpm which is required for this specific HEV application, and possible improvements in torque-speed characteristics of the optimized SRM will be investigated by comparing torque-speed and power-speed characteristics of both existing and optimized motors. The existing 18/12 SR motor is capable of developing 45.7 kW at 1200 rpm which is below the desired output power of 50 kW.

6.2 Optimization results for different pole combinations

In this section, output torque of the motor is taken as the objective function of the optimization problem, and the optimum geometry and excitation pattern in which torque density of the SRM is maximized will be determined. Five separate optimizations are done for five different N_s/N_r combinations (6/4, 8/6, 12/8, 18/12 and 24/18). As it is mentioned in chapter 5, number of populations in each generation is

selected to be 200. Moreover, function tolerance and number of stall generations are selected to be 0.1 and 10 in determination of genetic algorithm stopping criteria. Upcoming section discusses the results of five separate genetic algorithm optimizations for five different stator and rotor pole combinations carried out using GA toolbox of MATLAB software.

1. N_s/N_r= 6/4 (3- phase)

Results of genetic algorithm optimization for switched reluctance motors with 6/4 pole combinations are reported in the following table.

Table 6-1 Genetic algorithm results for pole combination of 6/4

λ/g	t_s/λ	t_r/λ	D_{or} (mm)	K	Excitation period (electrical degree)	Firing angle (electrical degree)	Torque (N.m.)
144.77	0.342	0.351	141.3	1.28	136.3	- 4.3	67.52

Using the design method proposed in previous chapters, dimensions and winding configuration of the optimized 6/4 SRM can be simply calculated. Following table summarizes computation results.

Table 6-2 Optimized 6/4 motor specifications

Rotor outer diameter	141.3 mm
Stator outer diameter	269 mm
Core length	116.2 mm
Axial length	155 mm
Stator back core width	24.3 mm
Shaft diameter	31.4 mm
Air gap length	0.77 mm
Rotor back core width	24.3 mm
Stator tooth Tapering angle	2.215 degree
Stator tooth width	37.9 mm
Rotor tooth width	38.9 mm
Stator pole depth	39.1mm
Rotor pole depth	30.7 mm
Number of turns per pole	79 turns
Wire diameter	0.6 mm
Number of strands	20

Chopping circuit characteristics and the optimized switching pattern of the machine, calculated using analytical method and the optimization, can be seen in Table 6-3.

Table 6-3 Optimized 6/4 motor switching pattern

I_{max}	127.5 A
I_{min}	117.68 A
Excitation period	0.7572 p.u. (136.3electrical degree)
Phase turn on angle	-4.3 (electrical degree)
Speed	1200 rpm

Dynamic performance characteristics of the machine are computed using the proposed analytical model. Copper loss, core loss, and motor efficiency are also calculated. Table 6-4 reports analytical performance calculation results.

Table 6-4 Optimized 6/4 motor performance calculation results

	Speed (rpm)	Average torque (N.m.)	Output power (kW)	RMS Current (A)	RMS current density (A/mm^2)	Peak tooth flux density (T)	Copper loss (kW)	Core loss (W)	Total loss (kW)	Input power (kW)	efficiency
Optimized 6/4 SRM	1200	67.52	8.49	17.46	3.1	2	1.8	162.1	1.96	10.45	81

As it can be seen form the table, maximum tooth flux density and RMS current density of the winding are below the maximum allowed values. Maximum allowed RMS current density is 33 Amm^2, however, in a 6/4 SR motor it reaches to 3 A/mm^2. This is because number of turns per pole is higher when lower number of stator and rotor poles are used. Note that maximum electric loading remains approximately the same (see Table 6-31). It can be observed that optimized 8/6 SR motor is not capable of developing output power of 50 kW. Copper and active iron mass of the machine is also calculated which can be seen in Table 6-5.

Table 6-5 Active mass and torque density calculations of optimized 6/4 SRM

	Iron mass (kg)	Copper mass (kg)	Total active mass (kg)	Torque density (N. m. /kg)
Optimized 6/4 SRM	32.88	9.4	42.28	1.597

2. N_s/N_r= 8/6 (4- phase)

Genetic algorithm optimization is carried out on switched reluctance motors with the pole combination of 8/6. Table 6-6 summarizes independent variables and the objective function (mean output torque) of optimization.

Table 6-6 Genetic algorithm results for pole combination of 8/6

λ/g	t_s/λ	t_r/λ	D_{or} (mm)	K	Excitation period (electrical degree)	Firing angle (electrical degree)	Torque (N.m.)
121.92	0.339	0.339	165.22	1.522	127.04	-7.68	123.71

SRM dimensions and winding configuration are designed simply for the optimum point. Table 6-7 reports geometric dimensions and winding configuration of 8/6 SRM.

The SRM motor is modeled at speed of 1200 rpm in order to achieve the highest possible torque. Chopping circuit characteristics and switching pattern of the SRM are summarized in Table 6-8.

Performance characteristics of the SRM including output power, losses, RMS current, and efficiency are calculated using the proposed analytical model. Results can be seen in Table 6-9.

It has to be noticed that both RMS current density and maximum tooth flux density are below the constrained values. The motor is not capable of developing output power of 50 kW. Active material mass of the machine including copper and core mass is calculated. The results are reported in Table 6-10.

Table 6-7 Optimized 8/6 motor specifications

Rotor outer diameter	165.22 mm
Stator outer diameter	269 mm
Core length	116.9 mm
Axial length	155 mm
Stator back core width	22.3 mm
Shaft diameter	63.8 mm
Air gap length	0.71 mm
Rotor back core width	22.3 mm
Stator tooth Tapering angle	2.215 degree
Stator tooth width	29.3 mm
Rotor tooth width	29.3 mm
Stator pole depth	28.4 mm
Rotor pole depth	28.4 mm
Number of turns per pole	51 turns
Wire diameter	0.6 mm
Number of strands	11

Table 6-8 Optimized 8/6 motor switching pattern

I_{max}	165 A
I_{min}	152.3 A
Excitation period	0.706 p.u. (127.04 electrical degree)
Phase turn on angle	-7.68 (electrical degree)
Speed	1200 rpm

Table 6-9 Optimized 8/6 motor performance calculation results

	Speed (rpm)	Average torque (N.m.)	Output power (kW)	RMS Current (A)	RMS current density (A/mm^2)	Peak tooth flux density (T)	Copper loss (kW)	Core loss (W)	Total loss (kW)	Input power (kW)	efficiency
Optimized 8/6 SRM	1200	123.71	15.55	23.63	7.6	2	4.9	304.8	5.2	20.75	74.93

Table 6-10 Active mass and torque density calculations of optimized 8/6 SRM

	Iron mass (kg)	Copper mass (kg)	Total active mass (kg)	Torque density (N. m. /kg)
Optimized 8/6 SRM	31.45	4.26	35.71	3.46

3. N_s/N_r=12/8 (3- phase)

Optimization results including final values of independent variables of the optimization and objective function of the optimization are summarized in Table 6-11.

Table 6-11 Genetic algorithm results for pole combination of 12/8

λ/g	t_s/λ	t_r/λ	D_{or} (mm)	K	Excitation period (electrical degree)	Firing angle (electrical degree)	Torque (N.m.)
81.2	0.431	0.452	166.2	1.297	149.35	-4.9	288.64

A design procedure is carried out on the optimized 12/8 SR motor which gives the following machine dimensions and winding configuration.

Table 6-12 Optimized 12/8 motor specifications

Rotor outer diameter	166.2 mm
Stator outer diameter	269 mm
Core length	137.2 mm
Axial length	155 mm
Stator back core width	18.2 mm
Shaft diameter	65.4 mm
Air gap length	0.804 mm
Rotor back core width	18.2 mm
Stator tooth Tapering angle	2.215 degree
Stator tooth width	28.1 mm
Rotor tooth width	29.5 mm
Stator pole depth	32.1 mm
Rotor pole depth	32.1 mm
Number of turns per pole	22 turns
Wire diameter	0.6 mm
Number of strands	24

Drive circuit characteristics including maximum and minimum chopping currents, and excitation pattern can be seen in Table 6-13.

Table 6-13 Optimized 12/8 motor switching pattern

I_{max}	357.19 A
I_{min}	329.7 A
Excitation period	0.8297 p.u. (149.35 electrical degree)
Phase turn on angle	-4.9 (electrical degree)
speed	1200 rpm

Performance characteristics of the optimized 12/8 SRM is computed using the proposed analytical model. Calculation results are shown in Table 6-14.

Table 6-14 Optimized 12/8 motor performance calculation results

	Speed (rpm)	Average torque (N.m.)	Output power (kW)	RMS Current (A)	RMS current density (A/mm^2)	Peak tooth flux density (T)	Copper loss (kW)	Core loss (W)	Total loss (kW)	Input power (kW)	efficiency
Optimized 12/8 SRM	1200	288.64	36.27	132.16	19.5	2	11.38	716.7	12.1	48.37	74.99

Note that RMS current density of the winding and maximum tooth flux density are below the maximum allowed values and the optimization constraints are met. However, the motor cannot develop 50 kW. Finally, active mass of the machine including copper and active iron weight is calculated for the proposed switched reluctance motor. Mass calculation results can be seen in Table 6-15.

Table 6-15 Active mass and torque density calculations of optimized 12/8 SRM

	Iron mass (kg)	Copper mass (kg)	Total active mass (kg)	Torque density (N. m. /kg)
Optimized 12/8 SRM	39.95	5.94	45.88	6.29

4. N_s/N_r=18/12 (3- phase)

The optimum point geometric dimensions and excitation pattern which are the independent variables of the optimization problem and torque value of the optimum point are summarized in Table 6-16.

Table 6-16 Genetic algorithm results for pole combination of 18/12

λ/g	t_s/λ	t_r/λ	D_{or} (mm)	K	Excitation period (electrical degree)	Firing angle (electrical degree)	Torque (N.m.)
98.73	0.391	0.432	190.58	1.376	150.09	-4.61	401.7

Using the independent variables, the SR motor can be simply designed using the method described in chapter 5. Table 6-17 contains geometric dimensions and winding configuration of the optimum switched reluctance motor for this pole combination.

Table 6-17 Optimized 18/12 motor specifications

Rotor outer diameter	190.578 mm
Stator outer diameter	269 mm
Core length	139.1 mm
Axial length	155 mm
Stator back core width	13.4 mm
Shaft diameter	123.3 mm
Air gap length	0.505 mm
Rotor back core width	13.4 mm
Stator tooth Tapering angle	2.215 degree
Stator tooth width	19.5 mm
Rotor tooth width	21.6 mm
Stator pole depth	25.3 mm
Rotor pole depth	20.2 mm
Number of turns per pole	14 turns
Wire diameter	0.6 mm
Number of strands	23

The SRM is simulated under following operating conditions. DC side voltage is unchanged and a 500 V is applied to the circuit. Maximum and minimum chopping

currents and excitation pattern can be found in Table 6-18. Note that in order to obtain the highest torque, minimum speed of 1200 rpm is selected.

Table 6-18 Optimized 18/12 motor switching pattern

I_{max}	343.1 A
I_{min}	316.7 A
Excitation period	0.834 p.u. (150.1 electrical degree)
Phase turn on angle	-4.61 (electrical degree)
speed	1200 rpm

Dynamic performance characteristics of the optimized 18/12 SRM using proposed analytical model can be seen in Table 6-19.

Table 6-19 Optimized 18/12 motor performance calculation results

	Speed (rpm)	Average torque (N.m.)	Output power (kW)	RMS Current (A)	RMS current density (A/mm^2)	Peak tooth flux density (T)	Copper loss (kW)	Core loss (W)	Total loss (kW)	Input power (kW)	efficiency
Optimized 18/12 SRM	1200	401.4	50.44	200.76	30.9	2	11.03	1131	12.16	62.6	80.58

Note that the constraints imposed on maximum RMS current density and maximum tooth flux density are satisfied. Moreover, the optimized motor can develop output power of 50.44 kW which is even higher than the desired power (50 kW) for this specific EV application.

At the end, active mass of the machine including winding copper mass and iron mass is calculated for the optimized 18/12 switched reluctance motor. Torque density of the machine is also calculated. Results are reported in Table 6-20.

Table 6-20 Active mass and torque density calculations of optimized 18/12 SRM

	Iron mass (kg)	Copper mass (kg)	Total active mass (kg)	Torque density (N. m. /kg)
Optimized 18/12 SRM	33.07	5.18	38.25	10.2

5. N_s/N_r=24/18 (4- phase)

Table 6-21 reports independent variables and objective function (mean output torque at 1200 rpm) of the optimization for the optimized 24/18 SRM.

Table 6-21 Genetic algorithm results for pole combination of 24/18

λ/g	t_s/λ	t_r/λ	D_{or} (mm)	K	Excitation period (electrical degree)	Firing angle (electrical degree)	Torque (N.m.)
86.53	0.392	0.44	191.05	1.5	140	-10	353.5

Machine dimensions and winding configuration of the optimized motor, calculated using the initial design process discussed in chapter 5, are summarized in Table 6-22.

Table 6-22 Optimized 24/18 motor specifications

Rotor outer diameter	191.05
Stator outer diameter	269
Core length	141
Axial length	155
Stator back core width	9.8
Shaft diameter	140.6
Air gap length	0.39
Rotor back core width	9.8
Stator tooth Tapering angle	2.215
Stator tooth width	13.1
Rotor tooth width	14.7
Stator pole depth	28.5
Rotor pole depth	15.4
Number of turns per pole	10
Wire diameter	0.6
Number of strands	31

Maximum and minimum chopping currents and excitation pattern of the SR motor are reported in Table 6-23.

Table 6-23 Optimized 24/18 motor switching pattern

I_{max}	458.1
I_{min}	422.9
Excitation period	0.778 p.u. (140 electrical degree)
Phase turn on angle	- 10 (electrical degree)
Speed	1200 rpm

Table 6-24 reports performance calculation results of the optimized 24/18 SR motor.

Table 6-24 Optimized 24/18 motor performance calculation results

	Speed (rpm)	Average torque (N.m.)	Output power (kW)	RMS Current (A)	RMS current density (A/mm^2)	Peak tooth flux density (T)	Copper loss (kW)	Core loss (W)	Total loss (kW)	Input power (kW)	efficiency
Optimized 12/8 SRM	1200	353.5	44.42	249.3	28.5	2	11.7	1287	12.98	57.4	77.4

It has to be noticed that maximum tooth flux density and RMS current density of the winding are below the maximum allowed values and optimization constraints are met. However, the motor cannot develop the desired output power of 50 kW. At the end, active mass and torque density calculation results of the optimized 24/18 SR motor are given in Table 6-25.

Table 6-25 Active mass and torque density calculations of optimized 24/18 SRM

	Iron mass (kg)	Copper mass (kg)	Total active mass (kg)	Torque density (N. m. /kg)
Optimized 12/8 SRM	28.44	6.34	34.78	10.16

6.3 Discussion on optimization results

In this section, genetic algorithm results presented in section 6.2, will be discussed and the optimum pole combination will be selected. Table 6-26 reports the optimized independent variables and objective function of the optimization for five different pole combinations.

Table 6-26 Independent variables and objective function of the optimization for different pole combinations

	λ/g	t_s/λ	t_r/λ	D_{or} (mm)	K	Excitation period (electrical degree)	Firing angle (electrical degree)	Torque (N.m.)
Optimized 6/4 SRM	144.77	0.342	0.351	141.3	1.28	136.3	- 4.3	67.52
Optimized 8/6 SRM	121.92	0.339	0.339	165.22	1.522	127.04	-7.68	123.71
Optimized 12/8 SRM	81.2	0.431	0.452	166.2	1.297	149.35	-4.9	288.64
Optimized 18/12 SRM	98.73	0.391	0.432	190.58	1.376	150.09	-4.61	401.7
Optimized 24/18 SRM	86.53	0.392	0.44	191.05	1.5	140	-10	353.5

In order to ease the comparison, five switched reluctance motor geometries are also reported together in Table 6-27.

Moreover, performance calculations for the optimized machine for each pole combination are summarized in Table 6-28.

Variation of the objective function of the optimization (mean output torque at 1200 rpm) for different pole combinations is presented in Figure 6-1.

Table 6-27 Specifications of optimized motors geometries

Pole combination	6/4	8/6	12/8	18/12	24/18
Rotor outer diameter	141.3 mm	165.22 mm	166.2 mm	190.578 mm	191.05 mm
Stator outer diameter	269 mm	269 mm	269 mm	269 mm	269 mm
Core length	116.2 mm	116.9 mm	137.2 mm	139.1 mm	141 mm
Axial length	155 mm	155 mm	155 mm	155 mm	155 mm
Stator back core width	24.3 mm	22.3 mm	18.2 mm	13.4 mm	9.8 mm
Shaft diameter	31.4 mm	63.8 mm	65.4 mm	123.3 mm	140.6 mm
Air gap length	0.77 mm	0.71 mm	0.804 mm	0.505 mm	0.39 mm
Rotor back core width	24.3 mm	22.3 mm	18.2 mm	13.4 mm	9.8 mm
Stator tooth Tapering angle	2.215 degree	2.215 degree	2.215 degree	2.215 degree	2.215 degree
Stator tooth width	37.9 mm	29.3 mm	28.1 mm	19.5 mm	13.1 mm
Rotor tooth width	38.9 mm	29.3 mm	29.5 mm	21.6 mm	14.7 mm
Stator pole depth	39.1mm	28.4 mm	32.1 mm	25.3 mm	28.5 mm
Rotor pole depth	30.7 mm	28.4 mm	32.1 mm	20.2 mm	15.4 mm
Number of turns per pole	79 turns	51 turns	22 turns	14 turns	10 turns
Wire diameter	0.6 mm	0.6 mm	0.6 mm	0.6 mm	0.6 mm
Number of strands	20	11	24	23	31

Table 6-28 Optimized motors performance calculation results

	Speed (rpm)	Average torque (N.m.)	Output power (kW)	RMS Current (A)	Copper loss (kW)	Core loss (W)	Total loss (kW)	Input power (kW)	Efficiency
Optimized 6/4 SRM	1200	67.52	8.49	17.46	1.8	162.1	1.96	10.45	81
Optimized 8/6 SRM	1200	123.71	15.55	23.63	4.9	304.8	5.2	20.75	74.93
Optimized 12/8 SRM	1200	288.64	36.27	132.16	11.38	716.7	12.1	48.37	74.99
Optimized 18/12 SRM	1200	401.4	50.44	200.76	11.03	1131	12.16	62.6	80.58
Optimized 24/18 SRM	1200	353.5	44.42	249.3	11.7	1287	12.98	57.4	77.4

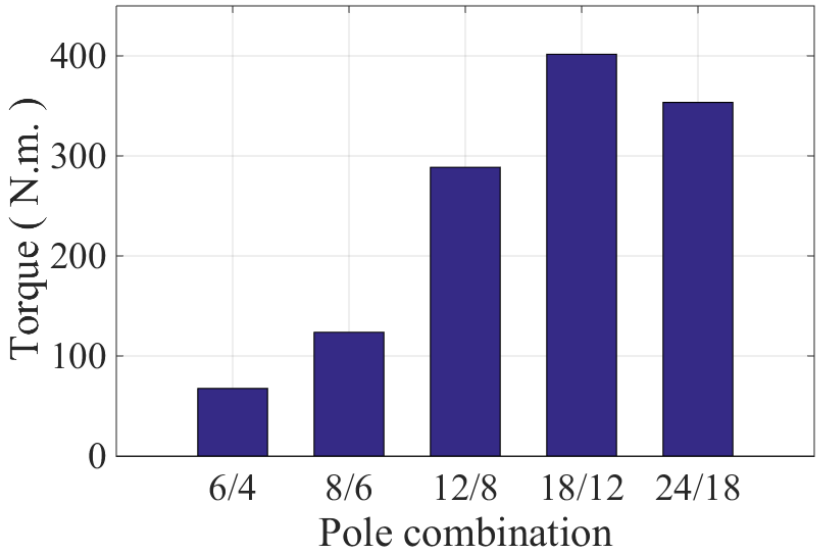

Figure 6-1 Variation of developed torque for different pole combinations

It can be easily concluded that developed torque of the SRM has its maximum value in the optimized 18/12 machine. So, this pole combination seems to be an appropriate candidate to be used in this hybrid electric vehicle application.

It is noticeable that in 6/4 and 8/6 switched reluctance motors only two poles belong to each phase. However, in a 12/8 SRM which is a three phase machine, 4 poles belong to each phase, and consequently developed torque will be higher. Furthermore, in a three phase 18/12 SRM and four phase 24/18 SR motor, each phase includes six poles which are excited at the same time. Therefore, motor is capable of developing more output torque. Note that the 18/12 SR motor develops more toque than the 24/18 machine. It can be concluded that a three phase SR motor, even with lower number of stator and rotor poles, can develop more output toque in comparison with a four phase SRM. It is also worth mentioning that maximum flux density constraint for each pole is the same for all pole combinations.

In order to examine the effects of variation in stator and rotor pole numbers in motor design and analysis, variations of some important variables will be discussed in this section. First of all, variation of number of turns per pole is plotted for different pole combinations which can be seen in Figure 6-2.

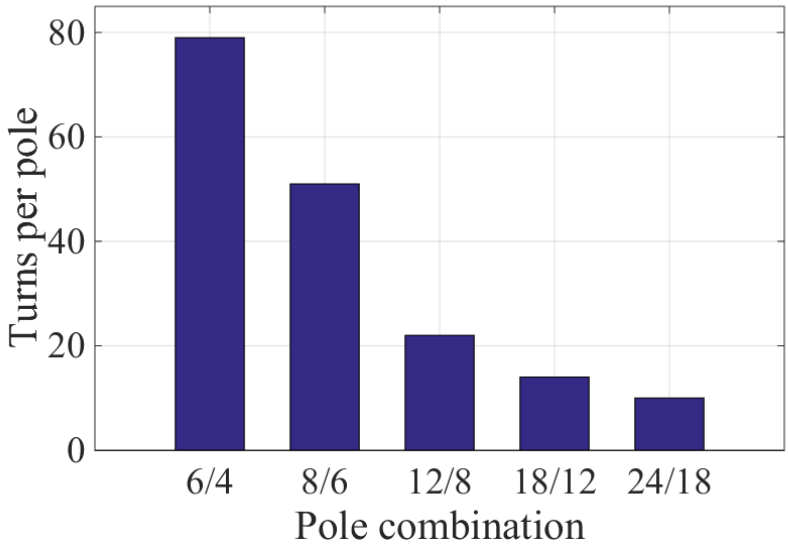

Figure 6-2 Variation of turns per pole for different pole combinations

As it is obvious form the figure, number of turns per pole is decreased by increasing number of stator and rotor pole numbers. Disadvantage of higher number of turns per pole is increment of end winding length of the machine and need for more space for winding inside the slots. Figure 6-3 represents variation of end winding length by changing stator and rotor pole numbers. Note that because of a constraint on axial length of the machine which is set 155 mm, shortening the end winding length will be a significant advantage. So, based on this figure, priority of using higher number of stator and rotor poles can be easily concluded.

Another issue associated with higher number of pole turns is lower rotor outer diameter and consequently bore diameter of the SR motor. Because of a constrained imposed on stator outer diameter and the space which is needed to place higher number of turns of winding, bore diameter of the machine is selected to be small by the optimization problem. It is obvious that larger bore diameter will result in a higher developed torque. Variation of Rotor outer diameter for different pole combinations can be seen in Figure 6-4.

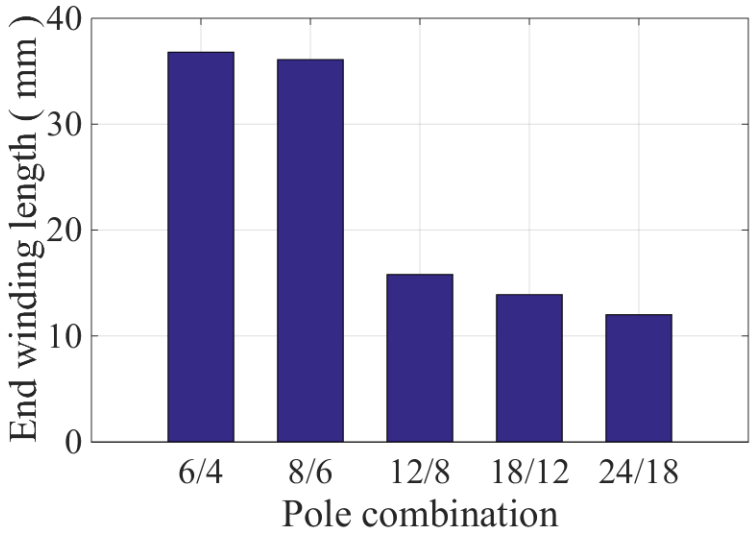

Figure 6-3 Variation of end winding length for different pole combinations

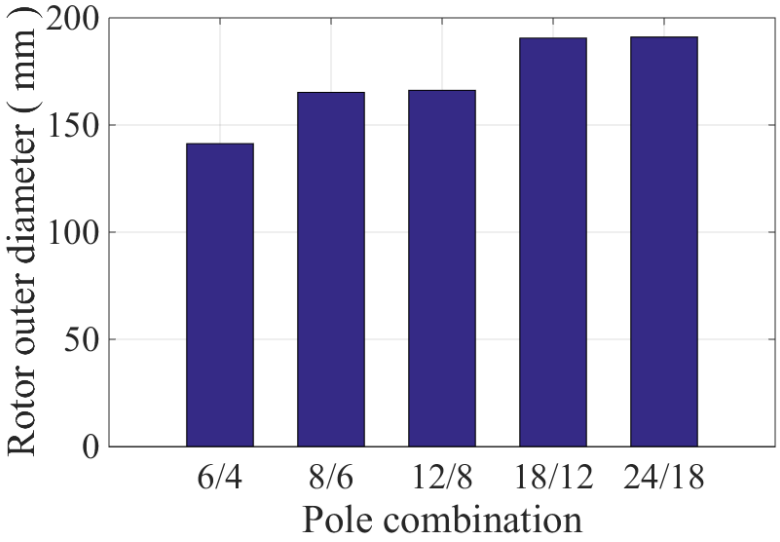

Figure 6-4 Variation of rotor outer diameter for different pole combinations

It is obvious that bore diameter of the optimized SR motors is increased by increasing number of stator and rotor poles. In addition to above mentioned geometrical and design problems, lower number of stator and rotor pole numbers leads to a lower RMS value of the input phase current. In other words, magnetic saturation of the core prevents the designer of increasing maximum and minimum chopping current values. Note that number of turns per pole is decreased by increasing number

of poles. Therefore, further increase in chopping currents while selecting lower number of stator and rotor poles will result in a huge MMF drop on the core and there will not be considerable increase in developed torque after the saturation level.

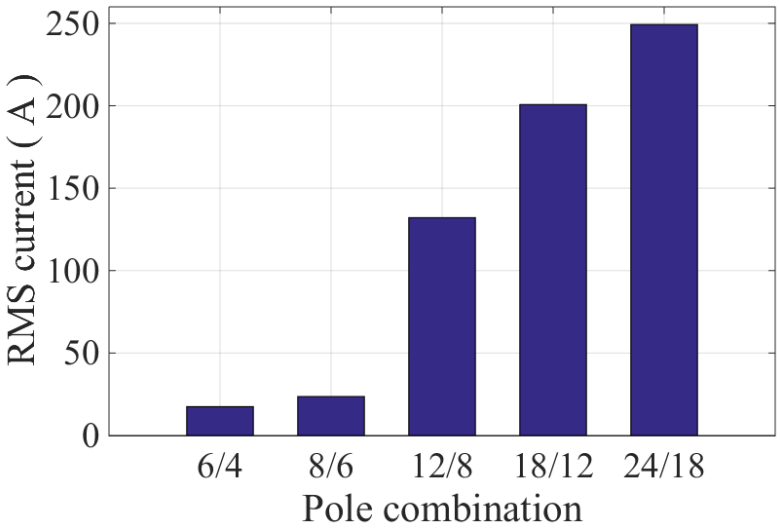

Figure 6-5 Variation of RMS current value for different pole combinations

Finally, variation of torque density of the optimized SR motors is plotted versus pole combination in Figure 6-6 to investigate the effect of changing stator and rotor pole numbers in toque per motor active mass.

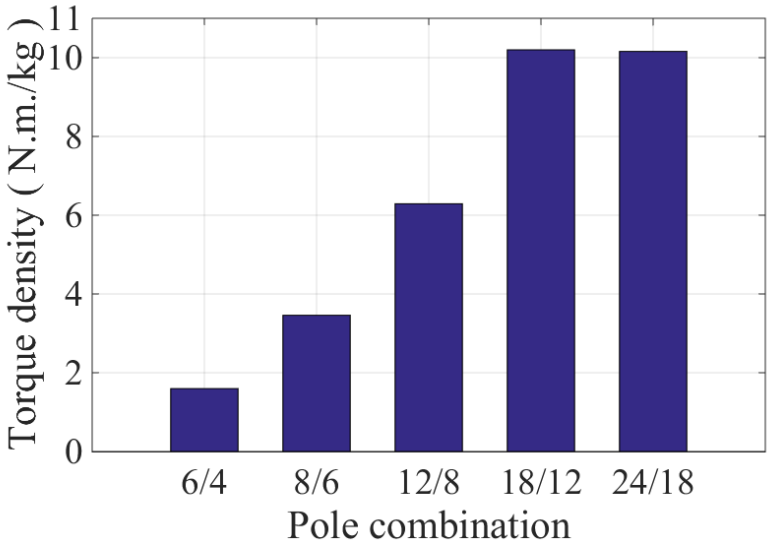

Figure 6-6 Variation of torque density for different pole combinations

It can be understood that by increasing stator and rotor pole numbers torque density of the machine will be increased. In other words, motor is capable of developing higher torque per unit mass of the SRM. Moreover, both 18/12 and 24/18 SR motors have the same torque densities. However, as discussed earlier, 18/12 motor is capable of developing more output torque.

As discussed earlier, in 6/4 and 8/6 SR motors only two poles are in conduction when one phase is excited. However, in 12/8 pole combination, 4 poles are in conduction simultaneously. Finally, in 18/12 and 24/18 SR motors 6 poles are in conduction at the same time. In order to have a better comparison of optimized motors performances, active area is determined for each SRM by calculating the area which is active (the flux passing area inside stator teeth) when one phase of the SR motor is excited. Torque per active area and power per active area are also given in Table 6-29.

Table 6-29 Comparison of active area and torque and power per active area for different pole combinations

	Torque (N.m.)	Output power (kW)	Active area (mm^2)	Torque per active area ($kN.m./m^2$)	Power per active area (kW/m^2)
Optimized 6/4 SRM	67.52	8.48	8808	7.67	963.3
Optimized 8/6 SRM	123.71	15.55	6850	18.06	2269.4
Optimized 12/8 SRM	288.64	36.27	15421	18.72	2352.1
Optimized 18/12 SRM	401.4	50.44	16275	24.66	3099.4
Optimized 24/18 SRM	353.5	44.42	11083	31.9	4008.3

It can be concluded from the table that torque and power per active area of the SR motor is increased by increasing the number of stator and rotor poles. It can be observed that active area of a 6/4 (3 phase) SRM is larger than that of an 8/6 (4 phase) SR motor. Moreover, active areas of both 12/8 (3 phase) and 18/12 (3 phase) motors

are larger than 24/18 (4 phase) SRM. Hence, it can be concluded that active area of a 3- phase SR motor is higher than a 4 phase SRM.

Another issue which can be understood from Table 6-29 is an unexpected lower output torque in 6/4 and 8/6 pole combinations. It is expected that the developed torque has to be higher than the calculated value. This issue can be due to saturation effects in calculation of back iron MMF drops. However, this claim needs more investigation which has to be considered as a future work of this study.

Another issue that has to be taken into account is the MMF drops in back core regions for each pole combination. Back core region of an SR motor consists of back teeth and back core regions as discussed in chapter 2. In 6/4 and 8/6 SR motors the flux completes its path from a pole which is 180 mechanical degrees apart. However, this flux path is shorter in other pole combinations depending on how many poles are in conduction at the same time once a phase winding is excited. Table 6-30 summarizes total excited MMF, back iron MMF drop and air gap MMF drop for different pole combinations.

Table 6-30 Excited MMF and MMF drops on back iron and air gap regions for different pole combinations

	Excited MMF (A.turns)	Back iron MMF drop (A.turns)	Air gap MMF drop (A.turns)	Back iron MMF drop to total MMF ratio (%)
Optimized 6/4 SRM	10072.5	1119.3	8953.2	11.1
Optimized 8/6 SRM	8415	189.3	8225.7	2.25
Optimized 12/8 SRM	7858.2	473	7385.2	6.02
Optimized 18/12 SRM	4803.4	300.2	4503.2	6.25
Optimized 24/18 SRM	4581	215	4366	4.7

As it can be seen form the table, both total excited MMF and air gap MMF are decreased by increasing number of poles, because both air gap length and back core length is reduced. In a 6/4 SR motor 11.1 % of the excited MMF is dropped on the

back iron region. However, this ratio is decreased by increasing number of stator and rotor poles.

At the end, maximum magnetic loading and maximum electric loading of the SR motors are calculated based on maximum flux density and maximum chopping current values. Note that maximum electric loading is calculated by dividing total MMF of conductors which are in conduction once one phase is excited by rotor outer circumference. In a similar way, maximum magnetic loading is calculated by dividing total flux passing the stator teeth by rotor outer circumference. The results are summarized in Table 6-31.

Table 6-31 Maximum electric loading and maximum magnetic loading for different pole combinations

	Maximum electric loading (A/m)	Maximum magnetic loading (T)
Optimized 6/4 SRM	45381	0.34
Optimized 8/6 SRM	32424	0.23
Optimized 12/8 SRM	60200	0.43
Optimized 18/12 SRM	48137	0.39
Optimized 24/18 SRM	45795	0.26

It can be observed that magnetic loading is higher for 3-phase SR motors (6/4, 12/8 and 18/12 pole combinations) in comparison with 4-phase SRMs (8/6 and 24/18). Moreover, although maximum electric loading remains approximately the same for 6/4 and 18/12 SR motors, Developed torque is much higher in an 18/12 SRM.

Based on all above mentioned discussions it can be simply concluded that 18/12 pole combination is a suitable candidate to be used in this specific hybrid electric vehicle application. Following sections include finite element simulations of the optimized 18/12 SRM. Furthermore, capability of the optimized machine in delivering the desired power at the speed range of 1200-6000 rpm which is required for this HEV application will be investigated.

6.4 Analytical calculations and FEM simulation results of the optimized machine

In this section, analytical calculations are carried out on the final optimized motor. To investigate accuracy of the results, the SRM is also simulated using FEM. Torque variation of the optimized SRM obtained using FEM simulations can be seen in Figure 6-7 and Figure 6-8. In Figure 6-7, M36 steel is used as the core material to compare simulation results with analytically obtained results. On the other hand, a simulation is carried out using 10JNEX900 material (Figure 6-8) to compare the results with the existing prototype in the literature.

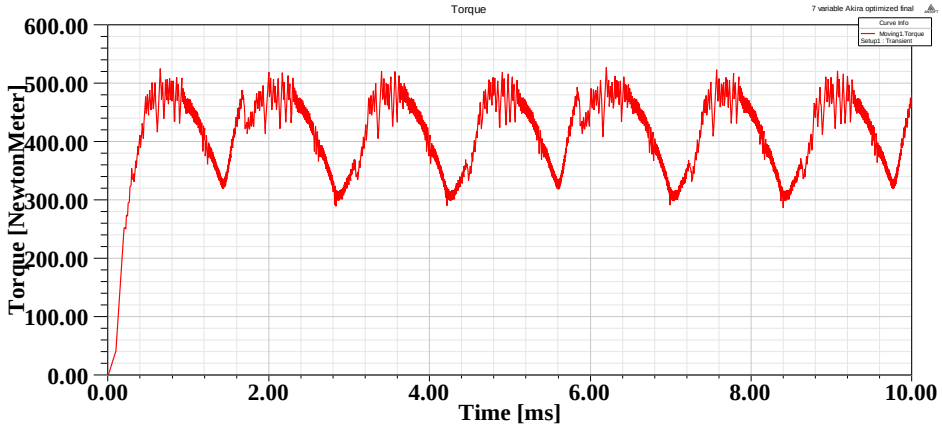

Figure 6-7 Developed torque of the optimized 18/12 SRM with M36 steel

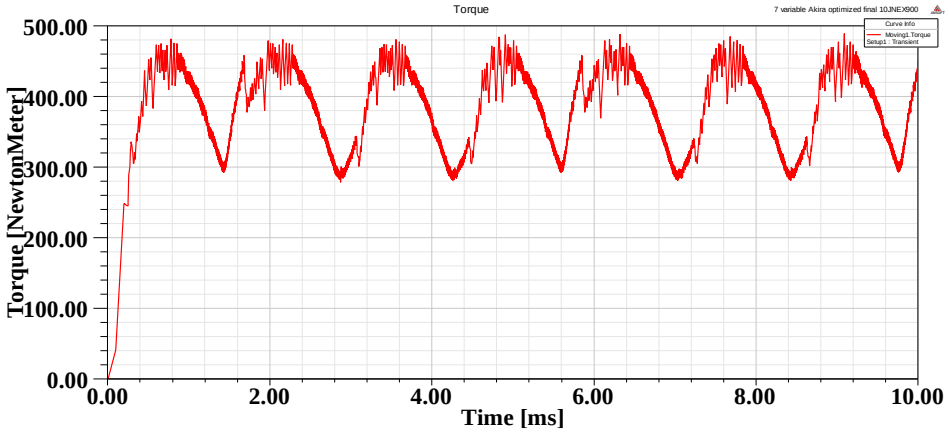

Figure 6-8 Developed torque of the optimized 18/12 SRM with 10JNEX900

Analytical calculations result of the optimized 18/12 switched reluctance motor is reported in Table 6-32. In order to ease the comparison, Finite Element simulation results are also provided in the table.

Table 6-32 Performance calculations results of optimized 18/12 SRM

	Speed (rpm)	Average torque (N.m.)	Output power (kW)	RMS Current (A)	Copper loss (kW)	Core loss (W)	Total loss (kW)	Input power (kW)	efficiency
Analytical calculations	1200	401.4	50.44	200.76	11.03	1131	12.16	62.6	80.58
FEM simulations with normal steel	1200	417.7	52.5	202.87	11.27	1379	12.65	65.14	80.6
FEM simulations with 10JNEX900	1200	390	49	203.6	11.35	1285	12.64	61.64	79.5

As it was mentioned earlier, produced normalized force and permeance data which are used as a look up table in analytical computations are obtained by carrying out FEM simulations on a symmetrically slotted geometry with core material of normal steel. So, calculated torque value is slightly higher in comparison with an SRM with core material of 10JNEX900.

Table 6-33 contains performance calculations of both existing and optimized SRM. As it can be concluded form the table, optimized SR motor can develop an approximate 3.25 kW higher power than the existing prototype in the literature at 1200 rpm. Moreover a slight improvement (1.4 %) in the efficiency of the optimized SR motor is also observed.

Table 6-33 Comparison of performance calculations of existing and optimized machines (with 10JNEX900 material)

	Speed (rpm)	Average torque (N.m.)	Output power (kW)	RMS Current (A)	Copper loss (kW)	Core loss (W)	Total loss (kW)	Input power (kW)	efficiency
FEM simulations of the existing machine	1200	364	45.74	191.3	12.42	418.3	12.84	58.58	78.1
FEM simulations of the optimized machine	1200	390	49	203.6	11.35	1285	12.64	61.64	79.5

Furthermore, Total active mass (copper and core iron weight) of the optimized SRM has been reduced. Although, torque per motor volume has not been changed while comparing the optimized machine and the existing one, there is an increase in torque per motor active mass of the SRM. Table 6-34 summarizes active mass and torque densities of the existing SRM and the optimized one.

Table 6-34 Comparison of active mass and torque density of existing and optimized machines

	Iron mass (kg)	Copper mass (kg)	Total active mass (kg)	Torque density (N. m. /kg)
Existing SRM	34.7	5.81	40.51	8.985
Optimized SRM	33.07	5.18	38.25	10.2
difference	-4.7 %	-10.8 %	-5.6 %	13.5 %

Thus, there is an approximate 5.6% reduction in motor active mass. On the other hand, motor torque density is increased about 13.5%.

6.5 Discussions on torque speed characteristic of the optimized SRM

It is shown in previous sections that the optimized machine is capable of developing the maximum output power of 49 kW at rotational speed of 1200 rpm, and its torque density is increased by 13.5% in comparison with the existing prototype in

the literature. On the other hand, the existing switched reluctance machine could only develop the output power of 45.74 kW. So, the motor is not capable of developing the desired 50 kW power at the speed range of 1200-6000 rpm which is required for this specific HEV application. It can be easily concluded that SRM performance has been significantly improved at 1200 rpm.

In this section, capability of the optimized SRM in developing output power of 50 kW at the whole speed range of 1200-6000 rpm will be investigated. For this purpose, torque-speed characteristic of the optimized machine is computed using analytical calculations.

6.5.1 Determination of torque-speed characteristic of the optimized machine

In order to determine torque speed characteristic of the optimized switched reluctance motor, motor performance is calculated using the proposed analytical model at the speed range of 500-10000 rpm with steps of 100 rpm. Calculated torque speed characteristic of the machine is shown in Figure 6-9.

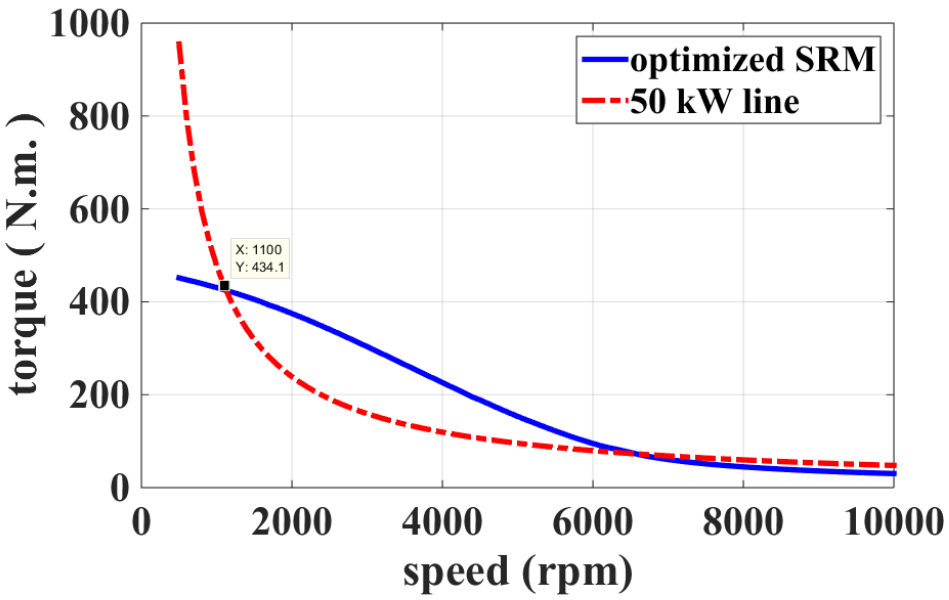

Figure 6-9 Torque-speed characteristic of the optimized motor

Note that the red line in this figure represents the torque which is required to develop output power of 50 kW at each rotational speed. As it is obvious from the figure the optimized machine is capable of developing 50 kW output power between rotational speeds of 1100 rpm and 6600 rpm. This capability can be shown in another way by plotting output power of the machine versus shaft speed which is depicted in Figure 6-10.

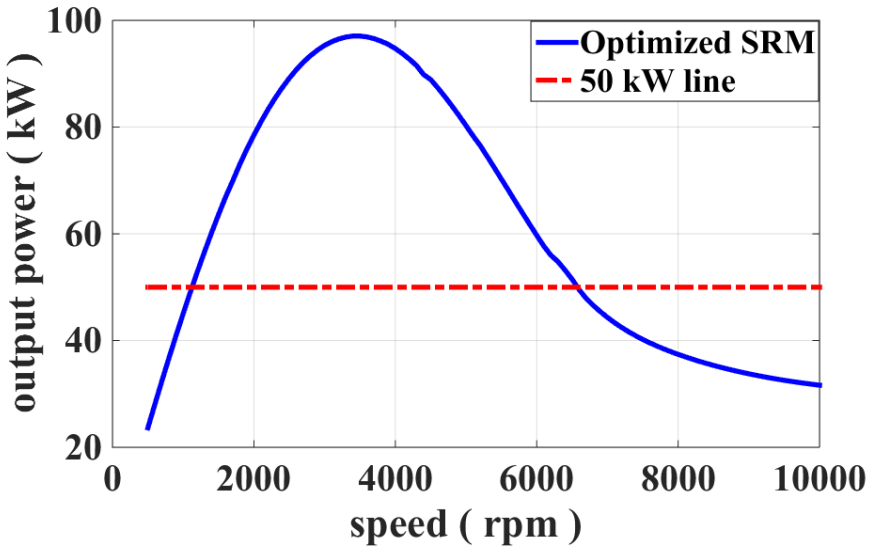

Figure 6-10 Output power-speed characteristic of the optimized motor

It can be easily understood that the optimized machine is capable of developing 50 kW power at the speed range of 1200-6000 rpm.

6.5.2 Losses and efficiency of the optimized machine versus speed

At this stage, variations of losses and efficiency of the machine versus rotational speed will be investigated. The optimized motor is simulated using proposed analytical model for different speeds varying from 500 rpm to 10000rpm. Copper losses, core losses and efficiency of the optimized switched reluctance motor are calculated at each rotational speed. Four following figures represent variations of copper losses, core losses, total losses and efficiency of the optimized switched reluctance motor versus shaft speed.

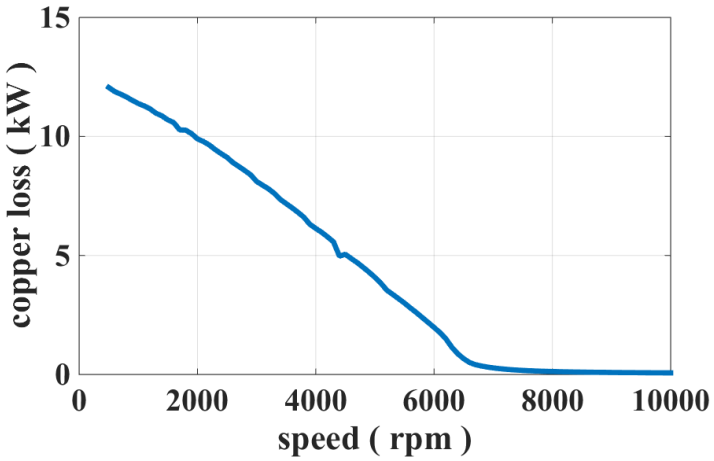

Figure 6-11 Copper losses of the optimized machine versus speed

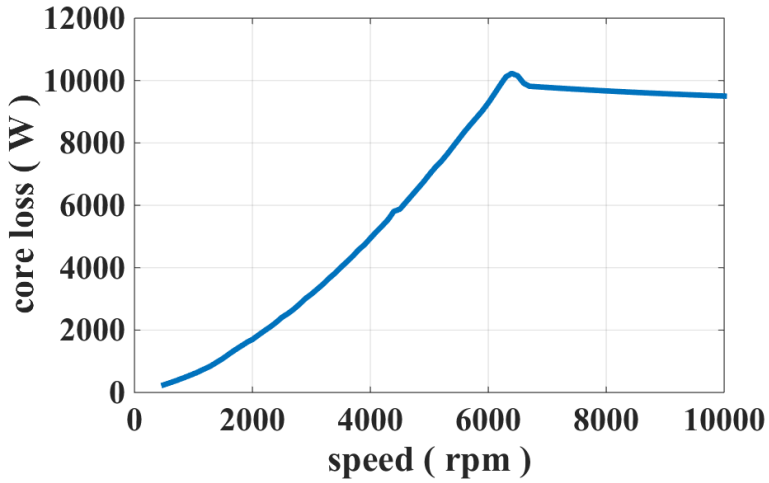

Figure 6-12 Core losses of the optimized machine versus speed

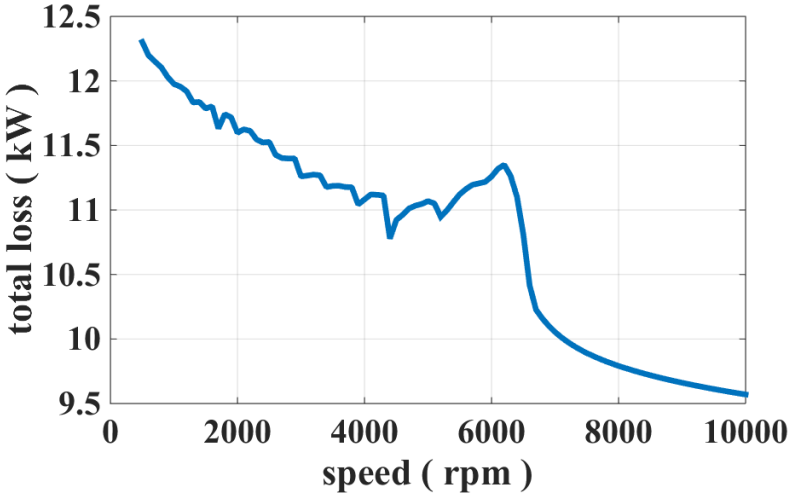

Figure 6-13 Total losses of the optimized machine versus speed

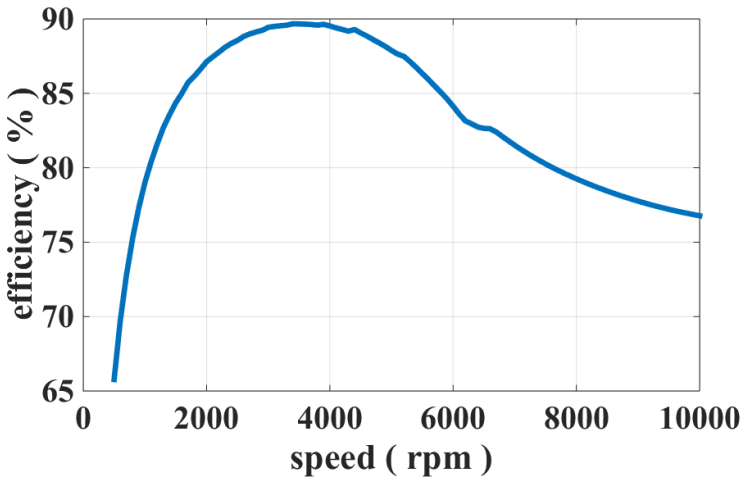

Figure 6-14 Efficiency of the optimized machine versus speed

It can be easily understood form the figures that copper losses of the machine are reduced by increasing the rotational speeds. At higher rotational speeds rise time and fall time of the current will be considerable in comparison with the time in which motor operates in the chopping mode. Furthermore, number of chopping actions is decreased by increasing rotational speed of the machine. Therefore, RMS value of the input current is decreased and consequently copper losses are reduced.

On the other hand, by increasing the rational speed, core losses are increased. At higher speeds, the motor operates at a higher frequency. Hence, core losses will be increased. Another point that has to be taken into account is reduction of core losses after 6400 rpm. After this rotational speed the current cannot reach to its maximum chopping value and consequently magnetic flux density inside the core is reduced. So, although the frequency is increased by increasing rotational speed, core losses of the machine is reduced with a very smooth pace.

Because increasing rotational speed leads to increment in core losses and reduction of copper losses of the machine. So, total losses of the switched reluctance motor gain its minimum value at 4400 rpm. However, efficiency-speed characteristic of the machine reaches to its maximum value at 3500 rpm. This is because of the difference in output powers of the SRM developed at 3500 rpm (97 kW) and 4400 rpm (90 kW).

As it can be easily understood form the figures, the optimized motor has an acceptable range of efficiency in the desired speed range of 1200-6000 rpm. The motor reaches its maximum possible efficiency (approximately 90 %) at 3500 rpm. However, it has to be noticed that the motor delivers output power of 97 kW at this rotational speed. The required 50 kW power can then be easily achieved by controlling chopping current values and decreasing RMS value of the input current. In this case, copper losses and core losses of the SRM will be considerably reduced due to reductions in RMS current and magnetic flux density in the core. Hence, efficiency will be higher. In order to validate this claim, the optimized SRM is simulated at 3500 rpm using both analytical calculations and Finite Element method. Maximum and minimum chopping current values are controlled in a way that the motor delivers output power of 50 kW.

Table 6-35 Chopping circuit specifications of optimized SRM at 3500 rpm

I_{max}	110.8 A
I_{min}	102.3 A
speed	3500 rpm
DC voltage	500 V

Table 6-36 includes analytical calculations and FEM simulations results of the optimized SRM at 3500 rpm. Chopping current values are selected in a way that (Table 6-35) the motor develops 50 kW at this rotational speed.

Table 6-36 Performance calculation results of optimized SRM at 3500 rpm

	Speed (rpm)	Average torque (N.m.)	Output power (kW)	RMS Current (A)	Copper loss (kW)	Core loss (W)	Total loss (kW)	Input power (kW)	efficiency
Analytical calculations	3500	137.5	50.4	62.19	1.06	3000	4.05	54.46	92.5
FEM simulations with normal steel	3500	142.5	52.2	66.75	1.21	2600	3.81	56.01	93.2

As it can be easily seen from the table, the motor is capable of developing 50 kW at rotational speed of 3500 rpm while having an approximate efficiency of 93 %. It has to be noticed that measured efficiency of the existing machine at 3500 rpm is approximately 93 % [4, 22]. So, the optimized motor has the same efficiency as the existing one while developing the same output power.

The same performance calculations are carried out at 6000 rpm using both analytical method and FE simulations. The SR motor is capable of developing maximum output power of 60 kW at 6000 rpm (see Figure 6-10) when the motor is operating under drive characteristics given in Table 6-18. It has to be noticed that maximum and minimum chopping currents are decreased so that the motor develops output power of 50 kW. Drive circuit characteristics are given in Table 6-37.

Table 6-37 Performance calculation results of optimized SRM at 6000 rpm

I_{max}	78.6 A
I_{min}	72.5 A
speed	6000 rpm
DC voltage	500 V

Phase RMS current of the SR motor and loss and efficiency calculation results at 6000 rpm are given in Table 6-38.

Table 6-38 Performance calculation results of optimized SRM at 6000 rpm

	Speed (rpm)	Average torque (N.m.)	Output power (kW)	RMS Current (A)	Copper loss (kW)	Core loss (W)	Total loss (kW)	Input power (kW)	efficiency
Analytical calculations	6000	79.1	49.7	126.5	0.466	6300	6.76	56.46	88
FEM simulations with normal steel	6000	82.3	51.7	141.1	0.519	5900	6.42	58.1	89

It can be concluded from the table that the motor has the efficiency of 89 % at rotational speed of 6000 rpm while output power is 50 kW. Measured efficiency of the existing SR motor is about 90 % at 6000 rpm [4, 22]. Comparing efficiency calculations of the optimized motor at two rotational speeds of 3500 rpm and 6000 rpm with the efficiency of the existing prototype in the literature shows that both motors have same efficiencies at these speeds while developing the constant output power of 50 kW. However, as discussed earlier, torque density (torque per motor active mass) of the optimized motor has been increased about 13.5 %.

6.5.3 Comparison of torque-speed characteristics

In this section torque-speed and power-speed characteristics of both existing SRM and the optimized machine which were computed in previous sections, are plotted in the same graph to investigate the possible improvements in torque speed characteristic of the optimized switched reluctance motor. Figure 6-15 and Figure 6-16 represent torque-speed and output power-speed characteristics of both existing motor and the optimized 18/12 SRM. Furthermore, the green line in the figures depicts the border for output power of 50 kW for different rotational speeds. In other words, torque speed and power speed characteristics of the SRM have to be above the green line to achieve the desired output power of 50 kW.

As it is obvious form the figures, there is an improvement in torque speed characteristic of the motor especially at speed range of 500-5600 rpm. Although in the small speed range of 5600-6000 rpm optimized machine develops lower torque than the existing one, the developed power is above the desired level of 50 kW. It has to be noticed that desired operating range of the machine is between 1200 rpm and 6000 rpm. Thus, it can be concluded that torque developing capability of the machine has been improved at the desired speed range.

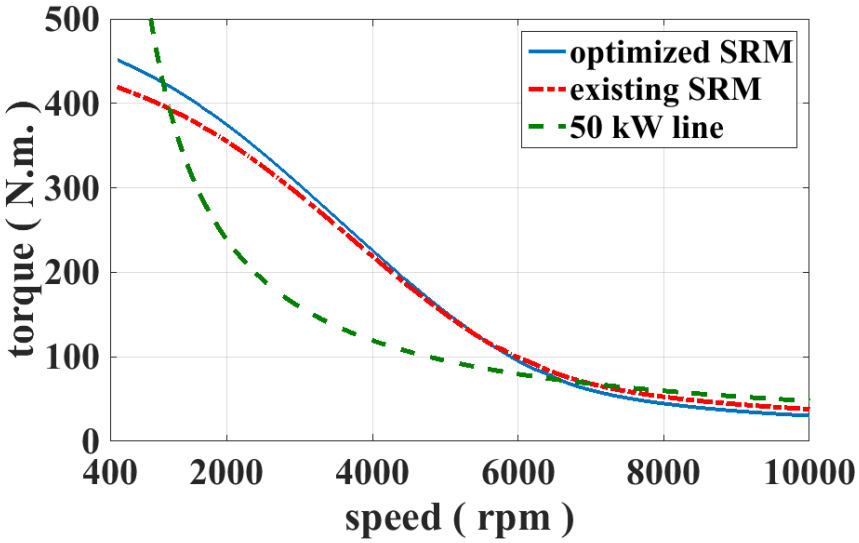

Figure 6-15 Comparison of torque-speed characteristics of existing and optimized motors

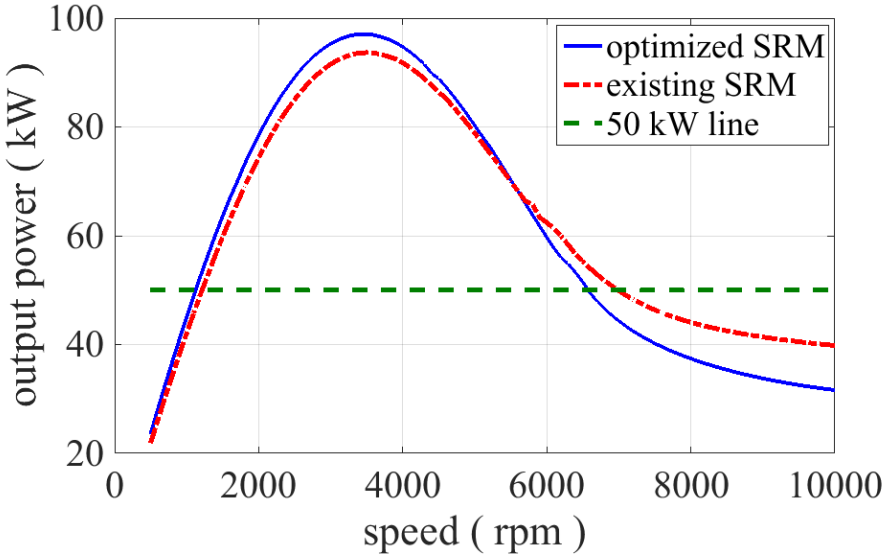

Figure 6-16 Comparison of output power-speed characteristics of existing and optimized motors

It has to be taken into account that the existing SRM delivers 45.7 kW at 1200 rpm, and cannot reach the desired output power 50kW. This problem has been effectively solved for the optimized machine using the proposed optimization method in this study. As mentioned earlier, the optimized motor is capable of developing 49

kW at 1200 rpm. Hence, there is a considerable improvement in torque density of the machine at 1200 rpm.

CHAPTER 7

CONCLUSIONS AND FUTURE WORKS

7.1 Conclusions

The aim of this thesis is to seek an optimum N_s/N_r ratio for a 50 kW electric vehicle motor. For seeking the optimum stator pole to rotor pole ratio, an accurate analytical performance calculation is highly desirable. For this purpose, a previously developed approach for analytical performance prediction of SR motors based on normalized air gap permeance and force data is used with some modifications. In this study, it is found that the pole leakage flux is very important for accurately predicting the flux-linkage versus flux density characteristics of a given doubly-salient geometry. An approach is presented for taking this factor into account and its accuracy is illustrated using numerical field solution.

In order to validate the proposed analytical model, two switched reluctance motors are simulated using finite element method. First SRM is an 8/6 motor existing at Electrical and Electronics Department laboratory of METU which is used for washing machine applications known as SRM1. The second one, is a 50 kW, 18/12 switched reluctance motor employed in hybrid electric vehicle applications known as SRM2. Comparison of measurement data and FEM simulation results with analytical computations illustrated the accuracy of the proposed method.

Once the accuracy of the model is validated, it is implemented for optimization purposes. For this purpose, a general design methodology is given which can be employed in designing any kinds of switched reluctance motors to be used in variety of applications. Finally, Genetic Algorithm optimization method is implemented to determine optimum pole combination, geometry and excitation pattern for switched reluctance motors to be used in a specific HEV application. It is noticeable that the

proposed optimization method is universal and can be used in optimizing switched reluctance motors for other applications. Selecting normalized independent variables for optimization problem guarantees the generality of the optimization method.

At the end, it is concluded that 18/12 pole combination gives the highest torque in comparison with other pole combinations. Variations of some geometric and performance characteristics of optimized switched reluctance motors are also investigated for different pole combinations. The optimized motor is simulated using FEM, and comparing the results again proved that the analytical method used is suitable for optimization purposes. It has to be mentioned that selected pole combination for existing prototype machine is also 18/12. However, comparison of calculation results for both optimized and existing motors shows that the optimized one can develop more torque per motor active mass. It is found that the motor active mass is reduced by 5.6 % and 13.5 % increase in torque density (torque per motor active mass) at 1200 rpm is observed, which is a considerable amount. Namely the existing motor can deliver an approximate output power of 45.7 kW at 1200 rpm, while the optimized one is capable of developing 49 kW at this specified rotational speed. Furthermore, there are also slight improvements in motor efficiency.

7.2 Future works

As a future work, following suggestions can be considered.

1. An important and vital issue is to investigate why at some N_s/N_r ratio values very little torque density is obtained. There is a possibility that the analytical model fails at these pole numbers or there is a problem with the way the optimization problem is set.

2. Modifying the basic geometry, which is used to produce the normalized date sets, in a way that takes the effect of pole leakage flux into account. For this purpose the excited MMF can be placed only on the middle and upper tooth.

3. Consideration of a multi-objective optimization problem with an objective function which takes into account other geometric and performance characteristics of the SR motor (efficiency, weight, etc.).

4. Another optimization can be carried out by consideration of developed torque of the SR motor at several rotational speeds as the objective function of the optimization.

5. Carrying out a thermal analysis by consideration of cooling type of the system (liquid cooling) and the insulation type in order to determine the operating temperature of the SR motor.

6. Investigating the effect of difference in B-H curves of the materials in analytical performance calculations

7. Investigating the effect of acoustic noise on SR motor performance based on the produced normalized data sets (normal force).

REFERENCES

[1] R. Krishnan, *Switched reluctance motor drives: modeling, simulation, analysis, design, and applications*: CRC press, 2001.

[2] P. Lawrenson, J. Stephenson, P. Blenkinsop, J. Corda, and N. Fulton, "Variable-speed switched reluctance motors," *Electric Power Applications, IEE Proceedings B,* vol. 127, pp. 253-265, 1980.

[3] K. Kiyota, T. Kakishima, and A. Chiba, "Cylindrical rotor design for acoustic noise and windage loss reduction in switched reluctance motor for HEV applications," in *Energy Conversion Congress and Exposition (ECCE), 2014 IEEE*, 2014, pp. 1814-1821.

[4] A. Chiba, K. Kiyota, N. Hoshi, M. Takemoto, and S. Ogasawara, "Development of a rare-earth-free SR motor with high torque density for hybrid vehicles," *Energy Conversion, IEEE Transactions on,* vol. 30, pp. 175-182, 2015.

[5] K. M. Rahman and S. E. Schulz, "Design of high-efficiency and high-torque-density switched reluctance motor for vehicle propulsion," *Industry Applications, IEEE Transactions on,* vol. 38, pp. 1500-1507, 2002.

[6] A. Chiba, Y. Takano, M. Takeno, T. Imakawa, N. Hoshi, M. Takemoto, *et al.*, "Torque density and efficiency improvements of a switched reluctance motor without rare-earth material for hybrid vehicles," *Industry Applications, IEEE Transactions on,* vol. 47, pp. 1240-1246, 2011.

[7] H. B. Ertan and K. Leblebicioğlu, "Optimum geometry for torque ripple minimization of switched reluctance motors," *Energy Conversion, IEEE Transactions on,* vol. 15, pp. 30-39, 2000.

[8] F. Sahin, "Optimum geometry for torque ripple minimization of switched reluctance motors," Master, Electrical and Electronics Engineering, Middle East Technical University, 1996.

[9] E. Bizkevelci, "A control algorithm to minimize torque ripple and acoustic noise of switched reluctance motors," Ph.D., Electrical and Electronics Engineering, Middle East Technical University, 2008.

[10] E. Bizkevelci, H. B. Ertan, and K. Leblebicioglu, "A novel noise reduction technology for switched reluctance motors," in *Power and Energy Society General Meeting-Conversion and Delivery of Electrical Energy in the 21st Century, 2008 IEEE*, 2008, pp. 1-4.

[11] J. Gao, H. Sun, L. He, Y. Dong, and Y. Zheng, "Optimization design of switched reluctance motor based on particle swarm optimization," in *Electrical Machines and Systems (ICEMS), 2011 International Conference on*, 2011, pp. 1-5.

[12] C. Ma and L. Qu, "Multiobjective Optimization of Switched Reluctance Motors Based on Design of Experiments and Particle Swarm Optimization," *Energy Conversion, IEEE Transactions on*, vol. 30, pp. 1144-1153, 2015.

[13] P. Rafajdus, A. Peniak, D. Peter, P. Makys, and L. Szabo, "Optimization of switched reluctance motor design procedure for electrical vehicles," in *Optimization of Electrical and Electronic Equipment (OPTIM), 2014 International Conference on*, 2014, pp. 397-404.

[14] X. Xue, K. W. E. Cheng, T. W. Ng, and N. C. Cheung, "Multi-objective optimization design of in-wheel switched reluctance motors in electric vehicles," *Industrial Electronics, IEEE Transactions on*, vol. 57, pp. 2980-2987, 2010.

[15] X. Xue, K. Cheng, and N. Cheung, "Selection of electric motor drives for electric vehicles," in *Power Engineering Conference, 2008. AUPEC'08. Australasian Universities*, 2008, pp. 1-6.

[16] K. Ohyama, M. Naguib, F. Nashed, K. Aso, H. Fujii, and H. Uehara, "Design using finite element analysis of a switched reluctance motor for electric vehicle," *Journal of Power Electronics*, vol. 6, pp. 163-171, 2006.

[17] N. Schofield, S. A. Long, D. Howe, and M. McClelland, "Design of a switched reluctance machine for extended speed operation," *IEEE Transactions on industry applications*, vol. 45, pp. 116-122, 2009.

[18] K. Watanabe, S. Aida, A. Komatsuzaki, and I. Miki, "Driving force characteristics of 40kW switched reluctance motor for electric vehicle," in *Electrical Machines and Systems, 2007. ICEMS. International Conference on*, 2007, pp. 1894-1898.

[19] P. A. Watterson, W. Wu, B. A. Kalan, H. C. Lovatt, G. Prout, J. B. Dunlop, *et al.*, "A switched-reluctance motor/generator for mild hybrid vehicles," in *Electrical Machines and Systems, 2008. ICEMS 2008. International Conference on*, 2008, pp. 2808-2813.

[20] M. D. Hennen, M. Niessen, C. Heyers, H. J. Brauer, and R. W. De Doncker, "Development and control of an integrated and distributed inverter for a fault tolerant five-phase switched reluctance traction drive," *IEEE Transactions on Power Electronics*, vol. 27, pp. 547-554, 2012.

[21] J. M. Miller, A. R. Gale, P. J. McCleer, F. Leonardi, and J. H. Lang, "Starter-alternator for hybrid electric vehicle: comparison of induction and variable reluctance machines and drives," in *Industry Applications Conference, 1998. Thirty-Third IAS Annual Meeting. The 1998 IEEE*, 1998, pp. 513-523.

[22] M. Takeno, A. Chiba, N. Hoshi, S. Ogasawara, M. Takemoto, and M. A. Rahman, "Test Results and Torque Improvement of the 50-kW Switched Reluctance Motor Designed for Hybrid Electric Vehicles," *IEEE Transactions on Industry Applications*, vol. 48, pp. 1327-1334, 2012.

[23] M. Moallem and C.-M. Ong, "Predicting the steady-state performance of a switched reluctance machine," *Industry Applications, IEEE Transactions on*, vol. 27, pp. 1087-1097, 1991.

[24] G. Ptakh, D. Zvezdunov, R. Mustafaev, and A. Ykovenko, "Static torque of high power switched reluctance motor: Calculation and experiment," in *Transportation Electrification Asia-Pacific (ITEC Asia-Pacific), 2014 IEEE Conference and Expo*, 2014, pp. 1-3.

[25] R. Gobbi, N. C. Sahoo, and R. Vejian, "Experimental investigations on computer-based methods for determination of static electromagnetic characteristics of switched reluctance motors," *Instrumentation and Measurement, IEEE Transactions on,* vol. 57, pp. 2196-2211, 2008.

[26] T. J. E. Miller and M. McGilp, "Nonlinear theory of the switched reluctance motor for rapid computer-aided design," in *IEE Proceedings B-Electric Power Applications*, 1990, pp. 337-347.

[27] P. Chancharoensook and M. F. Rahman, "Magnetization and static torque characterization of a four-phase switched reluctance motor: experimental investigations," in *Power Electronics and Drive Systems, 2001. Proceedings., 2001 4th IEEE International Conference on*, 2001, pp. 456-460.

[28] H. Ertan, "Analytical prediction of torque and inductance characteristics of identically slotted doubly-salient reluctance motors," *Electric Power Applications, IEE Proceedings B,* vol. 133, pp. 230-236, 1986.

[29] N. Besenek, "Numerically calculated force and permeance data for doubly salient geometries," Master, Electrical and Electronics Engineering, Middle East Technical University, 1988.

[30] I. Mahariq, "A NORMALIZED SET OF FORCE AND PERMEANCE DATA FOR DOUBLY-SALIENT MAGNETIC GEOMETRIES," MIDDLE EAST TECHNICAL UNIVERSITY, 2009.

[31] P. P. Acarnley, *Stepping motors: a guide to theory and practice*: Iet, 2002.

[32] J. Faiz, G. Shahgholian, and H. Ghazizadeh, "Analysis of dynamic behavior of switched reluctance motor-design parameters effects," in *MELECON 2010-2010 15th IEEE Mediterranean Electrotechnical Conference*, 2010, pp. 532-537.

[33] S.-M. Jang, D.-J. You, Y.-H. Han, and J.-P. Lee, "Analytical design and dynamic characteristics of switched reluctance motor with minimum torque ripple," in *Electrical Machines and Systems, 2007. ICEMS. International Conference on*, 2007, pp. 1236-1239.

[34] J.-Y. Lee, B.-K. Lee, T. Sun, J.-P. Hong, and W.-T. Lee, "Dynamic analysis of toroidal winding switched reluctance motor driven by 6-switch converter," *Magnetics, IEEE Transactions on,* vol. 42, pp. 1275-1278, 2006.

[35] H. B. Ertan and L. Yalciner, "Performance calculation of SR motors for optimum design and a washing machine application," in *Electrical Machines, 2008. ICEM 2008. 18th International Conference on*, 2008, pp. 1-6.

[36] W. M. Chan and W. Weldon, "Development of a simple nonlinear switched reluctance motor model using measured flux linkage data and curve fit," in *Industry Applications Conference, 1997. Thirty-Second IAS Annual Meeting, IAS'97., Conference Record of the 1997 IEEE,* 1997, pp. 318-325.

[37] S. Mir, I. Husain, and M. E. Elbuluk, "Switched reluctance motor modeling with on-line parameter identification," *Industry Applications, IEEE Transactions on,* vol. 34, pp. 776-783, 1998.

[38] S. Sadeghi, J. Milimonfared, M. Mirsalim, and M. Jalalifar, "Dynamic Modeling and Simulation of a Switched Reluctance Motor in Electric Vehicles," in *Industrial Electronics and Applications, 2006 1ST IEEE Conference on*, 2006, pp. 1-6.

[39] Q. Yu, B. Bilgin, and A. Emadi, "Loss and Efficiency Analysis of Switched Reluctance Machines Using a New Calculation Method," *Industrial Electronics, IEEE Transactions on,* vol. 62, pp. 3072-3080, 2015.

[40] K. Nakamura, S. Fujio, and O. Ichinokura, "A Method for Calculating Iron Loss of a Switched Reluctance Motor Based on Reluctance Network Analysis," in *Power Electronics and Motion Control Conference, 2006. EPE-PEMC 2006. 12th International*, 2006, pp. 1021-1026.

[41] Y. Hayashi and T. J. Miller, "A new approach to calculating core losses in the SRM," *Industry Applications, IEEE Transactions on,* vol. 31, pp. 1039-1046, 1995.

[42] P. Rafajdus, V. Hrabovcova, and P. Hudak, "Investigation of losses and efficiency in switched reluctance motor," in *Power Electronics and Motion*

Control Conference, 2006. EPE-PEMC 2006. 12th International, 2006, pp. 296-301.

[43] N. K. Sheth and K. Rajagopal, "Estimation of Core Loss in a Switched Reluctance Motor Based on Actual Flux Variations," in *Power Electronics, Drives and Energy Systems, 2006. PEDES'06. International Conference on*, 2006, pp. 1-5.

[44] J. C. Akiror and P. Pillay, "On the coefficients of core loss formulas for electrical machines," in *IECON 2012-38th Annual Conference on IEEE Industrial Electronics Society*, 2012, pp. 1927-1933.

[45] Y. Chen and P. Pillay, "An improved formula for lamination core loss calculations in machines operating with high frequency and high flux density excitation," in *Industry Applications Conference, 2002. 37th IAS Annual Meeting. Conference Record of the*, 2002, pp. 759-766.

[46] T. L. Mthombeni and P. Pillay, "Physical basis for the variation of lamination core loss coefficients as a function of frequency and flux density," in *IEEE Industrial Electronics, IECON 2006-32nd Annual Conference on*, 2006, pp. 1381-1387.

[47] G. Novak, J. Kokosar, A. Nagode, and D. S. Petrovic, "Core-loss prediction for non-oriented electrical steels based on the steinmetz equation using fixed coefficients with a wide frequency range of validity," *Magnetics, IEEE Transactions on*, vol. 51, pp. 1-7, 2015.

[48] K. M. Rahman, B. Fahimi, G. Suresh, A. V. Rajarathnam, and M. Ehsani, "Advantages of switched reluctance motor applications to EV and HEV: design and control issues," *Industry Applications, IEEE Transactions on*, vol. 36, pp. 111-121, 2000.

[49] Š. Mašić, S. Smaka, I. Salihbegović, and M. Ćosović, "The effects of magnetic circuit geometry on characteristics of switched reluctance motors," in *Electric Machines & Drives Conference (IEMDC), 2011 IEEE International*, 2011, pp. 1427-1432.

[50] W. Jazdzynski and M. Majchrowicz, "An Approach to Find an optimum Designed SRM for electric vehicle drive," in *Electrical Machines, 2008. ICEM 2008. 18th International Conference on*, 2008, pp. 1-6.

[51] T. Kosaka, A. Kume, H. Wakayama, and N. Matsui, "Development of high torque density and efficiency vswitched reluctance motor with 0.1 mm short airgap," in *Power Electronics and Applications, 2007 European Conference on*, 2007, pp. 1-9.

[52] J.-H. Choi, S. Kim, J.-M. SHIN, J. LEE, and S.-T. KIM, "The multi-object optimization of switched reluctance motor," in *Electrical Machines and Systems, 2003. ICEMS 2003. Sixth International Conference on*, 2003, pp. 195-198.

[53] J. Faiz and J. W. Finch, "Aspects of design optimisation for switched reluctance motors," *Energy Conversion, IEEE Transactions on,* vol. 8, pp. 704-713, 1993.

[54] Y. Li and D. C. Aliprantis, "Optimum stator tooth shapes for torque ripple reduction in switched reluctance motors," in *Electric Machines & Drives Conference (IEMDC), 2013 IEEE International*, 2013, pp. 1037-1044.

[55] Y. Ohdachi, Y. Kawase, Y. Miura, and Y. Hayashi, "Optimum design of switched reluctance motors using dynamic finite element analysis," *Magnetics, IEEE Transactions on*, vol. 33, pp. 2033-2036, 1997.

[56] S. Song, M. Zhang, L. Ge, and L. Wang, "Multiobjective Optimal Design of Switched Reluctance Linear Launcher," *Plasma Science, IEEE Transactions on*, vol. 43, pp. 1339-1345, 2015.

[57] N. Abdullah, K. Abdul Karim, R. Firdaus, M. Mohd Jamil, and M. Othman, "DESIGN OF SWITCHED RELUCTANCE MOTOR USING FINITE ELEMENT METHOD," *Science International*, vol. 26, 2014.

[58] M. Anwar, I. Husain, and A. V. Radun, "A comprehensive design methodology for switched reluctance machines," *Industry Applications, IEEE Transactions on*, vol. 37, pp. 1684-1692, 2001.

[59] J. Rizk, M. Nagrial, and A. Hellany, "Design and performance of switched reluctance motors," in *The 4th International Power Electronics and Motion Control Conference, 2004. IPEMC 2004.*, 2004.

[60] H. Sahraoui, H. Zeroug, and H. Toliyat, "Switched reluctance motor design using neural-network method with static finite-element simulation," *Magnetics, IEEE Transactions on,* vol. 43, pp. 4089-4095, 2007.

[61] T. Wichert, "Design and construction modifications of switched reluctance machines," 2008.

[62] P. Vijayraghavan, "Design of switched reluctance motors and development of a universal controller for switched reluctance and permanent magnet brushless DC motor drives," Virginia Polytechnic Institute and State University, 2001.

[63] B. Ertan, "Prediction of static torque of step motors," Ph.D., Electrical and Electronics Engineering, University of Leeds, 1977.

[64] Y. GÖYNÜK, "Development of an electrical machines analysis And optimum design software package," MIDDLE EAST TECHNICAL UNIVERSITY, 2008.

[65] L. B. Yalciner, "A software for analysis and design optimization of switched reluctance motor," Master, Electrical and Electronics Engineering, Middle East Technical University, 2004.

[66] T. C. O'Connell, *An investigation of boundary-based field analysis methods for electric machines: The Schwarz-Christoffel and boundary element methods*: ProQuest, 2008.

[67] M. Beale, M. Hagan, and H. Demuth, "MATLAB Neural Network Toolbox™ User's Guide, MathWorks, Version 8.0. 1 (Release 2013a)," 2013.

[68] B. Hudson, M. Hagan, and H. Demuth, "Neural Network Toolbox for Use with MATLAB," *User's Guide, the Math works,* 2012.

[69] M. Tohumcu, "Optimum design of switching reluctance motors," Ph.D., Electrical and Electronics Engineering, Middle East Technical University, 1985.

[70] P. N. Materu and R. Krishnan, "Estimation of switched reluctance motor losses," *IEEE Transactions on Industry Applications*, vol. 28, pp. 668-679, 1992.

[71] E. O. Brigham and E. O. Brigham, *The fast Fourier transform* vol. 7: Prentice-Hall Englewood Cliffs, NJ, 1974.

[72] H. J. Nussbaumer, *Fast Fourier transform and convolution algorithms* vol. 2: Springer Science & Business Media, 2012.

[73] Y. Takano, M. Takeno, N. Hoshi, A. Chiba, M. Takemoto, S. Ogasawara, *et al.*, "Design and analysis of a switched reluctance motor for next generation hybrid vehicle without PM materials," in *Power Electronics Conference (IPEC), 2010 International*, 2010, pp. 1801-1806.

[74] Y. Takano, T. Maeda, M. Takeno, A. Chiba, N. Hoshi, M. Takemoto, *et al.*, "Operating area of a switched reluctance motor with continuous current operation," in *Power and Energy Society General Meeting, 2010 IEEE*, 2010, pp. 1-4.

[75] T. Suzuki, S. Ito, N. Tanaka, A. Chiba, T. Fukao, and H. Ninomiya, "Development of high-efficiency switched reluctance motor," *Electrical Engineering in Japan*, vol. 162, pp. 73-82, 2008.

[76] M. Takeno, S. Ogasawara, A. Chiba, M. Takemoto, and N. Hoshi, "Power and efficiency measurements and design improvement of a 50kW switched reluctance motor for Hybrid Electric Vehicles," in *2011 IEEE Energy Conversion Congress and Exposition*, 2011, pp. 1495-1501.

[77] T. J. E. Miller, *Switched reluctance motors and their control*: Magna Physics Pub., 1993.

[78] K. Bieńkowski, J. Szczypior, A. Rogalski, B. Bucki, and A. Biernat, "Influence of geometrical parameters of Switched Reluctance Motor on electromagnetic torque," in *Proceedings of XVI International Conference of Electrical Machines, Kraków*, 2004, pp. 5-8.

[79] J. Corda and J. Stephenson, "Analytical estimation of the minimum and maximum inductances of a double salient motor," in *International Conference on Stepping Motors and Systems*, 1979, pp. 50-59.

[80] H. B. Ertan and L. B. Yalciner, "An analytical approach for the calculation of flux-linkage including end-effect for SR motors," in *Power Electronics, Electrical Drives, Automation and Motion, 2008. SPEEDAM 2008. International Symposium on*, 2008, pp. 307-311.

APPENDIX A

MATERIAL PROPERTIES

A.1 M36 steel (24 Gauge, 0.63 mm laminations)

1. B-H curve

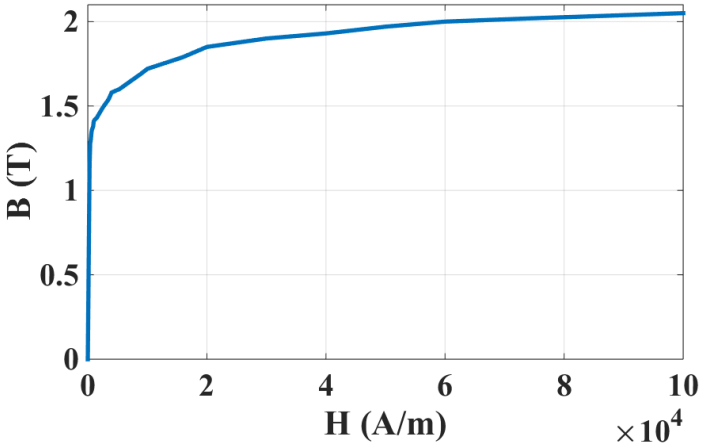

Figure A-1 B-H curve of M36 steel

Table A-1 B-H curve values of M36 steel

0	0
200	1.06
400	1.28
600	1.34
1000	1.41
4000	1.58
10000	1.72
20000	1.85
30000	1.9
60000	2

2. Core loss curves

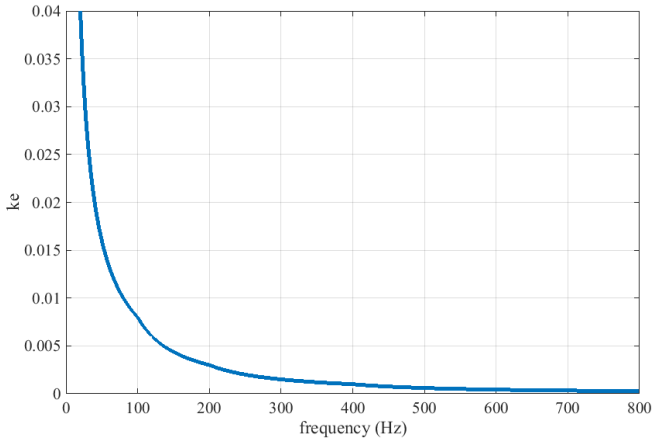

Figure A-2 k_e approximation versus frequency

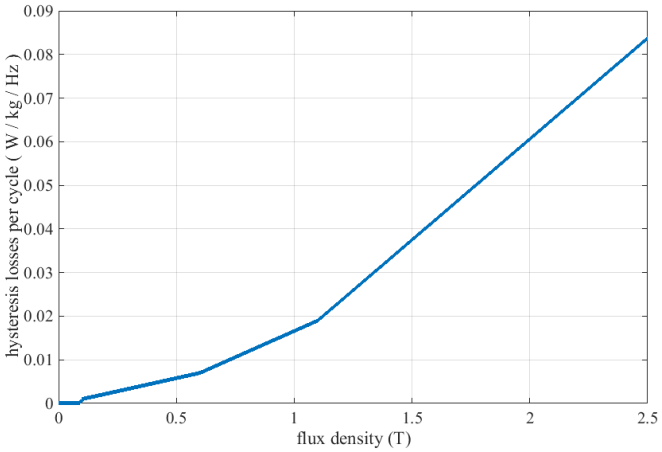

Figure A-3 Hysteresis losses per cycle versus flux density approximation

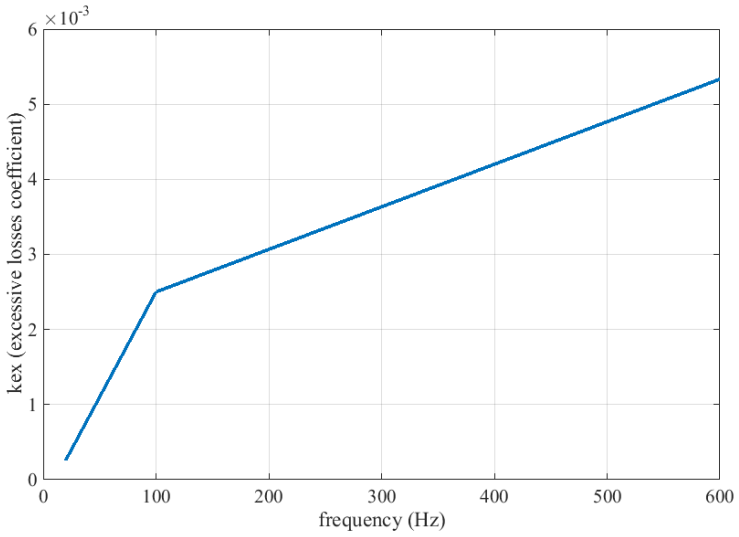

Figure A-4 k_{ex} approximation versus frequency

A.2 10JNEX900 (0.1 mm laminations)

1. B-H curve

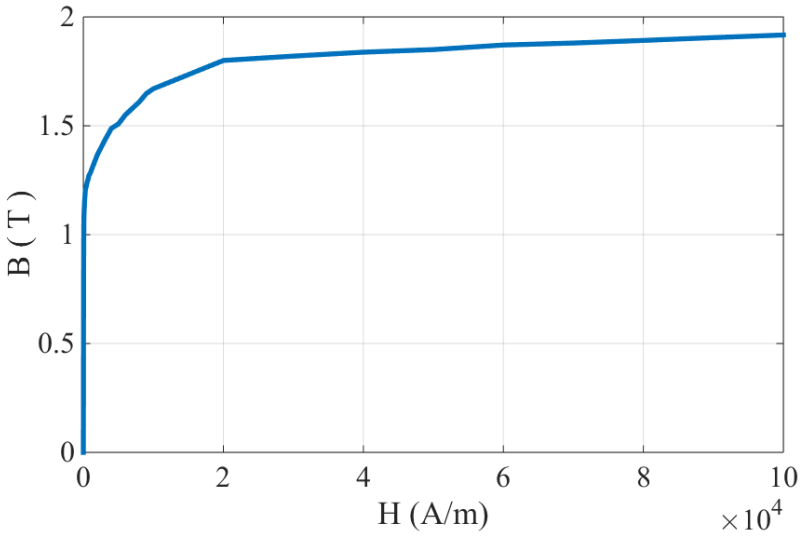

Figure A-5 B-H curve of 10JNEX900

Table A-2 B-H curve values of 10JNEX900

H (A/m)	B (T)	H (A/m)	B (T)
0	0	2000	1.367
30	0.69	4000	1.488
40	0.85	5000	1.508
60	1	7000	1.58
70	1.04	9000	1.65
90	1.09	10000	1.67
200	1.167	30000	1.82
300	1.21	50000	1.85
500	1.234	70000	1.88
800	1.27	90000	1.905
1000	1.284	100000	1.917

2. Core loss curve

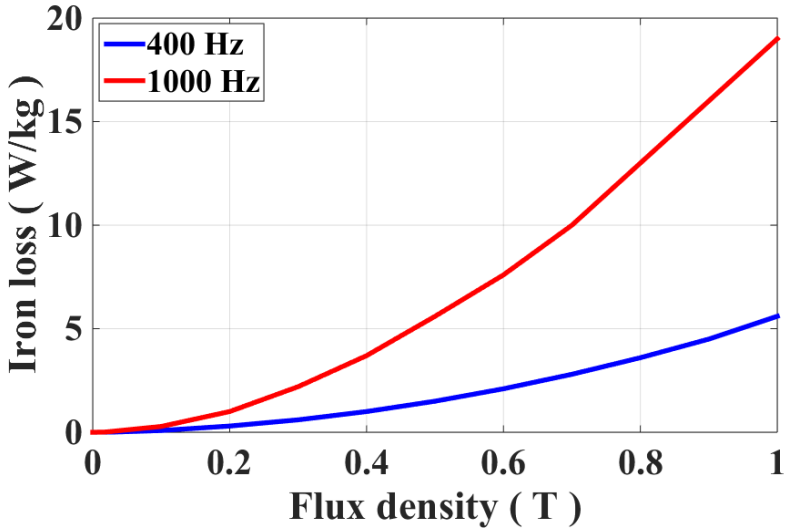

Figure A-6 Core loss curves of 10JNEX900

APPENDIX B

A NOTE ON END FRINGING CORRECTION

B.1 Comparison of end fringing flux linkage data at OUT position and I=3A

Modified flux linkage value is computed for SRM1 at a sample point of I=3A and OUT position using a FEM based method. For this purpose, the basic geometry which is used to obtain normalized data is modified to have λ/g and t/λ of SRM1 in FEM. Average pole flux density is calculated in OUT position while windings are excited with I=3A. It has to be noticed that air gap length is 0.217 mm in the equivalent basic geometry of the test motor. Average flux density is found to be 0.83 T in OUT position.

Now an equivalent air gap length of this geometry in IN position has to be determined in which the geometry has the same average flux density (0.83 T) and same normalized permeance. So, air gap length is increased up to g_f =2.034 mm to reach the same flux density value. Note that equivalent air gap length is calculated using a finite element based software.

At this stage effective length of the core can be simply calculated using Carter's coefficient.

$$\frac{g_f}{g} = \frac{2.034}{0.217} = 9.37 \tag{B-1}$$

$$\sigma = 0.9257 \tag{B-2}$$

$$L_{cf} = L + 2n(1-\sigma) = 40.4 + 2 \times 40 \times g \times (1-0.9257) = 42.33 \tag{B-3}$$

So, flux linkage value of the test SRM is changed by 4.78 %.

Percent of change=L_{cf} / L =42.33/40.4= 1.0478 (4.78 % increment)

Analytical calculations give flux linkage of 0.14 at OUT position and I=3A without taking fringing flux effect into account. So, by entering fringing flux effect into calculations flux linkage at this position will be increased by 4.78 %.

$$\text{Flux linkage} = 0.14 \times 1.0478 = 0.1466 \quad \text{(B-4)}$$

It has to be noticed that analytical calculations using MATLAB code gives modified flux linkage of 0.1463 which is in an excellent agreement with computed flux linkage value using a finite element based software.

B.2 Comparison of analytical end fringing correction results with the results in the literature

In a previous study, Levent Yalciner proposed a method for the calculation of end fringing effect on flux linkage characteristic of the SRM. This method is based on a work done by Corda and Stephenson [79]. The method is based on determination of an effective length for SRM core while the rotor is in fully aligned position. In other positions, an equivalent air gap length can be determined to convert the model to an equivalent model in IN position. Then, the effective core length can be calculated. The method is explained in details in [80].

When the software prepared for this purpose is investigated, it is found that there are some discrepancies between analytically obtained results in this study and the results in the literature. Following figure reveals analytical flux linkage data without and with end fringing modifications, measurements, and modified flux linkage data obtained by Levent Burak Yalciner and Yilmaz Goynuk [64, 65].

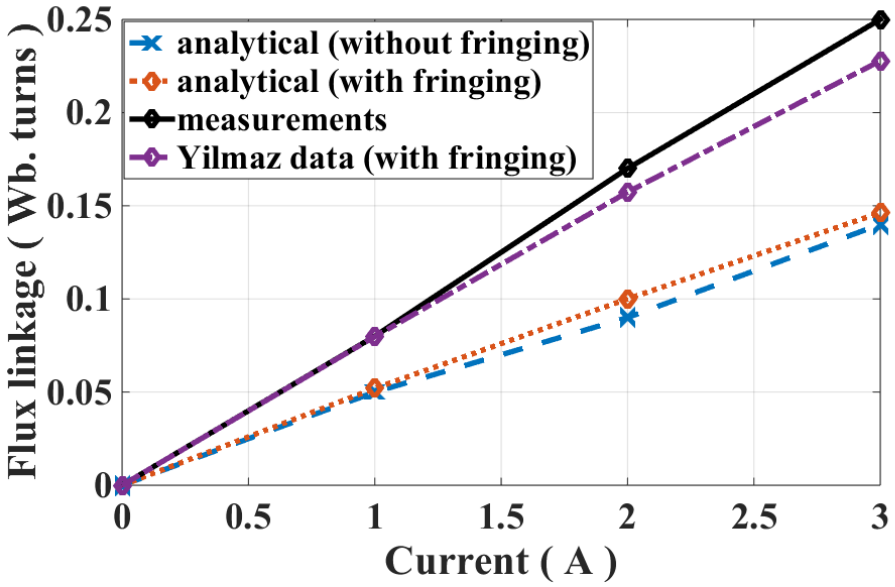

Figure B-1 Effect of end fringing flux and comparison with literature

It can be simply concluded that modified results in this study and modified flux linkage data in the literature are not in agreement. It is proved in this study that this discrepancy between analytical calculations in this study and the measurements is due to the flux leaking to two adjacent poles of an excite pole (slot leakage). A detailed discussion on this leakage flux is given in chapter 4. So, there has to be a problem in calculated modified flux linkage values in the literature. In order to prove this, Table B-1 is prepared which includes the percentage of change in flux linkage values due to fringing flux effect for various effective air gap lengths. Note that n is taken as 40g in analytical calculations. Furthermore, core length of SRM1 is 40.4 mm.

It is obvious that in a worst case scenario (I=3A and OUT position) effective air gap length is calculated to be 9.37g. So, maximum change in flux linkage value due to fringing flux effect can be around 5%. However, in the literature flux linkage values are changed about 50%. So, there is a problem in calculated analytical results in the literature [30, 64, 65, 80].

Table B-1 Percentage of change in flux linkage due to fringing flux effect for various effective air gap lengths

g_f	Sigma	2n (1-sigma) (mm)	L_{cf}	Change in flux linkage value (%)
g	0.992	0.208	40.608	0.51
2g	0.9841	0.4134	40.8134	1.02
5g	0.9602	1.0348	41.435	2.56
10g	0.9208	2.0592	42.459	5.1
20g	0.844	4.056	44.456	10.04
50g	0.6443	9.2482	49.648	22.89
100g	0.4295	14.833	55.23	36.71
500g	0.101	23.374	63.77	57.85
1000g	0.0508	24.679	65.08	61.1

APPENDIX C

SETS OF FORCE AND PERMEANCE DATA

1. $\lambda/g=40$

1.1. $t/\lambda =0.3$

Table C-1 Normalized data for $\lambda/g=40$, $t/\lambda =0.3$

X_n	MMF	B_t	P_n	F_t	F_n
0 (IN)	302	1.0557	0.3589	0	1576
	481	1.4925	0.3185	0	3150.9
	825	1.7661	0.2198	0	4364.5
	1235	1.9366	0.161	0	5160.2
0.2	302	0.8902	0.3026	102.6	1168.5
	481	1.3672	0.2918	249.8	2752
	825	1.701	0.2117	423.8	4173
	1235	1.8871	0.1569	572.2	4950.4
0.4	302	0.6522	0.2217	112.1	675.9
	481	1.0164	0.2169	283.2	1621.6
	825	1.4701	0.1829	713.2	2996.5
	1235	1.7287	0.1437	1054.1	3703.4
0.6	302	0.4054	0.1378	101.9	169.6
	481	0.6395	0.1365	249.7	408.2
	825	1.0558	0.1314	628.8	990.1
	1235	1.4756	0.1227	1095.8	1709.4
0.8	302	0.297	0.101	19.5	36.2
	481	0.473	0.101	49.3	91.9
	825	0.8106	0.1009	144.4	269.8
	1235	1.2095	0.1005	318.6	600.7
1 (OUT)	302	0.2783	0.0946	0	27.7
	481	0.4432	0.0946	0	70.1
	825	0.7603	0.0946	0	206.1
	1235	1.1362	0.0944	0	461.2

1.2. $t/\lambda = 0.4$

Table C-2 Normalized data for $\lambda/g=40$, $t/\lambda = 0.4$

X_n	MMF	B_t	P_n	F_t	F_n
0 (IN)	302	0.9993	0.4529	0	2076.2
	481	1.4545	0.4139	0	4399.6
	825	1.7322	0.2874	0	6200.9
	1235	1.8965	0.2102	0	7353.3
0.2	302	0.8762	0.3971	101.4	1670.3
	481	1.3503	0.3842	247.5	3966.8
	825	1.6786	0.2785	424.3	6050.9
	1235	1.8539	0.2055	579.4	7198.7
0.4	302	0.7006	0.3175	109.9	1183.1
	481	1.0940	0.3113	277.5	2874.6
	825	1.5101	0.2505	665.5	5116.6
	1235	1.7189	0.1905	1017.6	6063.8
0.6	302	0.5175	0.2346	111.4	683.8
	481	0.8073	0.2297	281.6	1641.4
	825	1.2023	0.1995	745	3121
	1235	1.5144	0.1678	1243.9	4169.7
0.8	302	0.3377	0.153	95.4	177.4
	481	0.5332	0.1517	233.4	427.9
	825	0.8838	0.1466	580.5	1047.9
	1235	1.2604	0.1397	1008.2	1873.9
1 (OUT)	302	0.2754	0.1248	0	54.5
	481	0.4386	0.1248	0	138.3
	825	0.7513	0.1246	0	406.1
	1235	1.12	0.1241	0	903.6

1.3. $t/\lambda = 0.5$

Table C-3 Normalized data for $\lambda/g=40$, $t/\lambda = 0.5$

X_n	MMF	B_t	P_n	F_t	F_n
0 (IN)	302	0.9644	0.5464	0	2574.1
	481	1.4291	0.5083	0	5656.8
	825	1.7108	0.3548	0	8073.3
	1235	1.8710	0.2592	0	9592.6
0.2	302	0.8673	0.4913	99.6	2170.3
	481	1.3392	0.4763	243.8	5181.7
	825	1.6652	0.3453	421.9	7942.1
	1235	1.834	0.2541	580.4	9477
0.4	302	0.7298	0.4134	106.8	1687.5
	481	1.1405	0.4057	269.2	4117.7
	825	1.5377	0.3189	616.1	7180
	1235	1.7217	0.2385	956.4	8432.4
0.6	302	0.5889	0.3336	105.5	1195.9
	481	0.9208	0.3275	266.8	2908.1
	825	1.3217	0.2741	704.5	5401.7
	1235	1.5615	0.2163	1146.7	6622.7
0.8	302	0.4555	0.2581	93.1	703.3
	481	0.7121	0.2533	235.4	1690.6
	825	1.0755	0.223	609.7	3263.6
	1235	1.4	0.1939	994.3	4559.1
1 (OUT)	302	0.3718	0.2106	0	326.5
	481	0.5849	0.2081	0	784.4
	825	0.9547	0.198	0	1887.8
	1235	1.3273	0.1839	0	3270.7

2. λ/g=70

2.1. t/λ =0.3

Table C-4 Normalized data for λ/g=70, t/λ=0.3

X_n	MMF	B_t	P_n	F_t	F_n
0 (IN)	175	1.0007	0.3354	0	1582.3
	220	1.248	0.3328	0	2461.7
	470	1.7529	0.2188	0	4794.3
	707	1.9329	0.1604	0	5715.2
0.2	175	0.7995	0.268	66.27	1132.4
	220	1.0016	0.2671	104.56	1778
	470	1.6284	0.2032	346.58	4522.7
	707	1.8247	0.1514	517.01	5331
0.4	175	0.54	0.181	70.06	623.4
	220	0.6762	0.1803	110.65	976.7
	470	1.207	0.1506	460.81	2719
	707	1.4938	0.1239	819.91	3452.1
0.6	175	0.2731	0.0916	63.76	98.8
	220	0.3424	0.0913	99.75	153.4
	470	0.7049	0.088	385.25	556.8
	707	1.0133	0.0841	701.35	987
0.8	175	0.1851	0.062	7.35	12.7
	220	0.2326	0.062	11.62	20.1
	470	0.4969	0.062	53.01	91.9
	707	0.7472	0.062	119.69	207.9
1 (OUT)	175	0.1732	0.058	0	9.7
	220	0.2177	0.058	0	15.3
	470	0.465	0.058	0	69.7
	707	0.6994	0.058	0	157.8

2.2. t/λ =0.4

Table C-5 Normalized data for λ/g=70, t/λ =0.4

X_n	MMF	B_t	P_n	F_t	F_n
0 (IN)	175	0.9615	0.4297	0	2088
	220	1.2018	0.4273	0	3263.2
	470	1.7206	0.2863	0	6642.6
	707	1.8922	0.2093	0	7944
0.2	175	0.8121	0.363	65.54	1642.2
	220	1.0176	0.3618	103.44	2581.3
	470	1.6255	0.2705	328.25	6442
	707	1.806	0.1998	504.71	7646.8
0.4	175	0.6207	0.2774	68.95	1141.1
	220	0.7778	0.2765	108.83	1793.1
	470	1.3435	0.2236	448.7	4965
	707	1.5548	0.1720	784.17	5891.8
0.6	175	0.4232	0.1891	69.84	626.9
	220	0.53	0.1884	110.33	982.4
	470	0.9524	0.1585	459.23	2733.4
	707	1.1968	0.1324	828.66	3504.8
0.8	175	0.2254	0.1008	61.43	101.4
	220	0.2827	0.1005	96.07	157.5
	470	0.5836	0.0971	368.37	575.7
	707	0.8425	0.0932	663.02	1029.5
1 (OUT)	175	0.1711	0.0765	0	19.2
	220	0.2151	0.0765	0	30.3
	470	0.4594	0.0765	0	138.2
	707	0.6907	0.0764	0	312.5

2.3. t/λ =0.5

Table C-6 Normalized data for λ/g=70, t/λ =0.5

X_n	MMF	B_t	P_n	F_t	F_n
0 (IN)	175	0.9366	0.5233	0	2589
	220	1.1721	0.5209	0	4055.9
	470	1.7002	0.3537	0	8503.2
	707	1.8671	0.2582	0	10179.6
0.2	175	0.8185	0.4573	64.7	2147.1
	220	1.026	0.456	102.06	3376.5
	470	1.6222	0.3374	311.19	8321.7
	707	1.7944	0.2481	491.92	9916.3
0.4	175	0.6687	0.3736	67.6	1652.2
	220	0.8384	0.3726	106.7	2598.7
	470	1.4176	0.2949	428.28	7095.3
	707	1.598	0.221	735.03	8312.5
0.6	175	0.5156	0.2881	67.4	1146.8
	220	0.6463	0.2872	106.44	1802.3
	470	1.1249	0.234	440.48	5001.3
	707	1.3315	0.1841	797.75	6030.8
0.8	175	0.365	0.2039	62.89	633.8
	220	0.4572	0.2032	99.35	993.3
	470	0.8316	0.173	408.87	2780.7
	707	1.0612	0.1467	714.44	3611.3
1 (OUT)	175	0.2556	0.1428	0	192.8
	220	0.3202	0.1423	0	299.2
	470	0.6517	0.1356	0	1080.3
	707	0.9242	0.1278	0	1899.8

3. λ/g=100

3.1. t/λ =0.3

Table C-7 Normalized data for λ/g=100, t/λ =0.3

X_n	MMF	B_t	P_n	F_t	F_n
0 (IN)	125	0.9877	0.3245	0	1624.8
	200	1.467	0.3012	0	3581.4
	350	1.7754	0.2083	0	5159.9
	525	1.955	0.1529	0	6113.4
0.2	125	0.767	0.2519	49.86	1146.2
	200	1.1981	0.246	126.43	2798.2
	350	1.5998	0.1877	294.96	4731.6
	525	1.7925	0.1402	471.99	5479.2
0.4	125	0.4972	0.1633	52.09	617.9
	200	0.7794	0.16	132.84	1502.1
	350	1.1125	0.1305	364.63	2677.2
	525	1.3545	0.1059	651.98	3275.4
0.6	125	0.2174	0.0714	47.47	71.8
	200	0.345	0.0708	117.21	173.1
	350	0.5837	0.0685	304.85	425.9
	525	0.8392	0.0656	548.97	744.2
0.8	125	0.1424	0.0468	3.84	6.9
	200	0.2279	0.0468	9.82	17.7
	350	0.3984	0.0468	30.08	54.2
	525	0.5978	0.0467	67.62	121.8
1 (OUT)	125	0.1338	0.0439	0	5.3
	200	0.2142	0.0439	0	13.6
	350	0.3744	0.0439	0	41.7
	525	0.5615	0.0439	0	93.8

3.2. $t/\lambda = 0.4$

Table C-8 Normalized data for $\lambda/g=100$, $t/\lambda = 0.4$

X_n	MMF	B_t	P_n	F_t	F_n
0 (IN)	125	0.9551	0.4183	0	2142.8
	200	1.4373	0.3935	0	4852.2
	350	1.7431	0.2727	0	7069.2
	525	1.9131	0.1995	0	8394.3
0.2	125	0.7921	0.3469	49.33	1670.7
	200	1.2365	0.3385	125.07	4078.4
	350	1.6142	0.2525	285.68	6742
	525	1.7869	0.1863	441.13	7859.5
0.4	125	0.596	0.261	51.33	1152.6
	200	0.9336	0.2556	130.86	2819.8
	350	1.2851	0.201	355.43	4954
	525	1.4717	0.1535	636.35	5780.2
0.6	125	0.3908	0.1712	52	620.1
	200	0.6121	0.1676	132.68	1507
	350	0.8802	0.1377	363.73	2684.9
	525	1.0789	0.1125	650.26	3292.2
0.8	125	0.179	0.0784	46.31	73.2
	200	0.2841	0.0778	114.23	176.5
	350	0.4821	0.0754	295.71	436.5
	525	0.695	0.0725	528.23	767.8
1 (OUT)	125	0.1304	0.0571	0	10.2
	200	0.2085	0.0571	0	26.2
	350	0.3651	0.0571	0	80.1
	525	0.5475	0.0571	0	180.2

3.3. $t/\lambda = 0.5$

Table C-9 Normalized data for $\lambda/g=100$, $t/\lambda = 0.5$

X_n	MMF	B_t	P_n	F_t	F_n
0 (IN)	125	0.9341	0.5114	0	2653.7
	200	1.4177	0.4851	0	6116
	350	1.7229	0.3369	0	8984.7
	525	1.8873	0.246	0	10688.8
0.2	125	0.8058	0.4412	48.83	2187.7
	200	1.2578	0.4304	123.36	5340.4
	350	1.6202	0.3168	276.63	8688.9
	525	1.7839	0.2325	450.36	10184.2
0.4	125	0.6534	0.3578	50.57	1678
	200	1.0245	0.3506	128.7	4180.2
	350	1.3896	0.2717	345.12	7202.6
	525	1.5515	0.2023	608.03	8235.7
0.6	125	0.4964	0.2718	50.58	1155.9
	200	0.7795	0.2667	129.1	2827.9
	350	1.0795	0.2111	350.46	4970.3
	525	1.2549	0.1636	629.48	5820
0.8	125	0.3346	0.1832	48.39	623.6
	200	0.525	0.1797	123.38	1516
	350	0.7636	0.1493	334.83	2711
	525	0.9475	0.1235	585	3351
1 (OUT)	125	0.2041	0.1118	0	140.7
	200	0.3232	0.1106	0	338.9
	350	0.5421	0.106	0	830.2
	525	0.7699	0.1004	0	1440.8

4. λ/g=150

4.1. t/λ =0.3

Table C-10 Normalized data for λ/g=150, t/λ =0.3

X_n	MMF	B_t	P_n	F_t	F_n
0 (IN)	90	1.0304	0.3134	0	1860.6
	150	1.5224	0.2778	0	4044.1
	250	1.7979	0.1969	0	5525.2
	380	1.9818	0.1428	0	6520.4
0.2	90	0.7774	0.2365	39.52	1299.1
	150	1.2287	0.2242	108.11	3231.6
	250	1.5478	0.1695	245.98	4828.8
	380	1.7354	0.125	426.26	5531.7
0.4	90	0.4826	0.1468	40.89	689.3
	150	0.7693	0.1404	112.36	1723.8
	250	1.0183	0.1115	273.11	2639.5
	380	1.22	0.0879	493.5	3125.6
0.6	90	0.175	0.0532	37.27	55.7
	150	0.288	0.0526	98.12	142
	250	0.4651	0.0509	229.36	314.7
	380	0.6779	0.0488	416.35	554.5
0.8	90	0.1113	0.0339	1.9	4.2
	150	0.1856	0.0339	5.28	11.7
	250	0.3093	0.0339	14.65	32.5
	380	0.4701	0.0339	33.83	75.1
1 (OUT)	90	0.1059	0.0322	0	3.4
	150	0.1766	0.0322	0	9.5
	250	0.2943	0.0322	0	26.4
	380	0.4473	0.0322	0	60.9

4.2. $t/\lambda = 0.4$

Table C-11 Normalized data for $\lambda/g=150$, $t/\lambda = 0.4$

X_n	MMF	B_t	P_n	F_t	F_n
0 (IN)	90	1.0015	0.4062	0	2448.3
	150	1.4955	0.3639	0	5448.2
	250	1.7657	0.2578	0	7500.3
	380	1.9384	0.1862	0	8877.2
0.2	90	0.8149	0.3305	39.04	1898.3
	150	1.2833	0.3123	106.45	4689.3
	250	1.5846	0.2314	234.53	6905.6
	380	1.7512	0.1682	407.05	7960.4
0.4	90	0.6005	0.2435	40.25	1303.7
	150	0.9525	0.2318	110.49	3246.6
	250	1.2191	0.178	265.73	4910.1
	380	1.3857	0.1331	484.04	5645
0.6	90	0.3761	0.1525	40.88	690.5
	150	0.6009	0.1462	112.36	1726.6
	250	0.7996	0.1167	272.73	2644.2
	380	0.9642	0.0926	492.27	3135.3
0.8	90	0.1425	0.0578	36.74	56.5
	150	0.235	0.0572	96.65	144.2
	250	0.3804	0.0555	225.24	320.9
	380	0.5561	0.0534	406.84	568.8
1 (OUT)	90	0.1002	0.0406	0	6
	150	0.1669	0.0406	0	16.7
	250	0.2782	0.0406	0	46.4
	380	0.4229	0.0406	0	107.1

4.3. t/λ =0.5

Table C-12 Normalized data for λ/g=150, t/λ =0.5

X_n	MMF	B_t	P_n	F_t	F_n
0 (IN)	90	0.9822	0.4979	0	3024
	150	1.4779	0.4495	0	6841.4
	250	1.7456	0.3186	0	9471.7
	380	1.9118	0.2295	0	11229.1
0.2	90	0.8352	0.4234	38.47	2484.6
	150	1.313	0.3994	104.94	6107.3
	250	1.6044	0.2928	228.48	8903.6
	380	1.7623	0.2116	396.6	10327.5
0.4	90	0.668	0.3386	39.65	1903.1
	150	1.0583	0.3219	108.57	4711.4
	250	1.3469	0.2458	259.09	7058.9
	380	1.5048	0.1807	471.07	8116.7
0.6	90	0.4951	0.251	39.95	1305.2
	150	0.7873	0.2395	109.55	3250.5
	250	1.0143	0.1851	262.83	4916.9
	380	1.1663	0.14	477.19	5659.6
0.8	90	0.3165	0.1604	39.13	692.1
	150	0.5068	0.1541	107.28	1731.3
	250	0.6811	0.1243	258.39	2657.6
	380	0.8314	0.0998	459.09	3166.8
1 (OUT)	90	0.1633	0.0828	0	109.4
	150	0.2685	0.0817	0	278.4
	250	0.4299	0.0784	0	614.6
	380	0.619	0.0743	0	1075.6

5. λ/g=200

5.1. t/λ =0.3

Table C-13 Normalized data for λ/g=200, t/λ =0.3

X_n	MMF	B_t	P_n	F_t	F_n
0 (IN)	70	1.0484	0.3075	0	1972.9
	110	1.4973	0.2795	0	4009.2
	190	1.7997	0.1945	0	5661.6
	270	1.9595	0.149	0	6547.2
0.2	70	0.7813	0.2292	32.03	1372
	110	1.1748	0.2193	78.31	3075.6
	190	1.5051	0.1626	195.27	4764.8
	270	1.6546	0.1258	316.89	5358.7
0.4	70	0.477	0.1399	33.01	722.8
	110	0.7221	0.1348	80.73	1629.7
	190	0.9688	0.1047	208.36	2579.1
	270	1.1144	0.0847	345.55	2925.4
0.6	70	0.1529	0.0449	30.12	45
	110	0.2381	0.0444	70.93	103
	190	0.3992	0.0431	176.34	242.3
	270	0.5499	0.0418	291.99	391.3
0.8	70	0.0985	0.0289	1.05	3.1
	110	0.1547	0.0289	2.6	7.8
	190	0.2673	0.0289	7.75	23.2
	270	0.3797	0.0289	15.66	46.8
1 (OUT)	70	0.0942	0.0276	0	2.7
	110	0.1481	0.0276	0	6.6
	190	0.2557	0.0276	0	19.8
	270	0.3634	0.0276	0	40

5.2. t/λ =0.4

Table C-14 Normalized data for λ/g=200, t/λ =0.4

X_n	MMF	B_t	P_n	F_t	F_n
0 (IN)	70	1.0205	0.3991	0	2589.1
	110	1.4712	0.3661	0	5371.4
	190	1.7674	0.2546	0	7642.7
	270	1.9171	0.1944	0	8851.3
0.2	70	0.8242	0.3223	31.57	2004.2
	110	1.2381	0.3081	77.02	4470.3
	190	1.5625	0.2251	188.61	6819.2
	270	1.6983	0.1722	306.67	7713.4
0.4	70	0.604	0.2362	32.44	1374.9
	110	0.911	0.2267	79.3	3082.8
	190	1.1932	0.1719	202.31	4792.9
	270	1.336	0.1355	336.41	5400.6
0.6	70	0.3715	0.1453	32.97	723.5
	110	0.5632	0.1402	80.67	1631.3
	190	0.7591	0.1094	208.09	2582.6
	270	0.8777	0.089	344.88	2932.5
0.8	70	0.1241	0.0485	29.82	45.7
	110	0.1934	0.0481	70.22	104.5
	190	0.3248	0.0468	174.26	246.8
	270	0.4484	0.0455	287.98	400.4
1 (OUT)	70	0.0869	0.034	0	4.3
	110	0.1366	0.034	0	10.7
	190	0.2359	0.034	0	31.9
	270	0.3352	0.034	0	64.5

5.3. $t/\lambda = 0.5$

Table C-15 Normalized data for $\lambda/g=200$, $t/\lambda = 0.5$

X_n	MMF	B_t	P_n	F_t	F_n
0 (IN)	70	1.0011	0.4894	0	3188.3
	110	1.4538	0.4522	0	6717.9
	190	1.7472	0.3147	0	9618.6
	270	1.8911	0.2397	0	11155.2
0.2	70	0.8467	0.4139	31.17	2618.5
	110	1.2727	0.3959	75.9	5827.4
	190	1.5894	0.2862	185.37	8795.6
	270	1.7194	0.2179	302.55	10006.5
0.4	70	0.675	0.33	31.91	2006.8
	110	1.0187	0.3169	77.91	4478.9
	190	1.3288	0.2393	197.2	6876
	270	1.4664	0.1858	328.11	7780.9
0.6	70	0.4965	0.2427	32.23	1375.4
	110	0.7502	0.2334	78.82	3084.3
	190	0.9892	0.1782	200.63	4797.1
	270	1.1122	0.141	333.06	5409.1
0.8	70	0.3093	0.1512	32.13	724.3
	110	0.4698	0.1461	78.24	1633.6
	190	0.6393	0.1151	200.48	2590.9
	270	0.7457	0.0945	329.56	2949.6
1 (OUT)	70	0.141	0.0689	0	88.4
	110	0.2189	0.0681	0	202.1
	190	0.3636	0.0655	0	473.2
	270	0.4964	0.0629	0	760

6. λ/g=250

6.1. t/λ =0.3

Table C-16 Normalized data for λ/g=250, t/λ =0.3

X_n	MMF	B_t	P_n	F_t	F_n
0 (IN)	55	1.0159	0.3034	0	1879.3
	90	1.5041	0.2745	0	4102.7
	160	1.8207	0.1869	0	5856.1
	230	1.9827	0.1416	0	6754.7
0.2	55	0.7518	0.2245	24.69	1304.7
	90	1.1706	0.2136	65.21	3109.8
	160	1.5179	0.1558	170.53	4770.3
	230	1.6613	0.1186	281.87	5352.2
0.4	55	0.4561	0.1362	25.39	685.3
	90	0.7147	0.1304	67.2	1648.9
	160	0.9592	0.0985	179.14	2576
	230	1.1021	0.0787	299.39	2897.5
0.6	55	0.1338	0.04	23.27	35
	90	0.2168	0.0396	59.15	86.2
	160	0.374	0.0384	152.58	210.2
	230	0.5215	0.0372	254.67	343.3
0.8	55	0.088	0.0263	0.58	2.4
	90	0.144	0.0263	1.56	6.5
	160	0.2561	0.0263	4.95	20.6
	230	0.3681	0.0263	10.26	42.5
1 (OUT)	55	0.085	0.0254	0	2.2
	90	0.1391	0.0254	0	5.8
	160	0.2472	0.0254	0	18.3
	230	0.3554	0.0254	0	37.8

6.2. $t/\lambda = 0.4$

Table C-17 Normalized data for $\lambda/g=250$, $t/\lambda = 0.4$

X_n	MMF	B_t	P_n	F_t	F_n
0 (IN)	55	0.9891	0.3938	0	2458.6
	90	1.4779	0.3596	0	5478.4
	160	1.7871	0.2446	0	7880.6
	230	1.9383	0.1846	0	9112.1
0.2	55	0.7949	0.3165	24.26	1903
	90	1.2381	0.3013	64.08	4511
	160	1.58	0.2163	166.17	6841.8
	230	1.7111	0.1629	275.69	7717
0.4	55	0.5813	0.2315	24.91	1306.2
	90	0.9092	0.2212	65.81	3113.9
	160	1.199	0.1641	173.28	4780.8
	230	1.3388	0.1275	290.33	5370.9
0.6	55	0.3535	0.1408	25.41	685.6
	90	0.5548	0.135	67.17	1649.8
	160	0.7492	0.1025	178.94	2579.5
	230	0.8663	0.0825	299.02	2904.7
0.8	55	0.1085	0.0432	23.15	35.5
	90	0.176	0.0428	58.78	87.5
	160	0.3042	0.0416	151.38	214.4
	230	0.4252	0.0405	252.18	352.1
1 (OUT)	55	0.0767	0.0305	0	3.3
	90	0.1254	0.0305	0	8.7
	160	0.223	0.0305	0	27.6
	230	0.3206	0.0305	0	57.1

6.3. $t/\lambda = 0.5$

Table C-18 Normalized data for $\lambda/g=250$, $t/\lambda = 0.5$

X_n	MMF	B_t	P_n	F_t	F_n
0 (IN)	55	0.9698	0.4827	0	3018
	90	1.4601	0.4441	0	6834.7
	160	1.7661	0.3022	0	9896.5
	230	1.9114	0.2275	0	11456.6
0.2	55	0.8176	0.407	23.86	2480.6
	90	1.2735	0.3874	63.05	5872.1
	160	1.606	0.2748	164.33	8845.3
	230	1.7322	0.2062	272.91	10036.6
0.4	55	0.6503	0.3237	24.49	1904.2
	90	1.0182	0.3097	64.64	4515.3
	160	1.3239	0.2265	169.52	6858
	230	1.4559	0.1733	284.54	7740.7
0.6	55	0.476	0.2369	24.78	1306.2
	90	0.7454	0.2267	65.5	3114.7
	160	0.9891	0.1692	172.33	4784.7
	230	1.1104	0.1322	288.34	5379.2
0.8	55	0.2926	0.1456	24.81	686
	90	0.4599	0.1399	65.6	1651.3
	160	0.6267	0.1072	174.08	2586.2
	230	0.7316	0.0871	288.74	2918.8
1 (OUT)	55	0.1217	0.0606	0	68.7
	90	0.1968	0.0598	0	168.9
	160	0.336	0.0575	0	410
	230	0.4638	0.0552	0	665.6